PROCEEDINGS BOOK OF THE 3RD INTERCONTINENTAL GEOINFORMATION DAYS

17-18 NOV 2021
MERSİN, TURKEY

MERSIN UNIVERSITY - ENGINEERING FACULTY
DEPARTMENT OF GEOMATICS ENGINEERING

IGD
Intercontinental Geoinformation Days

ISBN: 978 - 625 - 44303 - 7 - 4 | http://igd.mersin.edu.tr/

The proceedings of the

3rd Intercontinental Geoinformation Days

Editor-in-Chief

Prof. Dr. Murat YAKAR

Editors

Assoc. Prof. Dr. Erdinç AVAROĞLU

Asst. Prof. Dr. Muzaffer Can İBAN

Asst. Prof. Dr. Ali ULVİ

Asst. Prof. Dr. Lütfiye KUŞAK

Asst. Prof. Dr. Fatma BÜNYAN ÜNEL

Res. Asst. Aydın ALPTEKİN

Res. Asst. Abdurahman Yasin YİĞİT

Res. Asst. Mehmet Özgür ÇELİK

Eng. Engin KANUN

ISBN: 978-625-44303-7-4

Mersin, 2021

HONOR BOARD

Ali İhsan SU - Governor of Mersin Province
Prof. Dr. Ahmet ÇAMSARI - Rector of Mersin University
Prof. Dr. Orhan AYDIN - Rector of Tarsus University
Mehmet Zeki ADLI – Director of Turkish Land Registry and Cadastre
Prof. Dr. Rudolf STAIGER - FIG President
Prof. Dr. Christian HEIPKE - ISPRS President
Prof. Dr. Chryssy POTSIOU - FIG President (2015-2018)
Prof. Dr. Haluk ÖZENER – Boğaziçi University Director of Kandilli Observatory
Dr. Orhan ERCAN - FIG Vice President

EXECUTIVE COMMITTEE

Prof. Dr. Abdurrahman EYMEN – Erciyes University, TURKEY
Prof. Dr. Alexander SAGAYDAK – State University of Land Use Planning, RUSSIA
Prof. Dr. Alias Abdul RAHMAN – Universiti Teknologi Malaysia (UTM), MALAYSIA
Prof. Dr. Andreas GEORGOPOULOS – National Technical University of Athens, GREECE
Prof. Dr. Ariel BLANCO – University of Philippines at Daliman, PHILIPPINES
Prof. em. Dr.-Ing. Dr.h.c. Armin GRÜN – ETH Zürich, SWITZERLAND
Prof. Dr. Ashutosh MOHANTY – Shoolini University, INDIA
Prof. Dr. Aydın ÜSTÜN – Kocaeli University, TURKEY
Prof. Dr. Bashkim IDRIZI – University of Prishtina, KOSOVO
Prof. Dr. Bülent BAYRAM – Yıldız Technical University, TURKEY
Prof. Dr. Charles TOTH – Ohio State University, USA
Prof. Dr. Chryssy POTSIOU – National Technical University of Athens, GREECE
Prof. Dr. Çetin CÖMERT – Karadeniz Technical University, TURKEY
Prof. Dr. Dursun Zafer ŞEKER – Istanbul Technical University, TURKEY
Prof. Dr. Erkan BEŞDOK – Erciyes University, TURKEY
Prof. Dr. Ferruh YILDIZ – Konya Technical University, TURKEY
Prof. Dr. Fevzi KARSLI – Karadeniz Technical University, TURKEY
Prof. Dr. Füsun BALIK ŞANLI – Yıldız Technical University, TURKEY
Prof. Dr. Hacı Murat YILMAZ – Aksaray University, TURKEY
Prof. Dr. Hediye ERDOĞAN – Aksaray University, TURKEY
Prof. Dr. Haluk ÖZENER – Boğaziçi University, TURKEY
Prof. Dr. Hande DEMİREL – Istanbul Technical University, TURKEY
Prof. Dr. Jiyoon KIM – University of Seoul, REPUBLIC OF KOREA
Prof. Dr. Maria Antonia BROVELLI – Politecnico di Milano, ITALY
Prof. Dr. Mevlüt YETKİN – İzmir Katip Çelebi University, TURKEY
Prof. Dr. Muhammad Bilal – Nanjing University of Information Science and Technology, CHINA
Prof. Dr. Mustafa YANALAK – Istanbul Technical University, TURKEY
Prof. Dr. Naser EL-SHEIMY – University of Calgary, CANADA
Prof. Dr. Nebiye MUSAOĞLU – Istanbul Technical University, TURKEY
Prof. Dr. Nilanchal PATEL – Birla Institute of Technology Mesra, INDIA
Prof. Dr. Niyazi ARSLAN – Çukurova University, TURKEY
Prof. Dr. Pal NIKOLLI – University of Tirana, ALBANIA
Prof. Dr. Reha Metin ALKAN – Istanbul Technical University, TURKEY
Prof. Dr. Sebahattin BEKTAŞ – Ondokuz Mayıs University, TURKEY
Prof. Dr. Sujit MANDAL – Diamond Harbour Womens' University, INDIA
Prof. Dr. Tahsin YOMRALIOĞLU – Beykent University, TURKEY
Prof. Dr. Tayfun ÇAY – Konya Technical University, TURKEY
Prof. Dr. Tamer BAYBURA – Afyon Kocatepe University, TURKEY
Prof. Dr. Tarık TÜRK – Cumhuriyet University, TURKEY
Prof. Dr. Taşkın KAVZOĞLU – Gebze Technical University, TURKEY
Prof. Dr. Uğur DOĞAN – Yıldız Technical University, TURKEY
Prof. Dr. Yasemin ŞİŞMAN – Ondokuz Mayıs University, TURKEY
Prof. Dr. Youkyung HAN – Kyungpook National University, REPUBLIC OF KOREA
Assoc. Prof. Dr. Anargha DHORDE – Nowrosjee Wadia College, INDIA
Assoc. Prof. Dr. Aziz ŞİŞMAN – Ondokuz Mayıs University, TURKEY
Assoc. Prof. Dr. Bihter EROL – Istanbul Technical University, TURKEY
Assoc. Prof. Dr. Cevdet Coşkun AYDIN – Hacettepe University, TURKEY
Assoc. Prof. Dr. Erol YAVUZ – Uşak University, TURKEY
Assoc. Prof. Dr. Fatih DÖNER – Gümüşhane University, TURKEY
Assoc. Prof. Dr. Fatih POYRAZ – Cumhuriyet University, TURKEY
Assoc. Prof. Dr. Halil AKINCI – Artvin Çoruh University, TURKEY
Assoc. Prof. Dr. Khalil Valizadeh KAMRAN – University of Tabriz, IRAN
Assoc. Prof. Dr. Lyubka PASHOVA – Bulgarian Academy of Sciences, BULGARIA
Assoc. Prof. Dr. Murat UYSAL – Afyon Kocatepe University, TURKEY
Assoc. Prof. Dr. Özgün AKÇAY – Çanakkale Onsekiz Mart University, TURKEY
Assoc. Prof. Dr. Serdar EROL – Istanbul Technical University, TURKEY
Assoc. Prof. Dr. Şükran YALPIR – Konya Technical University, TURKEY

ORGANIZING COMMITTEE

Mersin University - Faculty of Engineering - Department of Geomatics Engineering

Prof. Dr. Murat YAKAR – Conference Chairman – Head of Department
Asst. Prof. Dr. Muzaffer Can İBAN – Conference Secretary
Assoc. Prof. Dr. Erdinç AVAROĞLU
Asst. Prof. Dr. Ali ULVİ
Asst. Prof. Dr. Fatma BÜNYAN ÜNEL
Asst. Prof. Dr. Lütfiye KUŞAK
Dr. Hakan DOĞAN – Turkish State Meteorological Service
Lect. Atilla KARABACAK
Lect. Şafak FİDAN
Res. Asst. Abdurahman Yasin YİĞİT
Res. Asst. Aydın ALPTEKİN
Res. Asst. Mehmet Özgür ÇELİK
Eng. Engin KANUN
Eng. Seda Nur Gamze HAMAL
Eng. Veli YILDIZ
Eng. Mücahit Emre ORUÇ

17 November 2021 - Wednesday	
09:15-09:45	Opening
09:45-10:15	Land Management (Chair: Prof. Dr. Chryssy POTSIOU – FIG Honorary President) **Spatio-Temporal analysis of climate change in India: A theoretical perspective** Rajaram Patil, Moushumi Datta **Investigation of assembly centers in the disaster areas in Merkez District of Uşak Province in Turkey** Fatma Yüksel, Fatih Taktak **Developing 3D real estate tax visualization / management system with GIS based procedural modelling approach** Sevket Bediroglu
10:15-10:30	Break
10:30-12:00	Remote Sensing & Photogrammetry - 1 (Chair: Dr. Artur GIL - University of the Azores, Portugal)
	Analysis of forest degradation by using GIS and remote sensing: A case study of Chandoli National Park Kolhapur in Maharashtra State Rajaram Patil, Govardhan Ubale **Mapping of flood areas using Sentinel-1 Synthetic Aperture Radar (SAR) images with Google Earth Engine cloud platform – A case study of Chamoli district, Uttarakhand- India** Mohammed Faizan, Gobinath Palanisamy **Using Sentinel-1 GRD Sar Data for volcanic eruptions monitoring: The Case-Study of Fogo Volcano (Cabo Verde) in 2014/2015** Rafaela Tiengo, José Pacheco, Jéssica Uchôa, Artur Gil **Determination of vineyards with support vector machine and deep learning-based image classification** Özlem Akar, Ekrem Saralıoğlu, Oğuz Güngör, Halim Ferit Bayata **Assessing the interrelationship between LST, NDVI, NDBI and land cover change in Amuwo-Odofin, Lagos Nigeria** Alfred Sunday Alademomi, Chukwuma John Okolie, Daramola Olagoke, Samuel Akinnusi, Elias Adediran, Hamed Olanrewaju, Abiodun Olawale Alabi, Tosin Salami, Joseph Odumosu **Detecting changes in Mangrove Forests along the Bintang Bolong Estuary, Gambia using Google Earth Engine, Sentinel-2 Imagery and random forest classification** Lisah Ligono, Chukwuma Okolie **Remote sensing approach for aerosol optical thickness (AOT) monitoring in relation to the road network in Lagos Metropolis, Nigeria** Chukwuma Okolie, Emmanuel Ayodele, Erom Mbu-Ogar, Samuel Akinnusi, Olagoke Daramola, Abdulwaheed Tella, Rose Alani, Alfred Alademomi
12:00-13:00	Lunch Break
13:00-14:15	Surveying & Geodesy (Chair: Assoc. Prof. Dr. Lyubka PASHOVA - National Institute of Geophysics, Geodesy and Geography – Bulgarian Academy of Sciences, Bulgaria)
	Vertical accuracy assessment of Dems around Jabal Al-Shayeb Area, Egypt Ali Shebl, Mohamed Atalla, Árpád Csámer **The current state of use of satellite-based positioning systems in Turkey** Nuri Erdem, Abdulsamet Demirel **Estimation of tidal constituents from sea level registrations in BAB "St. Kliment Ohridski", Livingston Island** Lyubka Pashova, Borislav Alexandrov **Accuracy assessment of positioning based on single and Multi-GNSS** Lukman Abdulmumin, Yusuf Ramalan, Haruna Ibrahim, Abubakar Adamu Musa **Monitoring bathymetric changes of Commodore Channel, Lagos Nigeria** Babatunde Anibaba, Peter Nwilo, Chukwuma Okolie, Michael Orji, Olagoke Daramola **Accuracy assessment of established control within University of Lagos, Nigeria** Abiodun Alabi, Alfred Alademomi, Tosin Salami, Adedayo Okutubo, Wale Oyedokun **Establishment of a geodetic network for the deformation monitoring of the Third Mainland Bridge** Samuel Akintoye, Hamed Olanrewaju, Hannah Abioye, Chukwuma Okolie, Samuel Akinnusi, Adegbite Usman
14:15-14:30	Break
14:30-16:00	Geographic Information Systems 1
	Suitability analysis of solid waste dumpsites in Igabi Lga, Kaduna State – Nigeria Kaka Atta, MUHAMMAD NURA Idris, Yabo Stephen, Lukman Olawunmi Giwa **Comparative analysis of pedestrian stride length methods** Nimet Karagöz, Fatih Gülgen **Monitoring and prediction of land cover change in Anambra River Basin using cellular automata and markov chain technique** Peter Nwilo, Nna-Njar Gertrude Njar, Utibe Bassey Inyang, Chukwuma John Okolie, Olagoke Emmanuel Daramola, Michael Joseph Orji, Hamed Olabode Olanrewaju, Samuel Akinbola Akinnusi, Andy Osagie Egogo-Stanley **Geospatial intelligence (Geoint) with Geographic Information Systems (GIS)** Halil İbrahim Onyil **Age and gender differences in perceptions and health impacts of noise in an academic environment** Alfred Alademomi, Johanson Onyegbula, Rahmat Adepo, Chukwuma Okolie, Abiodun Alabi, Babatunde Ojegbile, Olagoke Daramola, Nehemiah Alozie, Samuel Akinnusi, Taiwo Adewale **FAHP And GIS based land use suitability analysis for agriculture in Aksaray City, Turkey** Süleyman Sefa Bilgilioğlu

18 November 2021 - Thursday	
09:00-10:30	Remote Sensing & Photogrammetry 2 **SFM photogrammetry for land use change analysis in a Sub-Urban area of Nigeria** Chima Iheaturu, Chukwuma Okolie, Solomon Musa, Emmanuel Ayodele, Andy Egogo-Stanley **Monitoring the change of coastline with remote sensing and GIS: A case study from Izmit and Gemlik Gulfs, Turkey** Tümay Arda, Melis Uzar **Analysis of Land-Use/Land-Cover dynamics in Ibadan Metropolis, Oyo State, Nigeria** Aliyu Zailani Abubakar, Swafiyudeen Bawa, Yahaya Abbas Aliyu, Tarwase Tosin Youngu, Usman Sa'i Ibrahim, Ayo Olalekan Fatoyinbo **Fully automated drought analysis from the products of the moderate resolution imaging spectroradiometer (MODIS)** Ali Levent Yagci **Development of a user-friendly program: "Real-Time Image Properties Display"** James Olaleye, Abiodun Alabi, Alfred Alademomi, Damilola Olatayo, Tosin Salami **Determination of Karina Lagoon surface area water temperature changes using remote sensing methods** Elif Akyel, Özşen Çorumluoğlu **Using remote sensing to monitor aerosol optical thickness (AOT) and its relationship with land cover in Lagos Metropolis, Nigeria** Emmanuel Ayodele, Chukwuma Okolie, Samuel Akinnusi, Erom Mbu-Ogar, Olagoke Daramola, Abdulwaheed Tella, Rose Alani, Alfred Alademomi
10:30-10:45	Break
10:45-12:00	Geographic Information Systems 2 **Mapping federal government dams in Nigeria** Sola Oluwayemi, Adedayo Olayiwola **Monitoring the spatial distribution of CO2 within the University of Lagos Main Campus** Alfred Alademomi, Musa Animashaun, Oluwatimileyin Abolaji, Chukwuma Okolie, Babatunde Ojegbile, Olagoke Daramola, Nehemiah Alozie **Spatial relationship between NDVI, EVI, SAVI and land cover changes in the Lake Chad area from 1987 to 2017** Peter Nwilo, Chukwuma Okolie, Abdulkareem Umar, Samuel Akinnusi, Babatunde Ojegbile, Hamed Olanrewaju **Assessment of noise levels and associated health impacts in an academic environment** Alfred Alademomi, Johanson Onyegbula, Rahmat Adepo, Chukwuma Okolie, Babatunde Ojegbile, Abiodun Alabi, Olagoke Daramola, Nehemiah Alozie, Andy Egogo-Stanley, Inioluwa Ayantayo **Application of GIS and analytical hierarchy process for flood vulnerability assessment in Adamawa Catchment, Nigeria** Ayila Adzandeh, Dupe Olayinka-Dosunmu, Isa Hamid-Mosaku, Chukwuma Okolie, Peter Nwilo, Caleb Ogbeta **Locational analysis of infrastructural facilities in selected oil and non–oil producing areas of Akwa İbom State** Mbom-Abasi Inyang, Alabi Soneye, Chukwuma Okolie, Shakirudeen Odunuga, Johanson Onyegbula, Samuel Akinnusi, Hamed Olanrewaju
12:00-13:00	Lunch Break
13:00-14:15	Remote Sensing & Photogrammetry 3 **Comparative analysis of forest change by type of Natural Park using clear cuts method** Eun Ha Park, Ji Young Kim, Jin Won Kim, Byeong-Hyeok Yu **Shallow-water bathymetry using Landsat 8 imagery – Example of Ibafon Creek** Chukwuma Okolie, Emmanuel Ayodele, Oluwatobi Raji, Waliyah Adedokun, Olagoke Daramola, Samuel Akinnusi, Hamed Olanrewaju **Vegetation mapping from vegetation indices using a UAV-based sensor** Emmanuel Ayodele, Chukwuma Okolie, Imole Okediji **Evaluation of Landsat and MODIS imagery fusion for high-resolution evapotranspiration mapping over large agricultural area** Ayoub Moradi **Accuracy assessment and conflation of DEMs over Kaduna State, Nigeria** Swafiyudeen Bawa, Moses Mefe, Ebenezer ayobami Akomolafe, Monye Joseph Chukwuweta, Lukman Abdulmumin, Abubakar Adamu Musa **Applications of remote sensing in solving Myriads of Geological Problems: A review** Ogbonna Okpuru, Maruf Orewole, Sunday Olotu **3D modeling of underwater objects using photogrammetric techniques and software comparison** Seda Nur Gamze Hamal, Ali Ulvi **Documentation of cultural heritage by photogrammetric methods: a case study of Aba's Monumental Tomb** Engin Kanun, Aydın Alptekin, Murat Yakar

CONTENTS **Page**

Intercontinental Geoinformation Days

igd.mersin.edu.tr

Spatio-temporal analysis of climate change in India: a theoretical perspective

Rajaram Patil[*1], **Moushumi Datta** [2]

[1]*University of Mumbai, A. And C. College Phondaghat, Department of Geography, Sindhudurg, India*
[2]*University of Mumbai, N. K. College, Malad, Department of Geography, Mumbai, India*

Keywords
Climate change
Human life
Agriculture
Urban areas
Health

ABSTRACT

Climate Change has affected human activities directly and indirectly. There have been several causes and impacts of climate change. Due to climate change, there have been changes in the pattern of rainfall, rise in temperatures, evaporation, and salinization of sources of water due to rising sea levels. Glacial melting is increasing year by year. Climate change is due to the observable but micro level alterations in the Earth's orbit that are responsible for changing the amount of solar energy the planet receives. satellites orbiting around Earth and other related technological advances have given a helping hand to the scientists to be able to capture remotely sensed data so that the planet can be studied from all the angles and aspects. Though climate change is a global concern, its effects are being experienced all over the globe but, at varying degree. It will have negative impacts on agriculture, supply of water, quality of air, coastal areas and health of people. India is the second largest country in terms of population and heavily depends on the various sectors like agriculture, fisheries, and forests which are sensitive to changes in climate. It is, therefore, bound to face the worst adverse impacts of climate change.

1. Introduction

The World Bank suggests that the districts that fall in central India show maximum vulnerability to changes in climate as they lack the required infrastructure and depend on agriculture on a very large scale. The districts in Vidarbha region of Maharashtra state are especially vulnerable to the damages caused by climate change. A major source for the decline in income of the farmers has been the changes in the climate. Increased temperature and disturbed precipitation are found to be damaging the crop yields and, consequently, the wealth of the farmers. Industrialization induced climate change, is the major cause of global warming and changing patterns of rainfall. Also, according to the estimation of the World Bank, unattended climate change would cause the Indian average temperature to rise to 29.1°C in the next few decades. As the aspect of changing climate becomes more intense, it will affect several parts of India extremely. When the average temperature in 2009-18 to the that in 1950-80 are compared, it is found that some pockets have already been affected by climate change by becoming hotter than before. In several parts of states like Rajasthan, Gujarat, Tamil Nadu, Kerala, and the North-East, it is observed that, there has been a rise of nearly 1° C in the average temperature during the last decade. İt is higher than the historical average in the 1950-80 period.

Changes in climate have always been harmful to man. An increase of 0.3 - 0.6 ^{0}C is observed in the he average surface temperature of the globe since the several centuries. The rise in temperature may be minimal, but it can be disastrous with unrepairable impacts. There are noticeable impacts of changing climate which occur in the form of melting of glaciers, forest fires, changing rainfall patterns, rising of sea levels, coastal cities under water level, floods, and droughts. Tsunami (2004), Uttarakhand flash floods (2013), Kashmir floods (2014), Kerala flood (2018 & 2019) and Krishna River Basin floods (2019) are some examples in various parts of India. India has been able to create a stable platform to discuss and bring in better cooperation between the nations on issues related to climate through its pledge for Paris Agreement. Also, India is an example by committing to bring down its emission intensity of gross domestic product (GDP) by 33-35% of 2005 levels by 2030.

* **Corresponding Author**

*(drrajaram75@gmail.com) ORCID ID 0000-0003-3377-5307
(moushumi@nkc.ac.in) ORCID ID 0000-0002-0843-6613

Cite this study

Patil R & Datta M (2021). Spatio-temporal analysis of climate change in India: a theoretical perspective. 3rd Intercontinental Geoinformation Days (IGD), 1-5, Mersin, Turkey

2. Method

This paper based on secondary data collected from various articles, books, journals, reports and other related material published online and offline.

2.1. Research objectives

- To understand the concept of climate change
- To study the major causes of climate change
- To administer the impact of climate change in India

2.2. Study area

India is a country in South Asia. It comprises of twenty-nine states and eight union territories. Its population stands second in the world after China. Its latitudinal extension is between 68^0 and 96^0 East and longitudinal extension is between 8^0 and 36^0 North approximately. It is a major developing country in the world and is the largest democracy too. It is highly agrarian in nature due to its fertile soil and favorable climatic conditions. It is however now being affected by changes in climate making it a matter of concern.

Figure 1. Location of India with States

2.3. Factors leading to climate change greenhouse gases (GHGS)

Major source of climate change is greenhouse effect. The earth's surface warms due to the energy received from the Sun. Most (90 %) of the sun's insolation is absorbed by these gases and radiated back towards the surface. Out of the total energy passing the atmosphere, some of it gets scattered and only some of it gets reflected into the atmosphere from the surface of the Earth. Gases like CO2, methane, and Nox and water vapor, comprise less than 1% of the atmosphere. They are called 'greenhouse gases'. Human activities like decomposition of wastes in land fields, agriculture and rice cultivation and release of carbon dioxide during burning of fuels as coal, oil, and natural gas also lead to an increase in greenhouse gases.

2.3.1. Human activities

Most of the population in India is engaged in agriculture. The agro-based activities, various land-uses, etc., lead to rise in the levels of methane and nitrous oxide. Industries produce greenhouse gases like chlorofluorocarbons, whereas automobiles lead to ozone generation. According to 5th Report of IPCC, approximately 95 % human activities over the past 50 years led to global warming. İndustrialization and urbanization are major factors in the process.

2.3.2. Emission of CO_2

Volcanic eruption is one of the most-deadly natural disasters on the Earth's surface. The eruption releases carbon dioxide (CO_2) in large quantities. It is also emitted through natural processes such as respiration and manmade activities like burning of fossil fuels. This gas directly impacts the environment and human beings.

2.3.3. Ocean currents

71% of the Earth's surface comprises of oceans and water bodies. Hot and cold ocean currents flow along all coastlines. The vast water bodies absorb the sun's insolation twice the atmosphere. Therefore, the oceans form a major component of the climate system.

2.3.4. Water vapor

Atmosphere is getting heated due to solar energy, because of which the amount of water vapor is increasing in the atmosphere day by day. Water vapor rises as the temperature of the Earth's atmosphere rises leading to precipitation. This cycle is very important for the smooth functioning of the ecology on globe.

3. Discussion and results

According to scientists, global temperature will continue increasing for few decades, due to the greenhouse gases emitted due to human activities. It has resulted in the loss of glaciers, rise in sea level, huge floods, droughts, shifting of plant and animal ranges and a change in the pattern of floral reproduction and heat waves. Following are the impacts of climate change on environment and human life.

It is observed from table 01 that the annual mean temperatures of states of India have increased considerably in all the states. Only Chhattisgarh, Haryana, Jammu and Kashmir, Meghalaya, Orissa, Punjab, Uttar Pradesh, Uttarakhand and West Bengal do not show an increase. Sikkim (+0.05 o C/year) tops the chart followed by Manipur (+0.03 o C/year) and the least has been observed in Punjab (-0.01 o C/year). The major reasons for the change is the increase of carbon in the atmosphere and other greenhouse gases.

Table 02 represents that from 1901 to 2010, the highest fluctuations are observed in Meghalaya (+14.68 mm/year) and Andaman and Nicobar (-7.77 mm/year). The driving factors for changes in rainfall may include changes in wind direction and wind speed, occurrences of cyclones, changes in temperature, rate of evaporation and alterations in the land use of the areas. The changing trend implies that the states with high differences in average rainfall have undergone the above conditions and will continue to do so.

Table 1. Mean Temperature Trends, 1901-2010 (State level annual and seasonal mean temperature trends based upon 282 surface meteorological stations for 1951-2010. Increasing (+) and decreasing (-) trends significant at 95% level of significance are shown in bold and marked with '*' sign)

	Mean Temperature Trends in Degree Celsius Per Year				
State	Annual	Winter	Summer	Monsoon	Post monsoon
Andaman and Nicobar Islands	**+0.01***	**+0.01***	**+0.01***	**+0.01***	**+0.01***
Andhra Pradesh	**+0.01***	**+0.01***	**+0.01***	**+0.01***	**+0.01***
Arunachal Pradesh	**+0.01***	**+0.02***	+0.01	+0.01	**+0.02***
Assam	**+0.01***	**+0.01***	No trend	**+0.01***	**+0.02***
Bihar	**+0.01***	No trend	No trend	**+0.01***	**+0.02***
Chhattisgarh	No trend	No trend	-0.01	No trend	+0.01
Delhi	**+0.01***	+0.01	**+0.01***	+0.01	**+0.02***
Goa	**+0.02***	**+0.02***	**+0.02***	**+0.02***	**+0.03***
Gujarat	**+0.01***	**+0.02***	+0.01	**+0.01***	**+0.02***
Haryana	No trend	-0.01	No trend	**-0.01***	+0.01
Himachal Pradesh	**+0.02***	**+0.02***	+0.01	**+0.03***	**+0.02***
Jammu and Kashmir	-0.01	No trend	-0.02	-0.02	**-0.02***
Jharkhand	**+0.01***	+0.01	No trend	No trend	**+0.02***
Karnataka	**+0.01***	**+0.01***	No trend	**+0.01***	**+0.01***
Kerala	**+0.01***	**+0.01***	**+0.01***	**+0.01***	**+0.01***
Lakshadweep	**+0.01***	**+0.02***	**+0.02***	**+0.01***	**+0.01***
Madhya Pradesh	**+0.01***	No trend	No trend	No trend	**+0.03***
Maharashtra	**+0.01***	No trend	**+0.01***	+0.01	**+0.01***
Manipur	**+0.03***	**+0.04***	**+0.02***	**+0.02***	**+0.03***
Meghalaya	No trend	**+0.01***	-0.01	No trend	**+0.02***
Mizoram	**+0.01***	**+0.02***	No trend	**+0.02***	**+0.02***
Orissa	No trend	No trend	No trend	**-0.01***	+0.01
Punjab	**-0.01***	**-0.02***	-0.01	**-0.01***	No trend
Rajasthan	**+0.01***	**+0.01***	No trend	+0.01	**+0.02***
Sikkim	**+0.05***	**+0.05***	**+0.02***	**+0.05***	**+0.04***
Tamil Nadu	**+0.02***	**+0.03***	**+0.03***	**+0.02***	**+0.02***
Tripura	**+0.01***	**+0.01***	**-0.01***	**+0.01***	**+0.03***
Uttar Pradesh	No trend	No trend	-0.01	No trend	**+0.01***
Uttarakhand	-0.01	+0.01	-0.02	**-0.02***	+0.01
West Bengal	No trend	No trend	**-0.01***	**+0.01***	**+0.01***

Table 2. Average Rainfall Trends, 1901-2010 (State level annual and seasonal rainfall trends based upon 1451 rainfall stations for 1951-2010. Increasing (+) and decreasing (-) trends significant at 95% level of significance are shown in bold and marked with '*' sign)

	Mean Temperature Trends in Degree Celsius Per Year				
State	Annual	Winter	Summer	Monsoon	Post monsoon
Andaman and Nicobar Islands	**-7.77***	**-2.70***	-0.51	-2.93	-1.35
Andhra Pradesh	+1.31	+0.29	+0.35	-0.14	+0.46
Arunachal Pradesh	-3.63	-0.10	No trend	-2.30	-0.83
Assam	-2.96	0.08	-0.56	-2.19	-0.75
Bihar	+1.41	-0.06	**+0.59***	+1.11	+0.11
Chhattisgarh	-2.03	+0.02	+0.04	-2.38	+0.06
Delhi	-0.51	+0.16	**+0.40***	-0.32	-0.20
Goa	-3.82	No trend	-0.31	-2.61	+0.04
Gujarat	+1.41	No trend	-0.03	+1.27	-0.02
Haryana	+0.45	+0.07	**+0.39***	-0.01	**-0.23***
Himachal Pradesh	-3.26	-0.18	+0.31	-2.85	-0.21
Jammu and Kashmir	+2.13	**+1.88***	-1.07	-0.16	-0.37
Jharkhand	+0.84	-0.13	+0.43	+0.44	+0.03
Karnataka	-0.05	+0.10	-0.41	+0.61	+0.14
Kerala	-1.43	-0.40	-1.15	-2.42	+1.68
Lakshadweep	+3.22	-0.33	-0.44	+1.73	+0.83
Madhya Pradesh	-1.81	-0.06	No trend	-1.74	+0.03
Maharashtra	-0.71	+0.04	0.15	-0.29	-0.05
Manipur	+1.94	+0.10	+1.63	-0.89	+0.11
Meghalaya	14.68	**+0.52***	+2.25	+9.27	+2.04
Mizoram	+0.33	-0.31	+2.80	+7.71	-6.19
Orissa	+0.69	+0.06	**+0.65***	-0.23	-0.83
Punjab	-2.41	+0.09	+0.22	-1.49	-0.13
Rajasthan	+0.04	+0.02	**+0.17***	-0.09	-0.04
Sikkim	-3.12	-0.12	-0.83	-1.36	-0.11
Tamil Nadu	+0.80	-0.16	-0.47	-1.35*	+1.49
Tripura	+0.77	+0.11	+1.73	-1.11	-0.55
Uttar Pradesh	-4.42*	-0.22	+0.02	**-3.52***	-0.33
Uttarakhand	-1.07	-0.01	+0.86	-1.45	-0.63
West Bengal	**+3.63***	+0.16	**+1.34***	+1.45	+0.19

3.1. Impact of climate change on agriculture

The increasing population has resulted in scarcity of natural resources. Climate change has affected crop productivity due to alterations in temperature and rainfall. It has also caused changes in soil quality due to which the yield of cereals will decline in India.

3.2. Impact of climate change on atmosphere

Climate change may affect health of human beings as it increases ground-level ozone and the particulate matter causing air pollution. Ground-level ozone results in several health issues- diminished lung function, increased hospitalization and fatal incidences of asthma and premature deaths.

3.3. Impact of climate change on urbanization

India's urban system is the second largest on globe. It comprises of 310 million people spread across 5161 urban spaces in 2005. It is surprising to know that 5100 urban centers comprise roughly 30% of the total Indian population which is expected to rise to 40% by 2030. It is projected that the population of 70 urban spaces will rise to 1 million inhabitants by 2025.

3.4. Impact of climate change on health

Climate change affects maximum particularly children, pregnant women and old people. It is expected that between 2030 and 2050, changing climate change may lead to death of 2,50,000 people every year due to problems like malnutrition, malaria, diarrhea, and heat stroke.

3.5. Water borne diseases

Such diseases are vulnerable to climate change and represent variations according to changes in the season. Also, diarrheal diseases are another common occurrence during the monsoon season. Increased variability of rainfall as a result of climate change affect freshwater sources on a large scale globally. It is observed that scarcity of water has already affected 40% people all over the Earth.

3.6. Flood borne diseases

Floods have become common all over the globe which contaminates several freshwater resources and increases the risk of water-borne diseases. If the contamination is due to animal waste, it leads to epidemics of leptospirosis, rotavirus and cholera in the affected areas. Absence of basic sanitation is a major factor in increasing water borne diseases.

3.7. Impact of climate change on migration

Sudden changes in climate lead to migration of people as they become victims of droughts or floods in the rural areas. This leads to overcrowding of the urban spaces and related impacts are experienced. In India, a large chunk of population is estimated to be affected by issues related to global warming in the near future.

3.8. Impact of climate change on poor and the vulnerable people

Climate and weather have a direct and indirect relationship with mankind. Vulnerable and poor populations are mostly affected by climate change due to higher food prices, loss of income, water scarcity, declining health and forced outmigration. The slum dwellers and other migrants and poor who generally live-in vulnerable areas like the riverbeds, flood plains, hill slopes will be extremely affected.

3.9. Impact of climate change on food supply

Temperature is the main component of climate change. Rising temperature and uneven precipitation are responsible to decrease the production of staple crops. Ultimately it will increase the prevalence of malnutrition and under nutrition in most of the country.

3.10. Impact of climate change on transportation

Transportation is very important to human life. Due to disasters like storms, floods, cyclones, coastal flooding, etc., a great damage is caused to the infrastructure of the affected area. The carbon emission in India has always remained very high except the current year 2020 which may be due to the Coronavirus driven lockdown which has reduced the transportation and industrial activities to the minimum in the country.

3.11 Impact of climate change on economy

The World Bank estimates a loss of about 2% in National Gross Domestic Product of the country. It is a result of shortage of clean water and the damage caused to the sectors like agriculture and fisheries, tourism and energy. Therefore, it can be said that when the health is affected, the economy is also affected.

3.12. Impact of climate change on coastal area

According to Aggarwal and Lal, the Indian coast is predicted to undergo a rise in sea level between 30 and 80 cm over the next century. If timely measures are not taken, then, the people living in coastal areas may get affected badly. The coastal cities of Mumbai, Kolkata and Chennai are at an average elevation of 2-10 meters and lie in the Low Elevation Coastal Zone (LECZ) category. Hence, they are most likely to suffer from flooding.

4. Conclusion

From the above, it can be concluded that, in the Indian continent, there has been an increase in the annual mean temperature during the last century. The predicted climate change reveals that the country will experience disastrous events that will enormously impact human life. It must be agreed that the climate is changing and it will surely lead to detrimental impacts Therefore, thinking about measures for mitigation and adaptation, both is equally important. Same is the case with developed nations who are trying hard to cope with the challenges posed by changing climate. However, with a

very large and diverse population, India needs to put more efforts to counter the impacts.

5. Recommendations

Taking into consideration the increasingly changing climate, following are the recommendations to reduce the impact on human race.

- Boosting health care services
- Controlling the growth of vector
- Spreading awareness about health insurance
- Higher investment and greater research in climate change
- Undertaking health risk assessment studies
- Vulnerability mapping using GIS
- Establishment of baseline conditions
- Scenario modeling

Acknowledgement

The present study could not have been completed without the support of Prof. Dr. Mohamed Alkhuzamy Aziz, Dean of Social and Human Sciences, Galala University, Egypt & Principal Dr. Hemant Pednekar, Ex. Senate Member University of Mumbai and the infrastructure provided by respective institutions.

References

Attri, S. D. and Tyagi, Ajit. (2010). Climate profile of India, Met Monograph No. Environment Meteorology-01, Government of India, Ministry of Earth Sciences, India Meteorological Department.

De, U.S., Khole, M. and Dandekar, M.M. (2004). Natural hazards associated with meteorological extreme events. Natural Hazards, 31: 487-497. 21

Green, M.S. et al. (1994). Excess winter-mortality from İs chemic heart disease and stroke during colder and warmer years in Israel'. European Journal of Public Health, 4: 3-11.

Indian Meteorological Department (IMD). All India weekly weather report (Accessed on 17 August 2012) http://www.imd.gov.in. http://www.imd.gov. in/section/nhac/dynamic/week.htmrk.

Martens, P. and McMichael, A.J. (2002). Environmental change, climate, and health. Cambridge, UK, Cambridge University Press.

Marland G, Boden T. A., and Andres R. J. (2000). Global, regional, and national CO2 emission trends: A compendium of data on global change. Oak Ridge, Tennessee, USA: Carbon Dioxide Information Analysis Center, Oak Ridge National Laboratory, U.S. Department of Energy.

Moushumi Datta (2016), Analysis of Air Pollution in selected cities of Maharashtra, THE KONKAN GEOGRAPHER Journal, Vl. No. 15 published by Konkan Geographers Association of India, PP 05-09

Moushumi Datta (2020), Floods in India with special reference to Duars in West Bengal, THE KONKAN GEOGRAPHER Journal, Vl. No. 24 published by Konkan Geographers Association of India, PP 19-22

Pednekar H.M. (2026), Emerging Geo Environmental Issues and Challenges in 21st Century, THE KONKAN GEOGRAPHER Journal, Vl. No. 15 published by Konkan Geographers Association of India, PP 01-04

Vinod Joon and Vaishali Jais. Impact of Climate Change on Human Health in India: An Overview-

Wilby, R.L. (2003). Past and projected trends in London's urban heat island. Weather, 58: 251-260

Intercontinental Geoinformation Days

igd.mersin.edu.tr

Investigation of assembly centers in the disaster areas in Merkez district of Uşak province in Turkey

Fatma Yüksel Doğruyol[*1], **Fatih Taktak** [2]

[1]*Uşak University, Institute of Graduate Education, Uşak, Turkey*
[2]*Uşak University, Faculty of Engineering, Department of Surveying Engineering, Uşak, Turkey*

Keywords
Disaster
Post-Disaster
Geographical
Information Systems
Disaster Response
Planning

ABSTRACT

Within the scope of this study; post-disaster assembly areas in Merkez district of the Uşak province in Turkey, criteria for determining these areas, sizes of the areas, and compliance conditions with the specified standards, would be evaluated. Besides, the distribution of post-disaster assembly areas would be evaluated, and the maps prepared by using Geographical Information Systems (GIS). This study indicates that the assembly areas in Merkez/Uşak are not sufficient, especially in the populous neighborhood, and many of them have infrastructure problems. The distribution of the areas is also another problem in different neighborhoods from different reasons. The analysis made through the GIS also showed that the distribution of assembly areas is not homogenous in terms of accessibility.

1. Introduction

Turkey's Earthquake Regions Map, which was entered into force in 1996, was updated by AFAD in 2018 and entered into force on 1 January 2019 under the name of Earthquake Hazard Map of Turkey. In Figure 1, Earthquake Hazard Map of Turkey was adapted and the condition of Uşak province indicated. According to the information from Turkey's Earthquake Regions Map, Uşak province was located in the second-degree earthquake zone, except the Eşme district. Eşme district, was located in the first-degree earthquake zone. In Earthquake Hazard Map of Turkey, more detailed data is used instead of this degree system, and the concept of earthquake zone is no longer used. " The new map is prepared with much more detailed data taking into account the most recent earthquake source parameters, earthquake catalogs and new generation mathematical methods. Unlike the previous map, the new map shows the peak ground acceleration values rather than earthquake zones and replaces the 'earthquake zone' concept." (AFAD, 2019d).

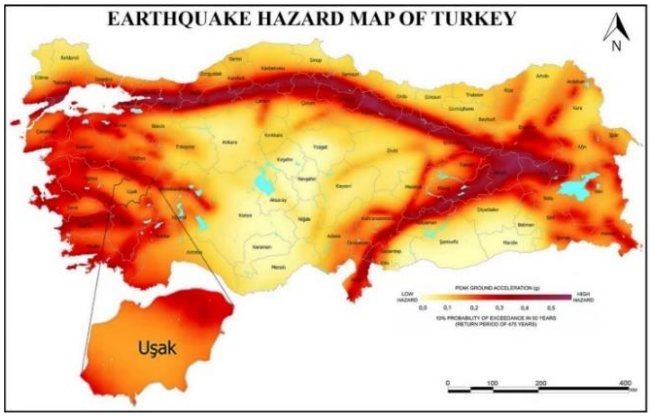

Figure 1. Earthquake Hazard Map of Turkey and the Condition of Uşak Province. (Adapted from the Earthquake Hazard Map of Turkey). (AFAD, 2019d).

2. Post-disaster assembly areas

Such criteria have included in many national and international research and studies. For example, "The Study on A Disaster Prevention/Mitigation Basic Plan in Istanbul including Seismic Microzonation in the Republic of Turkey" final report is prepared by the Istanbul Metropolitan Municipality (IMM) and Japan

* **Corresponding Author**

*(194125002@ogr.usak.edu.tr) ORCID ID 0000-0001-5616-1952
(fatih.taktak@usak.edu.tr) ORCID ID 0000-0003-1324-2036

Cite this study

Yuksel F & Taktak F (2021). Investigation of Assembly Centers in The Disaster Areas in Merkez District of Uşak Province in Turkey. 3rd Intercontinental Geoinformation Days (IGD), 6-9, Mersin, Turkey

International Cooperation Agency (JICA) in 2002. In this report, under the title of Parks and Open Space Availability for Primary Safety Evacuation of Residents, a new urban disaster emergency evacuation system has recommended. The recommended evacuation system consists of two phases. The first one is called as Primary Evacuation Areas and constitutes the post-disaster assembly areas. The latter is called Regional Evacuation Areas and functions as shelter areas and tent villages. In the report, both phases have been explained, and the criteria for their determination have been included also. Within the Primary Evacuation Areas part of the chapter, the report also stated how much area per person should be. According to the report, for all citizens and residents in the area, the gross minimum area should be determined as 1.5 m^2 per capita. The report also states that the evacuation area should be selected from publicly-owned lands. (Tezcan et al., 2021; Zhu et al., 2016; JICA and IMM, 2002).

In another study, which examined the factors related to the planning of post-disaster assembly areas and shelter areas, it was stated that five criteria should be considered when determining the assembly areas. In the accessibility criterion, it is emphasized that the assembly areas should be accessed by every individual easily. The connection with the road axis is determined as the second criterion by this study. In the criteria for availability and multi-functionality, some of the areas that may be recommended as assembly areas are given as an example, and some examples from active and passive green areas are presented. Within the scope of this criterion, the requirement that the area should not be smaller than 500 m^2 comes to the forefront. In the context of ownership, as indicated in the report on Istanbul as well, it is stated that publicly-owned lands should be preferred as a priority. The study includes the area sizes in the last criteria, and provides several examples from other studies, in addition to the JICA and IMM report which determined the minimum areas as 1.5 m^2 per capita. For example, in another study, it is stated that the area should be determined based on building block, and it is recommended that it should be specified as 2 m^2 minimum as well. (Aşıkkutlu et al. 2021; Çınar *et al.* 2018; Xu et al. 2016).

3. Assessment of post-disaster assembly areas in Merkez district of Uşak province

In the JICA and IMM report, the gross minimum area per capita was indicated as 1.5 m^2. The area per capita standard that would be taken into consideration in this study would be 1.5 m^2 per capita, as in the report. In the scope of this study, assembly areas will be evaluated in the neighborhoods of the Merkez district. The population data was obtained from the TurkStat address-based population registration data for 2018. The names, addresses, status of the infrastructure and superstructure, and area sizes of the assembly areas were reached through the Uşak Provincial Disaster and Emergency Directorate and via e-Government. Accordingly, the infrastructure status, which is one of the seven criteria indicated by AFAD, would be examined as well. Then, the capacities of the areas were calculated, and it was identified which assembly area could serve a population of how many during an emergency. The size of the area per capita in each neighborhood was calculated. Lastly, it was indicated whether the size of the area per capita in compliance with the standards or not.

A total of 43 determined assembly areas in 28 neighborhoods of Merkez district have listed. 11 of these 28 neighborhoods do not have any assembly areas. According to inquiries via e-Government, when you click on any area in these neighborhoods, the three assembly areas that are closest to that area are listed and shown on the map. When we analyze the neighborhoods that have assembly areas in the context of area per capita, 9 of them are not in compliance with the standards (calculations made according to the specified 1,5 m^2 standard). Kemalöz neighborhood, which has the most population, meets the standards in this context as its area per capita is 2.9 m^2. After Kemalöz, the two most populated neighborhoods are Cumhuriyet and Atatürk neighborhoods, respectively. Both of them are below the accepted 1.5 m^2 standard. The area per capita in these populous neighborhoods are quite less, and there are also the less populous neighborhoods that have less than 1 m^2 assembly area per capita. Besides, some neighborhoods are well above the standard, so the areas could be used by their immediate vicinity as well.

Another criterion to be considered when determining the area is ownership. When we look at the Central District of Uşak, all assembly areas consist of parks and picnic areas and are all public ownership. According to the information obtained from Provincial Disaster and Emergency Directorate, all assembly areas in Uşak province is composed of public ownership areas, and no expropriation has been mentioned.

Another criterion is the infrastructure status and whether it is capable of satisfying the basic needs or not. In this context, the status of the electricity, water, and sewer system of the areas was examined. Water infrastructure in four of the 43 assembly areas is not capable of satisfying the needs. At the same time, in all of these four parks, the sewer system is not suitable as well. The only park where electricity infrastructure is not suitable is Halil Kaya Gedik Park in Fatih neighborhood. The biggest problem, in terms of infrastructure, is the issue of the sewer system, 23 of the 43 assembly areas are not capable of satisfying the sewerage related needs. In fact, sewage infrastructure is not suitable in all assembly areas in Aybey, Durak, Fevzi Çakmak, Işık, and İslice neighborhoods.

4. Examination of the distrubution of post-disaster assembly areas with GIS

In this study, the distribution of the assembly areas in Merkez district has examined by using the coordinates obtained from Uşak Provincial Disaster and Emergency Directorate. The study examined the distribution of the areas in the district by using neighborhood boundaries and satellite image. Using coordinate information, the locations of the areas have marked, and the distribution of the areas on central neighborhoods has shown with ArcMap 10.6. Figure 2 shows the locations and distribution of 43 areas according to the neighborhoods.

Assembly areas that are near to the center have more densely located, and their numbers and frequency decrease as they move away from the center. The areas that are far from the center comprise the areas, which are generally larger and have a use as a picnic area. Towards the center, the parks, which are smaller and have the characteristics of neighborhood parks, are located as an assembly area. Especially as you move away from the center, the number of easily accessible areas is not much. However, some of the areas that are easily accessible and too close to the buildings have some safety concerns such as the collapse of buildings during an emergency.

The densities of the assembly areas are shown in Figure 2, according to their distribution and area sizes. The Kernel Density map prepared in ArcGIS with Kernel Density tool by using the point features of the assembly areas. "The Kernel Density tool calculates the density of features in a neighborhood around those features. It can be calculated for both point and line features." (Esri n.d.). As is seen from the kernel density map and the information so far, high-density areas are the large-sized assembly areas far from the center. Even though the number of areas is more in the center, their sizes are not even close to the ones with the highest density areas.

Another analysis in ArcGIS has made using the Multiple Ring Buffer tool. This tool creates multiple buffers around the input with specified distances. So in this study, the distances specified as 100, 300, and 500 meters around the assembly areas. Accessibility to the areas easily by each individual is crucial during an emergency. So, the walking should be 500 meters or less. (Aksoy *et al.* 2009; Çınar *et al.* 2018; Şentürk 2017; Tarabanis and Tsionas 1999). In that case, Figure 3 shows that they are not sufficient even in central neighborhoods, in terms of accessibility. The distances of 100 and 300 meters from the assembly areas could serve a very small area in each neighborhood. Even the maximum distance of 500 meters could not serve the whole neighborhoods. So, in emergency, the areas are not in the easily accessible distance for many individuals.

Acknowledgement

Assembly areas are of vital importance during the first 12-24 hour period after the disaster. Therefore, its role in disaster management and planning is quite much. In the event of a disaster, it is very crucial to reach the people who are exposed to the disaster to the assembly areas in the shortest time possible. Therefore, the capacity should be sufficient to serve all citizens. Although areas that are large and capable of serving many people are considered as favorable, the main point is the determination of building block scale and neighborhood-scale assembly areas that can serve each settlement. Easily accessible assembly areas would be lifesaving during a disaster, especially by raising public awareness about the areas beforehand. There should not be any problems in terms of infrastructure and superstructure in the assembly areas, and the areas should be in good condition to respond to the vital needs of the disaster victims. All of this is very valuable in the event of a possible disaster.

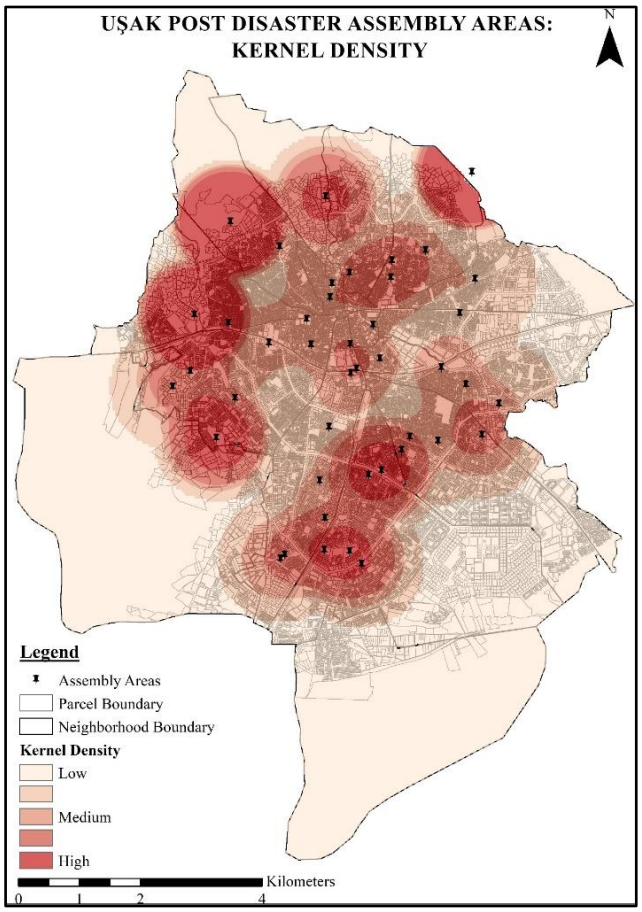

Figure2. Merkez/Uşak Post-Disaster Assembly Areas: Kernel Density.

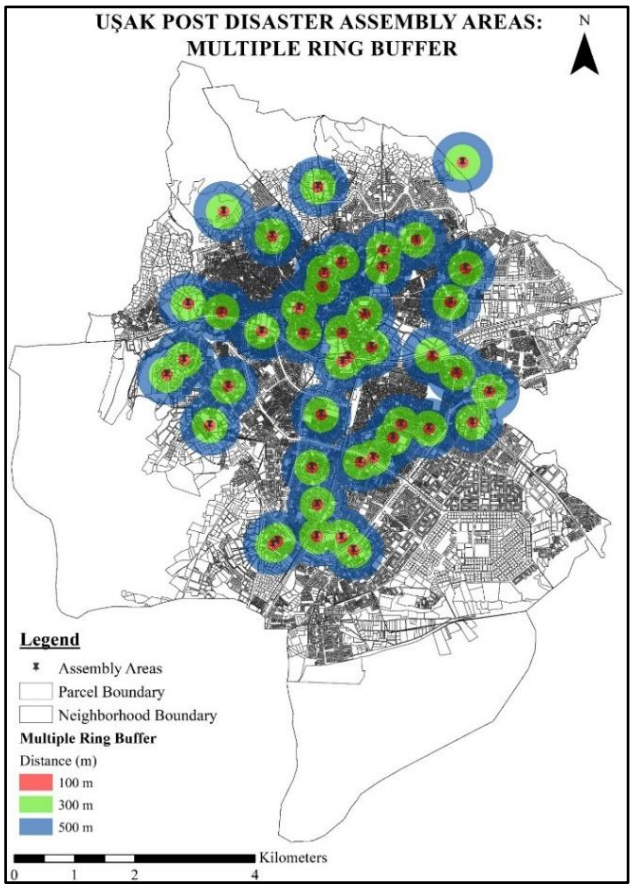

Figure 3. Merkez/Uşak Post-Disaster Assembly Areas: Multiple Ring Buffer.

In this study, the compliance with the standards of the assembly areas in Merkez/Uşak has examined, and the distribution of these areas has also evaluated by using GIS. All 43 assembly areas determined in the district are located in the central neighborhoods, and some of these areas are not sufficient, especially in the populous neighborhoods. While 11 of the 28 neighborhoods do not have any assembly area, area per capita is below the accepted standard in 9 of the 17 neighborhoods which have an assembly area. Besides, most of the assembly areas have infrastructure problems, especially in sewage infrastructure. In respect of the distribution of areas, while there is a more homogeneous distribution in some neighborhoods, there are problems, especially in neighborhoods where single and larger areas are determined as assembly areas. So, this distribution causes trouble in terms of accessibility to assembly areas. Also, the safety concerns such as collapse of buildings should be considered besides the accessibility. In the event of a disaster, accessibility to those areas in a safe way would be as important as the sufficiency of the areas. For this reason, easy-to-access areas that can respond to smaller settlements on the building block scale and neighborhood-scale should be determined as assembly areas. The deficiencies in the assembly areas need to be corrected, and new assembly areas need to be determined in the neighborhoods where the areas are not sufficient. With GIS, the analysis and use of spatial and non-spatial data could be achieved easily. That's why it would be very advantageous using GIS to identify deficiencies of the assembly areas and to determine the new areas.

References

AFAD (2019a). Earthquake hazard map of Turkey index.

AFAD (2019b). Earthquake hazard map of Turkey interactive web application.

AFAD (2019d). Turkey's new earthquake hazard map is published.

Aksoy Y (2010). The pre- and post earthquake evaluation of the existing and suggested green areas in the district of Zeytinburnu within the context of risk and disaster management. G.U. Journal of Science, 23(1), 107-117.

Aksoy Y, Turan A Ç & Atalay H (2009). İstanbul Fatih ilçesi yeşil alan yeterliliğinin marmara depremi öncesi ve sonrası değerleri kullanılarak incelenmesi. Uludağ Üniversitesi Mühendislik-Mimarlık Fakültesi Dergisi, 14(2), 137-150.

Anhorn J, Khazai B (2015). Open space suitability analysis for emergency shelter after an earthquake. Natural Hazards and Earth System Sciences, 15(4), 789 - 803. doi:10.5194/nhess-15-789-2015.

Arca D (2012). Afet Yönetiminde coğrafi bilgi sistemi ve uzaktan algılama. Karaelmas Science and Engineering Journal, 2(2), 53-61.

Aşıkkutlu H S, Aşık Y, Yücedağ C & Kaya L G (2021). Olası Deprem Durumunda Mahalle Ölçeğinde Burdur Kenti Acil Toplanma Alanlarının Yeterliliğinin Saptanması. MAKÜ, İktisadi ve İdari Bilimler Fakültesi Dergisi, 8(1), 442-456.

Balaban M Ş (2011). İstanbul Fatih ilçesi mevcut açık alan stokunun acil tahliye ve geçici barınma alanları olarak kullanılması durumunda erişilebilirlik ve yeterlilik analizi üzerine bir çalışma. Mimarlar Odası Ankara Şubesi Yayını, pp. 44-53.

Caymaz E, Akyon F V & Erenel F (2013). A model proposal for efficient disaster management: the Turkish sample. Procedia - Social and Behavioral Sciences, 99, 609-618.

Çelik H Z, Özcan N S & Erdin H E (2017). Afet ve acil durumlarda halkın toplanma alanlarının kullanılabilirliğini belirleyen kriterler. 4th International Conference on Seismology and Earthquake Engineering. Eskişehir, Anadolu University.

Çınar A K, Akgün Y & Maral H (2018). Afet sonrası acil toplanma ve geçici barınma alanlarının
planlanmasındaki faktörlerin incelenmesi: İzmir-Karşıyaka örneği. Planlama, 28(2), 179-200.

Demirci A & Karakuyu M (2004). Afet yönetiminde coğrafi bilgi teknolojilerinin rolü. Doğu Coğrafya Dergisi, 12, 67-101.

Esri. How kernel density works.

Gerdan S & Şen A (2019). Afet ve acil durumlar için belirlenmiş toplanma alanlarının yeterliklerinin değerlendirilmesi: İzmit örneği. idealkent. 10(28), 962-983.

Hermann J (2007). Disaster response planning & preparedness: phases of disaster.

Şentürk E & Erener A (2017). Determınatıon of Temporary Shelter Areas in Natural Dısasters By GIS: A Case Study, Gölcük/Turkey. International Journal of Engineering and Geosciences, 2 (3), 84-90.

Tezcan B, Alakaş H M, Özcan E & Eren T (2021). Afet Sonrası Geçici Depo Yeri Seçimi ve Çok Araçlı Araç Rotalama Uygulaması: Kırıkkale İlinde Bir Uygulama. Politeknik Dergisi, 1-1.

Zhu C, Wang Y, Ren W, Luo I, Yin Y, Xie W & Liu W (2016). The planning of green spaces to prevent and avoid urban disasters in dujiangyan. International Journal of Simulation: Systems, Science and Technology, 17(46), 271–276.

Xu J, Yin X, Chen D, An J & Nie G (2016). Multi-criteria location model of earthquake evacuation shelters to aid in urban planning. International Journal of Disaster Risk Reduction, 20, 51–62.

Intercontinental Geoinformation Days

igd.mersin.edu.tr

Developing 3D real estate tax visualization / management system with GIS based procedural modelling approach

Şevket Bediroğlu[*1]

[1]*Gaziantep University, Architecture Faculty, City and Regional Planning, Gaziantep, Turkey*

Keywords
GIS
3D Modelling
Real Estate Tax
Procedural Modelling

ABSTRACT

Creating detailed 3D building models with independent sections presents some challenging obstacles, including the gathering and managing of massive 2D and 3D datasets. In order to solve the problems that arise during the evaluation and management of real estate taxation, it is necessary to investigate what kind of advantages 3D systems can offer. Most part of the datasets to be used are not available directly (e.g. architectural plan, building models etc.). It is aimed to develop methods for saving time and standardizing by providing automations in the process of making these data available. It is aimed to develop a feasible, cost-effective approach that balances performance and quality in the subject-specific 3D model production process. Rule-based modelling was preferred as a 3D modelling method. With this modelling approach, necessary coding has been made in CGA language for producing 3D models. Thus, 3D models can be produced automatically with independent sections regardless of the number of buildings. The relational database was transferred with City Engine, a procedural 3D modelling program, with CGA codes prepared. Afterwards, 2D geometries of buildings and building independent sections were arranged in GIS program and associated with attribute data including real estate tax parameters and other GIS attributes.

1. Introduction

A 3D city model is by definition a three-dimensional graphic image capable of translating real city objects, like buildings or urban furniture, into a virtual scene (Catita et al., 2014). The use of geoinformation for enabling and facilitating smart city environments covers a wide range of fields including 3D modelling (Işıkdağ, 2020).

Compared with 2D, 3D GIS describes the objective world in a more realistic way, and shows geospatial phenomena to users via 3D modelling technology (Zhang et al., 2014). Incorporating 3D models into the land development industry addresses such challenges by providing data that better describes land and buildings in 3D (Kalantari and Nechifor, 2017). In the transformation from 2D GIS to 3D GIS, a great number of 3D datasets (e.g., city models) become necessary (Atila et al., 2013). 3D GIS would be a good solution for the representation, registration, and management of different legal information associated to cadastral location (Hajji et al., 2021). Işıkdağ et al., 2014 stated that 3D representations can support mass computation of net area and consequently facilitate taxations of properties (Işıkdağ et al., 2014). There will be positive impacts of the 3D cadastre as it is supportive of the land market for a larger number of land objects and so increases in the real estate contribution to GDP are anticipated (Griffith-Charlesand and Sutherland, 2013).

The objective of this paper was to enable GIS, 3D and real estate tax evaluation integration by creating 3D models for buildings with separate floors and independent sections. The term 'independent section' here corresponds to a section, which is separated from other sections by walls or other partitions and has its own title deed or certificate of ownership. In other words, a section, which is individually managed, sold or bought, is considered to be an independent section. This division is complicated and can be changeable, according to the different functions and architectural plans of the building. Large numbers of independent sections may exist on a floor, a floor may be a completely independent section, or the whole building may be one independent

* **Corresponding Author**

*(sevketbediroglu@gmail.com) ORCID ID 0000-0002-7216-6910

Cite this study

Bediroglu S (2021). Developing 3D real estate tax visualization / management system with GIS based procedural modelling approach. 3rd Intercontinental Geoinformation Days (IGD), 10-13, Mersin, Turkey

section. GIS based procedural 3D modelling method is used for creating building models with independent sections including real estate tax evaluation parameters. It is seen that this method is an efficient and cost-effective approach for purpose of study. With this paper, we plan to help solving these scientific problems. Investigating the advantages of 3D systems to detect great and minor errors and ensuring compliance with the principle of transparency that arise during the evaluation and management of real estate taxation. Conducting comprehensive research on 3D model production methods, detail levels of models and other parameters that can be used in real estate tax management. Developing an applicable, cost-effective approach that balances performance and quality in the subject-specific 3D model production process. Since the vast majority of data sets to be used cannot be used directly (e.g. architectural plan, etc.), developing methods for saving time and standardization by providing automation in the process of making these datasets available. Analyzing the cost-benefit analysis, efficiency and evaluating the result effects of 3D systems carried out for these purposes

2. Method

Workflow of whole system is shown at Figure 1. When the methods are considered in detail, hierarchical processing sequences were designed and implemented. Geodatabase was designed in GIS software ArcGIS. Related GIS attribute files about real estate tax determination were linked with main GIS geodatabase after preparation of UML schema shown at figure 2. Next step was applying real estate tax calculations with related parameters. CGA language was used for the purpose of procedural 3D modelling and each independent section of the building models was created. Attribute files related to these independent sections were then connected with the 3D model geometries. The independent sections were linked with the related attribute GIS files which included tabular data within footprints of sections. In the following stage, rule-based parameters and codes were created to extrude independent sections. These codes were created using CGA language, and GIS-based 3D models were generated via City Engine software. Orthoimagery was posed with the 3D land surface containing 3D models of the ground surface. For these operations, data such as orthoimagery and DEM are first prepared / arranged in the GIS program. In order to perform these operations in the City Engine program, orthoimagery and DEM are directly matched in places where there are no buildings. In places where there are buildings, with the "rule" file we prepared for the City Engine program, Orthoimagery parts corresponding to the roof of the buildings are assigned to the roof as "texture". Thus, image matching to the roof could be done automatically over a single orthoimagery without the orthoimagery breaking down. This 3D approach to model creation was applied to 121 buildings and 1814 independent sections related to them. The details of methodology and study is explained briefly in following section with case study.

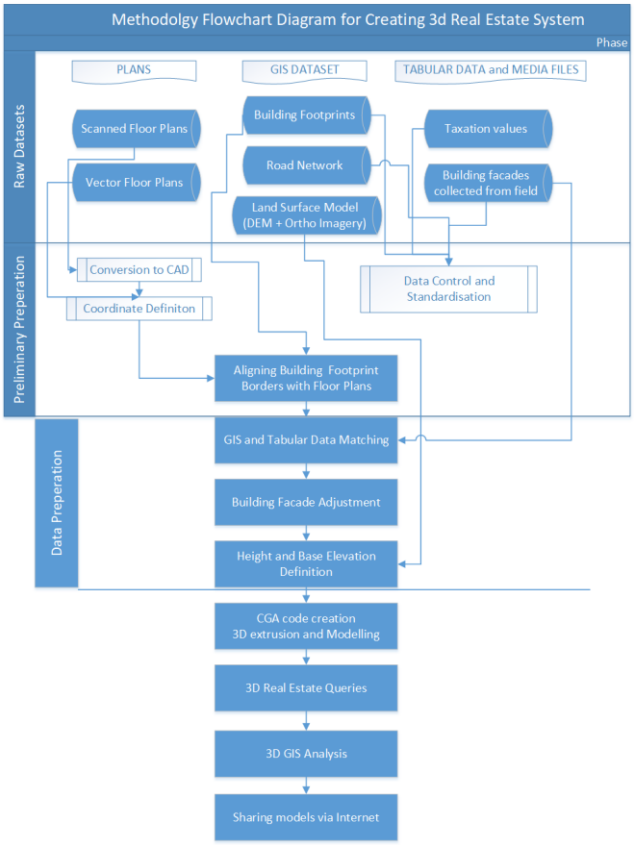

Figure 1. Methodology workflow diagram

2.1. Tax evaluation parameters

In order to generate the real estate tax values on the models produced in the study make the determination and tracking of tax values more accurate, current, transparent and fair we have investigated the real estate tax criteria applied in our country and in the world. During the research and determination of coefficients, we were in constant contact with the local government to think contrary to current practices. There are different and contradictory practices in our country regarding the determination of real estate tax rates. Although the coefficients and scoring differ according to the countries, similar parameters are generally used and these parameters and coefficients can be updated according to the need. These determined parameters and real estate tax value calculation formula is presented below.

α: General fair value on street basis
β: Material of the building (quality of building)
βk: Building material coefficient
θ: Age of the building
θk: Age coefficient
φ: Construction area of building
φk: Area coefficient
ω: Function of independent section (shop, flat, apartment etc.)
ωk: Function coefficient
ψ: Floor number of independent section (height from street)
ψk: Floor number coefficient
λ: Independent section real estate tax

2.2. Case study

2.2.1. Data preparation

This stage of study was the main part of job before 3D model creation. First step was matching and aligning floor plans and building footprints with ArcGIS software. Study area is located at Trabzon / Turkey. At the end of study final 3D models will be in 2 parts such as independent section 3D models and building exterior 3D models with facades. If these raw datasets were not aligned, final models will seem horizontally shifted. GIS data obtained from municipality includes too many essential GIS attributes but some part was relevant for our study and some part was not. Figure 2 shows a screen of raw data processing and gathering necessary data for model creation. Other side there was some non-standard attribute data and we corrected them. We have collected building facades from 4 sides (aspects) of buildings. Facades of buildings were stored in jpeg format and named in folder building_number_aspect, i.e. building_1001_north. These specially named facades will be automatically matched with related building exteriors with the help of CGA code and name of files.

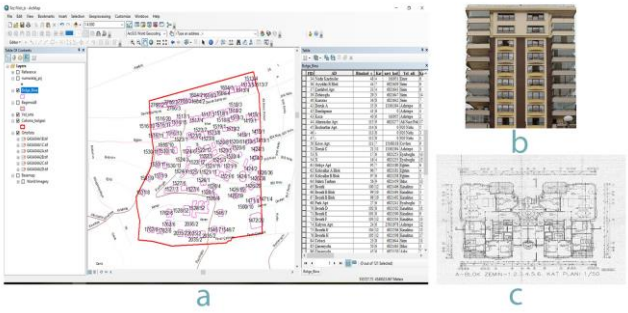

Figure 2. Data preparation stages

2.2.2. Extrusion of building independent sections in City Engine

After these three parameters were matched, the CGA rule was redesigned for the recognition of these height parameters. All the independent sections of the whole building from ground to roof were 3D extruded via City Engine (Figure 3). In Trabzon, 121 different buildings and 1814 related independent sections were modelled in 3D via procedural modelling. In addition to the 3D models of the independent sections, building façade models were created by taking photographs of the building façades in the field. The GIS information for these models was obtained from the local government and was associated with the relevant models in the database. General views of the 3D building models are shown in Figure 3.

3. Results

The procedural modelling method has proven to be suitable for studies conducted at the neighborhood, district or city scale level. First, its integration of GIS data into the system has advantages over other methods. In the case of a 3D model of a single building, software like 3d Max and SketchUp become advantageous because knowledge of professional 3D modelling is not required, and thus, there is no need for preliminary studies in the procedural modelling method. These systems are desirable for small projects; however, if the number of buildings subject to 3D modelling is overly numerous, the correct choice would be procedural modelling. As the number of buildings increases, the procedural modelling method makes a significant difference in the total number of iterations, i.e., the number of 3D models produced over time, the accuracy of the study, the details of the models, the total number of polygons within the model, etc. If the architectural plans used for modelling are in the form of precise CAD data and the buildings are produced in accordance with the plans, the produced 3D models will have high accuracy. On the other hand, if the data used is scanned raster data, like that which is currently stored in most of the local administrative systems, then the accuracy will be slightly reduced.

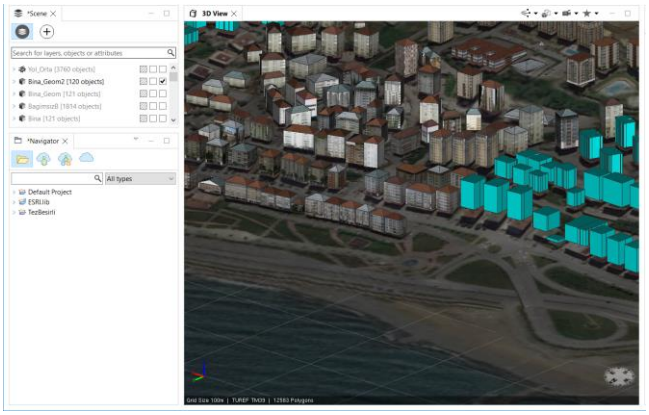

Figure 3. General view of created 3D building models

With the help of GIS based procedural 3D modelling technique, 3D visualizations can be made quickly in the system. In figure 4, 3D visualization of real estate taxes was made according to the square meter unit value. This visualization can definitely be done with normal modelling approaches, but thanks to procedural modelling, this visualization can be done very quickly with attribute data. For this purpose, we have created a colour ramp for real estate tax values and set RGB colour codes as attribute. CGA can directly visualize the colour due to attribute.

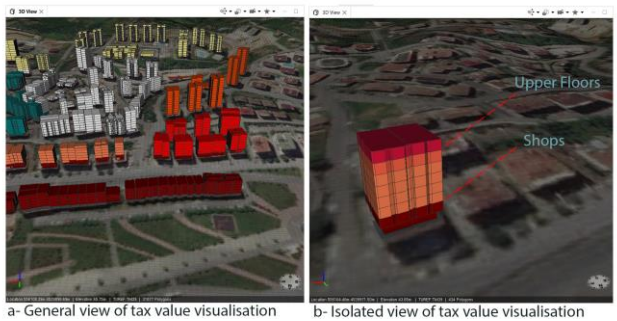

a- General view of tax value visualisation b- Isolated view of tax value visualisation

Figure 4. 3D visualization of real estate square meter unit value

Another visual output that may be produced quickly in the system is the 3D visualization of taxpayers who paid and did not pay the property tax in the past years. In order to make this visualization, the visualization shown

in figure 10 was made by using the attribute information in the database. For this purpose, we have created a color ramp for real estate tax payer and non-payers by setting RGB color codes as attribute. CGA can directly visualize the color due to attribute. Light green means taxpayer has no loan and dark green means taxpayer has one or two year tax loan. Shades of red means related taxpayers has more than two year accumulated loan.

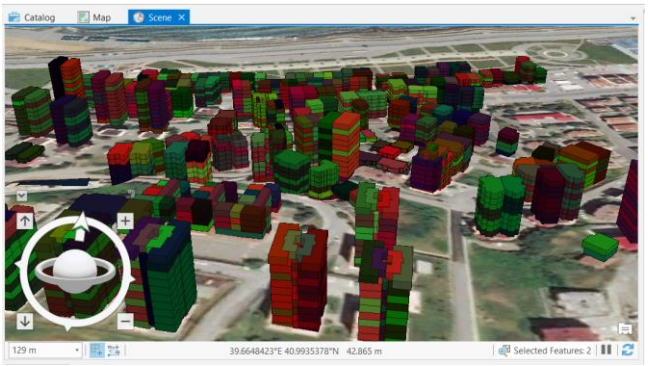

Figure 5. 3D visualization of paying and non-paying taxpayers

4. Conclusion

Results indicated that the procedural modelling is an efficient approach for creating the core features of 3D building components for 3D city models. Using 3D models produced in this study, 3D visualization of property tax values calculated by mass appraisal method could be made practically via GIS attribute information recently prepared by municipality technical works office. All the 3D models and GIS files can also be shared with citizens due to permission of administrator at local authority. System brings transparency and accountability for local government studies. In study, 2" cases were found most useful cases. First is colouring the independent sections and buildings due to update tax values. Second is colouring same objects due to payment status of taxes. With the help of parametric modelling users are able to make these visualizations and queries in a few seconds. Now this system is at evaluation and informing platform however the model may be a decision support system in recent future.

The system brings speed and flexibility to 3D modelling studies. One rule can be used for modelling many buildings, thus making the system fast. In addition, applying any changes to the 3D models for any possible scenario is easy, as the system provides an adaptable environment. This flexibility works in terms of changing 3D models in an automatic system for integration with other formats such as City GML and COLLADA. This study has shown that 3D modelling provides easy understanding and functionality for taxation applications with the help of visualization. Users can easily query tax values in 3D and get access about detailed GIS information related with the independent section.

References

Atila U, Karas I.R. & Abdul-Rahman A (2013). Integration of CityGML and Oracle Spatial for implementing 3D network analysis solutions and routing simulation within 3D-GIS environment. Geo-spatial Information Science, 16(4), 221-237.

Catita C.P., Redweik J, Pereira M & Brito C (2014). Extending solar potential analysis in buildings to vertical façades. Computers & Geosciences, 66, 1-12.

Griffith-Charles C. & Sutherland M (2013). Analysing the costs and benefits of 3D cadastres with reference to Trinidad and Tobago, Computers, Environment and Urban Systems, Volume 40, 2013,Pages 24-3 3, ISSN 0198-9715,

Hajji, Rafika, Reda Yaagoubi, Imane Meliana, Imane Laafou, and Ahmed E. Gholabzouri., 2021. "Development of an Integrated BIM-3D GIS Approach for 3D Cadastre in Morocco" ISPRS International Journal of Geo-Information 10, no. 5: 351. https://doi.org/10.3390/ijgi10050351

Işıkdağ Ü (2020). AN IOT ARCHITECTURE FOR FACILITATING INTEGRATION OF GEOINFORMATION. International Journal of Engineering and Geosciences, 5 (1), 15-25. DOI: 10.26833/ijeg.587023

Işıkdağ, Ü, Horharmer M, Zlatonova S, Kathman R & Oostterom P (2014). Semantically rich 3D building and cadastral models for valuation, 4th 3D Cadastre Workshop, Dubai

Kalantari M. & Nechifor M (2017). 3D Indoor Surveying – A Low Cost Approach. Survey Review, 49(353), 93-98.

Zhang H, Li Y, Liu B & Liu C (2014). The Application of GIS 3D Modeling and Analysis Technology in Real Estate Mass Appraisal – Taking landscape and sunlight factors as the example. Int. Arch. Photogramm. Remote Sens. Spatial Inf. Sci., XL-4, 363-367.

Intercontinental Geoinformation Days

igd.mersin.edu.tr

Analysis of forest degradation by using GIS and remote sensing: a case study of Chandoli National Park Kolhapur in Maharashtra State

Rajaram Patil[*1], **Govardhan Ubale** [2]

[1]*University of Mumbai, A. And C. College Phondaghat, Sindhudurg, India*
[2]*Shivaji University Kolhapur, Vivekanand College, Kolhapur, Kolhapur, India*

Keywords
Remote sensing
GIS
Land use
Land cover
Forest

ABSTRACT

The present study addresses the status of forest land cover mapping and analytical findings of practical conservation for sustainable development of forested area. Remote sensing and GIS technique are known for reminders special analysis. Chandoli forest area presented the biodiversity and it is essential for ecosystem. There is tropical evergreen, moist deciduous forests. It is including in Sahyadri tiger reserve. The study highlighted those forests are has degraded in small scale but it is the problem for sustainable ecosystem in this National Park Forest area. There should be some remedies for controlling the degradation by road network and settlement due to human activities. Forest cover in the world is 31%, where as in India have 24.56%, 16.50 % in Maharashtra State, 23.19 % in Kolhapur District and Shahuwadi tehsil is acquired 23.38%.

1. Introduction

Forest ecosystem plays very important role in global ecological balance and natural environment. Forest provides a valuable timber for domestic and commercial use many industries like paper mills, mat making, plywood, sports goods and furniture at directly based on raw materials derived from forest. Forest employment to about 4 million people to earn their livelihood in forest-based applications. Forest as the treasures of earth have as much important as they satisfy needs of the living beings and because of their significant role in the environmental harmony.

Recent decades the problem of deforestation in world had raised considerable international in interest due to the industrial revolution as well as human activities. The rapid development of GIS and remote sensing techniques have provided a reliable effective and practical way to characterized terrestrial ecosystem properties and used in planning for sustainable development as well as conservation of natural resources. According to United Nations study about forest, the total area of the world in 1900 was nearly 7000 million hectares and by 1975 it was reduced to 2890 million hectares. In the context of India according to recent state of the forest report the forest cover in India is 67.5 million hectors and it constitutes 20.5 percent of geographical area represented by 41.68 million hectares of dense forest and 25.87 million hectares an open forest. The biodiversity is essential for ecosystem that is present in the Chandoli forest. There are most of the floras and fauna recent plays a vital role in the forest ecosystem. Due to the human activities, there are fundamentally attaining the diversity of live and resulted in measure theory of species are currently declining.

2. Method

Satellite imagery of IRS of 1999 and 2015 satellite data have imported in address imagine software and Geo-rectified with image-to-image registration using UTM wgs84 projection the satellite data for land use and land cover are GIS software or have used for processing analysis and integration of spatial data simple statistical methods have used for data analysis cartographic technique used to draw the diagram.

Papers prepared in accordance with the principles of writing and approved by the review board are published.

* **Corresponding Author**

*(drrajaram75@gmail.com) ORCID ID 0000-0003-3377-5307
(govardhan84@gmail.com) ORCID ID 0000-0003-4588-1705

Cite this study

Patil R & Ubale G (2021). Analysis of forest degradation by using GIS and remote sensing: a case study of Chandoli National Park Kolhapur in Maharashtra State. 3rd Intercontinental Geoinformation Days (IGD), 14-17, Mersin, Turkey

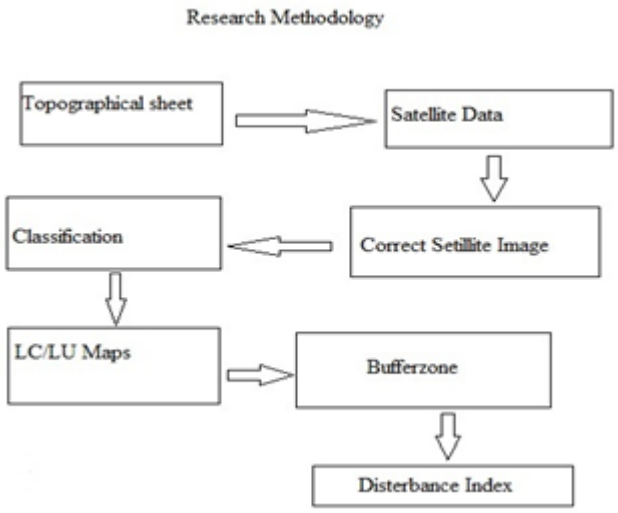

2.1. Research objectives

1. To assess the land use and land cover pattern of the study region.
2. To assess the changes in forest cover.

2.2. Study area

The study area is northern part of Kolhapur district. It is lies between 17^0 00'00" to 17^0 17' 00" North latitude and 73^0 41' 33" to 73^0 53' 30" East longitude. It is located entire in the Western Ghat. The study region covers about 317 square km of geographical area the average height of above mean sea level from 600 to 800 m it is comprises Northern Sahyadri mountainous region in Shahuwadi tehsil. It consists a semi evergreen an evergreen vegetation mixed with grassland 50 supporting to the variety of endemic plant and animal species Nearly 23 species of mammals, 122 species of birds, 20 species of amphibians and reptiles are known to be resident in the forest. Chandoli the total population is 1939 according to 2011 census.

Geographical location of the Shahuwadi tehsil lies between 16^0 54' 36" North and 73^0 56' 46" East longitude. Total area of the Shahuwadi tehsil is 104352 Sq. Hectors covered in 145 villages. According to the census of 2011 population of the Shahuwadi Tehsil was 1,85,661.

3. Discussion and results

The land use, land cover pattern shows that current utilization of land resources. India being one of the important countries for utilization of natural resources like land, soil, water and climatic conditions etc. India has experienced the utilization pattern of natural resources and land use pattern varies from place to place as well as state to state. Chandoli National Park is the most important for the research of forest cover and its current status. After creating the layer and its processing we have analyzed following results. Land-use of a region is a combined result of the natural set up and human dynamism within socio economic set up and technological development. Land-use context in a special context is essential to understand regional zone of the areas of optimum land-use degraded areas etc. The use of land constitutes a major item in national planning and this is especially in India.

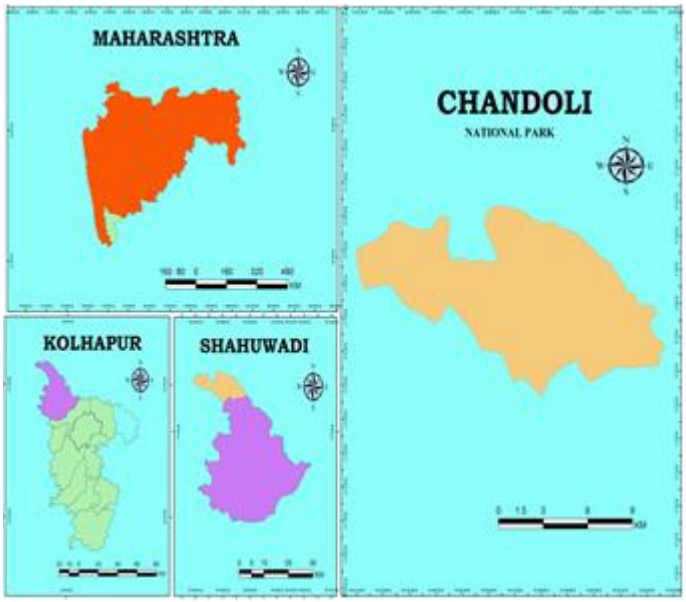

Figure 1. Location of Chandoli National Park (Source: Based on SRTM Data*)*

Table 1 shows that the land use and land cover pattern of Chandoli National.

Table 1. Chandoli National Park: LU/LC Pattern (1999 - 2015)

Name of Class	Year 1999		Year 2015		Change in Percent
	Area in H.	Area in %	Area in H.	Area in %	
Forest Cover	8479	75.03	7985	70.76	-6.18
Agri. Land	136.37	1.2	175.57	1.55	39.2
Barren Land	731.91	6.47	1200.08	10.62	63.96
Water Body	1858.35	16.44	1816.84	16.07	-2.24
Built up Land	93.96	0.83	122.10	1.08	29.94
Total Area	11299.59	100	11299.59	100	

Figure 2 and 3 reveal that, what type of land use and land cover pattern existing in the study region. The maximum proportion of the land cover presented from forest cover and minimum proportion is represented from the built-up land. Near about 70 per cent of the area occupied by forest during the year 1999 and it is reduced in the year 2015 and presented only 70.66 percent. It is reduced by 6.18 percent during this period. The area under water body has slightly decreased from 16.44 per cent in 1999 to 16.07 per cent in 2015. It is decreased by 2. 24 percent. Area under Barren land has increased by 468 hectors, it was 6.47 percent in 1999 and 10.62 percent in the year of 2015. In the year 1999 the area under agriculture was 1.2 percent. It is also increased in

year 2015 (1.5 5 per cent), it is increased by 39 percent. Area under built up land was 93.96 sq. ha (0.83 per cent) and 122.8 sq. ha (1.08 per cent) in the year 2015.

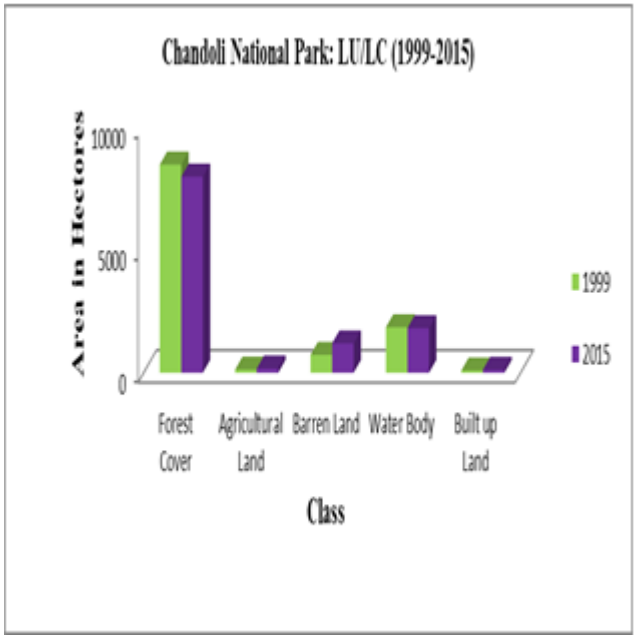

Figure 2. Chandoli National Park: LU/LC Pattern (1999 - 2015)

Figure 3. Map of Chandoli National Park: LU/LC Pattern (1999 -2015)

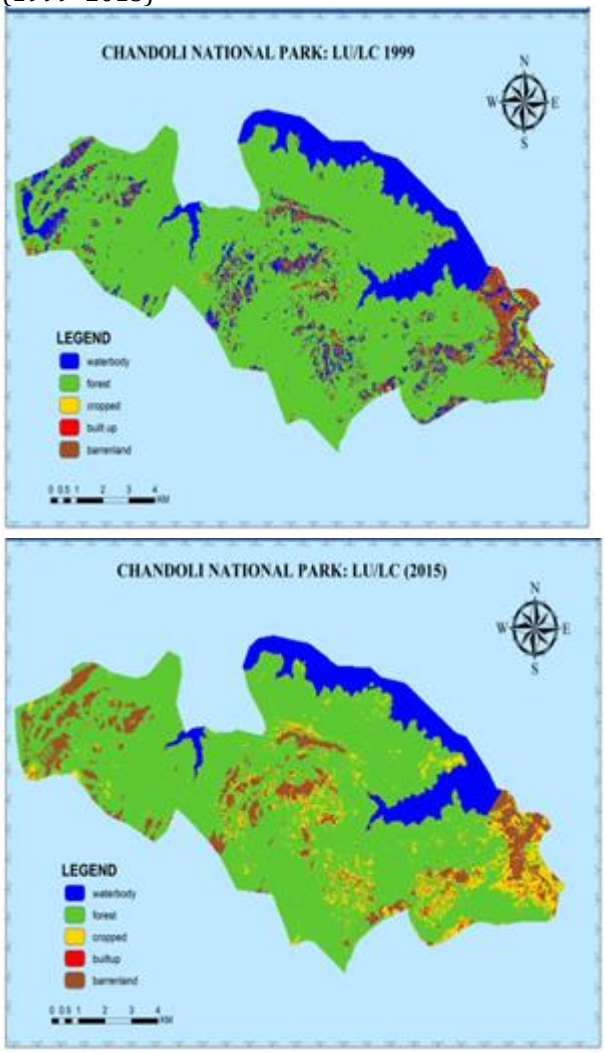

3.1. Degradation factors analysis

Present study indicates that, there are two factors also affected to degradation of forest area which are settlements and road network. We have prepared the map of buffer zone about settlements and road network which are affects to natural vegetation. There are more road network affects to forest less than settlements. We have created five buffer zones by 100-meter scale. Most of the area covered by cart road with is also affected to the natural vegetation and wildlife; it is the best method for environmental conservation and its management in the ecosystem Eco sensitive zone.

Figure 4. Buffer Zones of Road Network and Settlements (Source: Based on SRTM Data)

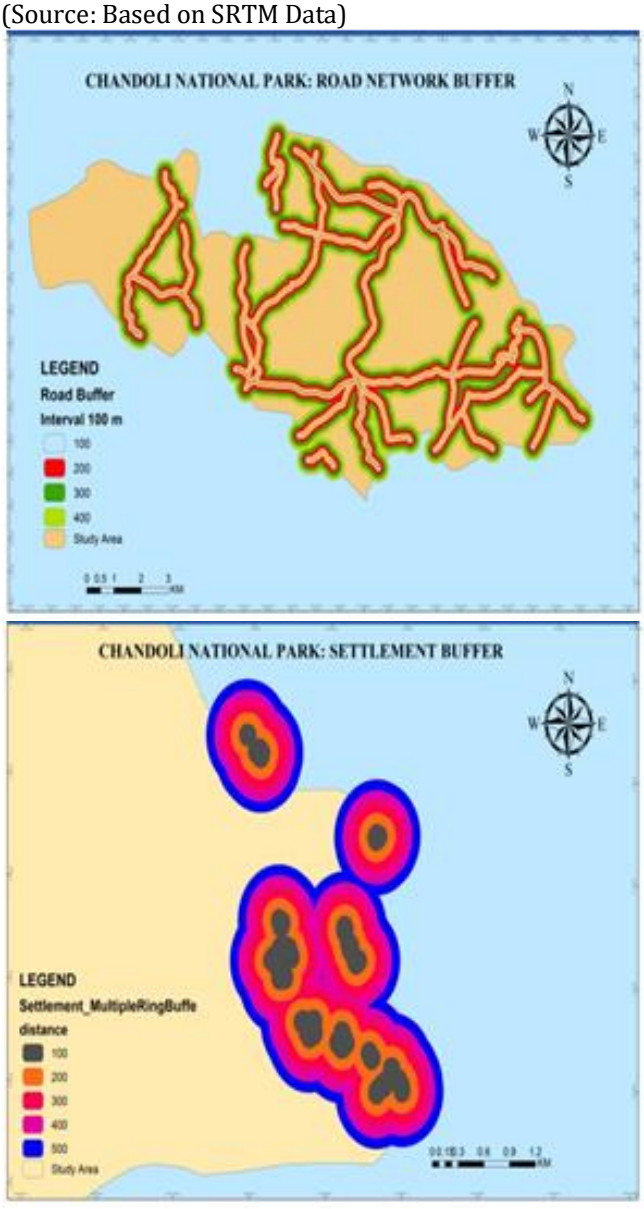

4. Conclusion

Chandoli forest are experienced and slightly degradation in the proportion of the forest area. The study has reveals, there are more than 70 percent land is occupied by forest land due to heavy rainfall and physiographic condition. The study area presented the Barren land increased by 63% due to the deforestation

existing in that area. There is agricultural land is increased with less rate, due to the growth of population and people are interested to practice of agricultural in this area. Study area experienced the increasing pattern in built up land due to the increasing population. Water bodies of the area are slightly decreased. Most degradation factors affect the forest land such as road network and settlements. The Chandoli national parks should be establishment of a forestation in a barren land and hill slopes. The human activities such as deforestation, grazing of livestock should be avoided in this area. Present study has highlighted that most advanced technique that is remote sensing and GIS provide a powerful tool for mapping and detecting changes current studies in forest distribution.

5. Recommendations

Following steps should be taken for conservation of forest.

1.Regulated and planned cutting of forest.
2.Reforestation
3.Check over forest clearance for agricultural purposes.
4.Proper utilization of forest product.

Acknowledgement

The present study could not have been completed without the support of Prof. Dr. Kanhaiya Sapkota, Central Department of Geography, Tribhuvan University, Nepal, & Prof. Dr. Idoko Ojochenemi, Department of Geography, Kogi State University, Anyigba, Nigera and the infrastructure provided by respective institutions.

References

Chauhan, P. S., Porwal, M. C., Sharma, L & Negi, J. D. 2003. Change detection in Sal Forest in Dehradun Forest division using remote sensing and geographical information system. *Journal of the Indian Society of Remote Sensing,* 31: 211-218.

Daniels, R., Gadgil, M. and Joshi, N. V. 1995, Impact of human extraction on tropical humid forests in the Western Ghats in Uttara Kannada, South India. *J. Appl. Ecol.* 32, 866–874.

Ganesh, T. and Davidar, P., 2001, Dispersal modes of tree species in the wet forests of southern Western Ghats. *Curr. Sci.,* 80, 394– 398.

Gadgil, M. and Vartak, V., 1977, Growth of forest of Mahabaleshwar – I Comparative account. J. Univ. Poona Sci. Technol., 50, 1–7.

Hussain MS, Sultana A, Khan JA, et al. 2008. Species composition and community structure of forest stands in Kumaon Himalaya Uttarakhand India. Tropical Ecology, 49: 167-181

Hame TH. 1988. Interpretation of forest changes from satellite scanner imagery. In: Satellite Imageries for Forest Inventory and Monitoring; Experiences, Methods, Perspectives, Research Notes, No. 21, Department of Forest

Imam E. 2005. Habitat suitability analysis for tiger in Chandoli National Park Kolhapur using Remote Sensing and GIS. Dissertation, Indian Institute of Remote Sensing,India

Patil R. B. and Govradhan Ubale (2015), General Land-Use Pattern in Satara District, Maharashtra: A geographical analysis, THE KONKAN GEOGRAPHER Journal, Vl. No. 13 Nov./Dec. published by Konkan Geographers Association of India, PP 72-76

Patil R. B. and Govardhan Ubale (2016), General Land-use Patterns in Devbag, Sindhudurg: A Geographical Analysis, THE KONKAN GEOGRAPHER Journal Volume No. 15. Oct/ Nov/, published by Konkan Geographers Association of India, 10-12.

Singh IJ, Mizaurahaman M, Kushwaha SPS. 2006. Assessment of effect of settlements on growing stock in Tahno range of Dehradun Forest Division using remote sensing and GIS. Journal of Indian Society of Remote Sensing, 34: 209-217

Shivraj, B., Barve, N., Kiran, M., Uma Shaanker, R. and Ganeshaiah, K., 2000, Mapping of forests based on biological diversity to identify conservation sites: A case study form Udupi and South Canara Districts of Karnataka. *J. Indian Inst. Sci.,* 80, 53 1–536.

Intercontinental Geoinformation Days

igd.mersin.edu.tr

Mapping of flood areas using Sentinel-1 synthetic aperture radar (SAR) images with Google Earth Engine cloud platform – A case study of Chamoli district, Uttarakhand- India

Mohammed Faizan*[1], Gobinath Palanisamy[2]

[1] *Institute of Remote Sensing, College of Engineering Guindy, Anna University, Chennai 600021, India*
[2] *School of Information Technology & Engineering, Vellore Institute of Technology, Vellore 632014, India*

Keywords
Remote sensing
Sentinel-1
Sentinel-2
Flood Mapping
Google Earth Engine
GIS

ABSTRACT

Flood inundation maps, which can be created using satellite images, offer useful information for flood risk preparation, control, communication, response, and mitigation during a disaster. This study discusses the Chamoli disaster, which occurred on February 7, 2021 in Uttarakhand state, India using Sentinel-1 data acquired pre, during, and post the flood to understand its impact on the region. This study also describes an automated flood inundation mapping method based on Sentinel-1 synthetic aperture radar (SAR) data using Google Earth Engine (GEE) platform. In this study, the backscattered product of SAR images after pre-processing from the GEE platform was used. For validation approaches both direct (field data) and indirect (secondary data) is used. Secondary data include optical Remote sensing images from the Sentinel-2 satellite, which were used in the study. For Sentinel-2 data processing ArcGIS has been used. The field data were obtained at different flood-affected areas on different time scales. To summarize, study results from Sentinel-1 SAR data using GEE can be a valuable method for monitoring flood inundation areas during a disaster, as well as enhancing existing efforts to save lives and livelihoods of populations, as well as safeguard facilities and industries.

1. Introduction

Floods are most often caused by hurricanes and torrential rain, or by flooding streams, rivers, or oceans; this form of natural disaster is one of the most common, affecting almost every demographic and region on Earth. Floods, since they are such diverse disasters, provide emergency planners with a vast range of perspectives. During a crisis, the immediate concern is for human life and the resources required to provide emergency service. The Floods Directive of the European Union (EU) describes a flood as the temporary covering of ground by water that is not usually flooded by water. During the monsoon season, heavy river drainage triggers extensive flooding. River flooding is a common natural occurrence that happens when a river catchment absorbs more water than it can handle due to runoff, melting snow, or ice . Floods will damage bridges and homes, destroy power grids, and even cut off parts of towns or rural communities from the first responders that need to access them Long-term worries about severe floods depend on structural damage; food is often the most serious problem since crops are lost and livestock drowns in major flood disasters.

Every disaster occurrence (floods, earthquakes, and cyclones) causes changes in the geometric, dielectric, or both properties of sensing materials, which can be easily tracked using SAR backscatter. The SAR backscatter from flood-affected areas differs from that of non-flooded areas, allowing for precise flood mapping. Several studies have been conducted to explore the effective use of SAR data in flood mapping.

Users with a cloud-based framework, such as Google Earth Engine (GEE), can retrieve and process large amounts of Sentinel-1 data directly in the cloud, rather than downloading and processing it locally. Data processing is done in parallel on Google's computing infrastructure, which greatly increases processing speed and opens up new possibilities for end users. In recent years, the GEE cloud technology has seen widespread use in a variety of remote sensing applications. Several studies make use of time-series EO data from the GEE catalog for a variety of operational purposes, including urban development mapping, global forest transition, global forest watch, and global surface water explorer.

* **Corresponding Author**

*(faizan15273@gmail.com) ORCID ID 0000 – 0001 – 8110 – 4087
(gopi.eac@gmailcom) ORCID ID 0000– 0002 – 6888 – 7539

Cite this study

Faizan M, Palanisamy G (2021). Mapping of flood areas using Sentinel-1 synthetic aperture radar (SAR) images with Google Earth Engine cloud platform – A case study of Chamoli district, Uttarakhand- India, 3rd Intercontinental Geoinformation Days (IGD), 18-21, Mersin, Turkey

The GEE platform has several benefits, including the inclusion of multitemporal EO datasets, a parallel processing architecture, and the potential to handle large datasets efficiently. All of the evidence mentioned above indicate that the cloud-based rapid flood mapping solution must be publicly accessible, effective, reliable, and user-friendly to stakeholders and decision-makers.

In this study, flood-affected areas were mapped using Sentinel-1 SAR images and a processing chain in the GEE cloud platform. The GEE is efficient in data handling, simple to implement with few user inputs, has a short processing time, is scalable to larger spatial extent flood mapping, and is universally applicable. GEE is evaluated in this study on the major flood event of Chamoli district, Uttarakhand state, India, on February 7, 2021. Finally, we use Sentinel-1 SAR images to generate operational high resolution flood maps.

2. Study area and datasets

2.1 Study area

The study area selected for this research work is a Chamoli district, which is the second largest district of Uttarakhand state of India and the location map of the study area is shown in the Fig. 1. Gopeshwar is the district's administrative headquarters. Chamoli district geographically located between 79º 15' 00" E to 80º 00' 00" E Longitude and 29º 15' 00" N and 31º 00' 00 N Latitude and falls in Survey of India toposheet numbers 53 O, M and N. The district has a geographical area of 7,604 square kilometers. The district's elevation ranges from 800-8000 m. The climate of the district is influenced by altitude. From November to March is the winter season. The district has a total population of 391,605, with male and female populations of 193,991 and 197,614, respectively. The population density is 49 people per square kilometer, and the gender ratio is 1000:1019. The national literacy rate is 82.65%, with male and female literacy rates of 93.40 and 72.32 percent, respectively.

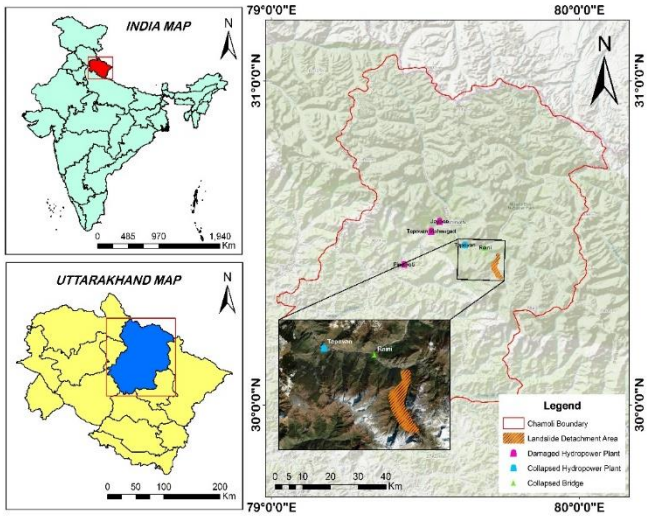

Figure 1. Location map of the study area

2.2 Datasets

For mapping the Chamoli flood event, both SAR and optical images are used. The available Sentinel-1 SAR images from pre, during, and post is used for flood mapping. Sentinel-1 Ground Range Detected (GRD) images collected from the GEE platform are already terrain-corrected σ^0images with a pixel scale of 10 × 10 m. To validate the results, Sentinel-2 optical images that are freely available from USGS Website are used. The Sentinel-2 image acquired pre and during the flood i.e., on 31 Jun 2021 and 10 Feb 2021 was used. The spatial resolution of Sentinel-2 optical images is 10m. In addition to these imaging satellite datasets, global surface water data and DEM, World Wildlife Fund (WWF) Hydro SHEDS data are fetched into the GEE platform for a better understanding of the area's flooding events. Global surface water data and WWF Hydro SHEDS have spatial resolutions of 30 m and 3 arc sec, respectively, and a detailed description of these datasets can be found in the Earth Engine Data Catalog.

3.Methodology

As it works on a parallel processing architecture, the GEE cloud platform can excellently perform various tasks ranging from data retrieval to flood mapping in a systematic way. The flood mapping processing chain is divided into 4 stages, i.e., 1) Sentinel-1 Data Collection, 2) Metadata Filtering, 3) Permanent Water Body Mask Creation and 4) Flood mapping using GEE. Figure 3 shows the conceptual structure of the proposed processing chain for flood mapping using Sentinel-1 with GEE.

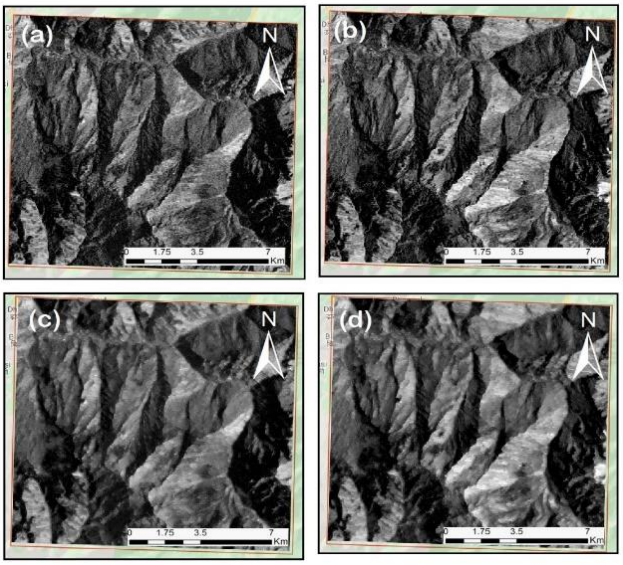

Figure 2. (a) Image captured pre-flood by sentinel-1, (b) Image captured During flood by sentinel-1, (c) Filtered image pre-flood (d) Filtered image During flood

3.4 Validation approach

Both direct (field data) and indirect (secondary data) validation approaches are used. Secondary data include optical remote sensing images from the Sentinel-2 satellite, which were used in the study. The field data

were obtained at different flood-affected areas on different time scales.

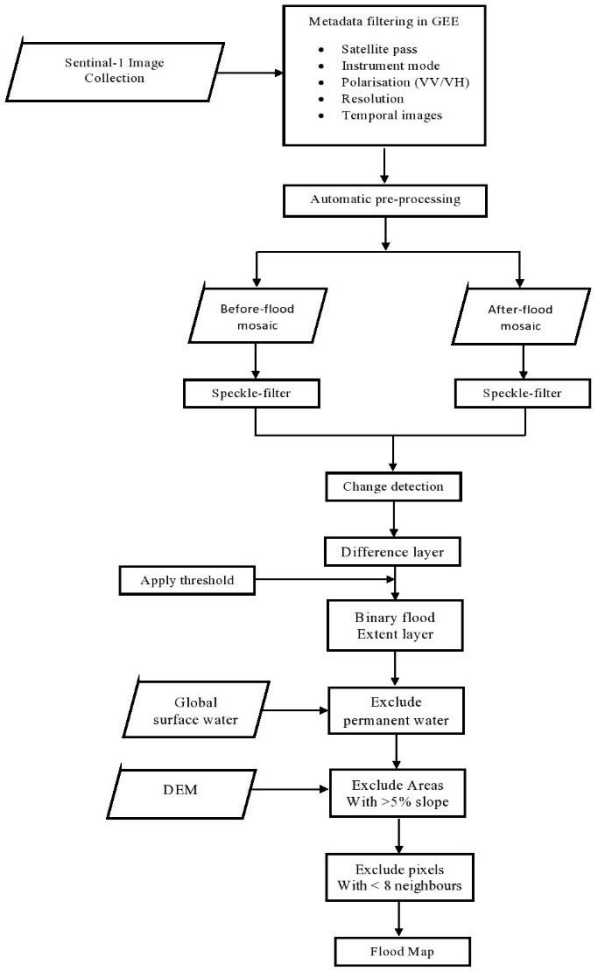

Figure 3. Methodology for processing Sentinel-1A SAR data

3.5 Sentinel-2 data collection and image processing

Optical images captured by Sentinel-2 during 31 Jun 2021 and 10 Feb 2021, are being analyzed and used to locate flooded areas. Optical imaging is commonly used for flood prediction and mapping due to a variety of advantages. The Sentinel-2 image acquired pre and during the flood i.e., on 31 Jun 2021 and 10 Feb 2021 was used. The detailed step-by-step method used on sentinel-2 pre-flood and during-flood images to extract permanent water bodies from the pre-image and to locate flooded areas from the during flood image is shown in Fig 4.

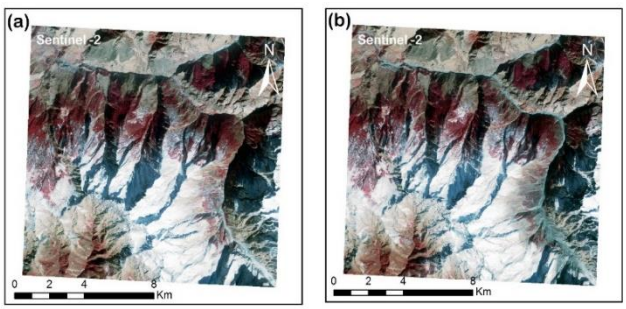

Figure 4. (a) & (b) Pre-flood and during flood image by sentinel- 2 respectively

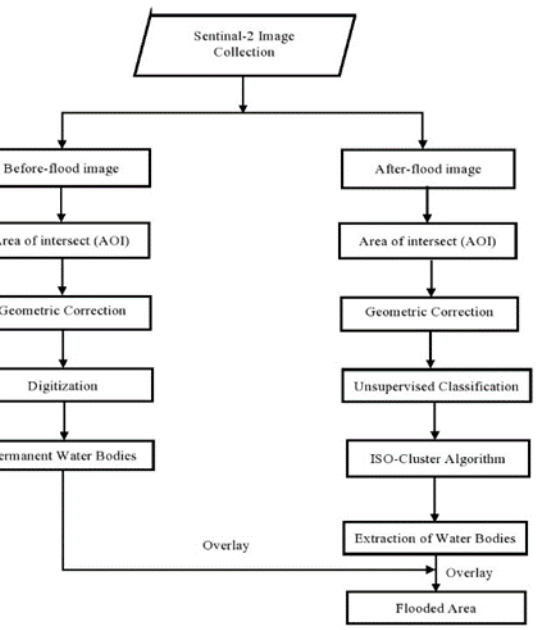

Figure 5. Methodology for processing sentinel-2 optical data

4 Results and discussions

4.1 Flood mapping using GEE for Sentinel -1 image

The images are classified as pre-flood, flood, and post-flood based on the duration of the flood. The images acquired are 10th of February designated as flood images.SAR images are naturally degraded by granular noise such as speckle noise due to the coherent nature of the scattering phenomena. All σ^0 images are converted to natural scale from decibel (dB) scale as the first step in the flood mapping process. For a refined Lee speckle filter with a 3 × 3 window size, a user-defined function is created. DEM available on the GEE cloud platform with a spatial resolution of 3 arc sec was used. When generating flood maps at the district level, it is important to mask out higher elevation regions to reduce computing time.This is accomplished by importing the HydroDEM into GEE from terrain data obtained with. Terrain() is an operation. Using the .select() operator, the slope image was obtained from the terrain dataset. Finally, the flood affected areas are extracted and the result is shown in the figure 6.

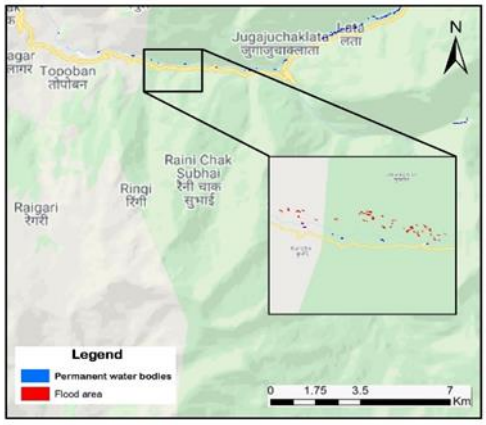

Figure. 6 Flood affected areas observed by Sentinel -1 SAR data using GEE

4.2 Flood mapping using ArcGIS for Sentinel -2 image

The optical sensors' inability to penetrate the clouds, as well as their reliance on the sun's illumination, limit the availability of optical imaging during the flood period. However, optical sensor data is less expensive and easier to read than SAR data. The optical image captured during the flood on 10 February 2021 with the Sentinel -2 sensor is taken into account. The image is first geometrically corrected. The satellite imagery is then classified using ISODATA, an unsupervised classification technique. It separates the image into several objects based on their homogeneous characteristics and classifies/clusters them. First, the image is divided into five class. The water features are then highlighted from the classified image using the recoding technique. The inundated areas are later extracted from the image by overlaying the digitized mask. The extracted resultant water layer is illustrated in Figure 8. Flood assessment and mapping are used not only to locate affected areas, but also to monitor the sustainability of environments.

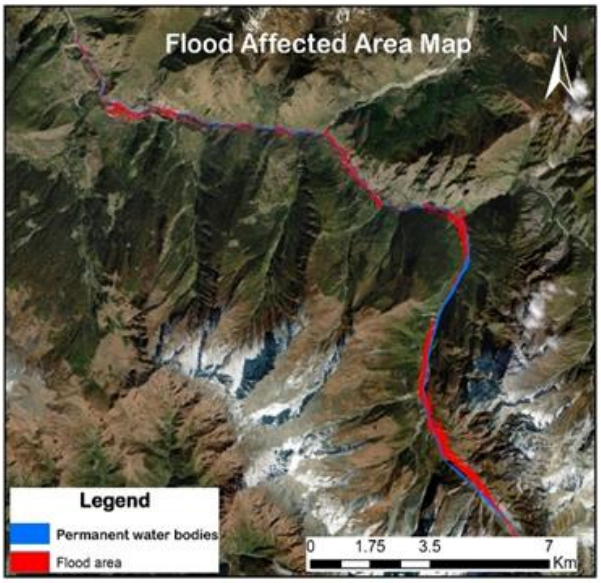

Figure 7. Flood affected areas observed by Sentinel -2 optical data

5.Conclusion

In this study, a practical technique for flood monitoring at the required spatial resolution was proposed using SAR images. Its specific aim was to highlight the possible use of Sentinel-1 SAR data sets from the European Earth Observation mission for flood monitoring in the Chamoli district of Uttarakhand state on February 7, 2021. Our analysis of the various Sentinel-1 parameters revealed that the best results were obtained using the VV polarization configuration.

The methodology for extracting the flood-affected region using optical images was also discussed in this study. The flooding zone is identified by overlaying the digitized pre-flood image mask on the extracted water layers. As a result, we may conclude that geospatial and earth observation tools provide timely data for effective decision-making and comprehensive flood disaster management. Because of the weather conditions during floods, it is difficult to obtain cloud-free optical data, and SAR data should be used to estimate the flooded region. This method was established by using a publicly accessible data and analysis tool, GEE, which can be especially beneficial to developing countries. The established flood prone areas will serve as crucial inputs for flood modelling and analysis, assisting in flood risk management.

Figure 8. Aerial and field photographs (a – i) showing Chamoli flood disaster

The research was carried out in Google Earth Engine, a cloud-based integrated development environment (IDE) platform, and code was written in JavaScript, which is the code link of the evaluated work and performance. https://code.earthengine.google.com/a28356f36fa16b6b78b31ee35edde970

References

Anusha N, Bharathi B (2020). Flood detection and flood mapping using multi-temporal synthetic aperture radar and optical data. The Egyptian Journal of Remote Sensing and Space Sciences 23, 207-291.

Tanguy, M, Chokmani K, Bernier M, Poulin J, Raymond S (2017). River flood mapping in urban areas combining Radarsat-2 data and flood return period data. Remote Sens. Environ. 198, 442–459.

Werle D, Martin T. C, Hasan K (2000). Flood and coastal zone monitoring in Bangladesh with Radarsat ScanSAR: technical experience and institutional challenges. Johns Hopkins APL Tech. Dig. 21(1), 148–154.

Rahman R, Thakur PK (2018). Detecting, mapping and analysing of flood water propagation using synthetic aperture radar (SAR) satellite data and GIS: A case study from the Kendrapara District of Orissa State of India. The Egyptian Journal of Remote Sensing and Space Sciences 21, S37-S41

Faizan M O (2021). Sentinal-1 SAR Data Preparation for Mapping of Water Bodies – A CASE STUDY, International Journal of Research Publication and Reviews Vol (2) Issue (2) 129-137

Li J, Wang S (2015). An automatic method for mapping inland surface waterbodies with Radarsat-2 imagery. International Journal Remote Sensing. 36(5), 1367–1384.

Intercontinental Geoinformation Days

igd.mersin.edu.tr

Using Sentinel-1 GRD SAR data for volcanic eruptions monitoring: the case-study of Fogo Volcano (Cabo Verde) in 2014/2015

Rafaela Tiengo*[1,2,3], José Manuel Rodrigues Pacheco[1], Jéssica Garcia Uchôa[1,2,3], Artur Gil[1]

[1] *Instituto de Investigação em Vulcanologia e Avaliação de Riscos (IVAR), Universidade dos Açores; Rua Mãe de Deus, Campus Universitário de Ponta Delgada, Edifício do Complexo Científico, 9500-321, Ponta Delgada, Portugal*
[2] *Universidade dos Açores, Faculdade de Ciência e Tecnologia, Universidade dos Açores; Rua Mãe de Deus, Campus Universitário de Ponta Delgada, Edifício do Complexo Científico, 9500-321, Ponta Delgada, Portugal*
[3] *cE3c: Centre for Ecology, Evolution and Environmental Changes & Azorean Biodiversity Group (cE3c-ABG), Faculdade de Ciências e Tecnologia da Universidade dos Açores; Rua Mãe de Deus, Campus Universitário de Ponta Delgada, Edifício do Complexo Científico, 9500-321, Ponta Delgada, Portugal*

Keywords
Remote sensing
Volcanology
Synthetic Aperture Radar
Ground Range Detected
Google Earth Engine

ABSTRACT

The last eruption in the Fogo Volcano, which began in November 2014, was the first eruptive event captured by the Sentinel-1 (S1) mission. The present work sought to complement previous research and explore the potential of utilizing data from the Synthetic Aperture Radar (SAR) S1 mission to better monitor active volcanic areas. S1 Ground Range Detected (GRD) data was used to analyze the changes that occurred in the area before, during, and after the eruptive event and was able to identify the progress of the lava flow and measure the affected area (3.89 km^2 in total). Using the GRD data on Google Earth Engine (GEE) platform demonstrated high potential in terms of response time to monitor and assess eruptive scenarios in near-real-time, which is fundamental to mitigate risks and to better support crisis management.

1. Introduction

The archipelago of Cabo Verde is located between latitudes 14º and 18º North and longitudes 22º and 26º West. Situated in the Atlantic, 1300 km from the Canary Islands, its territory has 10 islands and 13 islets and Fogo Island was the site of the last eruption (Fig. 1). Fogo Volcano is the most active volcano in this archipelago, with about 26 eruptions in the last 500 years.

After almost 20 years since the last eruption occurred in 1995, a new eruptive event with strombolian characteristics began in November 2014 and lasted approximately 78 days.

Fogo Island has an extensive eruptive history being the only island of the Archipelago of Cape Verde to have volcanic activity. The Fogo Volcano has a caldera with approximately 8 km in diameter that was formed from two collapses that occurred in the central part of the volcano and Pico do Fogo was formed in the sequence of collapses on the eastern flank of the island (Brum da Silveira et al., 1997).

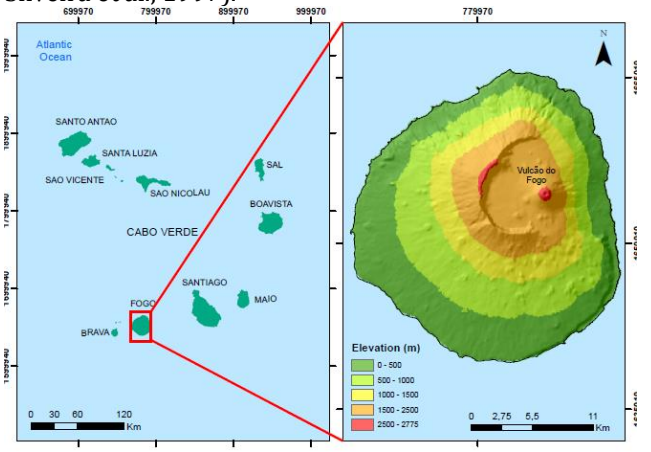

Figure 1. Map of Fogo Island, one of the ten volcanic islands of the Cabo Verde Archipelago. The Pico do Fogo (Fogo Volcano) constitutes the higher point of the island (2829m).

* **Corresponding Author**

*(rafaela.p.tiengo@azores.gov.pt) ORCID ID 0000-0002-9298-0178
(jose.mr.pacheco@azores.gov.pt) ORCID ID 0000-0002-9558-8868
(jessica.g.uchoa@azores.gov.pt) ORCID ID 0000–0002–5255-9207
(artur.jf.gil@uac.pt) ORCID ID 0000–0003–4450-8167

Cite this study

Tiengo, R., Pacheco, J. M. R., Uchôa, J. G., Gil, A. (2021). Using Sentinel-1 GRD SAR data for volcanic eruptions monitoring: the case-study of Fogo Volcano (Cabo Verde) in 2014/2015. 3rd Intercontinental Geoinformation Days (IGD), 22-25, Mersin, Turkey

Eruptive events may make it impossible to access affected areas and gather *in situ* data. Thus, the advancement of geospatial technologies proves critical in better understanding the genesis of these events remotely (Pyle et al., 2013; Jerram, 2018).

Mapping and updating the cartography of areas with active volcanism configures a fundamental task as it constitutes a tool to be used in the planning and crisis management process, as well as in the development of research, risk assessment, and crisis management (Fitz, 2008; Silva et al., 2018).

SAR data provides several advantages over other monitoring techniques due to the acquisition process of data in inaccessible and all-weather scenarios, by day or night. Besides that, S1 allows a relevant improvement for cost-effective monitoring and risk assessment of active volcanic areas. S1 pixel resolution is about 5x20 m in azimuth and range, respectively, with a revisiting cycle of 6 days. High spatial resolution SAR data is fundamental to allow the detection of unconformities in remote areas. SAR data is becoming essential in collecting relevant information about the dynamic processes by which an eruption can be generated (Fujira et al., 2017).

The GRD data from S1 mission was used in this study to identify the progress of the lava flow and measure the affected area, in order to assess its potential to monitor and assess eruptive scenarios in near-real-time, which is fundamental to mitigate risks and to better support crisis management.

2. Data and methods

This paper is focused on the application of S1 products in order to analyze eruptive scenarios. S1 GRD data was used to monitor the progression of the lava flows related to the 2014/15 eruption event through the detection of surface changes.

GRD is a S1 product that corresponds to SAR data detected, analyzed, and projected to the ground range taking into account the ellipsoidal Earth model, with separation capability in the object-target ratio of approximately 20 x 22m (ESA, 2016; ESA, 2021; Mullissa et al., 2021).

GRD consists in a product that presents the image amplitude values relative to backscattering, considering parameters such as surface roughness. These images require preprocessing to remove thermal noise. The workflow shown in Figure 2, suggested by Filipponi (2019), was applied to process this data in the SeNtinel Application Platform (SNAP) software.

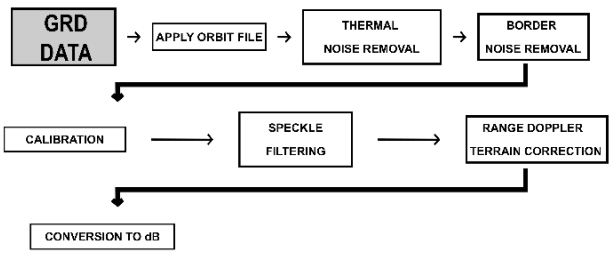

Figure 2. Workflow for removing thermal noise from S1 GRD data in SNAP software

The first stage of this procedure consists of the *Apply Orbit File* step, which corresponds to a refinement of the accuracy and the information referring to the position and speed of the satellite. Thenceforth, the *Thermal Noise Removal* step was applied in order to remove the thermal noise, thus normalizing the backscattering signal of the images. Subsequently, the *Border Noise Removal* procedure was used to compensate for the Earth's curvature levels, thus reducing the low-intensity noise contained in the images. *Calibration* step was then applied, ensuring that the image pixels were correlated with the backscattering that occurred during the information acquisition phase (ESA, 2021). Then, *Speckle Filtering* step was applied, which corresponds to the process of filtering speckles and noise. Afterward, *the* Range Doppler Terrain Correction step was undertaken to perform the geometric correction of the terrain to compensate for image distortions. The last step of this workflow consisted in converting the backscattering coefficient into decibels through a logarithmic transformation.

The GRD data acquired by the S1 mission is described in Table 1.

Table 1. S1 data used to generate the GRD of the area affected by lava flow

Image acquisition dates	Orbit
08 November 2014	Descending
27 November 2014	Ascending
09 December 2014	Ascending
21 December 2014	Ascending
02 January 2015	Ascending
07 February 2015	Ascending

To map the lava flow of the 2014/15 eruption, the GRD data was analyzed to identify the different paths that lava flow ran through day by day.

With the GRD data processed, the raster calculation tool of Arcmap 10.4 software was used to compute an Image Differencing Change Detection (Lu et al., 2004). In this procedure, each image after the start of the event is subtracted from a pre-event image. For this purpose, the value of an image referring to the last hours of the eruption was subtracted from an image prior to the beginning of the event. Very high ("change") and very low ("no change") values were thresholded in order to obtain the change detection map. To assess the accuracy and validate each change detection procedure, the Overall Accuracy was computed with independent validation datasets with 50 change/no change sampling points (Congalton and Green, 1999).

3. Results and discussion

In order to analyze the lava flow temporal progression, S1 GRD data was used to identify the affected area along the eruptive event. The successive change detection procedures showed Overall Accuracies ranging between 0.70 and 0.90. The surface changes that occurred during the 2014/15 eruption can be visualized in Figure 3. These changes are in line with the detailed

description made by Cabral (2015) for this eruptive event.

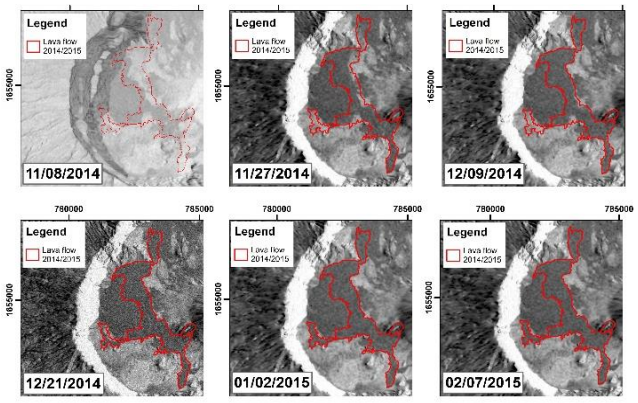

Figure 3. Level-1 GRD S1 multitemporal data used to illustrate the progression of the lava flow during the 2014/15 eruption.

In Figure 4, it is possible to note that some of the areas previously observed as affected by the 2014/15 lava flow were not identified in the change detection procedures with GRD data. It might be explained by the fact that there were no substantial roughness changes in the overlap area of 2014/15 lava flow with that of 1995 which occured at Chã das Caldeiras, as exposed by Bignami et al., (2020).

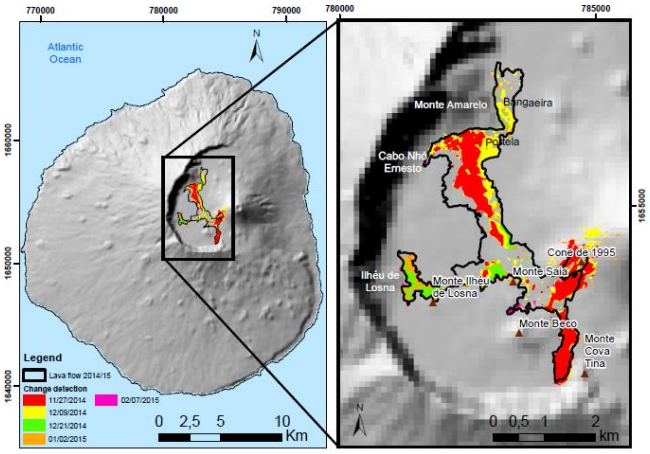

Figure 4. Changes detected with S1 GRD data throughout the 2014/15 eruptive event

The values of the total area affected by the lava flow were estimated to be approximately 3.89 km^2. The result is in relative agreement with other authors' findings when applying different techniques (Table 2).

Table 2. Total areas affected by the 2014/15 eruption, according to different authors

Area (km^2)	Reference
5,42	Cappello et al., (2016)
4,85	Richter et al., (2016)
4,97	Bignami et al., (2020)
4,8	Bagnardi et al., (2016)
4,53	Vieira et al., (2021)

The use of cloud-based platforms (e.g., GEE) allows their users to instantly access and analyze geospatial data through web interfaces (Gorelick et al., 2017). The user accesses all the cloud-hosted data without having to download the data of interest, in addition to the possibility of developing custom algorithms based on Python and JavaScript (JS) Application Programming Interfaces, which greatly reduces the computational constraint on the part of users (Navarro, 2017; Kumar & Mutanga, 2018; García et al., 2018).

A JS-based application was generated in GEE platform using a code by Google (2021) and adapted in order to compare the GRD images of S1 referring to the area affected by the lava flows resulting from the eruptive event. The data filtering parameters used in the JS script were applied to the GEE-based data collection entitled 'COPERNICUS/S1_GRD', with VV polarization corresponding to the IW mode.

The images in this application refer to the period from October 2014 to February 2015 (Fig. 5).

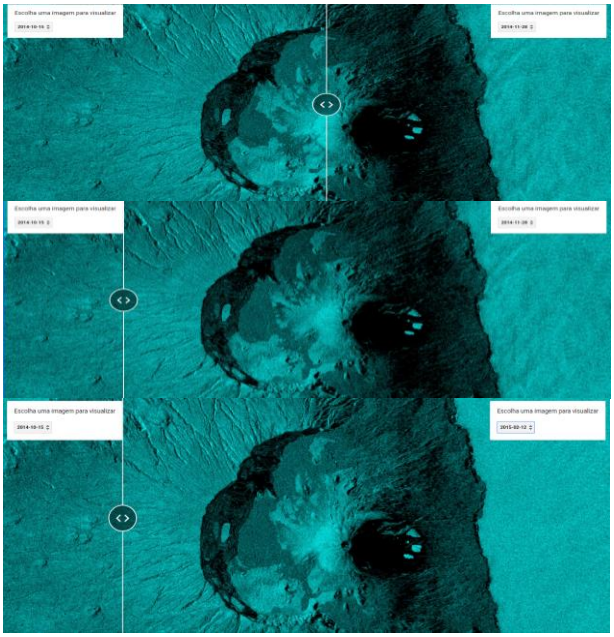

Figure 5. GEE-based application using S1 GRD data to observe the path of lava flows during the eruptive event. Above) Image from October 15th (2014) in a scenario prior to the eruption. Middle) Image from November 27th (2014) corresponding to the first hours of the eruptive event. Below) image from February 12th (2015) showing a post-eruption scenario. Application available at: <https://rafaelaptiengo.users.earthengine.app/view/fogocomparision>.

By selecting an image from before and after the eruptive event, the app is able to show the surface changes caused by the lava flow.

The use of GEE proves to be, therefore, a great asset to ensure greater speed of response, since it presents results in a matter of minutes after the script development.

4. Conclusion

Monitoring surface changes during eruptive events using S1 GRD data proved cost-effective in terms of data processing and analysis, with lower computational cost, and results consistent and coherent with those previously obtained with S1 SLC data or other types of

SAR data (including commercial high spatial resolution sensors). Therefore, this approach is pertinent and suitable for research but is especially valuable to integrate low-cost monitoring systems of active volcanic areas in near-real-time. The systematic use of GRD products can thus serve as the basis for event monitoring that confers greater agility in computation and analysis time for decision support. Furthermore, with the availability of the no-cost computing power provided by the GEE platform, and being GRD the only S1 data type currently available in the GEE catalog, this methodological approach can be considered as pertinent and cost-effective for supporting near-real-time monitoring and crisis management in active volcanic areas.

References

Bagnardi, M., P. J. González., & A. Hooper (2016). High-resolution digital elevation model from tri-stereo Pleiades-1 satellite imagery for lava flow volume estimates at Fogo Volcano, Geophys. Res. Lett., 43, 6267–6275, doi:10.1002/2016GL069457

Bignami, C., Chini, M., Amici, S., & Trasatti, E. (2020). Synergic Use of Multi-Sensor Satellite Data for Volcanic Hazards Monitoring: The Fogo (Cape Verde) 2014–2015 Effusive Eruption. Frontiers in Earth Science. Doi: 10.3389/feart.2020.00022

Brum da Silveira, A., Madeira, J., & Serralheiro, A. (1997). A estrutura da ilha do Fogo, Cabo Verde. Instituto de Investigação Científica Tropical. Lisboa, Portugal. 972-672-863-0

Cabral A J (2015). Avaliação dos perigos vulcânicos e fenómenos associados na ilha do Fogo (Cabo Verde): implicações para o planeamento de emergência e ordenamento do território. Ponta Delgada: Dissertação de doutoramento no ramo de Geologia, especialidade de Vulcanologia. Universidade dos Açores, Portugal.

Cappello, A., Ganci, G., Calvari, S., Pérez, N. M., Hernandéz, P. A., Silva, S. V., & Del Negro, C. (2016). Lava flow hazard modeling during the 2014–2015 Fogo eruption, Cape Verde. *Journal of Geophysical Research: Solid Earth*, 2290-2303p.

Congalton R., & Green K. (1999) Assessing the Accuracy of Remotely Sensed Data: Principles and Practices. Boca Raton, FL. CRC/Lewis Press, pp. 137.

ESA (2016). Sentinel 1 product definition: https://sentinel.esa.int/documents/247904/1877131/Sentinel-1-Product-Definition

ESA (2021). Level-1 GRD Products: https://sentinels.copernicus.eu/web/sentinel/technical-guides/sentinel-1-sar/products-algorithms/level-1-algorithms/ground-range-detected

Filipponi F (2019). Sentinel-1 GRD preprocessing workflow. The 3rd International Electronic Conference on Remote Sensing (ECRS 2019), 22 May–5 June 2019; Sciforum Electronic Conference Series, Vol. 3, 2019.

Fitz P R (2008). *Geoprocessamento sem complicação.* São Paulo: Oficina de Textos.

Fujira, S., Murakami, M., Nishimura, T., Tobita, M., Yarai, H., & Kobayashi, T. (2017). Volcanic deformation of Atosanupuri volcanic complex in the Kussharo caldera, Japan, from 1993 to 2016 revealed by JERS-1, ALOS, and ALOS-2 radar interferometry. *Springer*.

García, G. M., Chova, L. G., López, J. A., Marí, J. M., & Valls, G. C. (2018). Multitemporal Cloud Masking in the Google Earth Engine. *Remote Sensing*, 18.

Google (2021). *Sentinel-1 SAR GRD: C-band Synthetic Aperture Radar Ground Range Detected, log scaling*. Google Earth Engine: https://developers.google.com/earth-engine/datasets/catalog/COPERNICUS_S1_GRD

Gorelick, N., Hancher, M., Dixon, M., Ilyushchenko, S., Thau, D., & Moore, R. (2017). Google Earth Engine: Planetary-scale geospatial analysis for everyone. Remote Sensing of Environment, 202, 18-27. https://doi.org/10.1016/j.rse.2017.06.031

Jerram D (2018). *Introdução à vulcanologia.* São Paulo: Oficina de Textos.

Kumar, L., & Mutanga, O. (2018). Google Earth Engine Applications Since Inception: usage, trends and potential. *Remote Sensing*, 15.

Lu, D., Mausel, P., Brondizio, E., & Moran, E. (2004). Change detection techniques. *International Journal of Remote Sensing,* 25, 2365-2401.

Mullissa, A., Vollrath, A., Odongo-Braun, C., Slagter, B., Balling, J., Gou, Y., & Reiche, J. (2021). Sentinel-1 SAR Backscatter Analysis Ready Data Preparation in Google Earth Engine. *Remote Sensing*.

Navarro J (2017). First Experiences with Google Earth Engine. *Proceedings of the 3rd International Conference on Geographical Information Systems Theory, Applications and Management*.

Pyle, D. M., Tamsin A., & Mather, J. B. (2013). *Remote Sensing of Volcanoes and Volcanic Processes: Integrating Observation and Modelling* (Vol. 380). London: Geological Society

Richter, N., Favalli, M., de Zeeuw-van, E., Fornaciai, A., Fernandes, R. M., Pérez, N. M., Levy, J., Victória, S. S., & Walter, T. R. (2016). Lava flow hazard at Fogo Volcano, Cabo Verde, before and after the 2014–2015 eruption, Nat. Hazards Earth Syst. Sci., 16, 1925–1951, https://doi.org/10.5194/nhess-16-1925-2016.

Silva, C., Viveiros, F., Goulart, C., Pacheco, J. E., & Moreno, L. (2018). Perigos geológicos nos Açores: perigos vulcânicos - Emanações gasosas permanentes. (IVAR, Ed.) *Vulcânica*, 461.

Vieira, G., Mora, C., Pina, P., Ramalho, R., & Fernandes, R. (2021) - UAV-based very high resolution point cloud, digital surface model and orthomosaic of the Chã das Caldeiras lava fields (Fogo, Cabo Verde). Earth Syst. Sci. Data, 13, 3179-3201p. Doi: 10.5194/essd-13-3179-2021

Intercontinental Geoinformation Days

igd.mersin.edu.tr

Determination of vineyards with support vector machine and deep learning-based Image classification

Özlem Akar*[1], Ekrem Saralıoğlu [2], Oğuz Güngör [3], Halim Ferit Bayata [4]

[1]*Erzincan Binali Yıldırım University, Vocational School, Department of Land Registry and Cadastre, Erzincan, Turkey*
[2] *Artvin Coruh University, Faculty of Engineering, Department of Geomatics, Artvin, Turkey*
[3]*Ankara University, Faculty of Applied Sciences, Department of Real Estate Development and Management, Ankara, Turkey*
[4] *Erzincan Binali Yıldırım University, Faculty of Engineering and Architecture, Department of Civil Engineering, Erzincan, Turkey*

Keywords
Remote sensing
Worldview-2
Support vector machine
Deep learning
Image classification

ABSTRACT

The study aims to determine the spatial distribution of vineyards with support vector machines (SVM) and convolutional neural network (CNN) based deep learning model. Multispectral (MS) and Panchromatic (PAN) bands of the high spatial resolution Worldview-2 (WV-2) satellite image were used for the study area located in Erzincan Üzümlü district. MS and PAN bands were fused to enhance the spatial resolution of the WV-2 multispectral image, making the vineyards more distinct and visible. Then, training samples were collected for five predetermined classes (vineyard, forest, soil, road and shadow) within the boundaries of the study area to generate training and test data, and the satellite image was classified using both Support Vector Machine (SVM) and CNN algorithms. Classification results were investigated using error matrices, kappa analyzes, and Mcnemar tests. As a result of the accuracy analysis, general classification accuracies and kappa values for CNN and SVM were obtained as 86.00% (0.8536) and 63.33% (0.6077), respectively. It has been observed that the CNN classifier provides higher classification accuracy (24% higher than the SVM). In addition, it was examined whether the differences between the McNemar test and the classification results were significant or not. As a result of the McNemar test for CNN and SVM, a value of 10.298 χ^2 was calculated. The fact that the calculated χ^2 value is greater than 3.84 reveals that the CNN classifier significantly increases the classification accuracy at the 95% confidence interval.

1. Introduction

Remote sensing techniques and satellite images make great contributions in many areas such as the detection, tracking, protection of agricultural products, environmental and urban applications. Image classification is used in many different areas such as monitoring tropical forests (Christian ve Krishnayya 2009), which are of great importance in terms of being a rich natural resource with biological diversity, monitoring of coastal change (Gungor et al. 2010), monitoring of urban development (Chi et al. 2009), object extraction (Zhang et al. 2007), classification of land cover (Huang et al. 2011) and classification of product types (Sun and Di 2020). Image classification, also called information extraction, is the process of transforming this information into meaningful land cover information by using the pixel values in an image (Gao 2009). Image classification algorithms in remote sensing have been developed to meet the needs of various applications. In recent years, different learning-based algorithms have been developed for classification in order to quickly extract the most accurate and reliable information from satellite images. Commonly used learning-based classifiers include Random Forest, Bagging, Boosting, Decision Trees, Artificial Neural Networks, Support Vector Machines and K-Nearest Neighbor. These algorithms are also called machine learning methods. Machine learning methods using large enough data and parameters can automatically infer rules and constraints that users cannot see/notice directly. These methods try to find the most suitable model for the new data with the decision rules created with the training and test data. In addition, in recent years, deep learning algorithms, which are a sub-branch of machine learning methods, have been widely used for more accurate and reliable determination of agricultural products in precision agriculture applications. For

* **Corresponding Author**

*(ozlemerden@gmail.com) ORCID ID 0000-0001-6381-4907
(ekremsaralioglu@artvin.edu.tr) ORCID ID 0000-0002-0609-3338
(oguzgungor@gmail.com) ORCID ID 0000-0002-3280-5466
(hfbayata@erzincan.edu.tr) ORCID ID 0000-0001-8274-8888

Cite this study

Akar Ö, Saralıoğlu E, Güngör O & Bayata H F (2021). Determination of vineyards with support vector machine and deep learning-based Image classification. 3rd Intercontinental Geoinformation Days (IGD), 26-29, Mersin, Turkey

example, Grinblat et al. (2016) used deep learning algorithms to recognize plants from the vascular structures of plants and identified plants with high accuracy. Ferentinos et al. (2018) used deep learning algorithms to detect diseased plants. They detected the diseased ones on 25 different plant species with 99.53% accuracy. Chlingarian et al. (2018) made product yield predictions with deep learning algorithms. In addition, they defined plant species by classifying images with 99.58% accuracy with deep learning algorithms (Abdullahi et al. 2017). As can be seen from the studies, various satellite images and methods are used in the determination of agricultural products. It will be possible to detect agricultural products in a shorter time and accurately with the methods and satellite images selected according to the characteristics of the study area and the product. Cimin grape, which has economic value, is an endemic variety grown in the Üzümlü region. This study aims to determine the distribution of the cultivation areas of Cimin grape using satellite images.

1.1. Study area and dataset

An area of 25 hectares in Üzümlü district, where the Cimin, or Üzümlü grape, which is described as the Erzincan grape is grown, was determined as the pilot study area (Figure 1). Üzümlü District is located in the Upper Euphrates Section of the Eastern Anatolia Region, within the borders of Erzincan Province. A large part of the district land (80%) is located in the Öz Mountains (approximately 3500 m altitude.) region extending to the north of the Erzincan basin, and a small part (20%) is located in the Erzincan plain (approximately 1200 m altitude). Üzümlü (410 km2) is the second smallest district of Erzincan province after Otlukbeli (254 km2) in terms of area size (TR Erzincan Governorship, 2021).

The Worldview-2 (WV-2) satellite image used in the study has 8 MS bands (Coastal, Blue, Green, Yellow, Red, Red Edge, Near-Infrared 1, NearInfrared 2) with a spatial resolution of 2 m and a panchromatic band with a spatial resolution of 0.5 m. Radiometric, atmospheric and geometric corrections of this image used in the study were made by the company from which the satellite image was taken.

2. Method

The study includes accurate and reliable determination of grape fields using two widely used machine learning methods, Support Vector Machine (SVM) and convolutional neural network (CNN). In the study, the WV-2 MS and PAN images were fused using the Hyperspherical Color Space (HCS) pan sharpening method to discern the grape areas more clearly in the image. The HCS is a method developed for the Worldview-2 images (Padwick 2010), and there are various articles in the literature supporting that the HCS image fusion method gives successful results in terms of spectral and spatial aspects (Akar 2019; Li et al. 2015; Padwick et al. 2010; Anshu et al. 2017). For this reason, the HCS method was preferred in this study. Then, training pixels were collected in ENVI software for five classes (vineyard, forest, soil, road, shadow) over the fused image. A total of 70505 pixels were collected. Using this training data, the image was classified using SVM and CNN algorithms. Python programming language were used to classify the image with CNN. Optimum parameters for the image in classification were determined by a trial and error approach. The classification methods used for this study are explained theoretically below.

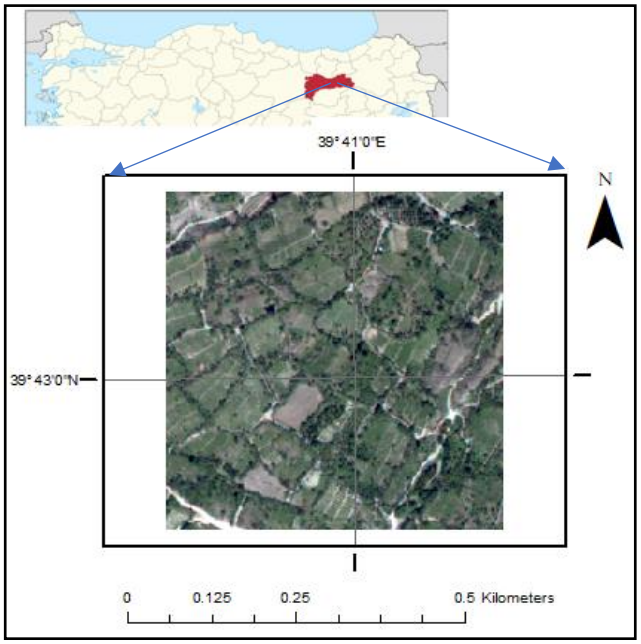

Figure 1. Study area

2.1. Support vector machine

The Support Vector Machine (SVM) classifier can classify data that is both linearly separable and nonlinearly separable. The aim is to determine the optimum hyperplane that separates the classes from each other (Vapnik 1995). If the classes are linearly separable from each other, it determines the planes with the greatest distance from the planes separating the classes from each other and uses these planes to create a linear discriminating function. Classes are separated by linear functions. If these classes cannot be separated linearly, they are moved to another higher-dimensional space where the classes can be separated linearly by using a positive C parameter and kernel functions that will minimize the classification error and maximize the distance between the planes. Classification takes place in this space (Özkan 2008; (Tso and Mather 2009; Stephens and Diesing 2014, Çölkesen and Yomralıoğlu 2014) The most widely used kernel function is the Radial basis function since it performs well (Thanh Noi and Kappas 2018); Kavzoglu and Çölkesen 2009).

2.2. Deep learning

Deep learning, which is usually characterized by neural networks containing more than two hidden layers, is recognized as one of the ten breakthrough

technologies of 2013 (Zhu et al. 2017). The deep learning model created in this study is based on the structure of convolutional neural networks. Convolutional neural networks (CNN), which are effectively used in image operations, are also successful in classifying satellite images (Saralioglu and Gungor 2020).

In the model created in this study, four 3D convolution layers were used. The filter size of each layer was set to be 3x3. The filter numbers were created as 128 in the first layer, 64 in the second layer, 32 in the third layer, and 16 in the 4th layer. After the convolution layers, two fully connected layers were used. The first is a dense layer that makes a rough classification of the features extracted by the convolutional layer. The second is the last layer in the model and is used with a Softmax classifier that extracts the class scores. The Softmax classifier produces values between 0 and 1 for each class and ensures that the class with the highest score is evaluated correctly. Parametric Rectified Linear Unit (PReLU) as activation function, Adam as optimization method, and categorical cross-entropy as subduction function was used in the model. The total number of parameters in the created deep learning model is 3118405.

3. Results and discussion

The accuracy of the thematic images (Figure 2) obtained as a result of the classification of the image with the SVM and CNN algorithms were examined with error matrices. In the accuracy analysis with error matrices, a total of 150 random points were scattered on the image proportionally to the area occupied by each class. When the overall classification accuracies produced from the error matrices were examined, the CNN method classified the image with an accuracy of 86.00% and the SVM method with an accuracy of 63.33% (Table 1). Accordingly, it is seen that the CNN method classifies the image 23% better. Calculated Kappa values also support this result.

Table 1. Overall classification accuracies and kappa analysis

	Overall Accuracy	Cohen's kappa
CNN	86.00	0.8536
SVM	63.33	0.6077

In addition, the success of these methods for each class was also examined by the Producer's (PA) and User's (UA) accuracies (Figure 3). According to Figure 3, in terms of PA, forest, road and shadow classes were classified 8%, 67% and 54% better, respectively, by the CNN method. According to UA, the CNN method was 22% more successful than SVM in vineyard class, 24% in forest class and 27% in soil class. In general, CNN method performed better than SVM. When the error matrices were examined, it was observed that the spectral characteristics of the forest and vineyard classes were very similar causing the most confusion among all classes. Similarly, granular stabilized roads in the Road class, very dark pixels in the Soil class and Forest class have similar spectral characteristics with the shadow class, resulting in incorrect classification results. SVM was not as successful as CNN in classifying these classes.

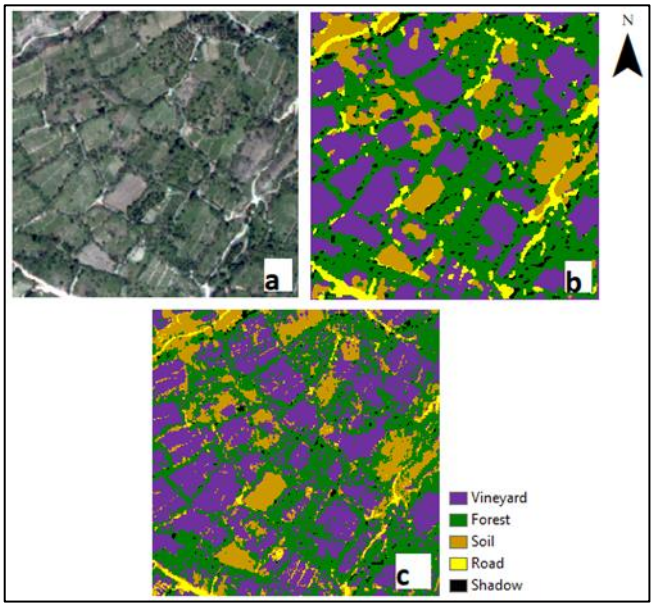

Figure 2. a) Fused image, b) Thematic images obtained from CNN, c) Thematic image obtained from SVM

In addition, it was examined whether the differences between the McNemar test and the classification results were significant. As a result of the McNemar test for CNN and SVM, the value of 10.298 χ^2 was calculated (Table 2). The fact that the calculated χ^2 value is greater than 3.84 reveals that the CNN classifier significantly increases accuracy in the 95% confidence interval in the classification process.

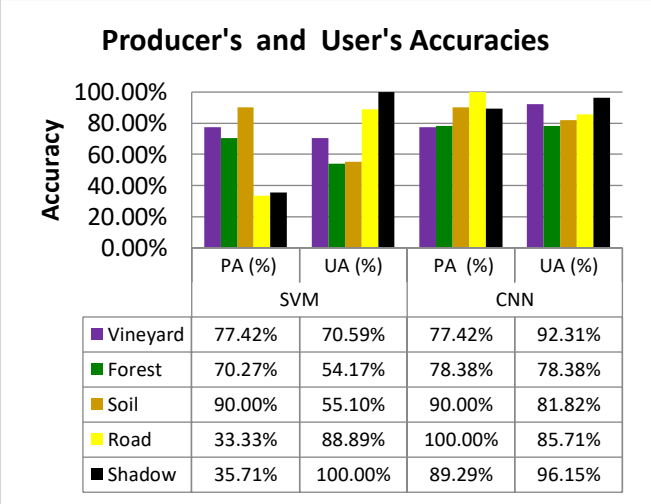

Figure 3. Producer's and User's Accuracies

Table 2. Assessment of the significance of the difference between CNN and SVM with McNemar test

	f_{11}	f_{12}	f_{21}	f_{22}	Total	χ^2
CNN-SVM	65	35	12	38	150	10.298

f_{11} : The number of samples that both methods can correctly classify, f_{22}: The number of samples that both methods cannot classify correctly, f_{12}: The number of samples misclassified by method 1 but correctly classifiedby method 2,f_{21}: The number of samples misclassified by method 2 but correctly classified by method 1.

4. Conclusion

In the study, it is aimed to determine the spatial distribution of the vineyards with the SVM and CNN algorithms, which are the most widely used machine learning approaches. As a result of the analysis, the CNN method classified the specified study area with an accuracy of 86.00% and the SVM with an accuracy of 63.33%. Accordingly, the CNN method showed 23% better classification performance than SVM and classified the spatial distribution of the vineyards more accurately. Kappa analyzes also support this result. In addition, the fact that the χ^2 value, which was calculated as 10.298 with the McNemar test, was greater than 3.84, shows that the results obtained from these two methods are significant and the performances of these two methods are different. As a result, the CNN method performed better than SVM in the classification of vineyards, which are agricultural products.

Acknowledgement

This study is supported by Erzincan Binali Yıldırım University Scientific Research Project [ID: 636] research grant.

References

Akar Ö (2019). Göktürk-2 ve Worldview-2 Uydu Görüntüleri için Görüntü Keskinleştirme Yöntemlerinin Değerlendirilmesi, Erzincan University Journal of Science and Technology, 12(2) 874-885. https://doi.org/10.18185/erzifbed.495854

Anshu SK , Pande H, Tiwari PS & Shukla S (2017). Evaluation of Fusion Techniques for High Resolution Data - A Worldview-2 Imagery, International Journal of Applied Remote Sensing and GIS, 4(1&2), 10-22.

Chi MV, Thi LP & Si ST (2009). Monitoring urban space expansion using remote sensing data in Ha Long City, Quang Ninh Province in Vietnam, 7th FIG Regional Conference Spatial Data Serving People: Land Governance and the Environment – Building the Capacity Hanoi, Vietnam.

Chlingaryan A, Sukkarieh S & Whelan B (2018). Machine learning approaches for crop yield prediction and nitrogen status estimation in precision agriculture: a review, Comput Electron Agric 151,61–69.

Christian B & Krishnayya NSR (2009). Classification of tropical trees growing in a sanctuary using Hyperion (EO-1) and SAM algorithm, Current Science, 96(12), 1601-1607.

Çölkesen İ. & Yomralıoğlu T (2014). Arazi Örtüsü ve Kullanımının Haritalanmasında WorldView-2 Uydu Görüntüsü ve Yardımcı Verilerin Kullanımı, Harita Dergisi, 152(2),12-24, Ankara.

Ferentinos KP (2018). Deep learning models for plant disease detection and diagnosis. Comput. Electron. Agric., 145, 311–318.

Gao J (2009) Digital Analysis of Remotely Sensed Imagery, The McGraw-Hill Companies, USA.

Grinblat GL, Uzal LC, Larese MG & Granitto PM(2016). Deep learning for plant identification using vein morphological patterns. Comput. Electron. Agric. 127, 418–424.

Gungor O, Boz Y, Gokalp E, Comert C & Akar A (2010) Fusion of low and high resolution satellite images to monitor changes on costal zones, Scientific Research and Essays,5(7), 654-662. https://doi.org/10.1371/journal.pone.0093950

Huang Y, Fipps G, Lacey RE, & Thomson SJ (2011). Landsat Satellite Multi-Spectral Image Classification of Land Cover and Land Use Changes for GIS-Based Urbanization Analysis in Irrigation Districts of Lower Rio Grande Valley of Texas. Applied Remote Sensing Journal, 2(1), 27-36.

Kavzoglu T & Colkesen I (2009). A kernel functions analysis for support vector machines for land cover classification, International Journal of Applied Earth Observation and Geoinformation, 11(5), 352- 359.

Li H, Linhai J, Yunwei Tang, Qingjie Liu, Haifeng Ding, Zhongchang Sun & Yu Chen (2015) Assessment of pan-sharpening methods applied to WorldView-2 image fusion, 2015 IEEE International Geoscience and Remote Sensing Symposium (IGARSS), doi: 10.1109/IGARSS.2015.7326524.

Özkan Y (2008). Veri Madenciliği Yöntemleri, Papatya Yayıncılık, İstanbul.

Padwick C, Deskevich M, Pacifici F & Smallwood S (2010). WorldView2 pan-sharpening, ASPRS 2010 Annual Conference, April 26-30, San Diego, California,

Saralioglu E & Gungor O (2020). Semantic segmentation of land cover from high resolution multispectral satellite images by spectral-spatial convolutional neural network. Geocarto International, 1-21.

Stephens D & Diesing M (2014). A Comparison of Supervised Classification Methods for the Prediction of Substrate Type Using Multibeam Acoustic and Legacy Grain-Size Data. PLoS ONE ,9(4):e93950, 1-14.

Sun Z, Di L, Fang H & Burgess A (2020). Deep Learning Classification for Crop Types in North Dakota. IEEE Journal of Selected Topics in Applied Earth Observations and Remote Sensing, 13, 2200-2213, 2020, doi: 10.1109/JSTARS.2020.2990104.

Thanh N P & Kappas M (2018). Comparison of Random Forest, k-Nearest Neighbor, and Support Vector Machine Classifiers for Land Cover Classification Using Sentinel-2 Imagery, Sensors,18(1),1-20.

TR Erzincan Governorate, 2021, http://www.erzincan.gov.tr/erzincan-uzumu, Date of access: 20.10.2021

Tso B & Mather PM, 2009. Classification Methods For Remotely Sensed Data, Second Editon, Taylor & Francis Group, United States of America.

Vapnik VN (1995). The Nature of Statistical Learning Theory, Springer-Verlag, New York.

Zhang W, Xue X, Sun Z, Guo Y, Chi M, Lu H (2007). Efficient feature extraction for ımage classification, *2007 IEEE* 11th International Conference on Computer Vision, 2007, 1-8, doi: 10.1109/ICCV.2007.4409058.

Zhu XX, Tuia D, Mou L, Xia GS, Zhang L, Xu F, & Fraundorfer F (2017). Deep Learning in Remote Sensing: A Comprehensive Review and List of Resources. IEEE Geoscience and Remote Sensing Magazine, 5(4), 8-36.

Intercontinental Geoinformation Days

http://igd.mersin.edu.tr/2020/

Assessing the interrelationship between LST, NDVI, NDBI and land cover change in Amuwo-Odofin, Lagos Nigeria

Alfred S. Alademomi[1,2,3], Chukwuma J. Okolie[1,2,3], Olagoke E. Daramola[1,2], Samuel A. Akinnusi[1,2], Elias Adediran[1,2], Hamed O. Olanrewaju[1,2], Abiodun O. Alabi[1,2*], Tosin J. Salami[1,2], Joseph Odumosu[2,4]

[1]*University of Lagos, Faculty of Engineering, Department of Surveying and Geoinformatics, Lagos, Nigeria*
[2]*Geospatial and Environmental Research Group, University of Lagos, Nigeria*
[3]*Centre for Multidisciplinary Research and Innovation (CEMRI), Abuja, Nigeria*
[4]*Federal University of Technology, School of Environmental Technology, Department of Surveying and Geoinformatics, Niger State, Nigeria*

Keywords
Land Cover
Land Surface Temperature
Normalized Difference Vegetation Index
Normalized Difference Built-up Index

ABSTRACT

Climate change is undoubtedly one of the greatest existential threats to humans. This threat is continuously being aggravated by continuous urbanization which leads to the rapid change of land cover profoundly affecting biodiversity and ecosystem function as well as local and regional climate. This study assesses the variation of land surface temperature (LST), normalized difference vegetation index (NDVI) and normalized difference built-up index (NDBI), and the relationship with land cover change in Amuwo-Odofin Local Government Area of Lagos State, Nigeria. Multi-date Landsat imageries for years 2002 and 2019 were classified using the parallelepiped technique into five land cover classes – vegetation, bare land, built-up area, water body and wetland. The spectral indices (NDVI and NDBI) were computed and the LST was determined using a single-channel algorithm. In the findings, there was a negative correlation between LST and NDVI, and between NDVI and NDBI. The distribution of the LST, NDVI and NDBI varied correspondingly in accordance with changes in land cover.

1. Introduction

In recent times, there has been renewed interest in understanding the dynamics of land cover change and its relationship with several environmental parameters. Some of these key environmental parameters that have received the attention of researchers include the land surface temperature (LST), normalized difference vegetation index (NDVI), and normalized difference built-up index (NDBI) (Guha et al., 2020; Al-Faisal et al., 2021). These three parameters (LST, NDVI and NDBI) are integral in the study and monitoring of land cover change (Alademomi et al., 2020; Abir and Saha, 2021). However, very few studies have investigated the link between LST, NDVI, NDBI and land cover change, and more studies are required to explore their interrelationship. Environmental parameters of relevance to human population and sustainability within an environment are mainly climatic factors which are easily influenced by land cover practices and the same holds for the reverse (Xiong et al., 2012).

LST is one of the key environmental parameters that is affected by changes in land cover. For many fields, measuring LST is significant, including climate variability and change, urban heat island impact, land/atmosphere feedback, fire monitoring, mapping and detection of land cover and change, geological studies, crop management and water management (Jaber, 2019). According to Weixin et al. (2011), the key causes of land surface temperature variations that are correlated with vegetation density are changes in vegetation. This was also corroborated by Fathizad et al. (2017). Although it is known that vegetation cover has a moderating effect on LST, vegetation types can vary in their ability to reduce the temperature of the surface.

* **Corresponding Author**

*(aoalabi@unilag.edu.ng) ORCID ID 0000-0002-4678-6059

Cite this study

Alademomi A S, Okolie C J, Daramola O E, Akinnusi S A, Adediran E, Olanrewaju H O, Alabi A O, Salami T J & Odumosu J (2021). Assessing the interrelationship between LST, NDVI, NDBI and Land Cover change in Amuwo-Odofin, Lagos Nigeria. 3rd Intercontinental Geoinformation Days (IGD), 30-33, Mersin, Turkey

A spectral index for detecting long-term differences in vegetation coverage and its status is the Normalized Difference Vegetation Index (NDVI) (Fathizad et al., 2017). With values ranging from -1 to +1, NDVI shows the condition and abundance of the green vegetation cover and biomass. Another interesting spectral index is the Normalized Difference Built-up Index (NDBI), which gives information on the extent of urbanization in a region as well as the land cover change. Similar to other spectral indices, the NDBI value ranges from -1 to +1 with higher values indicating presence of more impervious surface and vice versa. NDBI like other spectral indices which quantitively represent land cover type have been used widely in LST-land cover studies. NDBI plays an important role in urban areas where most of the human population are concentrated (Xiong et al., 2012).

This study is focused on the assessment of the interrelationship between LST, NDVI, NDBI and land cover change using multispectral Landsat imageries for 2002 and 2019. The objectives are: (i) supervised image classification of the Landsat imageries; (ii) calculation of the spectral indices: NDVI and NDBI; (iii) determination of the LST using the Landsat thermal bands and a single channel algorithm (iv) assessment of the correlation between LST, NDVI and NDBI, and the relationship with land cover changes. The findings of this study contribute to the body of knowledge on land cover change dynamics, and global and environmental change.

2. Methods

2.1. Study area

The study area is Amuwo Odofin local government area (LGA) in Lagos State, Nigeria (shown in Figure 1). The LGA covers an area of about 173km^2 and is located within the metropolitan area of Lagos. According to the 2006 Nigerian population census, Amuwo Odofin LGA had a population of over 524,971 and this figure was expected to rise to 766,111 in 2018 and over a million in 2021 (Annual Abstract of Statistics, 2019). Two air masses influence the climate of the area: the tropical maritime and tropical continental air masses. The former is wet and originates from the Atlantic Ocean, while the latter originates from the Sahara Desert and is warm, dry and dusty. The two main seasons recognized in the region are: the dry season (between November and March) and the rainy season (between April and October), with a brief break in the middle of August. Amuwo Odofin is divided into two distinct geographical spheres of riverine areas and upland. The area is richly blessed with mangroves and varieties of coastal wetlands. Tropical swamp forests are the dominant type of vegetation; fresh waters and mangrove swamp forests and dry lowland rain forest (FEPA, 1997).

2.2. Datasets

The Landsat imageries for this study were downloaded from the United States Geological Survey (USGS) Earth Explorer website (https://earthexplorer.usgs.gov/). Table 1 shows the imagery characteristics.

Table 1. Characteristics of the Landsat imageries

Dataset	Resolution	Date of Acquisition (DD-MM-YYYY)	Acquisition Time (GMT)
Landsat 7 ETM+	30m	28-12-2002	9:51:41
Landsat 8 OLI		01-01-2019	10:02:48

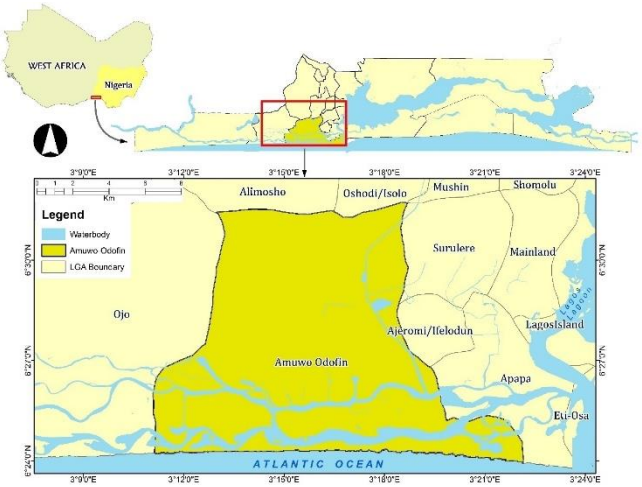

Figure 1. Map showing the location of Amuwo-Odofin LGA

2.3. Image pre-processing and enhancement

The Landsat imageries were combined into false color composites within the ENVI 5.2 software environment using the following band combinations: 5-4-3 for Landsat 8 OLI and 4-3-2 for Landsat 7 ETM+. Thereafter, the Gram-Schmidt spectral sharpening algorithm was used to pansharpen the image composites using the panchromatic band. This improved the spatial resolution from 30m to 15m thereby enhancing interpretation.

2.4. Land Cover, NDVI, NDBI and LST

Using the parallelepiped supervised classification algorithm, the Landsat imageries were classified into 5 information classes – vegetation, bare land, built-up area, water body and wetland. The theoretical background of the parallelepiped algorithm is already well explained in the extant literature (e.g., Obiefuna et al., 2021). Landsat Level 2 products were ordered and downloaded from the USGS Earth Resources Observation and Science (EROS) Centre Earth Science Processing Architecture (ESPA) on-demand interface. The ESPA is an incubation environment that provides users with an on-demand interface to process and customise Landsat science products. The NDVI is computed as the difference between the near-infrared (NIR) and red (RED) spectral reflectance bands divided by their sum. The NDBI is calculated as a ratio between the shortwave infrared (SWIR) and near infrared (NIR) values in traditional fashion.

$$NDVI = \frac{NIR-RED}{NIR+RED} \dots\dots\dots\dots\dots\dots\dots\dots\dots\dots (1)$$

$$NDBI = \frac{SWIR-NIR}{SWIR+NIR} \dots\dots\dots\dots\dots\dots\dots\dots\dots\dots (2)$$

Where;
Red = Band 4 (Landsat 8 OLI) or Band 3 (Landsat 7 ETM+)
NIR = Band 5 (Landsat 8 OLI) or Band 4 (Landsat 7 ETM+)

SWIR = Band 6 (Landsat 8 OLI) or Band 5 (Landsat 7 ETM+)

The LST was computed using the single channel algorithm. The theoretical basis and equations behind the single channel algorithm are already well explained elsewhere and only a brief explanation is provided here Landsat ETM Band 6_1, and TIRS Band 10 were used for the retrieval. This basically involved the following steps: (i) conversion of Digital Number (DN) to Spectral Radiance; (ii) conversion of Spectral Radiance to Top-of-Atmosphere Brightness Temperature; and (iii) conversion of Brightness Temperature to LST.

3. Results

This section presents the results of the different processing and analysis carried out in this study. These include the Land cover, LST, NDVI, and NDBI maps, and analysis of the interrelationships. Figures 2 and 3 present the land cover, NDVI, LST and NDBI maps respectively.

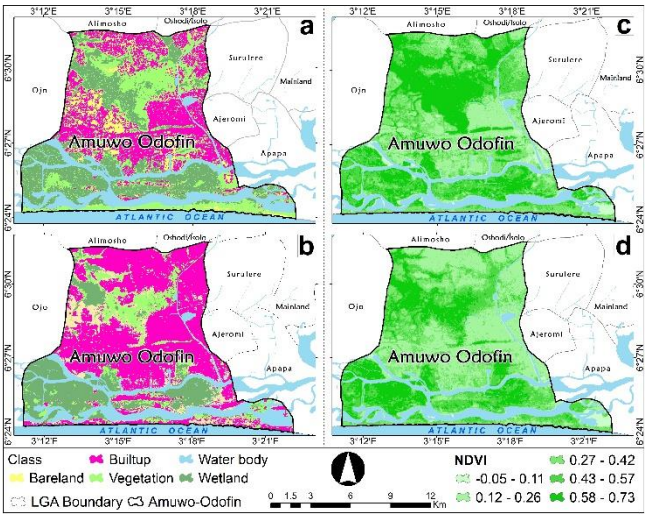

Figure 2. Land cover – (a) 2002 (b) 2019, and NDVI – (c) 2002 (d) 2019

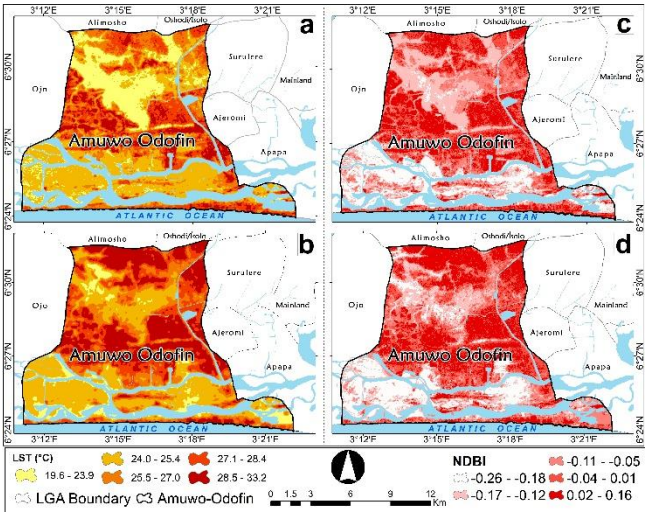

Figure 3. LST – (a) 2002 (b) 2019, and NDBI – (c) 2002 (d) 2019

Table 2 presents the coverage area of the land cover classes, while Tables 3 and 4 present the descriptive statistics of the LST, NDVI and NDBI for the different land cover classes. Table 5 presents the coefficient of correlation (r) between the LST, NDVI and NDBI.

Table 2. Coverage area of land cover classes

Land cover	Area -- 2002		Area -- 2019	
	km²	%	km²	%
Bare land	15.12	8.73	20	11.55
Built-up area	46.78	27	81.09	46.81
Mixed vegetation	44.93	25.94	18.88	10.9
Water body	23.82	13.75	22.73	13.12
Wetland	42.58	24.58	30.53	17.63
Total	173.23	100	173.23	100

Table 3. Descriptive statistics of LST, NDVI and NDBI per land cover class - 2002

Land cover		Bare land	Built-up area	Vegetation	Wetland
	Count	16783	51970	49908	47208
LST	Min	22.84	23.69	23.12	22.84
	Max	34.20	34.98	30.49	28.92
	Mean	28.94	28.21	26.03	24.88
NDVI	Min	0.06	0.04	0.00	0.03
	Max	0.49	0.60	0.64	0.64
	Mean	0.26	0.28	0.42	0.46
NDBI	Min	-0.07	-0.25	-0.46	-0.47
	Max	0.75	0.26	0.23	0.22
	Mean	0.15	0.05	-0.10	-0.26

Table 4. Descriptive statistics of LST, NDVI and NDBI per land cover class - 2019

Land cover		Bare land	Built-up area	Vegetation	Wetland
	Count	22100	89862	21007	33841
LST	Min	21.93	20.12	19.64	21.65
	Max	33.17	33.15	29.14	28.99
	Mean	26.32	28.08	24.77	24.27
NDVI	Min	0.04	0.05	0.06	0.21
	Max	0.72	0.61	0.73	0.73
	Mean	0.44	0.27	0.53	0.58
NDBI	Min	-0.23	-0.18	-0.25	-0.26
	Max	0.13	0.16	0.07	0.00
	Mean	-0.08	0.001	-0.14	-0.19

Table 5. Coefficient of correlation (r) between LST, NDVI, and NDBI

	LST 2002	LST 2019	NDVI 2002	NDVI 2019	NDBI 2002	NDBI 2019
LST 2002	1.00	0.81	-0.19	-0.26	0.86	0.69
LST 2019	0.81	1.00	-0.09	-0.37	0.83	0.86
NDVI 2002	-0.19	-0.09	1.00	0.79	-0.14	-0.29
NDVI 2019	-0.26	-0.37	0.79	1.00	-0.26	-0.63
NDBI 2002	0.86	0.83	-0.14	-0.26	1.00	0.80
NDBI 2019	0.69	0.86	-0.29	-0.63	0.80	1.00

4. Discussion

The observed increase in built-up area is in tandem with the findings of Obiefuna et al. (2018), Babalola and Akinsanola (2016), and Abiodun et al. (2005). All these studies examined the land cover changes in Lagos metropolis. The decline in wetland is also corroborated by Obiefuna et al. (2018) and Ajibola et al. (2012). Ajibola

et al. (2012), posited that the loss of wetlands in Lagos metropolis is as a result of human activities which include incessant sand filling and conversion of wetland environment to economic uses (through construction) and perennial flooding which is a common and regular occurrence in the metropolis. Other studies have also reported vegetation decline in Lagos (e.g., Abiodun et al., 2005; Obiefuna et al., 2018; Babalola and Akinsanola, 2016). The slight decrease in the waterbody area could be as a result of the expansion of the residential areas causing the inland water body to decline. Also, as earlier identified, another possible reason for decrease in water body could be the land reclamation projects within the study area.

The effect of these changes manifested in the distribution of LST, NDVI and NDBI. The spatial pattern of the LST was similar to built-up areas. This validates the known premonitions that built-up areas are major contributors to increase in LST. This relationship has been corroborated by several authors including Nse et al. (2020) and Obiefuna et al. (2021). According to Obiefuna et al. (2021), the main driver of land cover change is built-up area or urban development which had grown by over 770% since 1984 and as a result caused an increase in the mean LST over Lagos from 28.60°C in 1984 to 30.76°C in 2019. The low mean LST in the vegetated and wetland areas suggests relatively a higher rate of evapotranspiration and favoring of latent exchange between surface and atmosphere as compared with impervious surface like built-up and bare land areas (Alademomi et al., 2020).

The NDBI results exhibited similar trend as LST and this is backed by the strong positive correlation between the indices for all the years: 2002 (r = 0.86), and 2019 (r = 0.86). The low NDVI observed over bare land and built-up area and high values seen over mixed vegetation and wetland is a common trend which has been reported by different NDVI-land cover studies (e.g., Alademomi et al., 2020).

5. Conclusion

The interrelationship between LST, NDVI and NDBI within Amuwo Odofin LGA of Lagos State has been examined in this study in relation to the prominent land cover. The study observed that the pattern and values of the three parameters varied correspondingly in accordance to changes in land cover. The built-up area had the most significant change and as such, the LST increased consistently throughout the study period. Consequently, it can be concluded that increase in the built-up area is the major driver of LST, NDBI and NDVI with an observed relationship that NDBI and LST values increase with increase in built-up areas. Conversely, it was observed that there exists an inversely proportional relationship between NDVI and LST, and between NDVI and NDBI.

Acknowledgements

The authors are grateful to the USGS for access to the Landsat imageries and the USGS EROS Centre for the Landsat spectral indices used in this research. We also thank the editor and anonymous reviewers of this paper for their feedback which helped to improve the quality of the paper.

References

Abiodun, O. E., Olaleye, J. B., & Dokai, A. N. (2005). Land Use Change Analyses in Lagos State From 1984 to 2005. Spatial Information Processing II, May 2011, 18–22.

Ajibola, M. O., Adewale, B. A., & Ijasan, K. C. (2012). Effects of Urbanisation on Lagos Wetlands. International Journal of Business and Social Science, 3(17), 310–318.

Alademomi, A. S., Okolie, C. J., Daramola, O. E., Agboola, R. O., & Salami, T. J. (2020). Assessing the relationship of LST, NDVI and EVI with land cover changes in the Lagos Lagoon environment. Quaestiones Geographicae, 39(3), 87–109. https://doi.org/10.2478/quageo-2020-0025

Babalola, O. S., & Akinsanola, A. A. (2016). Change Detection in Land Surface Temperature and Land Use Land Cover over Lagos Metropolis, Nigeria. Journal of Remote Sensing & GIS, 5(3). https://doi.org/10.4172/2469-4134.1000171

Faisal, K. A., Yue, W., Abdullahi Abubakar, G., Hamed, R., & Noman Alabsi, A. A. (2021). Analyzing urban growth and land cover change scenario in Lagos, Nigeria using multi-temporal remote sensing data and GIS to mitigate flooding. Geomatics, Natural Hazards and Risk, 12(1), 631–652. https://doi.org/10.1080/19475705.2021.1887940

Fathizad, H., Tazeh, M., Kalantari, S., & Shojaei, S. (2017). The investigation of spatiotemporal variations of land surface temperature based on land use changes using NDVI in southwest of Iran. Journal of African Earth Sciences, 134(2017), 249–256. https://doi.org/10.1016/j.jafrearsci.2017.06.007

Guha, S., Govil, H., Gill, N., & Dey, A. (2020). Analytical study on the relationship between land surface temperature and land use/land cover indices. Annals of GIS, 26(2), 201–216. https://doi.org/10.1080/19475683.2020.1754291

Jaber, S. M. (2019). On the relationship between normalized difference vegetation index and land surface temperature: MODIS-based analysis in a semi-arid to arid environment. Geocarto International, 0(1010–6049), 1–19. https://doi.org/10.1080/10106049.2019.1633421

Nse, O. U., Okolie, C. J., & Nse, V. O. (2020). Dynamics of Land Cover, Land Surface Temperature and Ndvi in Uyo Capital City, Nigeria. Scientific African, 10(2020), 00599. https://doi.org/10.1016/j.sciaf.2020.e00599

Obiefuna, J. N., Nwilo, P. C., Okolie, C. J., Emmanuel, E. I., & Daramola, O. (2018). Dynamics of Land Surface Temperature in Response to Land Cover Changes in Lagos Metropolis. Nigerian Journal of Environmental Sciences and Technology, 2(2), 148–159. https://doi.org/10.36263/nijest.2018.02.0074

Obiefuna, Jerry N., Okolie, C. J., Nwilo, P. C., Daramola, O. E., & Isiofia, L. C. (2021). Potential Influence of Urban Sprawl and Changing Land Surface Temperature on Outdoor Thermal Comfort in Lagos State, Nigeria. Quaestiones Geographicae, 40(1), 5–23. https://doi.org/10.2478/quageo-2021-0001

Intercontinental Geoinformation Days

igd.mersin.edu.tr

Detecting changes in mangrove forests along the Bintang Bolong Estuary, Gambia using Google Earth Engine, Sentinel-2 imagery and Random Forest classification

Lisah Khadiala Ligono*[1], Chukwuma John Okolie [2]

[1]*Jomo Kenyatta University of Agriculture and Technology, Department of Geomatics Engineering and Geospatial Information Science, Nairobi, Kenya*
[2]*University of Lagos, Department of Surveying and Geoinformatics, Lagos, Nigeria*

Keywords
Mangroves
Land Cover
Sentinel-2 Imagery
Google Earth Engine
Random Forest

ABSTRACT

The changes in mangrove areal distribution can result in significant changes in the coastal ecosystem. In order to curb this, conservation efforts have been adopted especially in developing nations due to the ease of implementation of some of those initiatives. Despite their positive impacts, poor monitoring and evaluation of these initiatives have introduced gaps when it comes to accountability. This majorly results in project failures and economic losses. The Google Earth Engine cloud computing platform was utilized in the analysis of mangrove changes and land cover transitions. The resulting info-graphics illustrated the changes that occurred in the Bintang Bolong estuary in the years 2017 and 2020. This provides scientific evidence on the outcomes of the ongoing restoration projects thus further aiding sustainably driven mangrove restoration efforts.

1. Introduction

Mangrove ecosystems are an essential component of wetland biodiversity. They play a big role in the mitigation of climate change (Rahman, 2010) through carbon sequestration (Alongi, 2002, 2008; EL Gilman, 2008; Giri, 2011). Their diverse benefits are what make them the most vulnerable habitats (Kenduiywo et al., 2020). Conservation of these ecosystems is in line with the United Nations Sustainable Development Goal (SDG) 15 on life on earth (Mondal et al., 2019) through targets 15.1 and 15.2. Mangroves cover a vast stretch in the tropics with approximately 20% in Africa spread unevenly along the east and west coasts (Giri, 2011).
Mangrove forests on the east coast are relatively well-studied compared to those on the west coast (Giri, 2011). The coverage of mangroves in the Gambia is approximately 51,911 Km^2 (Bryan et al., 2020)and they grow farther inland at a stretch of approximately 100 km due to the intrusion of River Gambia (Corcoran et al., 2007; Njisuh Z. & Gordon N., 2011). Despite this vast occurrence of mangroves within the country, their distribution has received little or no attention in the existing literature. The country prior to 1980, had a total of about 68,000 ha of mangrove forest with the main area of die-back being along the Bintang Bolong area, extending into the Cassamance Region of Senegal (Dia Ibrahima, 2012). However, the trend of the loss is not linear. Several initiatives have been introduced by the Gambian government to address the loss of mangrove forests in the country. These intervention measures have not been well documented. Consequently, there is a limited understanding of biological and morphological changes brought about by these interventions. Often it leads to poor scientific input into ecological planning and goal setting. This leads to failures and economic losses in these well-intentioned projects.

This study utilizes multi-spectral and multi-temporal Sentinel-2 imageries to assess changes in mangrove forests, and the relationship with ongoing land cover transitions in the Bintang Bolong estuary in Gambia. The areal extent of the mangroves and other land cover classes were extracted using random forest classification within the Google Earth Engine (GEE) application. The observed changes were quantitatively and qualitatively analyzed and validated with a field survey. This study informs knowledge-based mangrove intervention and restoration efforts, and enables sound decision making.

* **Corresponding Author**

*(lisahligono@gmail.com) ORCID ID 0000 – 0002 – 9138 – 6898
(cokolie@unilag.edu.ng) ORCID ID 0000 – 0003 – 4542 – 7051

Cite this study

Ligono L K, & Okolie C J (2021). Detecting changes in mangrove forests along the Bintang Bolong Estuary, Gambia using Google Earth Engine, Sentinel-2 imagery and Random Forest classification. 3rd Intercontinental Geoinformation Days (IGD), 34-37, Mersin, Turkey

2. Methods

This section presents the materials and methods adopted for this study including the data acquisition, processing and analysis stages. Figure 1 shows the methodology workflow diagram.

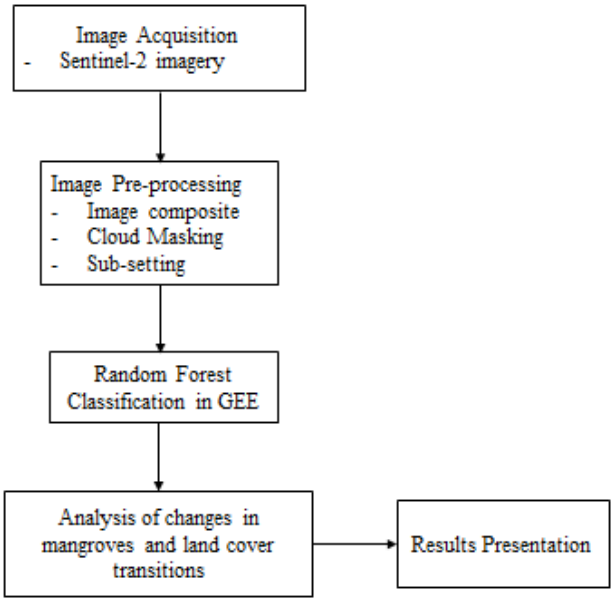

Figure 1. Methodology workflow diagram

2.1. Study area

The study area is the Bintang Bolong estuary in the Kiang West Lower River Region which is part of the Gambia River, centered approximately between latitude 13° and 14° N (Figure 2). It is bordered on the north, south and east by the Republic of Senegal and on the west by the Atlantic Ocean. The climate of Gambia is largely semi-arid with two distinct seasons –wet season (June to October) and dry season (December to May) (Gambia Department of Water Resources, 2018).

The country is host to some of the sub-regions tallest mangroves (+20m)The Bintang Bolong estuary has experienced more of the mangrove die-back with the level of degradation estimated at approximately 90% (Dia Ibrahima, 2012). The majority of the dieback is believed to have been caused by a severe drought in the 1970s, the Sahel drought, leading to deeper tidal penetration, and higher soil and water salinity and also its proximity to the Cassamance region in Senegal (Rivera-Monroy et al., 2017).

This situation has led to community involvement in the restoration and rehabilitation of mangroves especially in the Kiang West District along the estuary. Communities such as Sankandi, Keneba, Jiffarong, Bajana etc are very such involved in these efforts coupled with their strategic locations as shown in Figure 4.

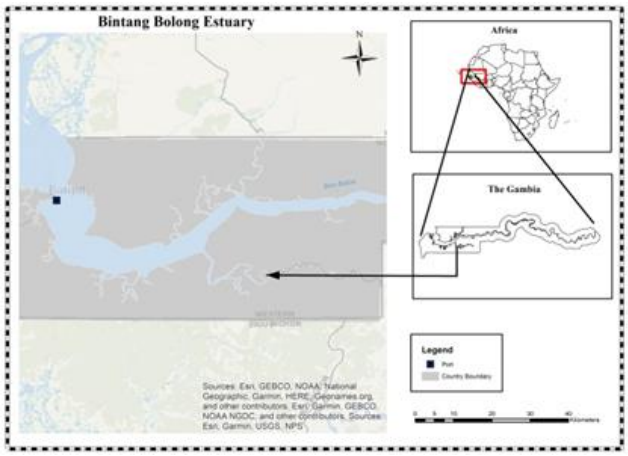

Figure 2. Map of the Bintang Bolong Estuary

2.2. Sentinel-2 imagery

The main datasets used for this study are Sentinel-2 multi-spectral imageries acquired at the following dry season periods- January 11 2017 and May 14 2020. Sentinel-2 is a Copernicus mission launched in 2015 comprising of twin (Sentinel 2A/B) polar-orbiting satellites with a high revisit time dependent on the latitude. Sentineel-2 contributes to the Copernicus themes: atmosphere, marine, land, climate, emergency and security. Several researchers have adopted Sentinel-2 imageries for mapping and monitoring of changes in mangroves (e.g., Cissell et al.,, 2021; Ghorbanian et al., 2021; Jamali, 2020; Tieng et al., 2019; Wu et al., 2020). The Sentinel-2 Multi-spectral Instrument (MSI) has 13 spectral bands with different spatial resolutions.

2.3 Image classification

The Random Forest (RF) classifier was used in the extraction of mangroves and other land cover classes within the Google Earth Engine (GEE) platform (See Figure 3). The Sentinel-2 imageries were imported into GEE and sub-set to the area of interest (AOI). Image composites were generated with spectral bands in the following order- band 4 (red), band 3 (green) and band 2 (blue). Interpretation of the composite revealed 4 main land cover classes- mangroves, water bodies, bare lands and mixed forests. Training data were created at selected points on the imageries to represent the land cover classes. The classification was executed with the RF classifier and the results were converted to GeoTIFF format for further analysis in ArcGIS.

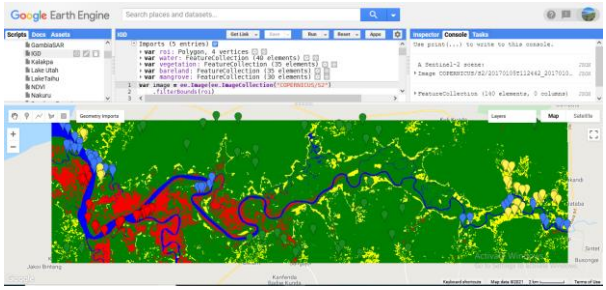

Figure 3. Image showing the 2017 classified image in the Google Earth Engine GUI. The points (Red, Blue,

Green and Yellow) are training data sampled for classification

3. Results

Figure 6 presents the land cover maps for 2017 and 2020. Results show an increase in mangroves, bare land and water body land cover at 38.6 Km² in 2017to 41.5 km² in 2020; 23.8 km² in 2017to 29.4 km² in 2020 and 36.8 km² in 2017to 79.0 km² in 2020 respectively. In the contrary, there was a dramatic decrease in in mixed vegetation at 410.7 Km² in 2017to 360.1 km² in 2020 as illustrated in Figure 7. A total of 0.3618 km² and 9.9783 km² of water bodies and bare lands land covers in 2017 were converted into mangroves land cover in 2020. These results are supported by field survey exercise carried out in Sankandi village during a tree planting exercise (Figures 4 and 5).

Figure 4. Mangroves in a rehabilitated bare land at Sankandi 2-Feb. Source: Field survey, 2021

Figure 5. Sections of bareland and planted mangrove trees at Sankandi 2-Feb. Source: Field survey, 2021

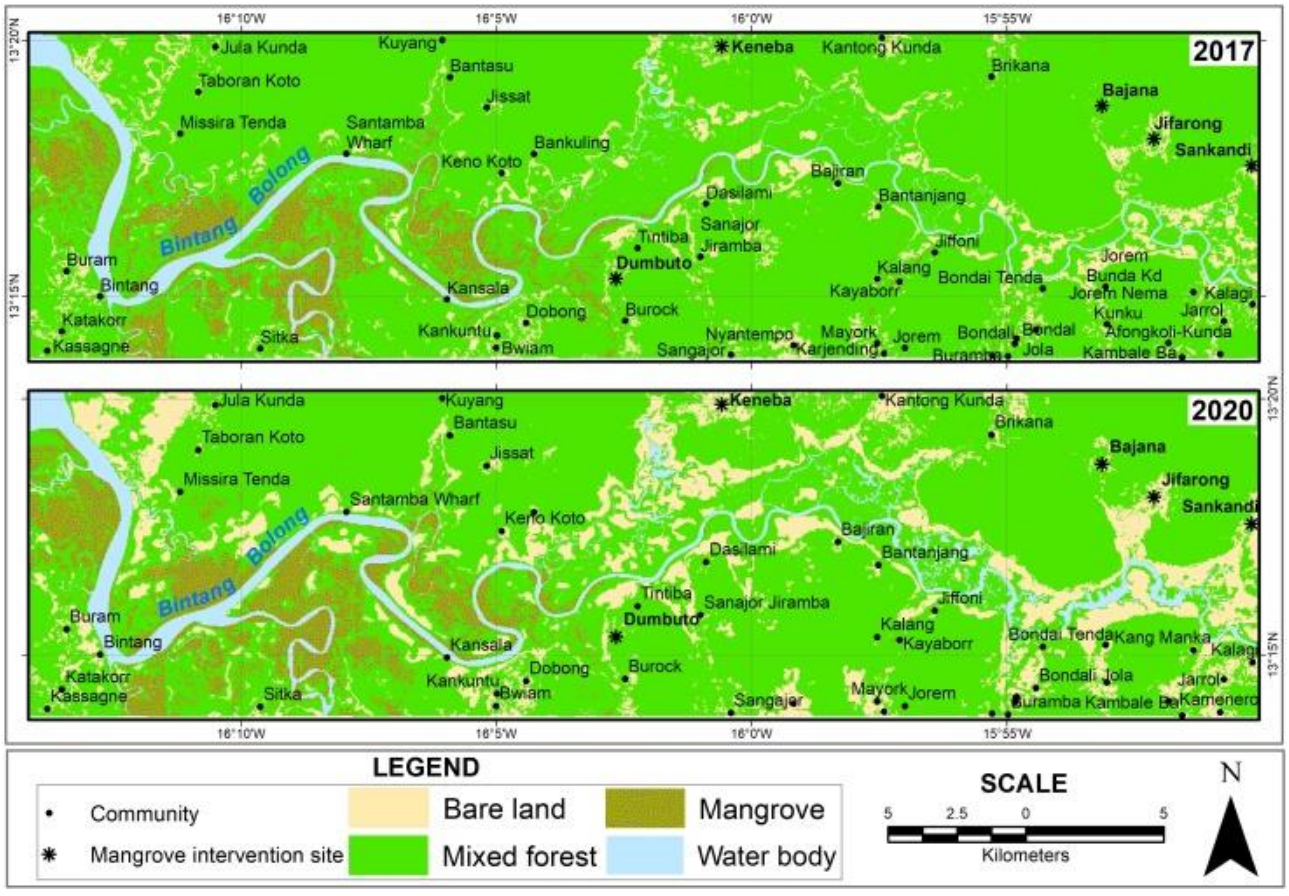

Figure 6. Land cover map of Bintang Bolong river

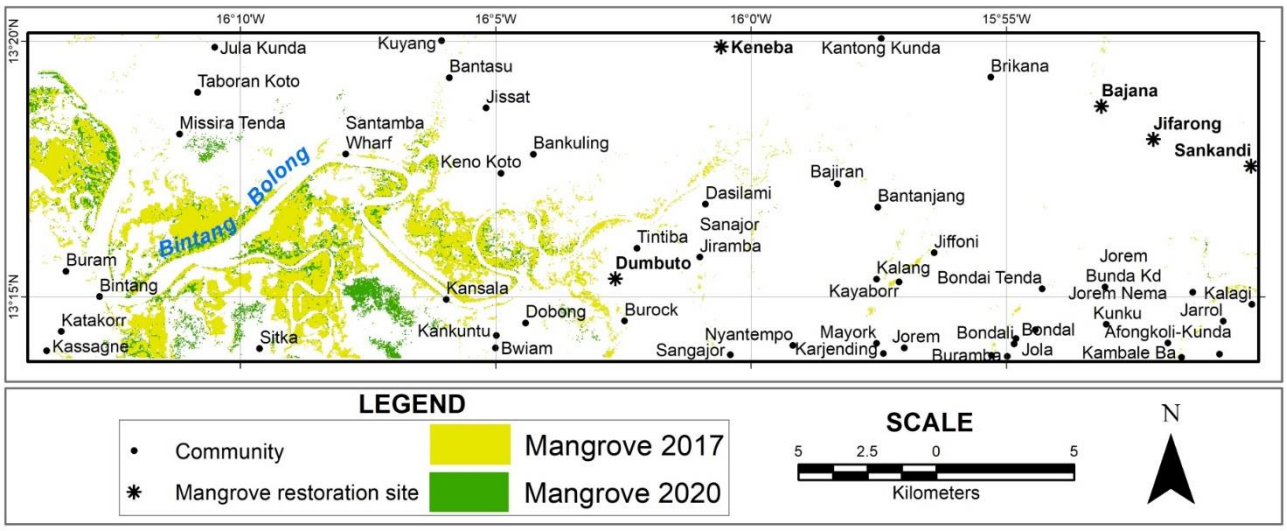

Figure 7. Overlay of the mangrove change at Bintang Bolong

Table 1. Land cover change statistics

Land Cover	2017 (Km²)	2017 (%)	2020 (Km²)	2020 (%)	Change (Km²)
Water bodies	23.8	4.7	29.4	5.8	5.5
Mangroves	38.6	7.6	41.5	8.1	2.9
Mixed forests	410.7	80.5	360.1	70.6	-50.6
Bare lands	36.8	7.2	79.0	15.5	42.2

4. Discussion

Despite the decline of mangroves globally, mangroves in Bintang Bolong estuary appear to have rapidly increased from 2017 to 2020. This could be attributed to the mangrove planting activities spearheaded by some communities within the Kiang West District. These findings align with those of (Elmahdy et al., 2020) who conducted a spatiotemporal mapping and monitoring of mangrove forest change in the United Arab Emirates. Consequently implying that mangrove loss trend in the Gambia is non-linear that keeps fluctuating for different years.

5. Conclusion

The study presented an approach in monitoring the effects that mangrove related interventions could bring to an area thus enabling accountability.

Acknowledgement

The authors would like to thank the Sankandi Youth Development Association for their contribution in field survey data thus making this research possible

References

Alongi, D. (2002). Present state and future of the world's mangrove forests. *Environ. Conserv.*, *29*(3), 331–349. https://doi.org/10.1017/s0376892902000231

Alongi, D. (2008). Mangrove forests: Resilience, protection from tsunamis, and responses to global climate change. *Estuar. Coast Shelf Sci.*, *76*(1), 1–13. https://doi.org/10.1016/j.ecss.2007.08.024

Bryan, T., Virdin, J., Vegh, T., Kot, C. Y., Cleary, J., & Halpin, P. N. (2020). Blue carbon conservation in West Africa: a first assessment of feasibility. *Journal of Coastal Conservation*, *24*(8). https://doi.org/10.1007/s11852-019-00722-x

Cissell, J. R., Canty, S. W. J., Steinberg, M. K., & Simpson, L. T. (2021). Mapping national mangrove cover for belize using google earth engine and sentinel-2 imagery. *Applied Sciences (Switzerland)*, *11*(9). https://doi.org/10.3390/APP11094258

Corcoran, E., Ravilious, C., & Skuja, M. (2007). *Mangroves of West nd Central Africa*.

Dia Ibrahima. (2012). *Vulnerability Assessment of Central Cosatal Senegal (Saloum) and the Gambia Marine Coast and Estuary to Climate Change Induced Effects.* Retrieved from http://www.crc.uri.edu.

https://doi.org/10.1016/j.aquabot.2007.12.009

Elmahdy, S. I., Ali, T. A., Mohamed, M. M., Howari, F. M., Abouleish, M., & Simonet, D. (2020). Spatiotemporal Mapping and Monitoring of Mangrove Forests Changes From 1990 to 2019 in the Northern Emirates, UAE Using Random Forest, Kernel Logistic Regression and Naive Bayes Tree Models. *Frontiers in Environmental Science*, *0*, 102. https://doi.org/10.3389/FENVS.2020.00102

https://doi.org/10.3390/rs13132565

Giri, C. (2011). Status and distribution of mangrove forests of the world using earth observation satellite data. *Glob. Ecol. Biogeogr.*, *20*(1), 154–159. https://doi.org/10.1111/j.1466-8238.2010.00584.x

Rivera-Monroy, V. H., Kristensen, E., Lee, S. Y., & Twilley, R. R. (2017). *Mangrove ecosystems: A global biogeographic perspective: Structure, function, and services*. *Mangrove Ecosystems: A Global Biogeographic Perspective: Structure, Function, and Services*. https://doi.org/10.1007/978-3-319-62206-4

Intercontinental Geoinformation Days

http://igd.mersin.edu.tr/2020/

Remote sensing approach for aerosol optical thickness (AOT) monitoring in relation to the road network in Lagos Metropolis, Nigeria

Chukwuma Okolie[1,4], Emmanuel Ayodele[1], Erom Mbu-Ogar[*1], Samuel Akinnusi[1], Olagoke Daramola[1], Abdulwaheed Tella[2,4], Rose Alani[3,4], Alfred Alademomi[1]

[1]*University of Lagos, Faculty of Engineering, Department of Surveying and Geoinformatics, Lagos, Nigeria*
[2]*Universiti Teknologi PETRONAS (UTP), Department of Civil and Environmental Engineering, Geospatial Analysis and Modelling (GAM) Research Laboratory, Malaysia.*
[3]*University of Lagos, Faculty of Science, Department of Chemistry, Lagos, Nigeria*
[4]*University of Lagos, Air Quality Monitoring (AQM) Research Group, Lagos, Nigeria*

Keywords
Aerosol Optical Thickness
Road Network
Look-up Table
Air Quality

ABSTRACT

There are knowledge gaps in understanding the dynamics between air quality and road network traffic. This study used Landsat imageries of Lagos Metropolis at two epochs (2002 and 2020) as well as in-situ data to assess the AOT levels and its variation along the road networks of Lagos Metropolis. The python based 6S model was used to simulate AOT using land surface reflectance and top of atmosphere reflectance, and the AOT concentration levels across the road networks were mapped. It was observed that the AOT concentration throughout the study period was higher along the major roads. This can be attributed to the high level of air pollutants released from vehicles, including home/office generators and industries along the road corridors. As a result, the government and air quality agencies should establish more programs or measures to curb this high air pollution concentration.

1. Introduction

Lagos State being the fastest-growing urban center in Nigeria, has been experiencing air pollution problems in all its severity over the past decades. This is associated with high density of industries, transport networks, and open waste burning (Njoku et al., 2016). An increase in technological, industrial and agricultural advancement, coupled with increase in population growth, has triggered the deterioration of environmental air quality in Lagos State (Njoku et al., 2016). In Lagos, the socio-economic conditions, traffic congestion, proximity to emission sources and access to healthcare create a differential susceptibility to ill health attributable to air pollution (Komolafe et al., 2014). Daily, more than eight million people, moving in five million vehicles, cram into a very small network of roads every day (CNN Travel, 2019). The Lagos metropolis has been recognized as one of the world's megacities undergoing rapid urbanization and urban sprawl. According to some recent findings on the cost of air pollution in Lagos (World Bank, 2020), it was discovered that ambient air pollution led to premature death and economic loss of $2.0 billion in the state in 2018. In the same year, ambient air pollution led to about 11,200 premature deaths. Notably, the concentration levels of $PM_{2.5}$ recorded in Lagos have exceeded the WHO annual mean concentration guideline. For example, Lagos had recorded levels of 68 µg/m^3, in the same range as other polluted megacities such as Mumbai (64 µg/m^3), Cairo (76 µg/m^3), and Beijing (73 µg/m^3). The major source of ambient air pollution in the state is due to vehicular emissions. It is noteworthy that each kilometer of the road is clogged by 227 vehicles every day, which is a very high density. Also, most vehicles use old emission technologies and fuel with sulphur levels that are 200 times higher than the standards for diesel in the U.S. Besides, industrial emission is another source of air pollution in Lagos. Industrial and commercial activities in the metropolis have high levels of pollution. Emissions from generators that supply about 50% of the total energy in the state are another major source of air pollution. Consequently, this study monitored the changes in air pollution

* **Corresponding Author**
*(erom.ogar@gmail.com) ORCID ID 0000-0002-3339-4152

Cite this study
Okolie, C. Ayodele E, Mbu-Ogar E, Akinnusi S, Daramola O, Tella A, Alani R & Alademomi A S (2021). Remote sensing approach for aerosol optical thickness (AOT) monitoring in relation to the road network in Lagos metropolis, Nigeria. 3rd Intercontinental Geoinformation Days (IGD), 38-41, Mersin, Turkey

concentration over Lagos metropolis and its relationship with road network traffic over 2 epochs (2002 and 2020).

2. Methods

2.1. The study area

The study location is Lagos, Nigeria. It is the commercial center and most populous city of the country and Africa's second-largest city, with a total population of 21.3 million people within the Lagos metropolitan area. Lagos Metropolis lies between latitudes 6°20'00''N - 6°42'10''N and longitudes 3°02'30''E - 3°42'40''E. Fifty percent of Nigeria's industrial activities, including 300 industries, are located in this area. With its high rate of urbanization and industrial growth. Lagos is one of the world's most densely populated areas. The area has the highest concentration of economic activities in the country and provides employment to the work force of the country leading to highly trafficked roads. Lagos accounts for about 40% of new vehicle registrations in Nigeria and it is the most industrialized with greenhouse gas emissions.

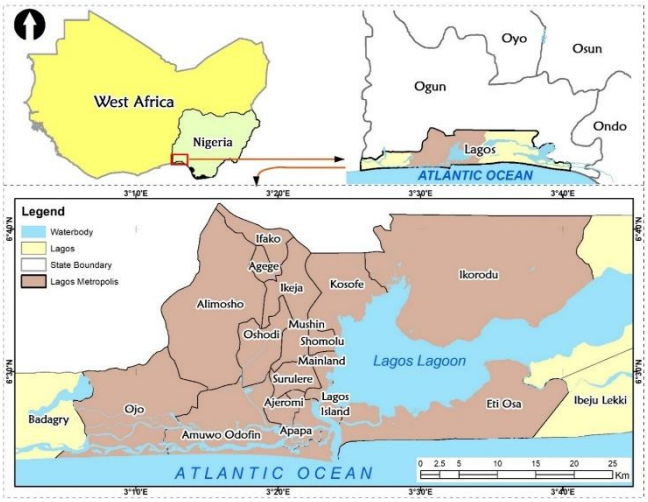

Figure 1. Map of the study area

2.2. Data acquisition

2.2.1. Satellite imagery

Landsat imagery was used for the AOT retrieval in this study. The Landsat 8 OLI and Landsat 7 ETM+ imagery scenes (Path: 191, Row: 55) covering Lagos metropolis for the year 2002 (28th December) and 2020 (20th January) respectively were downloaded from USGS Earth explorer data archive.

2.2.2. Particulate matter

Particulate matter ($PM_{1.0}$, $PM_{2.5}$, and PM_{10}) data were obtained with the ground-based air quality egg instrument. At the selected sites (Ojota, Iwaya, and Mushin), the device was used to acquire the PM data. The data were measured on a weekly basis between 9:00 am and 5:00 pm from February 2019 – July 2019.

2.2.3. Road network

The road network data is readily available on the OpenStreetMap platform, and it can be downloaded for free. The data was downloaded with the BBBIKE web-based tool (https://extract.bbbike.org/) from the OpenStreetMap archive. The downloaded road layer came in different road categories including expressway, main road, minor road, and street. The road type used for this study is the expressway and main road.

2.3. Data processing

2.3.1. Surface reflectance

The DDV technique was adopted in this study to estimate the surface reflectance. This was done using the improved dark-pixel method developed by Levy et al. (2010), which is dependent on Normalized Difference Vegetation Index (NDVI) and scattering angle. The equations for determining the surface reflectance are as follows (Luo et al., 2015; Ou et al., 2017):

Calculating the surface reflectance using Landsat 8 OLI and Landsat 7 ETM:

$$\rho_{s(0.66)} = f(\rho_{s(2.1)}) = \rho_{s(2.1)} \times slope_{0.66/2.1} + yint_{0.66/2.1} \ldots (1)$$

$$slope_{0.66/2.1} = slope_{0.66/2.1}^{NDVI_{SWIR}} + 0.002 \times \Theta - 0.27 \ldots\ldots\ldots (2)$$

$$yint_{0.66/2.1} = -0.00025\Theta + 0.033 \ldots\ldots\ldots\ldots\ldots\ldots\ldots\ldots\ldots (3)$$

$$slope_{0.66/2.1}^{NDVI_{SWIR}} = 0.48 \quad (NDVI_{SWIR} < 0.25)$$

$$slope_{0.66/2.1}^{NDVI_{SWIR}} = 0.58 \quad (NDVI_{SWIR} > 0.75)$$

$$slope_{0.66/2.1}^{NDVI_{SWIR}} = 0.48 + 0.2 \times (NDVI_{SWIR} - 0.25) \quad (NDVI_{SWIR} < 0.25)$$

Calculating the vegetation index:

$$NDVI_{SWIR} = \frac{\rho_{TOA(1.6)} - \rho_{TOA(2.1)}}{\rho_{TOA(1.6)} + \rho_{TOA(2.1)}} \ldots\ldots\ldots\ldots\ldots\ldots\ldots (4)$$

$$\Theta = \cos^{-1}(\cos\theta \cos\theta_0 + \sin\theta \sin\theta_0 \cos(\Delta\varphi)) \ldots\ldots (5)$$

Where:

$\rho_{s(0.66)}$ = red-band surface reflectance (ref)
$\rho_{s(2.1)} = apparent\ ref, SWIR\ 2$ (band 7: L8 & band 6: L7)
$\rho_{TOA(1.6)} = apparent\ ref\ SWIR\ 1$ (band 6 - L8 & band 5: L7)
$\rho_{TOA(2.1)} = apparent\ ref\ SWIR\ 2$ (band 7: L8 & band 6: L7)
Θ = scattering angle
$\theta = sensor\ zenith\ angle$
$\theta_0 = solar\ zenith\ angle$
$\Delta\varphi = relative\ azimuth\ angle$
$NDVI_{SWIR} = Normalized\ difference\ Vegetation\ index$

2.3.2. Look-up table

Py6S is a Python interface to the 6S model. In this study, the 6S model was run on the Python interface to simulate the atmospheric properties of the Landsat 8 OLI and Landsat 7 ETM sensor for blue and red bands.

3. Results

This section presents the results of the different processing and analysis carried out in this study. These include the AOT maps, Road network-AOT maps, and analysis of the relationship using correlation coefficient (r), between PMs, AOT and the road networks. These are presented in Figures 2 and 3 and Tables 1 and 2 respectively. These results are discussed in Section 4.

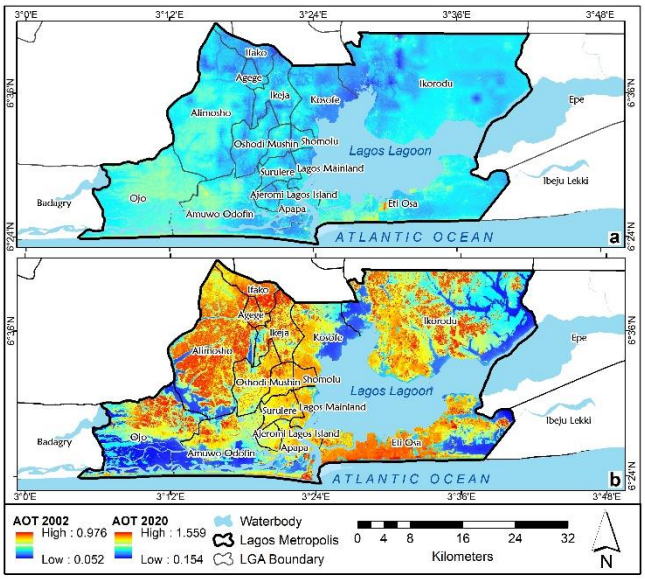

Figure 2. AOT distribution map in Lagos metropolis - (a) 2002 (b) 2020

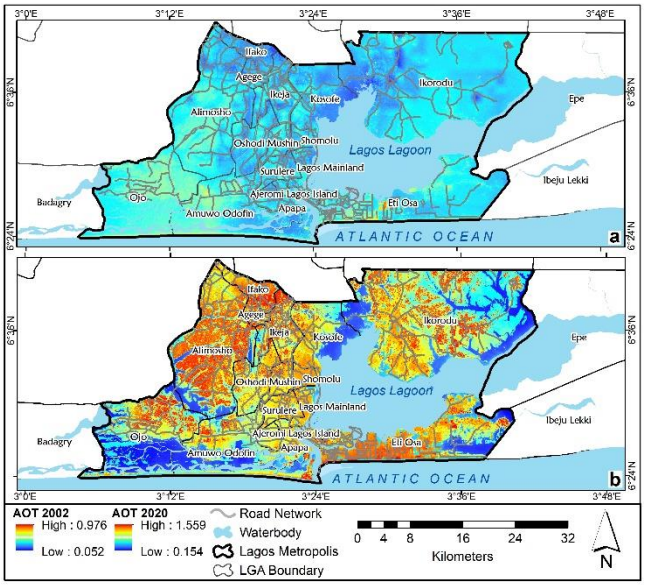

Figure 3. AOT distribution along Lagos road network – (a) 2002 (b) 2020

Table 1. Coefficient of correlation (r) between imagery-derived AOT for year 2020 and in-situ PM data at three locations in Lagos Metropolis

Location		PM_1	$PM_{2.5}$	PM_{10}	AOT
Ojota	PM_1	1.000	0.999	0.996	-0.616
	$PM_{2.5}$	0.999	1.000	0.997	-0.616
	PM_{10}	0.996	0.997	1.000	-0.669
	AOT	-0.616	-0.616	-0.669	1.000
Iwaya	PM_1	1.000	0.994	0.989	0.256
	$PM_{2.5}$	0.994	1.000	0.996	0.284
	PM_{10}	0.989	0.996	1.000	0.285
	AOT	0.256	0.284	0.285	1.000
Okobaba	PM_1	1.000	0.9865	0.977	0.705
	$PM_{2.5}$	0.987	1.000	0.999	0.726
	PM_{10}	0.977	0.999	1.000	0.728
	AOT	0.705	0.726	0.728	1.000

Table 2. Concentration of aerosol optical thickness on road corridors

Year	Region	Area (km^2)	AOT				
			Min	Max	Range	Mean	SD
2002	ARN	114	0.07	0.92	0.85	0.35	0.07
	ORN	1451	0.05	0.98	0.92	0.33	0.07
2020	ARN	114	0.43	1.71	1.28	1.31	0.15
	ORN	1451	0.36	1.75	1.39	1.05	0.38

Note: ARN – Along road network; ORN – Outside road network

4. Discussion

4.1. AOT distribution

There has been an increase in the AOT levels over Lagos metropolis, and this could be explained by the increasing urbanization in the state (Offor et al., 2016). The pollution from vehicular emissions, population congestion, industrial and commercial activities in Lagos State, and especially the metropolis have a deleterious impact on the wellbeing of residents. Akinyoola et al. (2018) reported that the aerosol loading/concentration is of high increase in Nigeria's south-south and south-western (coastal) region, and this corroborates the generally high aerosol concentration observed in the study area our findings.

4.2. Relationship between AOT and PM

Table 1 presents the correlation of ground-based sample PM data and year 2020 AOT concentration at selected locations of Lagos Metropolis. $PM_{2.5}$ and PM_1, PM_{10} and PM_1 have a high positive association in Ojota. There is a negative association between AOT and PM in Ojota. The association between AOT and PM is positive but not high at Iwaya, but the correlation between $PM_{2.5}$ and PM_1, PM_{10} and PM_1, PM_{10} and $PM_{2.5}$ is quite strong. In Okobaba, there is a strong positive correlation between AOT and PM. There is also a strong positive correlation between $PM_{2.5}$ and PM_1, PM_{10} and PM_1, PM_{10} and $PM_{2.5}$. It can be observed that the correlation between AOT and the different sizes of PM in Ojota are negative, possibly due to the evening time of day this data was observed as opposed to the high positive correlation value in Okobaba, which was acquired during the daytime. The values showing the correlation between AOT and PM in Iwaya are positive but less in values compared to that in Okobaba.

4.3. Relationship between AOT and Road Network traffic

The concentration of AOT along the major roads in the Lagos Metropolis was also examined. Due to the low spatial variability of aerosol over a small area, a road buffer of 60 meters was used to examine AOT concentration along the road network. From the results, it was observed that the AOT concentration throughout the study period is higher along the major roads. This can be attributed to the high level of air pollutants emitted from vehicles, including home/office generators and industries located along the road corridors. From Table

2, the mean AOT along road network (ARN) is higher than that observed outside road network (ORN) for both years. From Figure 3, it was observed that the AOT concentration is higher along the major roads, especially in the center of the metropolis and over Eti-Osa region, except for the year 2002. The high AOT in these regions can be attributed to daily traffic experienced in the highly urbanized Eti-Osa LGA and the heavy vehicular activities in the metropolis.

5. Conclusion

This study has provided evidence of increased AOT levels and deteriorating air quality along major roads in Lagos State. The paucity of ground-based data limited the level of analysis performed to examine the relationship between AOT and particulate matter at a full scale. The lack of clear satellite imagery also limited the study to examine seasonal changes in the AOT concentration.

According to UNEP (2016), Nigeria is one of the countries without Ambient Air Quality Standards and air quality laws and regulations. The high AOT concentration observed in the metropolis necessitates the need to establish Ambient Air Quality Standards by the government. Air quality monitoring and modeling, in addition to the provision of AAQS, are significant instruments for air quality management. However, most countries only monitor air quality on a sporadic basis, if at all. Because there is a scarcity of air quality data, evaluating the potential air quality impacts on a country from multiple sources is challenging. As a result, the government should consider the establishment of multiple air quality monitoring stations to acquire real-time air quality information. The pollution from traffic activities in the metropolis manifested in the AOT concentration observed along the road network. The government should consider exploring clean mobility by creating national electric mobility strategies to reduce vehicular emissions. In addition, the government should enforce proper city planning to manage the urbanization growth in the metropolis.

Acknowledgements

The authors would like to thank NASA/USGS for free access to Landsat imageries and the Air Quality Monitoring (AQM) Research Group, University of Lagos for providing the ground-based PM data. The authors also commend Jorge Vicent Servera for their support in the use of the Py6S model.

References

Akinyoola, Julius Adekola, Emmanuel Olaoluwa, and Eresanya O. O. I. Orimoogunje. 2018. “Monitoring the Spatio-Temporal Aerosol Loading over Nigeria.” Modeling Earth Systems and Environment 4(4):1365–75. doi: 10.1007/s40808-018-0485-2.

Komolafe, A. A., Abdul-Azeez, A. S., Biodun, A. A. Y., Omowonuola, A. F., & Rotimi, A. D. (2014). Air pollution and climate change in Lagos, Nigeria: Needs for proactive approaches to risk management and adaptation. American Journal of Environmental Sciences, 10(4), 412–423. https://doi.org/10.3844/ajessp.2014.412.423

Luo, Nana, Man Sing, Wenji Zhao, Xing Yan, and Fei Xiao. 2015. “Improved Aerosol Retrieval Algorithm Using Landsat Images and Its Application for PM 10 Monitoring over Urban Areas.” Atmospheric Research 153:264–75. doi: 10.1016/j.atmosres.2014.08.012.

Njoku, L. K., Rumide, J. T., Akinola, M. O., Adesuyi, A. A., & Jolaoso, A. O. (2016). Ambient Air Quality Monitoring in Metropolitan City of Lagos, Nigeria. Journal of Applied Science and Environment, 20(1), 178–185. https://doi.org/10.4314/jasem.v20i1.21

Offor, Ifeanyi F., Gilbert U. Adie, and Godson R. E. E. Ana. 2016. “Review of Particulate Matter and Elemental Composition of Aerosols at Selected Locations in Nigeria from 1985-2015.” JH&P 6(10).

Ou, Yang, Fantao Chen, Wenji Zhao, Xing Yan, and Qianzhong Zhang. 2017. “Landsat 8-Based Inversion Methods for Aerosol Optical Depths in the Beijing Area.” Atmospheric Pollution Research 8(2):267–74. doi: 10.1016/j.apr.2016.09.004.

Sun, Lin, Jing Wei, Muhammad Bilal, Xinpeng Tian, Chen Jia, and Yamin Guo. 2016. “Aerosol Optical Depth Retrieval over Bright Areas Using Landsat 8 OLI Images.” Remote Sensing 8(23):1–14. doi: 10.3390/rs8010023.

Wilson, R. T. 2013. “Py6S: A Python Interface to the 6S Radiative Transfer Model.” Computers and Geosciences 51:166–71. doi: 10.1016/j.cageo.2012.08.002.

Intercontinental Geoinformation Days

igd.mersin.edu.tr

Vertical accuracy assessment of DEMs around Jabal al-Shayeb area, Egypt

Ali Shebl [*1,2], **Mohamed A Atalla**[3,4], **Árpád Csámer** [1]

[1] *Debrecen University, Department of Mineralogy and Geology, Egyetem tér 1, 4032 Debrecen, Hungary*
[2] Tanta University, Department of Geology, Tanta 31527, Egypt.
[3]Higher Institute of Arts Studies, Geography Department, King Marriott, Egypt.
[4]*Al-Arish University, Geography Department, faculty of arts, Egypt.*

Keywords
DEMs
ALOS PALSAR
NASADEM
geomorphological
ASTER GDEM

ABSTRACT

As a quantitative and numerical representation of earth surface topography, Digital Elevation Models (DEMs) are widely used in several applications including geological, hydrological, and geographical Aspects. With the availability of several types of DEMs, various intrinsic errors may be incorporated due to sensor acquisition inconveniences, or processing techniques compared to the actual land surface measurements. Consequently, this study aims to analysis and test the vertical accuracy of NASADEM, Advanced Spaceborne Thermal Emission and Reflection Radiometer–Global Digital Elevation Model (ASTER GDEM) and Advanced Land Observing Satellite (ALOS) Phased Array L-type band Synthetic Aperture Radar (PALSAR) DEM compared to the actual ground control points (GCPs) derived from topographic maps through calculating Mean Absolute Percentage Error (MAPE) and Root Mean Square Error (RMSE). Our results revealed the sublimity of ALOS PALSAR DEM over NASADEM and ASTER GDEM. Thus, ALOS PALSAR DEM is recommended for further geomorphological studies.

1. Introduction

Over the last three decades, prolonged efforts are dedicated to enhancing the capability of obtaining accurate and enhanced global DEMS (Hirano et al., 2003; Welch and Marko, 1981). Several environmental studies mostly include a 3D representation of the investigated locations utilizing DEMs. Thus, it becomes a fundamental element in comprehensive environmental and geomorphological studies. Dems significantly contribute to solving geomorphological, agricultural, hydrological, geological, pedological, and ecological problems (Pulighe and Fava, 2017) and their modeling (Marzolff and Poesen, 2009; Schumann et al., 2008; Siart et al., 2009). DEMs could also be extracted from digital stereo imagery (Pieczonka et al., 2011; Pulighe and Fava, 2017). Whatever the source of utilized DEMs, assessing the accuracy is an indispensable issue as errors could directly cause unwise decisions that could finally negatively affect the environment or human life. DEMs are utilized in calculating Aspect and slope maps(Ashmawy et al., 2018; Ibrahim-Bathis and Ahmed, 2016; Panahi et al., 2017; Shebl and Csámer, 2021; Webster et al., 2006) that largely control the strength and direction of several flash floods, which could cause several geohazards. Consequently, this study aims to assess the vertical accuracy of three widely utilized DEMs to recommend the best for usage in further investigations.

2. Study area

The study area (Jabal al-Shayeb area) is a mountainous region, about 45 km southwest of Hurghada city, Egypt. Jabal al-Shayeb area is located between latitudes 26° 54′, 27° N and longitudes33° 23′,33° 29′E. It covers an area of 13 km x 11 km (143 km^2). Elevations range from 710 m up to over 2140 m a.s.l., the average slope is 20° and most of the reliefs are facing southeast-west southwest. This region is mostly covered by granitic rocks with some occurences of Phanerozoic sedimentary rocks. Figure 1 depicts the study area and Figure 2 depicts the locations of the GCPs collected from a 1:100,000 scale topographic map (Military Survey Authority, 1992). The surface of the study area is the result of combined influence of internal and external processes, and the developed drainage network in it was formed as a result of heavy rainfall, during pluvial phases particularly in Pleistocene.

* **Corresponding Author**

*(ali.shebl@science.tanta.edu.eg) ORCID ID 0000-0001-7285-285X
(atallahm763@gmail.com) ORCID ID 0000-0001-6708-2408

Cite this study

Shebl A, Atalla M A & Csámer Á (2021). Vertical accuracy assessment of DEMs around Jabal al-Shayeb area, Egypt. 3rd Intercontinental Geoinformation Days (IGD), 42-45, Mersin, Turkey

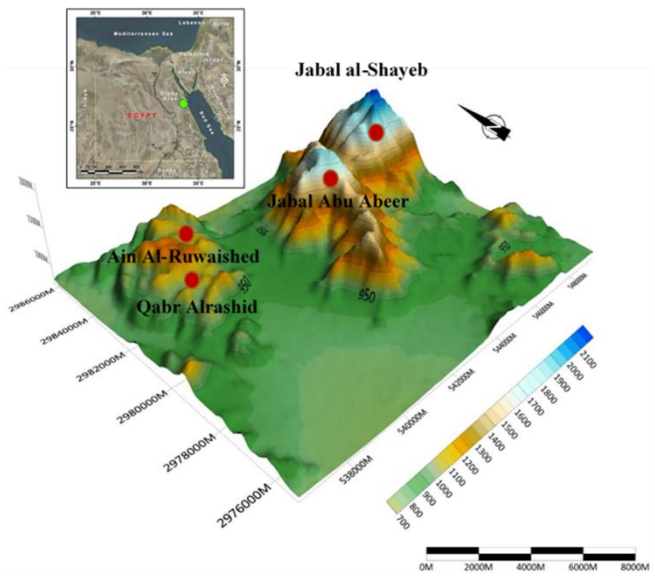

Figure 1. Location of the study site (Source: https://lpdaac.usgs.gov)

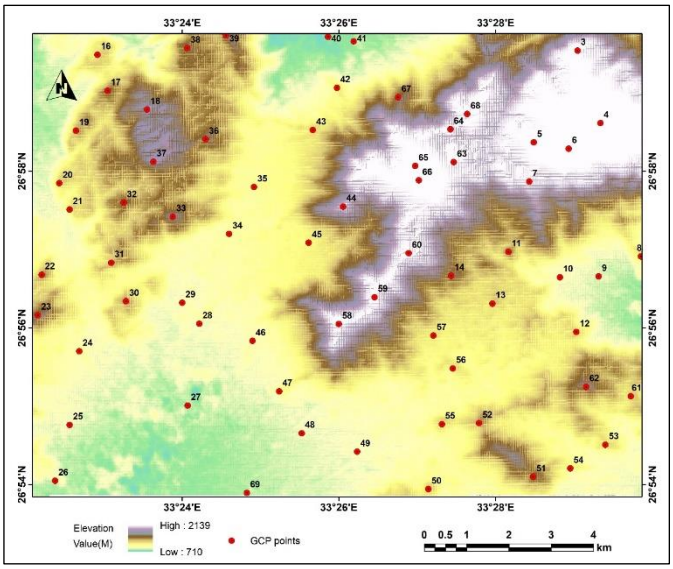

Figure 2. Depicts the locations of the GCPs collected from a 1:100,000 scale topographic map (Source: Topographic map scale 1:100,000)

3. Materials and methods

In the current study, three DEMs are analysed regarding their vertical accuracy and compared to topographic maps. NASADEM product (30m) is a state-of-the-art global digital elevation model derived from a combination of SRTM processing improvements, elevation control, void-filling, and merging with data unavailable at the time of the original SRTM production. NASA DEM is distributed in 1◦ by 1◦ tile and consist of all land between 60◦ N and 56◦ S latitudes. For this study, National Aeronautics and Space Administration (NASA) DEM was obtained from the USGS web-based data (https://lpdaac.usgs.gov/).

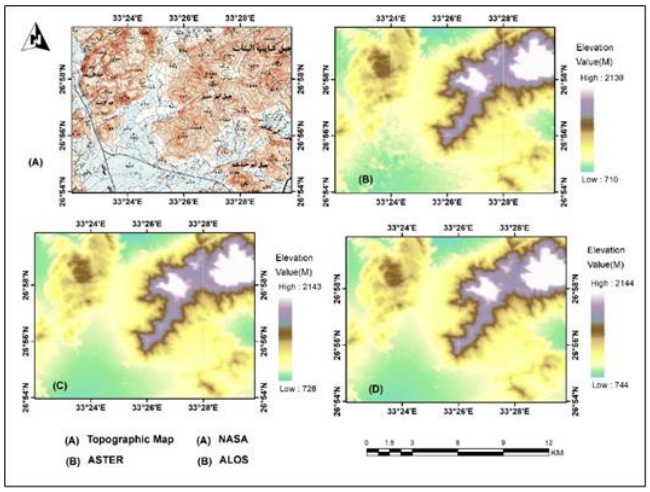

Figure 3. The colour levels represent the DSM dataset and the reference DSM data (Source: https://lpdaac.usgs.gov; topographic map (modified after Military Survey Authority, 1996).)

Advanced Spaceborne Thermal Emission and Reflection Radiometer–Global Digital Elevation Model (ASTER GDEM) has 1 arc-second (30 m) spatial resolution, and this project is done by the Ministry of Trade, Economy and Industry (METI) of Japan and the United States NASA to provide high-resolution DEM to the public. The Advanced Land Observing Satellite (ALOS) was launched on January 24, 2005. ALOS is provided with the Phased Array L-type band Synthetic Aperture Radar (PALSAR) for day-and-night and all-weather land observation. PALSAR sensor is an active microwave sensor (help to avoid weather barrier conditions and day or night effect), L-band (1.27 GHz) synthetic aperture radar aid at achieving high-resolution DEM products (Shebl and Csámer, 2021). In the current study, we applied Mean Absolute Percentage Error (MAPE) which represents the average of absolute errors divided by actual observation values. To ensure a wise comparison, we resampled the ALOS PALSAR DEM data (12.5m) to 30m (the same resolution for NASA and ASTER DEMs). Then, the four DEMs including ALOS PALSAR (12.5m), resampled ALOS PALSAR (30 m), NASA (30 m) and ASTER (30 m) DEMs are used in the mathematical calculations using 69 GCPs (which represents the actual values in the current studies). As shown in figures (2; 3). Using Extract Multi Values to Points function in ArcMap, the points are compared then evaluated according to equation 1.

$$\mathrm{MAPE} = \frac{\sum_{t=1}^{n} \left| \frac{A_t - F_t}{A_t} \right|}{n} \times 100$$

Where At –Ft represents the error value, | At -Ft| is the absolute error value, n accounts for number of points which is 69 points in the current study (Fig. 2).

Additionally, the Root Mean Square Error (RMSE) (Hirano et al., 2003; Rawat et al., 2019; Santillan et al., 2016; Zhao et al., 2011) +was calculated according to the following equation.

$$\mathrm{RMSE} = \sqrt{\frac{\sum_{t=1}^{n} (A_t - F_t)^2}{n}}$$

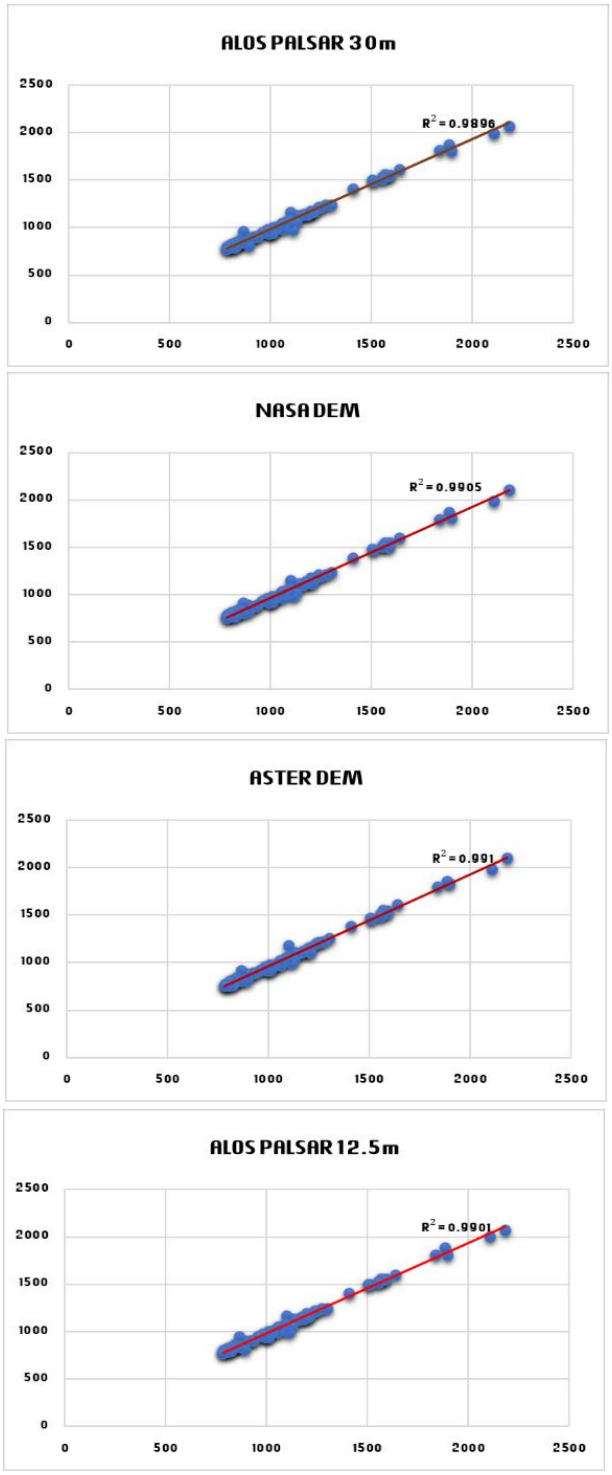

Figure 4. Determination coefficient of the actual and tested values for the four utilized DEMs

4. Results

Our results reported the effectiveness of ALOS PALSAR DEM over NASA and ASTER DEMs. MAPE values were 2.71, 2.78, 3.68, and 4.01 for ALOS PALSAR (12.5m), resampled ALOS PALSAR (30 m), NASA (30 m) and ASTER (30 m) respectively. However, the data are linearly correlated as shown in figure (4), the RMSE is a significant value indicating the higher error value between the measured (topographic) and DEM values. RMSE values were 42.8, 41.4, 51.4, and 52.5 for ALOS PALSAR (12.5m), resampled ALOS PALSAR (30 m), NASA (30 m) and ASTER (30 m) respectively. This could be attributed to the time gab between topographic map measurements and DEMs data acquisition, however the study strongly recommends DEMS evaluation in terms of their accuracy whenever possible. ALOS PALSAR DEMs (radar data) superiority was attributed to the absence of weather conditions effect (Adiri et al., 2017; Shebl and Csámer, 2021). It should be emphasized that the data utilized for validation should be acquired at an acquisition time closely related to that of the models to be away from any inconveniences (e.g., anthropogenic or natural changes that could affect the accuracy assessment process).

5. Conclusion

In the current study, ALOS PALSAR DEM, NASA and ASTER DEMs were evaluated regarding their vertical accuracy to recommend the best for usage in future geomorphological applications. Our results disclosed That the three sensors delivered a reliable data for further investigations however it is recommended to implement PALSAR data as their Mean Absolute Percentage Error is smaller than the others. Its higher accuracy was attributed to independence of radar data from any weather conditions.

References

Adiri, Z., El Harti, A., Jellouli, A., Lhissou, R., Maacha, L., Azmi, M., Zouhair, M., Bachaoui, E.M., 2017. Comparison of Landsat-8, ASTER and Sentinel 1 satellite remote sensing data in automatic lineaments extraction: A case study of Sidi Flah-Bouskour inlier, Moroccan Anti Atlas. Adv. Sp. Res. 60, 2355–2367.

Ashmawy, M.H., Abd El-Wahed, M.A., Kamh, S.Z., Shebl, A., 2018. Scientific Journal of Basic and Applied Sciences Comparative study of the drainage basin morphometry extracted from topographic maps and SRTM DEMs: an example from Ghadir watershed, Eastern Desert, Egypt. Sci JBAS 39, 52–64.

Hirano, A., Welch, R., Lang, H., 2003. Mapping from ASTER stereo image data: DEM validation and accuracy assessment. ISPRS J. Photogramm. Remote Sens. 57, 356–370. https://doi.org/10.1016/S0924-2716(02)00164-8

Hirano, A., Welch, R., Lang, H., 2003. Mapping from ASTER stereo image data: DEM validation and accuracy assessment. ISPRS J. Photogramm. Remote Sens. 57, 356–370. https://doi.org/10.1016/S0924-2716(02)00164-8

Ibrahim-Bathis, K., Ahmed, S.A., 2016. Geospatial technology for delineating groundwater potential zones in Doddahalla watershed of Chitradurga district, India. Egypt. J. Remote Sens. Sp. Sci. 19, 223–234. https://doi.org/10.1016/J.EJRS.2016.06.002

Marzolff, I., Poesen, J., 2009. The potential of 3D gully monitoring with GIS using high-resolution aerial

photography and a digital photogrammetry system. Geomorphology 111, 48–60. https://doi.org/10.1016/J.GEOMORPH.2008.05.047

Military Survey Authority, topographic maps, scale 1: 1,000,000 plates, Jabal al-Shayeb Al_banat, 1996

Panahi, M.R., Mousavi, S.M., Rahimzadegan, M., 2017. Delineation of groundwater potential zones using remote sensing, GIS, and AHP technique in Tehran–Karaj plain, Iran. Environ. Earth Sci. 2017 7623 76, 1–15. https://doi.org/10.1007/S12665-017-7126-3

Pieczonka, T., Bolch, T., Buchroithner, M., 2011. Generation and evaluation of multitemporal digital terrain models of the Mt. Everest area from different optical sensors.

Pieczonka, T; Bolch, T; Buchroithner, M (2011). Gener. Eval. multitemporal Digit. terrain Model. Mt. Everest area from Differ. Opt. sensors. ISPRS J. Photogramm. Remote Sensing, 66(6)927-940. 66, 927–940. https://doi.org/10.1016/J.ISPRSJPRS.2011.07.003

Pulighe, G., Fava, F., 2017. DEM extraction from archive aerial photos: accuracy assessment in areas of complex topography. https://doi.org/10.5721/EuJRS20134621 46, 363–378. https://doi.org/10.5721/EUJRS20134621

Rawat, K.S., Singh, S.K., Singh, M.I., Garg, B.L., 2019. Comparative evaluation of vertical accuracy of elevated points with ground control points from ASTERDEM and SRTMDEM with respect to CARTOSAT-1DEM. Remote Sens. Appl. Soc. Environ. 13, 289–297. https://doi.org/10.1016/J.RSASE.2018.11.005

Santillan, J.R., Makinano-Santillan, M., Makinano, R.M., 2016. Vertical accuracy assessment of ALOS World 3D - 30M Digital Elevation Model over northeastern Mindanao, Philippines. Int. Geosci. Remote Sens. Symp. 2016-November, 5374–5377. https://doi.org/10.1109/IGARSS.2016.7730400

Schumann, G., Matgen, P., Cutler, M.E.J., Black, A., Hoffmann, L., Pfister, L., 2008. Comparison of remotely sensed water stages from LiDAR, topographic contours and SRTM. ISPRS J. Photogramm. Remote Sens. 63, 283–296. https://doi.org/10.1016/J.ISPRSJPRS.2007.09.004

Shebl, A., Csámer, Á., 2021. Reappraisal of DEMs, Radar and optical datasets in lineaments extraction with emphasis on the spatial context. Remote Sens. Appl. Soc. Environ. 24, 100617. https://doi.org/10.1016/J.RSASE.2021.100617

Shebl, A., Csámer, Á., 2021. Stacked vector multi-source lithologic classification utilizing Machine Learning Algorithms: Data potentiality and dimensionality monitoring. Remote Sens. Appl. Soc. Environ. 100643. https://doi.org/10.1016/J.RSASE.2021.100643

Siart, C., Bubenzer, O., Eitel, B., 2009. Combining digital elevation data (SRTM/ASTER), high resolution satellite imagery (Quick bird) and GIS for geomorphological mapping: A multi-component case study on Mediterranean karst in Central Crete. Geomorphology 112, 106–121. https://doi.org/10.1016/J.GEOMORPH.2009.05.010

Webster, T.L., Murphy, J.B., Gosse, J.C., Spooner, I., 2006. The application of lidar-derived digital elevation model analysis to geological mapping: An example from the Fundy Basin, Nova Scotia, Canada. Can. J. Remote Sens. 32, 173–193. https://doi.org/10.5589/m06-017

Welch, R., Marko, W., 1981. Cartographic potential of a spacecraft line-array camera system - Stereosat. PgERS 47, 1173–1185.

Zhao, S., Cheng, W., Zhou, C., Chen, X., Zhang, S., Zhou, Z., Liu, H., Chai, H., 2011. Accuracy assessment of the ASTER GDEM and SRTM3 DEM: an example in the Loess Plateau and North China Plain of China. https://doi.org/10.1080/01431161.2010.532176 32, 8081–8093. https://doi.org/10.1080/01431161.2010.532176

Intercontinental Geoinformation Days

igd.mersin.edu.tr

The current state of use of satellite-based positioning systems in Turkey

Nuri Erdem *[1], **Abdulsamet Demirel** [1]

[1]*Osmaniye Korkut Ata University, Faculty of Engineering, Department of Geomatics Engineering, Osmaniye, Turkey*

Keywords
Satellite Based Geolocation,
Satellite Signal,
Signal Receiver

ABSTRACT

Nowadays, the cartography sector has also been affected by the rapid developments in the field of technology. Recently, satellite-based positioning systems have been used instead of the classic land measurements made with total station and engineer's level. In this study, the general structure of satellite-based global and regional positioning systems is examined. The general usage densities of the system in the public and private sectors in Turkey and the status of the signals that can be received and the average sales prices of devices on the market have been investigated. The results were presented in the form of tables and graphs, and it was found that the most ideal device for our country is the device called Kolida K58 Pus, which can work with systems such as GPS/GLONASS/SBAS/GALILEO/QZSS/BEIDOU and receive signals from many satellites of these systems.

1. Introduction

Mankind has always wanted to improve itself in the field of communication from the very beginning of its existence. It has used a different communication method in each cycle by producing new communication systems. After a while, satellites were sent to space and satellite-based communications began. Today, satellites are widely used both for communication and for providing location data. In this study, the number of satellites seen by devices using the data of satellite-based positioning systems and the variety of signals it can receive from these satellites are presented as tables and graphs. Then, with the help of the relevant tables and graphs, recommendations were made about which brand and model could be the most suitable GNSS buyer for our country.

2. Structure and components of satellite-based positioning systems

The GPS system, first developed in the early 1940s for military requirements, was developed during World War II. It is based on similar ground-based radio-navigation systems used during World War II, such as LORAN (LORAN - Long Range Navigation) and the Decca Navigator, which later became a solution for that period. The first use of GPS was intended for use in military plans and for the control of guided rockets. The GPS system was opened for civilian use only in the 1980s [1, 2]. GLONASS operated by the Russian Aerospace Defense Forces, both civilian and military-service space-based satellite navigation system. Although the development of GLONASS is somewhat delayed, it has parallels with GPS [3]. GALILEO's satellite team, a positioning system with global coverage, consists of a total of 30 mid-orbit (MEO) satellites, including 24 main and 6 backup ones. The GALILEO satellite team was originally planned to consist of 27 active and 3 reserve satellites in order to meet the Life Safety (SOL) service requirements [4]. BeiDou means "Big Bear Team Star" in Chinese. The Big Bear is considered to be the most important star team that allows people to find direction in the northern hemisphere. Although this name was naturally chosen when China decided to create its own satellite-based navigation system, the COMPASS name was used as the English name of the system for many years [5]. GPS-intensive, Japan, in dense urban areas and resolve their own problems encountered during the use of GNSS satellite-based positioning capability to create Quasi-Zenith Satellite System (QZSS) is called to establish a regional positioning system continues to work. QZSS satellites can also act as additional GPS satellites and work in an integrated way with GPS. The system, the first satellite of which was launched in 2010, is expected to reach full operational capability in 2018 [6]. The NavIC satellite suite consists of 7 satellites. 3 of the satellites are in an earth-stationary orbit, and 4 are in an oblique earth-synchronous orbit. When designing the satellite set in question, attention was paid to minimizing the sensitivity loss (DOP value), maximizing the number of satellites visible over the targeted area, and using the fewest

* **Corresponding Author**

*(nurierdem@osmaniye.edu.tr) ORCID ID 0000-0002-1850-4616
(demirel.6699@gmail.com) ORCID ID 0000-0003-0435-3404

Cite this study

Erdem N & Demirel A (2021). The Current State of Use of Satellite-Based Positioning Systems in Turkey. 3rd Intercontinental Geoinformation Days (IGD), 46-49, Mersin, Turkey

possible satellites. All of the satellites in the NavIC satellite suite are constantly visible from the Indian region [7].

3. Experimental method

The current use status of satellite-based position systems in our country, public and private sector users have been contacted by phone, website and mail to determine which of their respective devices have seen how many satellite systems and which signals they have received. The obtained results are given in Table 1.

Table 1. Current status of satellite-based position sites in Turkey

Companies	Devices	Used Satellite Systems	Monitored Signals
Kaya Harita	E-Survey E600	GPS /GLONASS /BeiDou /Galileo /QZSS /NAVIC /SBAS	L1 ,L1P,L1C,L2P,L2C,L5 / G1,G2,P1,P2 / B1,B2,B3 / E1BC , E5A,E5B /L1,L2C,L5,L1C / L1 ,L5 /WAAS, EGNOS,MSAS,GAGAN
Paksoy Teknik M	Topcon Hıper Hr	GPS /GLONASS /BeiDou /Galileo /QZSS /NAVIC /SBAS	L1,L2,L2C,L5/L1,L2,L2C,L3/B1,B2,B3/E1,E5a,E5b,AltBOC,E6/L1,L2C,L5,L6 / L5 /WAAS, EGNOS, MSAS, GAGAN
Sistem A.Ş.	Leica Viva Gs16	GPS /GLONASS /BeiDou /Galileo /QZSS /NAVIC /SBAS	L1,L2,L2C,L5/L1,L2,L2C,L3/B1,B2,B3/E1,E5a,E5b,AltBOC,E6/L1,L2C,L5,L6/L5 / WAAS, EGNOS, MSAS, GAGAN
Sistem A.Ş.	Leica GS18 T	GPS /GLONASS /BeiDou /Galileo /QZSS /NAVIC /SBAS	L1,L2,L2C,L5/L1,L2,L2C,L3/B1,B2,B3/E1,E5a,E5b,AltBOC,E6/L1,L2C,L5,L6 / L5 /WAAS,EGNOS, MSAS,GAGAN
Baytekin Müh.	Sanding Aquila T66 Pro	GPS /GLONASS /BeiDou /Galileo /QZSS /NAVIC /SBAS	L1,L2,L2C,L5/L1,L2,L2C,L3/B1,B2,B3/E1,E5a,E5b,AltBOC,E6/L1,L2C,L5,L6 / L5 /WAAS,EGNOS, MSAS, GAGAN
Geomatik Hizmetler	Geomax Zenith 40	GPS /GLONASS /BeiDou /Galileo /QZSS /NAVIC /SBAS	L1,L2,L2C,L5 /L1,L2,L2C,L3/B1,B2,B3/E1,E5a,E5b,altboc,E6/L1,L2C,L5,L6/L5/EGNOS,WAAS,MSAS,GAGAN
Sistem A.Ş.	Leica GS07	GPS /GLONASS /BeiDou /Galileo /QZSS /NAVIC /SBAS	L1,L2,L2C,L5/L1,L2,L3/B1,B2,B3/E1,E5a,E5b,AltBOC,E6/L1,L2,L5,LEX / L5 /WAAS,EGNOS, MSAS, GAGAN
Geomatics Group	Spectra Geospatial S	GPS /GLONASS /BeiDou /Galileo /QZSS /NAVIC /SBAS	L1 C/A ,L1P,L2C,L2P,L5 / L1 C/A,L1P,L2 C/A,L2P,L3 /B1,B2 /E1,E5a,E5b/ L1 C/A,L1C,L2C,L5 / L5 / L1 C/A,L5
Geoteknik Müh.	Kolida K58 Pus	GPS /GLONASS /SBAS /GALİLEO /QZSS /BEİDOU	L1C/A, L1C, L2C, L2E, L2P, L5 /L1C/A, L1P, L2C/A, L2P, L3 / L1 C/A, L5 /GIOVE-A ve GIOVE-B, E1 , E5A, E58, E5AltB0C, E6 /L1C/A. SAIF, L1C, L2C, L5, LEX /B1,B2,B3
Kaya Harita Müh.	E-Survey E300 PRO	GPS/GLONASS/BeiDou/Galileo/SBAS/QZSS	L1 C/A, L1P, L1C, L2P, L2C, L5 /G1, G2,G3 / B1L,B2L,B3L,B1C,B2A,B2B,ACEBOC /E5A, E5B, E5AltBOC, E6 /L1,L5 /L1 C/A,L1C,L2C,L5,LEX
Sistem A.Ş.	Leica GS18 I	GPS/GLONASS/BeiDou/Galileo/ QZSS/SBAS	L1,L2,L2C,L5/L1,L2,L2C,L3/E1,E5a,E5b,AltBOC,E6/B1I,B1C,B2I,B2a,B3I/L1,L2C,L5,L6/ WAAS,EGNOS,MSAS,GAGAN L-bant
Geoteknik Müh.	Kolida K1 PRO	GPS /GLONASS /QZSS /GALİLEO /SBAS /BEİDOU	L1C/A, L1C, L2C, L2E, L5 / L1C/A, L1P, L2C/A, L2P, L3 /L1 C/A, L5 /GIOVE-A ve GIOVE-B, E1, E5A, E5B, E5AltBOC, E6 /WAAS, MSAS, EGNOS, GAGAN /B1, B2,B3
Paksoy Teknik	Topcon MR-2	GPS /GLONASS /BeiDou /Galileo /SBAS /QZSS	L1 C/A , L1C,L1P,L2P,L2C,L5 / L1 C/A ,L1P,L2 C/A,L2P,L3C / E1,E5a,E5b,AltBOC /B1,B2 /WAAS, MSAS, EGNOS/L1 C/A,L1C,L2C,L5C
Eksen Teknik	Foif A90	GPS / GLONASS/ BEİDOU / GALİLEO /SBAS/QZSS	L1 C/A ,L1P , L1C ,L2P , L2C ,L5 / G1,G2,P1,P2 / B1,B2,B3 / E1BC, E5a,E5b,E5AltBOC ,E6 / L1,L5 / L1 C/A ,L2C, L5,L1C
Geoteknik Müh.	South Galaxy G1	GPS /GLONASS /SBAS /GALİLEO /QZSS /BEİDOU	L1C/A, L1C, L2C, L2E, L5 /L1C/A, L1P, L2C/A, L2P, L3 / L1 C/A, L5 /GIOVE-A ve GIOVE-B, E1 , E5A, E5B, E6altB0C /L1C/A, L1C, L2C, L5 /B1,B2,B3
Satlab Geosolut	Satlab SLC	GPS /GLONASS /SBAS / BeiDou /GALİLEO /QZSS	L1 C/A, L1C,L2P,L5 /L1,L2 / WAAS,EGNOS,MSAS,GAGAN/B1,B2/E1,E5a,E5b,AltBOC/L1,L2C,L5,L6
Geomatics Group	Spectra SP60	GPS /GLONASS /BeiDou /GALİLEO /QZSS /SBAS	L1 C/A ,L1P,L2C,L2P,L5 / L1 C/A,L1P,L2 C/A,L2P,L3 /B1,B2 /E1,E5a,E5b/ L1 C/A,L1C,L2C,L5 / L1 C/A,L5
Baytekin Müh.	Sanding T28	GPS /GLONASS /Galileo / BeiDou /SBAS /QZSS	L1 C/A ,L1C,L2C,L2E,L5 / L1 C/A, L1P , L2 C/A ,L2P,L3 / GİOVE-A , GİOVE-B,E1, E5A ,E5B / L1 C/A ,L5 / WAAS,EGNOS,MSAS,GAGAN/L1,L2C,L5,L6
Doğa Elektro.	Stonex S700A	GPS /GLONASS /BeiDou /Galileo /QZSS /NAVIC	L1,L2,L2C,L5/L1,L2,L3/B1,B2,B3/E1,E5a,E5b,AltBOC,E6/L1,L2,L5,LEX / L5
Doğa Elektro.	Stonex S850a	GPS /GLONASS /BeiDou /Galileo /QZSS /NAVIC	L1,L2,L2C,L5/L1,L2,L3/B1,B2,B3/E1,E5a,E5b,AltBOC,E6/L1,L2,L5,LEX / L5
Ifa Grup Müh.	Sokkia GCX3	GPS/GLONASS /BeiDou /Galileo /SBAS /QZSS	L1 C/A , L1C,L2P,L2C / L1 C/A , L1P , L2 , L2P / B1,B2 /E1 / L1 ,WAAS,MSAS,EGNOS,GAGAN / L1 C/A ,L1C,L2C
Gnss Teknik	Chcnav İ73 İmu Mini	GPS /GLONASS /SBAS / BeiDou /GALİLEO /QZSS	L1,L2,L5/ L1,L2 /L1 / B1,B2,B3 / E1, E5a,E5b / L1,L2,L5
Baytekin Müh.	Sanding T66	GPS/GLONASS/BEİDOU/Galileo/ SBAS	L1 C/A ,L1 , L1C ,L2,L2C,L2E,L5 / L1, L1 C/A ,L1P ,L2, L2 C/A ,L2P ,L3 / B1,B2,B3 / GIOVE-A,GIOVE-B,E1,E2-L1, E5A,E5B,E6-ALTBOC/WAAS,MSAS
Geoteknik Müh.	South Galaxy G1 P	GPS/GLONASS/SBAS/GALİLEO/SBAS	L1C/A, L1C, L2C, L2E, L5 / L1C/A, L1P, L2C/A, L2P, L3 / L1 , L5 / GIOVE-A ve GIOVE-B, E1, E5A, E5B, E5AltBOC, E6 / WAAS, MSAS, EGNOS, GAGAN
Baytekin Müh.	Gıntec G9	GPS/GLONASS/BeiDou/GALİLEO /SBAS	L1 ,L2E,L2C,L5/ L1 C/A,L1P,L2 ,L2P / B1,B2/ L1 BOC,E5A,E5B,E5 ALTBOC1 /L2 CBOC,E5A,E5B,E5 ALTBOC1 / WAAS,EGNOS,MSAS,GAGAN
Baytekin Müh.	Pentax G6Tİ	GPS/GLONASS/BeiDou/Galileo/SBAS	L1 ,L2E,L2C,L5 / L1 C/A,L2 , L3 CDMA / B1,B2 / E1,E5A,E5B,E5 ALTBOC / L1 C/A ,L1 SAIF,L2C,L5 / L1 C/A ,L5

Sistem A.Ş.	Leica Viva GS18T	GPS/GLONASS/BeiDou/Galileo/ QZSS	L1,L2,L2C,L5/L1,L2,L2C,L3/B1,B2,B3/E1,E5a,E5b,AltBOC,E6/L1,L2C,L5,L6
Doğa Elektron.	Stonex S900	GPS/GLONASS/BeiDou/Galileo/ QZSS	L1,L2,L2C,L5/L1,L2,L2C,L3/B1,B2,B3/E1,E5a,E5b,AltBOC,E6/L1,L2C,L5,L6
Doğa Elektron.	Stonex S980	GPS/GLONASS/BeiDou/Galileo/ QZSS	L1,L2,L2C,L5/L1,L2,L2C,L3/B1,B2,B3/E1,E5a,E5b,AltBOC,E6/L1,L2C,L5,L6
Doğa Elektron.	Stonex S990	GPS/GLONASS/BeiDou/Galileo/ QZSS	L1,L2,L2C,L5/L1,L2,L2C,L3/B1,B2,B3/E1,E5a,E5b,AltBOC,E6/L1,L2C,L5,L6
Kordil Müh.	Hemispe re S321	GPS/GLONASS/GALİLEO/BeiDou /QZSS	L1,L2,L2C,L5/L1,L2,L2C,L3/B1,B2,B3/E1,E5a,E5b,AltBOC,E6/L1,L2C,L5,L6
Baytekin Mühen.	Gıntec G10	GPS/GLONASS/BeiDou/Galileo/S BAS	L1 C/A ,L1C,L2C,L2E,L5/ L1 C/A ,L1P,L2 C/A,L2P,L3 / B1 ,B2, optinal B3/ E1,E5a,E5b/WAAS,EGNOS,MSAS,GAGAN
Baytekin Müh.	Pen tax G6Nİ	GPS/GLONASS/BeiDou/Galileo/S BAS	L1 C/A,L1C,L2C,L2P,L5/ L1 C/A,L2C,L2P,L3,L5/B1,B2,B3/ E1,E5 ALTBOC,E5a,E5b,E6/L1 C/A,L1C,L2C,L5,L6/L1,L5
Sistem A.Ş.	Leica Viva Gs14	GPS/GLONASS/BeiDou/Galileo/S BAS	L1,L2,L2C/L1,L2/B1,B2/E1,E5b/WAAS,EGNOS,MSAS,GAGAN
Sistem A.Ş.	Leica Viva Gs14	GPS/GLONASS/BeiDou/Galileo/S BAS	L1,L2,L2C/L1,L2/B1,B2/E1,E5b/WAAS,EGNOS,MSAS,GAGAN
Graftek Müh.	Trimble SPS855	GPS/GLONASS/SBAS/GALİLEO/ BeiDou	L1 ,L2,L2C,L5 /L1, L2 /L1 C/A ,L5 / E1,E5a,E5B /B1,B2
Graftek Müh.	Trimble TDC150	GPS/GLONASS/SBAS/GALİLEO/ BeiDou	L1 C/A,L1P,L2P,L2C /L1 C/A,L2 C/A, / L1 C/A /E1,E5B /B1,B2
Graftek Müh.	Trimble R1	GPS/GLONASS/SBAS/GALİLEO/ BeiDou	L1 / G1 / 4 Kanal/E1/ L1
Doğa Elektron.	Stonex S500	GPS/GLONASS/BeiDou/Galileo	L1,L2,L2C,L5/L1,L2,L2C,L3/B1,B2,B3/E1,E5a,E5b,AltBOC,E6
Doğa Elektr.	Stonex S70G	GPS/GLONASS/BeiDou/Galileo	L1,L2,L2C,L5/L1,L2,L2C,L3/B1,B2,B3/E1,E5a,E5b,AltBOC,E6
Graftek Müh.	Trimble SPS555	GPS/GLONASS/GALİLEO/BeiDou	L1 C/A ,L2C,L2E,L5 /L1 , L2 C/A,L1 ,L2P /L1 CBOC,E5A,E5B, E5 ALTBOC /B1,B2
Gnss Teknik	Chcnav İ50	GPS/GLONASS/ BeiDou /GALİLEO	L1 C/A ,L2C,L2E,L5 / L1 C/A ,L1P, L2 C/A ,L2P ,L3 /B1,B2 / E1,E5A,E5B
Adastek Müh.	Comnav G200	GPS/GLONASS/BeiDou/SBAS	L1 C/A ,L2C,L2P /L1 C/A, L1P,L2 C/A , L2P / B1,B2/WAAS,EGNOS,MSAS,GAGAN
Adastek Müh.	Comnav T300	GPS/GLONASS/BeiDou/SBAS	L1 C/A, L1C,L2P,L5 /L1,L2/B1,B2,B3/WAAS,EGNOS,MSAS,GAGAN
GNSS Teknik	Chcnav İ90 İmu	GPS/GLONASS/GALİLEO/BeiDou	L1,L2,L5 /L1,L2 / E1,E5a,E5b /B1,B2,B3
Geomati cs Group	Spectra Precision SP	GPS/GLONASS/ BeiDou /GALİLEO	L1,L2 /L1,L2/ B1,B2 /E1,E5b
Geo Teknik	Dji Matrice 300 Rtk	GPS/BeiDou/GLONASS/Galileo	L1,L2 /B1,B2 /L1,L2 / E1,E5a
Gnss Tekn	Phantom 4	GPS/BeiDou/GLONASS/Galileo	L1,L2 /B1,B2 /L1,L2 / E1,E5a
Paksoy Teknik	Topcon Hıper Sr	GPS/GLONASS/QZSS	L1,L2,L2C/L1,L2,L2C/L1,L2C
Leo Müh.	Nv08c-Csm	GPS/GLONASS/GALİLEO	L1 C/A ,L1C, L2C,L2E,L5 / L1 C/A , L2 C/A ,L2P/E1,E5 ALTBOC,E5a,E5b,E6
Geomati cs Group	Spectra Precision	GPS/GLONASS/GALİLEO	L1 C/A ,L1P,L2C,L2P,L5 / L1 C/A,L1P,L2 C/A,L2P,L3 /E1,E5A,E5B
Geomati cs Group	Spectra Precision	GPS/GLONASS/SBAS	L1 C/A ,L1P,L2C,L2P,L5 / L1 C/A,L1P,L2 C/A,L2P,L3 / L1 C/A,L5
Geomati cs Group	Spectra Precision	GPS/GLONASS/BeiDou	L1 C/A ,L1P,L2C,L2P,L5 / L1 C/A,L1P,L2 C/A,L2P,L3 /B1,B2
Ifa Grup Müh.	Sokkıa GRX2	GPS/GLONASS/SBAS	L1 CA,L1 , L2 P - code ,L2C/L1,L2 CA,L2P-code/WAAS,EGNOS,MSAS,QZSS
GNSS Tekn	Chcnav Lt6	GPS/GLONASS/ BeiDou	L1 C/A ,L2C,L2E,L5 / L1 C/A ,L1P, L2 C/A ,L2P ,L3 /B1,B2
Leo Müh.	Nv08c-Rtk-A	GPS/GLONASS/BeiDou	L1 C/A ,L1C, L2C,L2E,L5 / L1 C/A , L2 C/A ,L2P/B1,B2,B3
Satlab Geosolut	Satlab SL600	GPS/GLONASS/SBAS	L1 C/A, L1C,L2P,L5 /L1,L2 / WAAS,EGNOS,MSAS,GAGAN
Graftek Müh.	Trimble Geo 7x	GPS/GLONASS/SBAS	L1 C/A ,L2C,L2E / L1 C/A,L1P,L2 C/A / L1 C/A
Graftek Müh.	Trimble SPS461	GPS/SBAS	L1 C/A,L1-L2 / 4 Kanal

Using Table 1, a ranking was made from the device that sees the least satellite system and signal to the maximum and a visual graph was created (Figure 1). As a result, it has become easier to examine the device that receives the most signals and sees the most satellite systems via the corresponding table. Accordingly, it has been seen that the most ideal device for our country is the Kolida K58 Pus device, which can work with systems

such as GPS /GLONASS /SBAS / GALILEO / QZSS / BEIDOU and receive signals from many satellites of these systems (Figure 1).

Figure 1. Number of Satellite systems and signals used (The number of signals it sees, the number of satellites he has seen)

4. Conclusions

The importance of satellite-based position systems in terms of their application in the cartography sector has been increasing in recent years. Although each country wants to produce its own satellite system, the important thing is that these satellite systems can be used by other countries. In this study, first of all, the general characteristics of satellite systems and their ability to work throughout our country are summarized. Then, the current state of use of these satellite systems in our country was determined by contacting public and private sector users by phone, website and mail, which of their respective devices have seen how many satellite systems and which signals they have received. Then, based on this table, a ranking was made from the device that sees the least satellite system and signal to the maximum and a visual graph was created. As a result, it has become easier to examine the device that sees the most signals and sees the most satellite systems via the table. According to this; it has been seen that the most ideal device for our country is the device called Kolida K58 Pus, which can work with systems such as GPS /GLONASS /SBAS / GALILEO /QZSS /BEIDOU and receive signals from many satellites of these systems.

References

[1].URL-1: https://pgm.uab.gov.tr/uploads/pages/tezler/emre-icen-kuresel-ve-bolgesel-konumlama-sistemleri-teknolojileri-ve-uygulamalari.pdf
[2]. URL-2: https://tr.wikipedia.org/wiki/GPS
[3]. URL-3: https://tr.wikipedia.org/wiki/GLONASS
[4]. URL-4: https://tr.wikipedia.org/wiki/GALİLEO
[5]. URL-5: https://tr.wikipedia.org/wiki/BEİDOU
[6]. URL-6: https://tr.wikipedia.org/wiki/QZSS
[7]. URL-7: https://tr.wikipedia.org/wiki/IRNSS.

Intercontinental Geoinformation Days

igd.mersin.edu.tr

Estimation of tidal constituents from sea level registrations in BAB "St. Kliment Ohridski", Livingston Island

Lyubka Pashova*[1], Borsilav Alexandrov[2]

[1]*National Institute of Geophysics, Geodesy and Geography – Bulgarian Academy of Sciences, Department of Geodesy, Sofia, Bulgaria*
[2]*University of Architecture Civil Engineering and Geodesy, Faculty of Geodesy, Sofia, Bulgaria*

Keywords
Tide gauge
Sea level
Tidal constituents
BAB "St. Kliment Ohridsky"
Livingston Island

ABSTRACT

The report presents the first results of the tidal analysis from sea level records obtained from TG installed in the aquatory of the Bulgarian Antarctic base "St. Kliment Ohridski" (BAB) on Livingston Island, Antarctica. Sea level data are available from two Antarctic Expeditions, 26-st during 2017/2018 with more than 83-daily 15-minutes records and 28-th in the period January-December 2019. The tides in the aquatory of the BAB vary in the range of 2.4 m, and about 30 tidal constituents are determined to be significant using UTide software. The obtained results show that tides are mixed with semi-diurnal behaviour and a daily inequality between high and low waters. Comparisons have been made with the results of tidal regime analyzes from other studies for the Livingston Island area. The planned geodetic research activities in the area of BAB are briefly described.

1. Introduction

Making long-term recordings of sea-level variations to accurately determine the height of tides and their forecasting in the Antarctic region has essential scientific and practical value. Tidal oscillations at the ice-ocean interface of the Antarctic coast influence the location and extent of grounding zones control heat transfer and ocean mixing in cavities beneath the marine cryosphere and the calving and drift of icebergs (Padman et al. 2018). Tides range under most ice shelves fringing Antarctica are typically between 1-2 m, but spring tides can reach 2-4 m and occasionally exceed 6 m under the Filchner-Ronne Ice Shelf and in the southern Weddell Sea (Padman et al. 2002).

The Bulgarian Antarctic base "St. Kliment Ohridski" (http://www.bai-bg.net/bulgarian-base.html, Fig. 1) is located on the island of Livingston near the Spanish base "Juan Carlos I" (Vidal et al. 2012). The access to the BAB is by sea only, so it is essential to determine the tidal regime for unimpeded navigation, acoustics on the shore, and studying variations in sea level at different temporal and spatial scales under climate change conditions.

Tidal observations at BAB have been started in the last few years. Given that the permanent installation of sea level sensors must be per the extreme seasonal dynamic and harsh coastal conditions, the hydrostatic pressure sensor type "TideMaster" of Valeport Ltd, the UK, has been selected to be installed in a selected and protected location during the 26th Bulgarian expedition in 2017/2018 (Alexandrov 2019). This sensor measures the hydrostatic pressure of the water column at a fixed point and converts this to sea level. The goal was to overcome the damage to installed devices and cables that connect them to their onshore data logger and power supplies. The sensor is anchored at 3 m below sea level in the Emona Bay and records with sampling intervals of

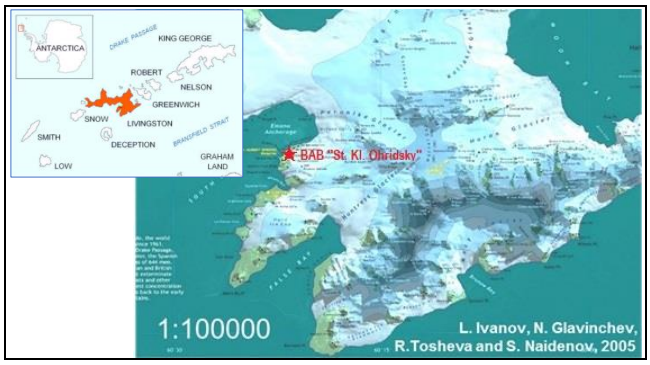

Figure 1. Location of the BAB "St. Kl. Ohridsky" on Livingston Island (shown in red on the inset map)

* **Corresponding Author**

*(lpashova.niggg@geophys.bas.bg) ORCID ID 0000-0002-8058-9905
(alekb_fgs@uacg.bg) ORCID ID xxxx-xxxx-xxxx-xxxx

Cite this study

Pashova L, Alexandrov B (2021). Estimation of tidal constituents from sea level registrations in BAB "St. Kliment Ohridski", Livingston Island. 3rd Intercontinental Geoinformation Days (IGD), 50-53, Mersin, Turkey

15 minutes. The relative sea level was measured from Jan 3 to Feb 15 and from Apr 16 to May 22, 2018. A strong storm tears off the sensor and throws it ashore. The sensor was reinstalled again in another place during the 28th expedition after repairing the cables. The sea-level records are collected from Jan 9 until Oct 16, 2019, with two minor interruptions of several hours. Unfortunately, due to a sharp deterioration of the weather and heavy ice drift in the bay on Livingston Island, the power cable is was cut off, and the sensor stopped recording. The test location of the TG sensor installation in 2017 is with coordinates 62°38'39.9" S, 60°22'29.1" W (WGS'84), and the second in the Emona Bay has coordinates 62°38'32" S, 60°22'17" W, closer to the permanent GNSS site KOH2 established in 2019 (Alexandrov 2020).

This report provides the first analyses of the TG data collected from two sea-level campaign observations using UTide software (Codiga 2011). This study continues the previous one, as the time series of the sea level data have been supplemented with new ones, and other processing software has been used (Alexandrov and Pashova 2021). The obtained main tidal components through harmonic analysis (HA) are compared with the previous results and similar studies performed in this region. We estimated about 30 statistically significant tidal components and the tidal form factor F. We showing that the tidal regime in the Emona bay is mixed mainly semi-diurnal (0.25 < F < 1.5), similar to our previous result and confirming results of other studies (Vidal et al. 2012; Jigena et al. 2015). Studies of sea-level changes and tidal forecasting in the BAB region are needed for many other studies and applications. For example, tides are a vital component in the assimilation of sea level data into refined global and regional tidal models setup, investigation of the effect of future SLR on the tidal regime in this area of the Antarctic and the response of the primary tidal constituents to various SLR scenarios (see, e.g. Llanillo et al. 2019; Zhou et al. 2020).

2. Dataset and methodology

2.1. TG sea-level records

The selected sea-level datasets were subjected to data management procedures. All data undergo the QA/QC and convert into appropriate formats to use UTide software (Codiga 2011). In this study, two sea-level campaigns in 2018 and 2019 shown in Table 1 are used to evaluate the tidal regime at the BAB. Two more short observation periods are available, Apr 16 - May 22, 2018 and Jan 9 - Feb 19, 2019, but they are excluded from further analysis due to outliers in the data. For example, tidal records from the first observation period of 2018, obtained from the TG sensor, are presented in Fig. 2. The time series shows a maximum range of 2.28 m at TG BGLIV, defined as the largest difference between the maximum and the next minimum. Therefore, it can be classified as meso-tidal (spring tidal range of 1-2m).

A form number, F, has been defined as the sum of amplitudes of diurnal tidal species over semi-diurnal species (Defant 1958). A simplified definition of the F-ratio number is F = (K1+O1)/(M2+S2), and it can be used to characterize tidal types. If F is less than 0.25, the tide is semi-diurnal; if F is between 0.25 and 3.0 the tides are considered mixed, and if it is greater than 3.0, the tide is diurnal. The total 15-minute values used in this study are 24,294, and their histogram distribution is shown in Fig.3.

Table 1. 15-minute sea-level data used in this study

Year	Observed period		Days	Number of records
	start	end		
2018	3 Jan 12:15 LT	10 Feb 07:30 LT	38	3630
2019	14 Mar 21:15 LT	16 Oct 03:00 LT	215	20664

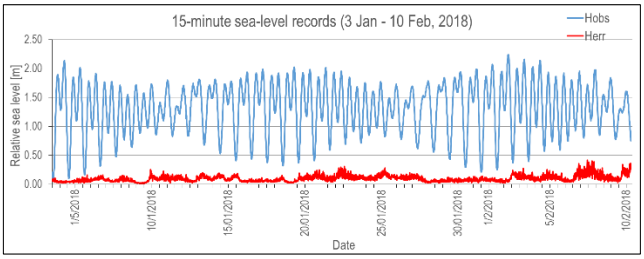

Figure 2. Tidal records H_{obs} (blue line) and residual series H_{err} (red line) at TG BGLIV on Livingston Island

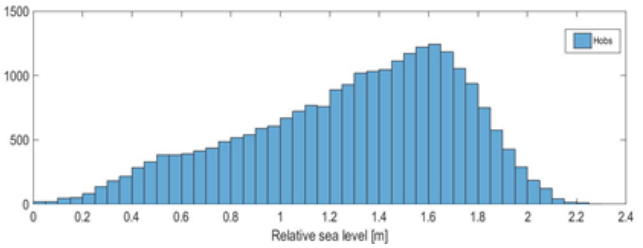

Figure 3. Histogram of sea-level data sets

2.2. Harmonic analysis

The standard tool for tidal analysis is usually based on HA, and Utide was selected to calculate all tidal constituents (Codiga 2011). HA codes model tidal heights $h(t_j)$ as a function of time t_j, with known tidal constituent frequencies f_k and unknown amplitudes a_0, $a_{1,k}$ and $a_{2,k}$; thus,

$$h(t_j) = a_0 + \sum_{k=1}^{n} [a_{1,k} \cos(f_k t_j) + a_{2,k} \sin(f_k t_j)].$$

Several experimental calculations using the UTide software tool (Codiga 2011) are performed (not shown) with different options of the iteratively reweighted least squares (IRLS) and the ordinary least squares (OLS) methods separately for the two observational periods. They show a minimal effect on the obtained results. Here, we show in Table 2, the most common tidal harmonic constituents - daily O1, K1, P1, Q1, sub-daily M2, S2, N2, K2 and three long-term constituents MF, MSF, SSA with their accuracy evaluation. Phase lags are referenced to Greenwich. More detail for practical application and interpretation of tidal analysis and prediction is provided in Parker (2007).

3. Results

The obtained results (Table 2) show that the most significant tidal amplitudes are the principal lunar M2 and principal solar S2. Diurnal constituents K1 and O1

also dominate the amplitudes. The significant differences between our results are not discovered, which confirm that the TG data obtained at the BGLIV station are reliable. Calculated values for 2(M2+S2) = 1.20 m, 2(K1+O1) = 1.04 m, and the tidal form factor F= (K1+O1)/(M2+S2) = 0.86, which shows that the prevailing tides are mixed.

Table 2. Tidal constituents at BGLIV station on Livingston Island and their accuracy estimation

Tidal component		Amplitude [cm]	Error [cm]	Phase [°G]	Error [°G]
Daily	K1	26.2	0.1	23.5	0.2
	O1	25.9	0.1	6.1	0.2
	P1	8.1	0.1	16.0	0.8
	Q1	5.7	0.1	358.0	1.2
Sub-daily	M2	39.6	0.1	191.0	0.2
	S2	20.6	0.1	249.0	0.3
	K2	5.9	0.1	246.0	0.7
	N2	5.3	0.1	153.0	0.9
Long-term	MF	5.5	2.2	286	22.5
	MSF	2.5	2.0	274	46.5
	SSA	9.1	2.2	97.6	11.8

The harmonic constituents are determined from the sea level data of the TG station LIVMAR at the Spanish base (Vidal et al. 2012; Oreiro et al. 2014; Jigena et al, 2015) close to the TG BGLIV, agree well with our results. In practice, the values of the main daily and sub-daily tidal components are the same within the accuracy they are estimated. The small residuals could be attributed to local forcing by wind stress and air pressure fluctuations (inverse barometer effect). The water level variations are exclusively driven by astronomical tides. The values of the long-term dominant harmonics have larger amplitudes for the local area of the Bulgarian base in comparison with those estimated from the Spanish TG LIVMAR, which is located in the south-southwest direction of the South Bay on t Livingston Island. The values of the estimated phases differ by about 50° for the diurnal and about 100° for the half-day tidal components. This fact can be explained by the LT (UTC - 3h) used in the data processing, in which registrations are made at sea level through TG BGLIV at BAS.

Further, we compare our results with the published main tidal constituents from global Tidal Analysis using different data sources for the Antarctic Peninsula (Padman et al. 2002; Oreiro et al. 2014; Howard et al. 2020; Weikang et al. 2021). They are also in good conformity with the main tidal constituents obtained through global and regional tidal models developed in the last two decades. The established differences in the amplitudes are of the order of ± 4-5 cm, with what accuracy the tidal components are presented in the global and regional models

4. Discussion

The HA is one of the most popular methods to investigate the tidal regime and its change. This study provides the first results of tidal harmonics using the 15-minute sea-level records; the results show high consistency with the results estimated with the HA method and the independent regional tidal solution for the Livingston Island. The obtained results are auspicious to be used for further analysis and comparison with the satellite altimetry data and to be assimilated into numerical models for regional and local weather and ocean forecasting. Changes in tidal characteristics over time are usually associated with local changes in morphology and tidal currents. In addition to morphological changes and SLR that affect the propagation pattern of tidal currents (which depend on water depth and the shape of coastlines and bays), the changes in mixed layer depth are caused by the warming of the upper ocean layer may induce additional unknown baroclinic changes in currents (Llanillo et al. 2019).

Global changes in tidal properties may have significant spatial variations since different mechanisms may dominate different coasts. Recent studies highlight that mean SLR, intensifying coastal threats at some locations (see, e.g., Pickering et al. 2017), modifies tidal propagation in shallow waters. Further long-term sea-level observations at the TG BGLIV could be used to study time-dependent changes in tidal amplitudes under climate change conditions.

The research activities at the BAB envisaged for the next Bulgarian expedition to Livingston Island include re-establishing the tide gauge, performing precise GNSS levelling to link with TGBM and GNSS site KOH2 for long-term vertical datum control (Alexandrov and Pashova 2021). The IOC (2020) recommendations for the management of in-situ sea level monitoring stations will be taken into account when restoring the TG station and ensuring its smooth operation. Data can be recorded with improved time resolution, for example, every 1 minute, which will increase their amount, accuracy and ability to be used in the study of short-term high-frequency processes lasting from minutes to hours captured by the TG sensor.

5. Conclusion

Many factors can be taken into account when analyzing data from GT sea-level registrations that can give a clearer picture of actual water surface fluctuations and the relationship to the SLR and global climate change. To study the exact mechanism of how changes in shallow water in the bay in front of the BAB and changes in the wave field can affect the tidal variability in the local region require the installation of other equipment and additional research. Initial ocean parameters measurements (salinity, temperature and conductivity) were made during the 2019-20201 campaign near the shore and inland in front of the base. These data were pre-processed and will be used in future joint analyzes and comparisons with data from other sources. Furthermore, changes in the tidal characteristics over time are usually associated with local morphology and tidal currents. In addition to morphological changes and SLRs, which affect the pattern of tidal currents depending on the depth of the water and the shape of the shores and bays, additional unknown baroclinic changes in the currents may be caused by warming of the upper ocean layer. In this regard, hydrographic measurements in the

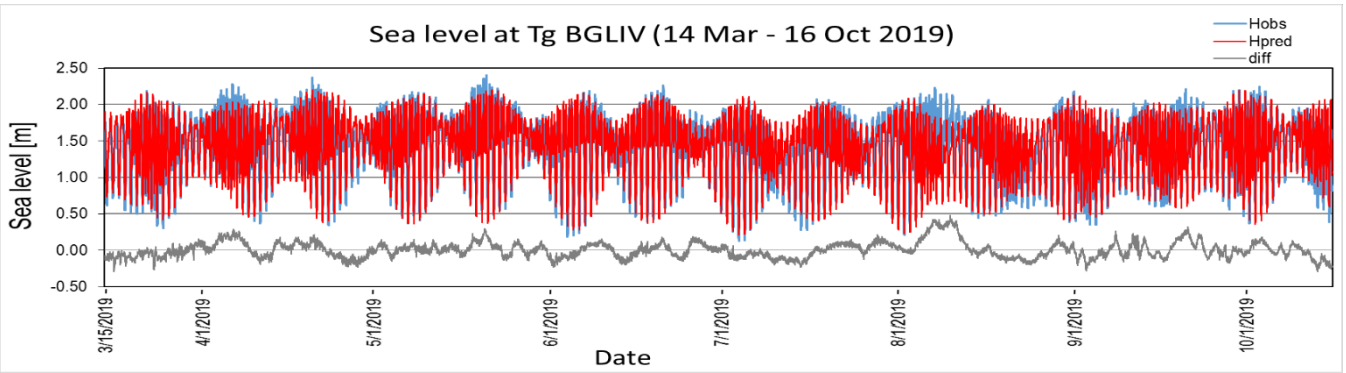

Figure 4. Sea level data, predicted tides and their residuals for the period 14 Mar – 16 Oct 2019 using UTide software

area of the Bulgarian base were performed to prepare a bathymetric map (Alexandrov 2019; Alexandrov and Pashova 2021).

In the last three decades, Bulgarian scientists working on the harshest continent on the Earth have contributed to the implementation of several international and national projects related to the current earth science topics. Seven Bulgarian surveyors contribute to the development of geodetic science and practice in the extreme conditions of Antarctica. They are part of the established experts who have contributed to the study and development of human knowledge about our planet. The construction of a permanent tide gauge station in the BAB "St. Kl. Ohridsky" area is essential for multi-disciplinary studies. TG BGLIV will be used for long-term research; the data will be processed, archived and analyzed together with those from other observations performed regularly. Its maintenance requires the provision of good logistics, providing a constant power source of energy for its year-round operation and finding a suitable data transfer in near or real-time to a Centre of the Bulgarian Antarctic Institute in Sofia, which are in progress.

Acknowledgement

The first author is grateful for funding the current study by the project КП-СЕ-КОСТ/8/25.09.2020.

References

Alexandrov B (2019). The first Bulgarian Maritime Station in Antarctica, Livingston Island, Geod., Cart. Land Manag., 1-2, 3-6, (In Bulgarian).

Alexandrov B (2020). Antarctica and the Bulgarian Presence in it, Geod., Cart. Land Manag., 1-2, 3-8, (In Bulgarian).

Alexandrov B & Pashova L (2021). Geodetic surveys of BAB "St. Kliment Ohridski" on Livingston Island and their contribution to the study of modern geophysical processes, In: Proc. of X National Geoph. Conf., 1-10, https://doi.org/10.48368/bgs-2021.1.N1.

Codiga D L (2011). Unified Tidal Analysis and Prediction Using the UTide Matlab Functions. University of Rhode Island, Narragansett, 59 p.

Defant A (1958). Ebb and Flow: The Tides of Earth, Air, and Water, University of Michigan Press, 121 pp.

Jigena B., Vidal J & Berrocoso M. (2015). Determination of the tide constituents at Livingston and Deception Islands (South Shetland Islands, Antarctica), using annual time series. DYNA 82 (191), 209-218, https://doi.org/10.15446/dyna.v82n191.45207

UNESCO/IOC (2020). Quality Control of in situ Sea Level Observations: A Review and Progress towards Automated Quality Control, Vol. 1. Paris, UNESCO. IOC Manuals and Guides No.83. (IOC/2020/MG/83Vol.1),

Howard S L, King M & Padman L (2020) "Antarctic Tide Gauge Database, version 1" U.S. Antarctic Program (USAP) Data Center. doi: https://doi.org/10.15784/601358.

Llanillo P J, Aiken C M, Cordero R R et al. (2019). Oceanographic Variability induced by Tides, the Intraseasonal Cycle and Warm Subsurface Water intrusions in Maxwell Bay, King George Island (West-Antarctica). Sci Rep 9, 18571, https://doi.org/10.1038/s41598-019-54875-8

Oreiro F A, D'Onofrio E., Grismeyer W., Fiore M & Saraceno M (2014). Comparison of tide model outputs for the northern region of the Antarctic Peninsula using satellite altimeters and tide gauge data. Polar Science, 8(1), 10–23. doi:10.1016/j.polar.2013.12.001

Padman L, Fricker H A, Coleman R, Howard S & Erofeeva L (2002). A new tide model for the Antarctic ice shelves and seas. Annals of Glaciology, 34, 247–254. doi:10.3189/172756402781817752

Parker B B (2007). Tidal Analysis and Prediction. National Oceanic and Atmospheric Administration Special Publication NOS CO-OPS 3. Silver Spring, MD.

Pickering M D, Horsburgh K J, Blundell J R et al. (2017). The impact of future sea-level rise on the global tides, Continental Shelf Research, 142, 50–68, doi:10.1016/j.csr.2017.02.004.

Vidal J, Berrocoso M & Fernández-Ros A (2012). Study of tides and sea levels at Deception and Livingston islands, Antarctica. Antarctic Science, 24(02), 193–201, doi:10.1017/S095410201100068X.

Zhou X, Zhu G & Hu S (2020). Influence of tides on mass transport in the Bransfield Strait and the adjacent areas, Antarctic. Polar Science, 23, 100506. doi:10.1016/j.polar.2020.100506

Weikang S, Xinghua Z, Dongxu Z & Yanfei S (2021). Development and accuracy of tide models in Antarctica. Chinese Journal of Polar Research, 33(1): 13-26, DOI: 10. 13679/j.jdyj.20200061

Intercontinental Geoinformation Days

igd.mersin.edu.tr

Accuracy assessment of positioning based on single and MULTI-GNSS

Abdulmumin Lukman*[1,2], Ramalan Yusuf [1], Ibrahim Haruna [1] Adamu Abubakar Musa [1]

[1]*Nuhu Bamalli Polytechnic, School of Environmental Studies, Department of Surveying and Geoinformatics, Zaria, Nigeria*
[2] *Ahmadu Bello University, Faculty of Environmental Design, Department of Geomatics, Zaria, Nigeria*

Keywords
Single GNSS
Multi-GNSS
Precise Point Positioning (PPP)
PPPH
International GNSS Service (IGS)

ABSTRACT

Global Navigation Satellite System (GNSS) globally gives users 24-hour service of 3D positioning, velocity, and time with the aid of radio signals transmitted from satellites orbiting in space. More satellites present during observation bring improvement in satellite geometry and redundancy which gives better quality of GNSS positioning result. This study aims at testing the positional accuracy of the use of multi-GNSS as compared to using a single satellite. Five International GNSS Service (IGS) stations (MRO1, PTVL, TONG, XMIS, and YAR3) were used for the study and the data obtained from these stations were post-processed using the PPPH software. In the single satellite category, GPS and GLONASS produced similar results with RMSE values of approximately >0.1m in both horizontal and vertical components. On the other hand, the combination of GPS+GLONASS gave the best result in the multi-GNSS category with RMSE values identical to those obtained from the GPS and GLONASS single satellites.

1. Introduction

Global Navigation Satellite System (GNSS) is the general term for all those navigation systems that provide users globally with a 3-dimensional positioning, velocity, and time solution 24-hour service with the use of transmitted radio signals from orbiting satellites in space (Garcia et al., 2019). Global Positioning System (GPS) for the United States, GALILEO for Europe, for Russians is the GLONASS, BeiDou for the People's Republic of China, and the QZSS for Japan.

The advent of the GNSS has made surveying and mapping applications easier, accurate, and more precise. This is the reason why geodesists are interested in utilizing forefront GNSS strategies. Recently, GNSS can be said to be one of the developments and useful advances to the field of surveying and geodesy. Since its inception, it has evolved to give overall all-weather navigation as well as precise and accurate positioning sureness capabilities to its users (Abdulmumin et al., 2020; Isioye et al., 2018).

The advantage of using multi-GNSS is in the availability of a larger number of satellites, which will benefit the user in; reducing signal acquisition time, improving positioning and accuracy in time, reducing problems caused by obstructions such as buildings and foliage, and Improving the spatial distribution of visible satellites, leading in improvement in dilution of precision (DOP) (Jeffrey, 2010; Langley et al., 2017).

Precise Point Positioning (PPP) is a GNSS positioning application known for its high precision and accuracy level; using a single receiver and undifferenced observations by application of the precise satellite orbit and clock products from the International GNSS Services (IGS), it provides a user with centimeter to millimeter level positioning globally. GPS was the only system that the PPP was mainly performed on some time ago. Today, the GLONASS, Beidou, and the GALILEO, multi-GNSS positioning that can highly improve the positioning, continuity, availability, and accuracy become the order of the day in GNSS-based applications (Wang et al., 2018).

Many kinds of research were conducted to test for the positional accuracy of the use of multi-GNSS (see Andreas et al., 2019; Bu et al., 2021; Fang et al., 2019; Garcia et al., 2019; Li et al., 2015; Tao et al., 2021; Wang et al., 2018).

The current study aims to assess the positional accuracy of multi-GNSS for geodetic and mapping applications.

* **Corresponding Author**

*(labdulmumin54@gmail.com) ORCID ID 0000–0003– 0750–3914
(yusuframalan2019@gmail.com) ORCID ID 0000–0001–9674–9080
(harunajulious@gmail.com) ORCID ID 0000–0002–1567–7634
(abusumayya2018@gmail.com) ORCID ID 0000–0003–1863–0089

Cite this study

Abdulmumin L, Yusuf R, Haruna I & Musa A A(2021). Accuracy assessment of positioning based on single and Multı-GNSS. 3rd Intercontinental Geoinformation Days (IGD), 54-57, Mersin, Turkey

2. Method

The dataset used for this study was obtained from five International GNSS Service (IGS) Stations (see Table 1) through its website (ftp://cddis.gsfc.nasa.gov/gnss/data/daily/). The choice of these stations was based on multi-GNSS capabilities and those with consistent data. Seven days RINEX data files of the year 2019 were downloaded from day 359 to 365 which was equivalent to day 20853 to 20862 GPS calendar. Figure 1 shows pictorially the locations of these IGS GNSS sites.

The obtained data were then post-processed using the PPPH software to determine the obtainable positional accuracy using these multi-constellation permanent GNSS sites.

Figure 1. The Geographic Locations of the used IGS Stations

To compare the results obtained from the PPPH software with the known coordinates of the stations used, the difference in X, Y, Z, and XY components was computed and used in analyzing the results subsequently. Also, Root Mean Square Error was computed using Equations (1), (2), (3), and (4).

$$\mathrm{RMSE_x} = \sqrt{\sum_{i=1}^{n} \frac{\Delta x_i^2}{n}} \quad 1$$

$$\mathrm{RMSE_y} = \sqrt{\sum_{i=1}^{n} \frac{\Delta y_i^2}{n}} \quad 2$$

$$\mathrm{RMSE_z} = \sqrt{\sum_{i=1}^{n} \frac{\Delta Z_i^2}{n}} \quad 3$$

Where Δx_i *and* Δy_i are the differences between the obtained result from the PPPH software and the reference (true) coordinates of the used IGS stations.

Calculation of the Root Mean Square coordinate error RMSExy, which is a characteristic of point sets accuracy and is one of the most common accuracy measures in geodesy. RMSExy is calculated as follows;

$$RMSE_{xy} = \sqrt{0.5(RMSE_X)^2 + \left(RMSE_y\right)^2} \quad 4$$

3. Results

The coordinates of the five used IGS stations are presented in Table 1. Similarly, all 3D coordinates obtained from the PPPH software were converted to the same coordinate system for easy comparison.

Table 1. Showing the used IGS stations, the cities and countries they belong to, their coordinates, and systems

STATIONS	COUNTRY	X (m)	Y (m)	Z (m)	SYSTEMS
MRO1	Australia	-2556629.766	5097138.226	-2848385.220	QZSS+GPS+GLO+GAL+BDS
PTVL	Vanuatu	-5950573.211	1230677.184	-1932017.019	QZSS+GPS+GLO+GAL+BDS
TONG	Tonga	-5930303.5403	-500148.768	-2286366.298	QZSS+GPS+GLO+GAL+BDS
XMIS	Australia	-1696344.7609	6039590.001	-1149275.083	QZSS+GPS+GLO+GAL+BDS
YAR3	Australia	-2389043.7708	5043313.583	-3078524.391	QZSS+GPS+GLO+GAL+BDS

The RMSE for each station has been computed using equations (1)-(4). These results are presented in tables 2, 3, 4, 5, and 6 for stations MRO1, PTVL, TONG, XMIS, and YAR3 respectively.

Considering the results from the single satellites, GPS and GLONASS produced identical results in both horizontal and vertical components with RMSE values less than 0.1 m in all the used stations (see Figure 2).

On the other hand, the combination of GPS and GLONASS (GPS+GLONASS) satellites proves to be better in the multi-GNSS category with RMSE values similar to that of GPS and GLONASS (>0.1 m) in the single satellite. The combinations of GPS and BEIDOU (GPS+BEIDOU), and GLONASS and BEIDOU (GLONASS+BEIDOU) produced poor results (see also Figure 2).

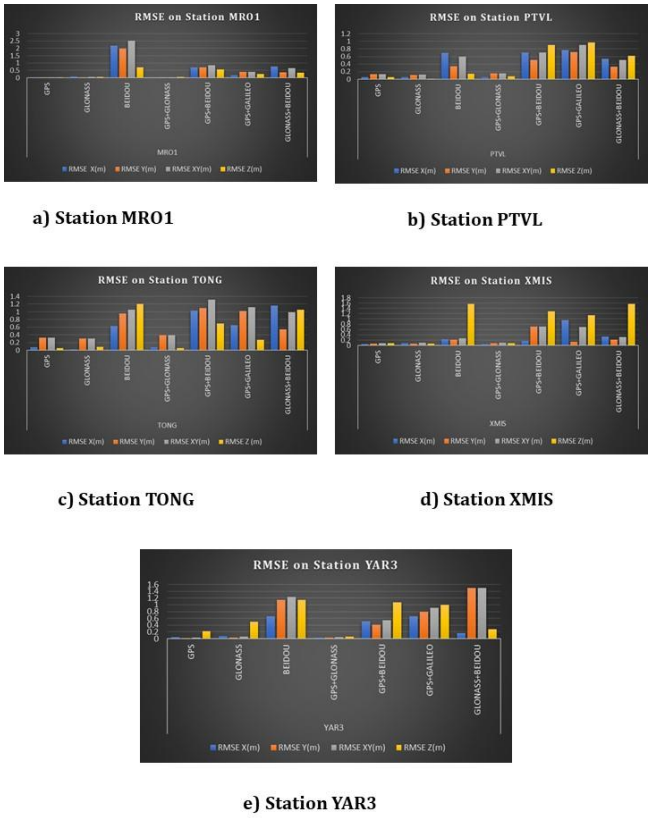

a) Station MRO1

b) Station PTVL

c) Station TONG

d) Station XMIS

e) Station YAR3

Figure 2. RMSE in coordinates of all the five used stations

4. Discussion

Although not all multi-GNSS combinations give the required accuracy, multi-GNSS capability can solve many GNSS project problems. Based on the current study, GPS and GLONASS have the best results when compared to the other single constellation (i.e., BEIDOU). On the other hand, the synergy between GPS and GLONASS (GPS+GLONASS) comes on top when considering the accuracy of the multi-GNSS systems.

Generally, it can be said that the GPS, GLONASS, and GPS+GLONASS systems have similar results based on the present study. This implies that these systems can be integrated when there is a need or in the absence of GPS or GLONASS signal. The use of all other constellations apart from that can be discouraged based on the results obtained.

5. Conclusion

The use of multi-GNSS constellations can go a long way in solving the problems of GNSS mapping problems; in reducing the cases of signal loss, improving accuracy, and the likes. But this is not always achieved as proved in the just-completed study. If one must use it, GPS+GLONASS is the best.

Table 2. RMSE of Coordinates over the Station MRO1

STATION	SYSTEM	RMSE X (m)	RMSE Y (m)	RMSE XY (m)	RMSE Z (m)
MRO1	GPS	0.01122209	0.019920642	0.021442939	0.019221268
	GLONASS	0.07193277	0.026292212	0.057257682	0.068788550
	BEIDOU	2.16433165	1.992064209	2.512067984	0.706914569
	GPS+GLONASS	0.01072881	0.030276334	0.031212338	0.065561738
	GPS+BEIDOU	0.70344904	0.703063347	0.861230715	0.559836358
	GPS+GALILEO	0.15614839	0.380931349	0.396610454	0.243052520
	GLONASS+BEIDOU	0.75261300	0.378810029	0.653230588	0.330026654

Table 3. RMSE of Coordinates over the Station PTVL

STATION	SYSTEMS	RMSE X (m)	RMSE Y (m)	RMSE XY (m)	RMSE Z (m)
PTVL	GPS	0.055789283	0.130304436	0.136145026	0.057082015
	GLONASS	0.051122379	0.111169206	0.116898850	0.013628663
	BEIDOU	0.692271956	0.340628681	0.596362414	0.142641936
	GPS+GLONASS	0.053567458	0.152522690	0.157155678	0.075845406
	GPS+BEIDOU	0.699314189	0.506091667	0.707565505	0.905610153
	GPS+GALILEO	0.770024867	0.718223702	0.901284879	0.966270324
	GLONASS+BEIDOU	0.543639478	0.329314972	0.506182074	0.618524800

Table 4. RMSE of Coordinates over the Station TONG

STATION	SYSTEMS	RMSE X (m)	RMSE Y (m)	RMSE XY (m)	RMSE Z (m)
TONG	GPS	0.077604333	0.324084028	0.328696933	0.054437393
	GLONASS	0.023352265	0.311908094	0.312344878	0.086983963
	BEIDOU	0.629147622	0.953409063	1.052094201	1.203708856
	GPS+GLONASS	0.077413208	0.394794706	0.398571527	0.054437393
	GPS+BEIDOU	1.032198487	1.09483042	1.315815529	0.701663042
	GPS+GALILEO	0.650360825	1.024119742	1.122633443	0.277398973
	GLONASS+BEIDOU	1.159477708	0.54328713	0.983542161	1.048145364

Table 5. RMSE of Coordinates over the Station XMIS

STATION	SYSTEMS	RMSE X (m)	RMSE Y (m)	RMSE XY (m)	RMSE Z (m)
XMIS	GPS	0.043040494	0.071178059	0.077411615	0.082712
	GLONASS	0.084461850	0.070957578	0.092746320	0.064840
	BEIDOU	0.239802219	0.212843815	0.272130560	1.567636
	GPS+GLONASS	0.043040494	0.091178059	0.096123257	0.082712
	GPS+BEIDOU	0.169091541	0.706395001	0.716442511	1.284794
	GPS+GALILEO	0.962279309	0.140709576	0.694830857	1.143372
	GLONASS+BEIDOU	0.325883206	0.211420254	0.312727446	1.567636

Table 6. RMSE of Coordinates over the Station YAR3

STATION	SYSTEMS	RMSE X (m)	RMSE Y (m)	RMSE XY (m)	RMSE Z (m)
YAR3	GPS	0.050063747	0.01223673	0.037455666	0.218742
	GLONASS	0.068645985	0.027060598	0.055573479	0.501584
	BEIDOU	0.657043034	1.143607581	1.234378821	1.137980
	GPS+GLONASS	0.032646931	0.031324730	0.038912078	0.066095
	GPS+BEIDOU	0.515621678	0.412027338	0.550181229	1.067270
	GPS+GALILEO	0.657043034	0.790054190	0.916536086	0.996559
	GLONASS+BEIDOU	0.162068287	1.497160971	1.501540555	0.276233

References

Abdulmumin, L., Isioye, O. A., Bawa, S., & Muhammed, A. (2020). Exploring the Usability and Suitability of Smartphone Apps for Precise and Rapid Mapping Applications. *Intercontinental Geoinformation Days*, 36–39. http://igd.mersin.edu.tr/2020/

Andreas, H., Abidin, H. Z., Sarsito, D. A., & Pradipta, D. (2019). *Study the capabilities of RTK Multi GNSS under forest canopy in regions of Indonesia*. *01021*.

Bu, J., Yu, K., Member, S., & Qian, N. (2021). *Performance Assessment of Positioning Based on Multi-Frequency Multi-GNSS Observations : Signal Quality , PPP and Baseline Solution*. 5845–5861.

Fang, Z., Nie, W., Xu, T., & Liu, Z. (2019). *Accuracy Assessment and Improvement of GNSS Precise Point Positioning Under Ionospheric Scintillation* (Vol. 2). Springer Singapore. https://doi.org/10.1007/978-981-13-7759-4

Garcia, H. H., Mercurio, M. E., Noveloso, D. P., & Reyes, R. B. (2019). *POSITIONAL ACCURACY ASSESSMENT USING SINGLE AND MULTI-GNSS*. *XLII*(November), 14–15.

Isioye, O. A., Moses, M., & Abdulmumin, L. (2018). Comparative Study of Some Online GNSS Post-Processing Services at Selected Permanent GNSS Sites in Nigeria. In *Accuracy of GNSS Methods* (p. 19). IntechOpen. https://doi.org/10.5772/intechopen.79924

Jeffrey, C. (2010). *An Introduction to GNSS* (Fisrt). NovAtel Inc.

Langley, R. B., Teunissen, P. J. G., & Montenbruck, O. (2017). Introduction to GNSS. In *Springer Handbooks*. https://doi.org/10.1007/978-3-319-42928-1_1

Li, X., Ge, M., Dai, X., Ren, X., Fritsche, M., Wickert, J., & Schuh, H. (2015). *Accuracy and reliability of multi-GNSS real-time precise positioning : GPS , GLONASS , BeiDou , and Galileo*. https://doi.org/10.1007/s00190-015-0802-8

Tao, Y., Liu, C., Chen, T., Zhao, X., Liu, C., Hu, H., Zhou, T., & Xin, H. (2021). *Real-Time Multipath Mitigation in Multi-GNSS Short Baseline Positioning via CNN-LSTM Method*. *2021*.

Wang, L., Li, Z., Ge, M., Neitzel, F., Wang, Z., & Yuan, H. (2018). Validation and Assessment of Multi-GNSS Real-Time Precise Point Positioning in Simulated Kinematic Mode Using IGS Real-Time Service. *Remote Sensing*, 1–19. https://doi.org/10.3390/rs10020337

Intercontinental Geoinformation Days

igd.mersin.edu.tr

Monitoring of bathymetric changes in the Commodore Channel, Lagos State Nigeria

Peter Nwilo[1], Babatunde Anibaba[1], Chukwuma Okolie[1], Michael Orji[1,2], Hamed Olanrewaju[1], Samuel Akinnusi[1], Olagoke Daramola[1], Chukwuma Azuike[3]

[1]*University of Lagos, Faculty of Engineering, Department of Surveying and Geoinformatics, Lagos, Nigeria*
[2]*University of Strathclyde, Faculty of Engineering, Department of Naval Architecture, Ocean and Marine Engineering, Glasgow, United Kingdom*
[3]*Nigerian Navy, Nigerian Navy Hydrographic Office (NNHO), Nigeria*

Keywords
Lagos harbour
Bathymetry
Commodore Channel
Kriging
Dredging

ABSTRACT

The Commodore Channel in Lagos State is located at the seaside entrance into the Lagos Harbour thus exposing it to the action of dynamic coastal forces such as high waves, tidal currents, and storm surges. The combined effects of these forces affect the stability of the sediments on the channel's seabed. This study assessed changes in the channel's bathymetry using data on water depth from a time series of bathymetric charts covering the channel at the following periods: 2008, 2010, 2012, 2014, 2016 and 2018. The charts were acquired from the Nigerian Navy Hydrographic Office (NNHO), scanned and georeferenced. The depths were digitized within the ArcGIS 10.4.1 software environment. Using Kriging interpolation, bathymetric surfaces were produced, and coincident points for depth comparison were extracted. There was an average decrease of 0.02m in depth values from 2008 to 2010 and an average decrease of 0.03m between 2010 to 2012. From 2012 to 2018, the average depth increased consistently. There was also a rapid increase in surface volume from 2008 – 2014, and a slight decrease in volume in 2016. Continuous monitoring of channel bathymetry is essential for safe navigation.

1. Introduction

Seafloor data are primarily collected by measuring the time that laser light, or an acoustic sonar pulse, takes to travel through the water column to the seafloor and back, based on the speed of sound in water, sensor characteristics, time and other variables (Kearns et al., 2010). Monitoring the changes in riverbed topography is important because they provide data from which morphological parameters are estimated. Bathymetric surveys involve the measurement of the depth of water bodies as well as the mapping of underwater features. Several methods can be used for bathymetric surveys including multi-beam and single beam echo sounder surveys, and remote sensing methods. Bathymetric surveys are important for many purposes such as sedimentation purposes to check for accretion or erosion, and pre/post dredge bathymetry to determine the status of the water body or ascertain the dredged volume (Chukwu and Badejo, 2015). Bathymetric information is vital in navigation safety, water volume computation, pollution control, underwater engineering construction and maintenance (Temitope and Kehinde, 2019). In bathymetric surveys, charts are produced to support safety of surface or sub-surface navigations which usually shows seafloor relief, and such charts provides surface navigational information (Temitope and Kehinde, 2019). The regular updating of bathymetric charts is a daunting task that cannot be ignored due to its importance in estimating or determining temporal changes in an ocean floor which provides accurate information in terms of planning, engineering design, and regulation of navigation, flood control and coastal engineering projects (Chukwu and Badejo, 2015). Comparison of digital bathymetric data for the same region but at different time periods enables the estimation of net movement of sediments in (accretion) and out (erosion) of the Commodore channel in Lagos State (Temitope and Kehinde, 2019).

This study aims to monitor and visualize the bathymetric changes in the Commodore Channel of Lagos State (shown in Figure 1) using a time series of

* **Corresponding Author**
*(tundeanibaba@yahoo.com) ORCID ID 0000 – 0002 – 5965 – 5672

Cite this study
Nwilo P, Anibaba B, Okolie C, Orji M, Olanrewaju H, Akinnusi S, Daramola O & Azuike C (2021). Monitoring of bathymetric changes in the Commodore Channel, Lagos State Nigeria. 3rd Intercontinental Geoinformation Days (IGD), 58-61, Mersin, Turkey

bathymetric data for the following periods - 2008, 2010, 2012, 2014, 2016 and 2018. We also assess the changes in channel volume that have occurred over time and infer the causative factors for observed changes in the Commodore Channel and its implications for safe navigation.

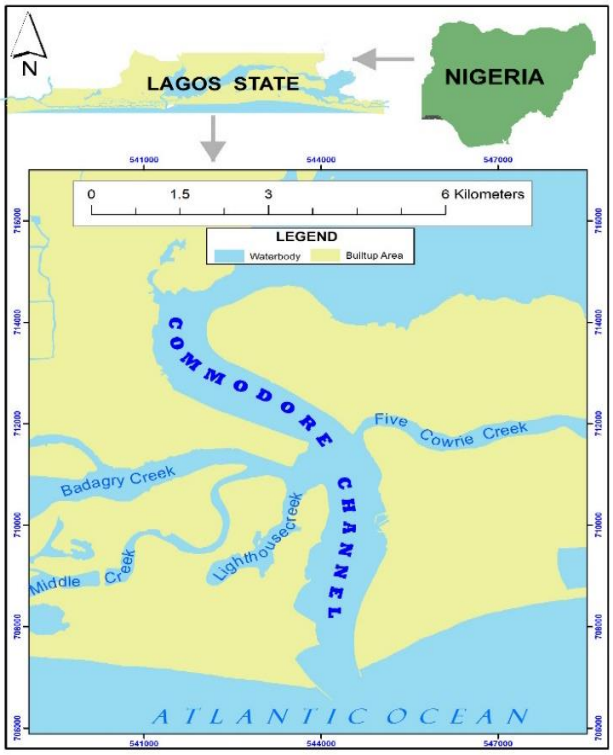

Figure 1. Map showing the location of Commodore Channel

2. Methods

2.1. Data acquisition

Bathymetric charts published by the Lagos Channel Management (LCM) for 6 epochs (2008, 2010, 2012, 2014, 2016 and 2018) were acquired from the Nigerian Navy Hydrographic Office (NNHO).

2.2. Data conversion

The bathymetric charts were scanned, georeferenced and referenced to the WGS84 datum. The study area falls within Zone 31N of the UTM zone. Vectorization of the charts was done in ArcGIS software.

2.3 Kriging and quantitative analysis

Using kriging interpolation in ArcGIS, bathymetric models for the six epochs were generated from the depth points. The changes in depth were computed using the ArcGIS raster calculator. The calculation of the depth change was done using raster calculator expressed as "depth map of the more recent year – depth map of the preceding year". The surface volume tool in ArcGIS was used to calculate the surface volume at each epoch.

3. Results

Table 1 shows the statistics of sampled depths. There was an average decrease of 0.02m in depth values from 2008 to 2010 and an average decrease of 0.03m between 2010 to 2012. From 2012 to 2018, the average depth increased consistently.

Table 1. Statistics of the sampled depths

Statistics	Chart depths (m)					
	2008	2010	2012	2014	2016	2018
Min	22.1	21.65	21.89	21.85	21.67	32.59
Max	3.2	1.47	1.50	1.43	1.61	2.01
Range	18.9	20.18	20.39	20.43	20.06	30.57
Mean	11.3	11.28	11.25	11.81	12.02	12.33
Std. Dev.	3.4	3.646	3.781	3.840	3.796	4.053

The descriptive statistics of depth changes are presented in Table 2. Positive values indicate an increase in depth while negative values indicate a decrease.

Table 3 presents the surface volumes computed for the six periods. There is a rapid increase in volume from 2008 – 2014. However, there is a slight decrease in volume in 2016.

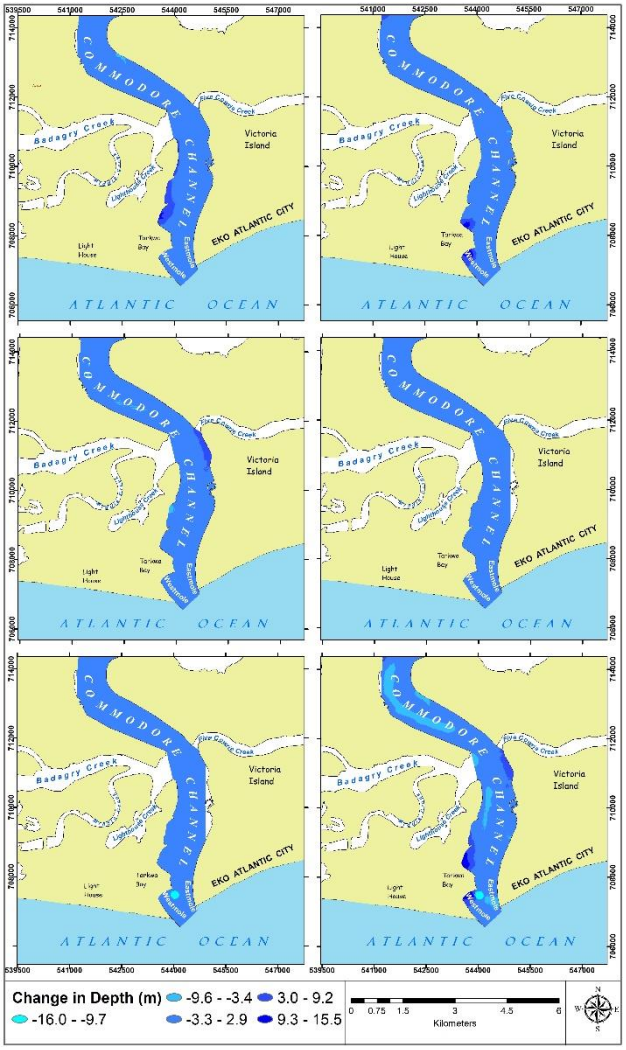

Figure 2. Maps showing changes in depth (ΔH) – (a) 2008-2010 (b) 2010-2012 (c) 2012-2014 (d) 2014-2016 (e) 2016-2018 (f) 2008-2018

Table 2. Statistics of depth changes (ΔH) in metres

	2008-2010	2010-2012	2012-2014	2014-2016	2016-2018	2008-2018
Max (-ve)	4.01	4.51	4.91	3.58	16.40	15.96
Max (+ve)	10.34	15.06	8.25	2.61	2.87	15.51
Range	14.35	10.55	13.16	6.18	19.27	31.47
Mean	+0.08	-0.02	-0.57	-0.15	-0.36	-0.97
Std. Dev.	1.44	1.59	1.29	0.66	1.10	2.87

Table 3. Statistics of surface volume

Year	Volume (m^3)
2008	69,238,215.866
2010	83,783,538.873
2012	83,404,963.764
2014	88,842,339.010
2016	86,655,377.418
2018	88,152,424.554

4. Discussion

The historical archive from the bathymetric charts (2008 – 2018) offers added advantages for monitoring changes over a lengthy period or since the last hydrographic survey of the channel was done. These products can serve as stand-alone information in inaccessible areas or can be used in combination with ancillary data to give informed perspectives on river channel morphology.

5. Conclusion

Historical bathymetric data is a valuable resource for monitoring the changes in the underwater topography of rivers and creeks. The digital bathymetric models produced provide a layer for the development of a coastal characterization procedure of the local coastal habitats. The results of this study clearly show the relevance of digital bathymetric data in urban planning which is primarily concerned with the control of the use of land and design of the urban environment, to guide and ensure the orderly development of settlements and communities. Integrating such data enables us create more comprehensive and strategic plans for development and fosters more sustainable cities.

ACKNOWLEDGEMENTS

We thank the Nigerian Navy Hydrographic Office (NNHO) for provision of the bathymetric charts of Commodore Channel.

REFERENCES

Adeaga, O., Labesa, S., & Okolie, C. J. (2017). Assessment of the Changing Underwater Topography of Commodore Channel , Lagos. March 2019.

Badejo, O.T. (2010). Contemporary Issues in Surveying and Geoinformatics: Modern Trends in Hydrography. pp 425-469. Edited by Professor Francis Fajemirokun, June 2011.

Badejo, O.T., Olaleye, J.B. and Alademomi, A.S. (2014). Tidal Characteristics and Sounding Datum Variation in Lagos State. International Journal of Innovative Research and Studies ISSN 2319-9725

Bentum, K. M. Van, Hoyng, C. W., Ledden, M. Van, Luijendijk, A. P., & Stive, M. J. F. (2012). The Lagos coast – Investigation of the long-term morphological impact of the Eko Atlantic City project. https://doi.org/10.3990/2.199

Chukwu, F.N., & Badejo, O.T. (2015). Bathymetric Survey Investigation for Lagos Lagoon Seabed Topographical Changes. Journal of Geosciences and Geomatics, 3(2), 37–43. https://doi.org/10.12691/jgg-3-2-2

Connon, B. D., States, U., & Nairn, R. (2010). Economic Impact of Hydrographic Surveys Economic Impact of Hydrographic Surveys. April 2010, 11–16.

Dierssen, H.M., Zimmerman, R.C., Leathers, R.A., Downes, T.V. and Davis, C.O. 2003: Ocean colour remote sensing of seagrass and bathymetry in the Bahamas Banks by high resolution

Gao, J. (2009). Bathymetric mapping by means of remote sensing: Methods, accuracy and limitations. Progress in Physical Geography, 33(1), 103–116. https://doi.org/10.1177/0309133309105657

Haskoningdhv, R., & V, A. V. B. (2012). Sediment Dynamics in Lagos Harbour.Ibrahim, P. (2014). Bathymetric Survey and Volumetric Analysis for Sustainable Management Case Study of Suleja Dam , Niger State , Nigeria. 4(18), 24–32.

Internationale, C., Math, P., Unesco, C., & Pr, A. (n.d.) 2010. Introduction Materials and Method Results Discussion Conclusions.

Jakobsson, M., Calder, B., Huff, L. C., & Mayer, L. A. (2005). On the Use of Historical Bathymetric Data to Determine Changes in Bathymetry : An Analysis of Errors and Application to Great Bay Estuary , NH.

Kearns, T. A., Breman, J., Barry, W.E., Taylor Martin, C., Meaden, G., Vaz, S., et.al. 2010. Bathymetry — The Art and Science of Seafloor Modelling for Modern Applications, pp. 1-36. http://downloads2.esri.com/ESRIpress/images/169/OGLOBE.toc.pdf

Kumari, P., & Ramesh, H. (2020). Remote sensing image based nearshore bathymetry extraction of Mangaluru coast for planning coastal reservoir. In Sustainable Water Resource Development Using Coastal Reservoirs. Elsevier Inc. https://doi.org/10.1016/b978-0-12-818002-0.00013-7

Okolie, C. J., & Olayinka, D. N. (2017). Satellite Derived Bathymetry for Detecting Changes in Lighthouse Creek ' s Underwater Topography. March 2019.

Reid, I., Carling, P., Walling, D. E., & Webb, B. (1997). Sediment erosion, transport, and deposition. July 2017.

Rinaldi, M., Gurnell, A. M., Tánago, M. G., Bussettini, M., & Hendriks, D. (2015). Classification of river morphology and hydrology to support management and restoration Classification of river morphology and hydrology to support management and restoration. Aquatic Sciences, 78(1), 17–33. https://doi.org/10.1007/s00027-015-0438-z

Rodriguez, R.R. 2015. Integration of Topographic and Bathymetric Digital Elevation Model Using ArcGIS Interpolation Methods. A Case Study of the Klamath River Estuary. MSc Thesis, Geographic Information Science and Technology, University of Southern California. May 2015.

Sawczyński, S., & Kaczmarek, L. M. (2015). Modeling bathymetry changes in the coastal zone – State of knowledge analysis MODELING BATHYMETRY CHANGES IN THE COASTAL ZONE – STATE OF KNOWLEDGE. July.

Temitope, B. O., & Kehinde, A. G. (2019). Bathymetric Survey and Topography Changes Investigation of Part of Badagry Creek and Yewa River, Lagos State, Southwest Nigeria. Journal of Geography, Environment and Earth Science International, August, 1–16. https://doi.org/10.9734/jgeesi/2019/v22i430153

Van Bentum, K. M., Hoyng, C. W., Van Ledden, M., Luijendijk, A. P., & Stive, M. J. F. (2012a). The Lagos coast – Investigation of the long-term morphological impact of the Eko Atlantic City project. January. https://doi.org/10.3990/2.199

Van Bentum, K. M., Hoyng, C. W., Van Ledden, M., Luijendijk, A. P., & Stive, M. J. F. (2012b). The Lagos coast – Investigation of the long-term morphological impact of the Eko Atlantic City project. https://doi.org/10.3990/2.199

Vol, G., Mining, N., & Society, G. (2012). Assessment of Environmental Impact on Benthic Foraminiferal Distribution in Lagos Lagoon, Nigeria. 48(1), 68–78.

Intercontinental Geoinformation Days

igd.mersin.edu.tr

Accuracy assessment of established control within University of Lagos, Nigeria

Alabi Abiodun Olawale [1], Alademomi Alfred Sunday [1], Okutubo Adedayo David [1], Oyedokun Wale Rufus [1], Salami Tosin Julius [1]

[1]*University of Lagos, Faculty of Engineering, Department of Surveying and Geoinformatics, Lagos, Nigeria*

Keywords
Accuracy Assessment
Survey Controls
Continuously Operating Reference Station
Global Positioning System

ABSTRACT

This paper focuses on assessing the accuracy of established control within the University of Lagos campus. Taking full advantage of advancement and revolutions in surveying techniques, Differential Global Positioning System(DGPS) linked with Continuously Operating Reference Stations(CORS) was embraced for data acquisition to minimise the uncertainties surrounding the process. The acquired data was adjusted/reduced using Trimble Business Center and resulted in the production of a list of new coordinates. Besides, determined was Pearson correlation coefficient and t-statistics at ninety-nine per cent confidence level in Excel application for decision making between existing and newly acquired data. For the Eastings and Northings, the p-values were smaller (E = 0.002768695 and N = 0.00036642) than the 0.01 p-value specified for the computation; communicating the existence of a significant difference between the data thereby inferring the rejection of existing Eastings and Northings coordinates. For the Height, the p-value is larger (0.069657705) than the 0.01 entered value; signifying there exist no significant difference between the height data. Hence, we do not reject the existing elevation data. Finally, a map was produced in accordance with best surveying practices.

1. Introduction

Several studies have shown the existence of considerable discrepancies in data reports of all the previous attempts made to coordinate and re-coordinate Survey Control points/stations within the University of Lagos campus in Lagos, Nigeria. Iyoyojie 2014; Owodunni 2015 both re-coordinated XST347 presumed to be a first-order control and ends up producing two coordinate values (Table 1) with a significant difference. This then prompts a question of "how accurate or precisely determined are all these controls?" Survey control stations are reference monuments to which other survey works of lower accuracy are connected (John, 2020). The purpose of a control system is to prevent the accumulation of errors, by connecting detail work to a reliable geometrical network system of points that are accurate enough for projects.

Great care is taken to ensure that these controls are sufficiently accurate (Dimal et al. 2009).

Control networks consist of stable, identifiable points with published datum values derived from observations that tie the points on the Earth's surface together; (John, 1984). Given the foregoing, this study assesses the accuracy of control points within the University of Lagos. Observations were carried out on the control points using a Differential Global Positioning System (DGPS). The DGPS was linked to a Continuously Operating Reference Station (CORS). The observed coordinates of the controls were compared with the previously documented coordinates, and the differences were statistically analysed.

Table 1. Control Points with Multiple Coordinate varying Value (WGS84 Zone 31)

Station	Eastings(X_o)	Northings(Y_o)	Height(Z_o)
CR 7	543302.330	720161.975	3.193
CR7	543308.485	720161.118	3.458
CR7	543308.350	720161.709	3.288
XST 347	543235.430	719894.220	4.701
XST 347	543245.510	719884.330	4.735

* **Corresponding Author**

*(adeokutubo@gmail) ORCID ID 0000 – 0001 – 7281 – 3965
(subwale@yahoo.com) ORCID ID 0000 – 0002 – 1517 – 7269
(aoalabi@unilag.edu.ng) ORCID ID 0000 – 0002 – 4678 – 6059

Cite this study

Alabi A O, Alademomi A S, Okutubo A D, Oyedokun W R & Salami T J (2021). Accuracy Assessment of Establıshed Control wıthın Unıversıty of Lagos, Nigeria. 3rd Intercontinental Geoinformation Days (IGD), 62-65, Mersin, Turkey

2. Method

Figure 1 presents the methodology workflow for this study.

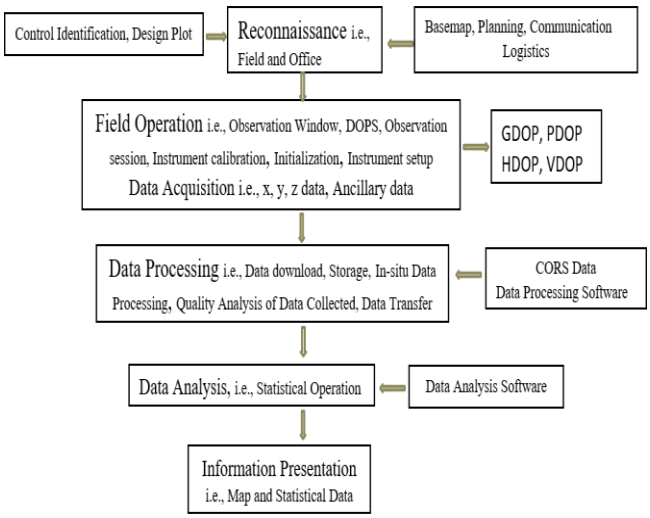

Figure 1. Methodology Workflow

2.1. Study area

The University of Lagos is within the Geographic location 06°31' 0" N, 03°23' 10" E. It is largely surrounded by the scenic view of the Lagos lagoon on 802 acres (324.5579 Hectares) of land in Akoka, North Eastern part of Yaba, Lagos Nigeria. Below figures 2, 3 and 4 are three out of the forty-two control monuments in the study area.

Figure 2. XST347

Figure 3. CR 7

Figure 4. GME 03

2.2. Reconnaissance

Field investigation conducted revealed the control beacons are physically present on the ground with some in bad states. The office inspections further validated the need for the research due to inconsistencies within the sourced existing data leading to a conceptual comprehensive plan devised toward instrumentation, data acquisition and processing. Furthermore, Trimble GNSS planning online software abetted the planning process, i.e. Fig. 6 below.

2.3. Instrumentation

Stonex S900A GPS Receivers and Continuous Operating Reference Station (CORS) were deployed for data acquisition. Trimble Business Center, ArcGIS, Global Mapper and Microsoft Excel were installed for data processing/statistical analysis.

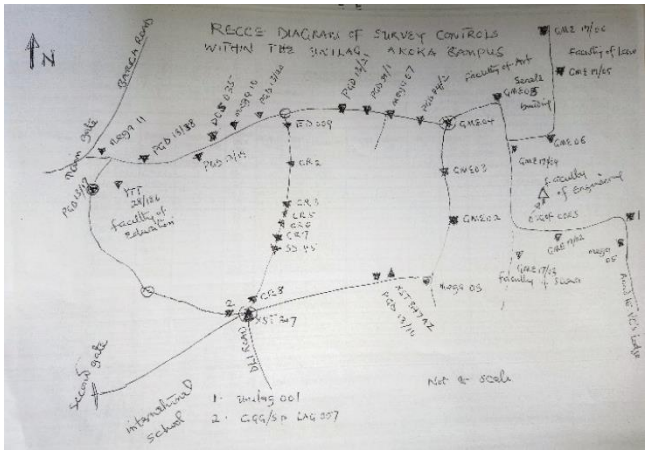

Figure 5. Recce diagram of the study area

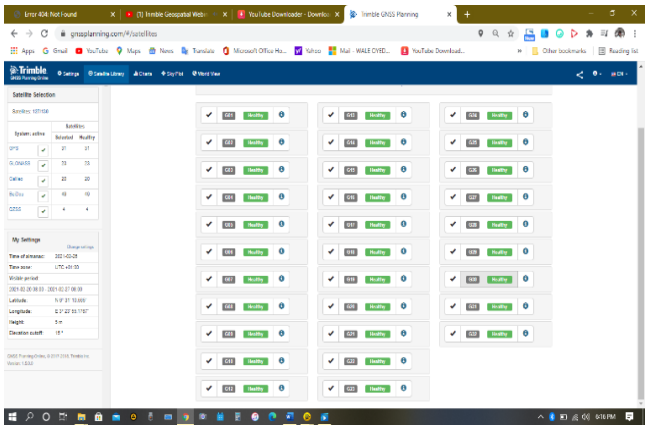

Figure 6. Satellite's Health Status for one of the Observation Days seen in Trimble GNSS Planning Online. (Source: Trimble GNSS online)

2.4. Data acquisition

Based on the expected accuracy standard (1:50,000) for second-order classification, to eliminate noisy data and unhealthy satellites, an hour Static GPS/GNSS positioning technique was applied to be the most accurate method of GPS observations.

To reduce the detrimental effects of atmospheric refraction and multipath signals, a 15° minimum elevation angle for the receiver's antenna was observed to enable a clear sky view for the satellite's microwave signal. Where power-line, metallic objects, trees and fences that could lead to imaging became inevitable, such stations were indicated in the field note. The observation window where the satellite constellation is good was critically observed. PDOP less than 4 (four) was considered. The batteries were fully powered to avoid loss of power.

Having set up and initialized the receiver, the data was acquired for each control station.

2.5. Data processing

Receiver INdependent Exchange(RINEX) Format raw data from NIGNET CORS code-named LGLA (situated in the University of Lagos), Nigerian Institution of Surveyors (NIS) CORS (Lagos branch) both corresponding to the observation epoch and the DGPS receiver were imported into the TBC. The NIS CORS coordinate values given in the geographical coordinate

system was converted to their UTM equivalent using Global Mapper. The raw data were processed and adjusted using the CORS as baseline controls. The TBC uses the Chi-square test to adjust the data until the initial apriori error estimates agree with the adjusted errors for the network vectors. The CORS assigns standard estimated error values to each control point based on its quality. The TBC also determines the root mean square error which evaluates the quality of predictions.

3. Results

Table 2 shows the chi-square test performed on the data at 95% confidence level was successful and the fixed result obtained surpassed the expected second-order accuracy standard (1:50,000) for the control survey.

Table 3 gives the Root Mean Square error of XST347 and CR7 for the referenced CORS while table 4 give the final processed WGS84 zone-31 coordinates.

Table 2. Adjustment Statistics

Operation	Result
Number of Iterations for Successful Adjustment:	**3**
Network Reference Factor:	1.00
Chi-Square Test (95%):	Passed
Precision Confidence Level:	95%
Degrees of Freedom:	368
Post Processed Vector Statistics	
Reference Factor:	1.00
Redundancy Number:	368.00
A Priori Scalar:	2.62
Fixed	0.000001(Meter)

Table 3. Processing summary for two points from two baselines

Observation	Solution Type	RMS	Distance
LGLA- CR7	Fixed	0.0150	704.43660
LGLA - X347	Fixed	0.0107	889.65660
NIS CORS-CR7	Fixed	0.0284	12054.7301
NIS CORS- XST347	Fixed	0.0288	12283.5743

Table 4. Eight of the Final processed Points WGS84 zone 31 coordinate list

Station	Eastings(X_1)	Northings(Y_1)	Height(Z_1)
CR 7	543303.42167	720160.24663	3.39415
XST347	543236.44025	719895.00637	4.79219
GME 17/04	544062.90674	720527.94721	5.97133
GME 03	543939.76545	720408.73090	7.52536
PGD 21/13	543545.36986	720566.01726	6.35497
UNILAG 001	544473.83120	720456.66867	1.51893
YTT 28/186	542622.77768	720383.12109	6.40460

4. Discussion

Ninety-one per cent of the observed controls were used for analyzing the data. The criteria are the presence of existing coordinates and stable conditions. Determining the correlation coefficient (r), equation 1 was applied between the existing variables, *x* (X_1, Y_1, Z_1) and the newly acquired variables, *y*(X_o, Y_o, Z_o). Table 5 gives a very high linear relationship between *x* and *y*.

$$r = \frac{n(\Sigma xy)-(\Sigma x)(\Sigma y)}{\sqrt{\{n\Sigma x^2-(\Sigma x)^2\}\{n\Sigma y^2-(\Sigma y)^2\}}} \qquad \text{Equation 1}$$

Table 5. The Correlation coefficient between *x* and *y*

	New Easting	Existing Easting
New Easting	1	
Existing Easting	0.999985879	1
	New Northing	**Existing Northing**
New Northing	1	
Existing Northing	0.999993	1
	New Elevation	**Existing Elevation**
New Elevation	1	
Existing Elevation	0.998153	1

Determining the *x* horizontal points geometry vector deviation distance, *S* using *y* data as standard, equation 2 was applied. The maximum displaced point at PGD84/2 with 22.6201m(outlier) and the least displaced, PGD21/13 with 0.0825m. In the vertical point data, MEGA10 has the least difference with 0.01120m higher than the newly observed height while CR6 is with the highest difference of -0.28274m. Fig. 7 shows the corresponding difference between (X_1, Y_1, Z_1) and (X_o, Y_o, Z_o).

$$S = \sqrt{\Delta E^2 + \Delta N^2} \qquad (2)$$

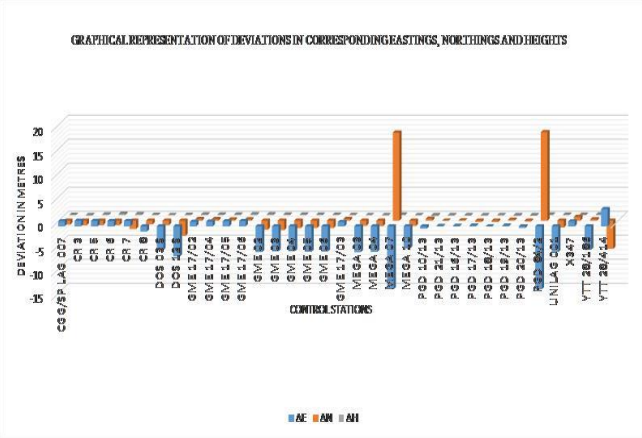

Figure 7. Chart Depicting the Difference between Two Corresponding Eastings, Northings and Heights

With a two-sample t-test for means of (X_o, X_1), (Y_o, Y_1) and (Z_o, Z_1), equation 3 was used to produce the $p-value$ based on the $t-distribution$.

$$T - Statistic = \frac{\bar{x}_i - \bar{y}_i - Hypothesized\ difference}{SE_{\bar{x}_i - \bar{y}_i}} \qquad (3)$$

The mean difference between the sample means, $\bar{x}_i - \bar{y}_i$ The Standard error of the difference in the Aspin-Welch unequal-variance t-test for the unequal variance case is:

$$SE_{\bar{x}_1 - \bar{x}_2} = \sqrt{\frac{s_1^2}{n_1} + \frac{s_2^2}{n_2}} \qquad (4)$$

n_1 *and* n_2 are the assumed sample sizes for groups *x* and *y*.

H_0: $\bar{x}_i - \bar{y}_i$ = Hypothesized Difference

Since the Hypothesized difference is zero, the t-Statistic formula reduces to:

$$T - Statistic = \frac{\bar{x}_i - \bar{y}_i}{SE_{\bar{x}_i - \bar{y}_i}} \quad (5)$$

For the unequal variance case:

$$df = \frac{\left(\frac{S_1^2}{n_1} + \frac{S_2^2}{n_2}\right)^2}{\frac{\left(\frac{S_1^2}{n_1}\right)^2}{n_1 - 1} + \frac{\left(\frac{S_2^2}{n_2}\right)^2}{n_2 - 1}} \quad (6)$$

Table 6 present the result summary of the hypothesis calculations. There was a statistically significant difference at 99% confidence level in the horizontal control coordinates but no significant difference between the height data. For the Eastings and Northings, the p-values were smaller (E = 0.002768695 and N = 0.00036642) than the 0.01 p-value. For the Height, the p-value is larger (0.069657705) than the specified 0.01 p-value.

Table 6. Summary of two-sample t-test for means *x* and *y*

	mean	variance	t-stat	t-critical two-tail
X_o	543517.792	296791.317		
X_1	543516.078	296318.464	3.2606253	2.74999565
Y_o	720334.439	58484.4529		
Y_1	720333.773	58499.9592	4.0149979	2.74999565
Z_1	5.54964097	3.78898635		
Z_o	5.58976516	3.73290145	-1.8813701	2.74999565

5. Conclusion

Since there is evidence of significant difference at 99% confidence level for the Eastings and Northings and no significant difference for the height, we infer the rejection of the exiting Eastings/Northings, keep the newly acquired Eastings/Northings and fail to reject the existing height of control coordinates of the University of Lagos.

Acknowledgement

The authors are grateful for the contributions of the Nigerian Institution of Surveyors (NIS), Lagos Chapter and Olalekan Jimoh in providing the CORS Data used. Special thanks to Chukwuma John Okolie for his reviews and helpful feedback which has contributed greatly to improving the quality of this research. Appreciation to Forte-Land International Limited for making their DGPS equipment available for spatial data acquisition.

References

Ayodele, E. G. Okolie, C. J. Ezeigbo, C. U. and Fajemirokun, F. A. (2017). '*Evaluating the Stability and Adequacy of NIGNET for the Definition of Nigerian Geodetic Reference Frame'.* Department of Surveying and Geoinformatics, University of Lagos; Global Geodetic Solution Limited, Unilag Consult, University of Lagos, Vol. 17, No. 1.

Dimal, M. O. Dimal, R. L. and Balicanta L. (2009). *Comparative Analysis of GPS Azimuth and Derived Azimuth for the Establishment of Project Controls.* 7th FIG Regional Conference. Hanoi, Vietnam.

Iyoyojie, H. A. (2014). '*Re-coordination of Survey Controls within the University of Lagos using total station and digital level'.*

John A. Dulton (2020). 'The Nature of Geographic Information'. e-education Institute, College of Earth and Natural Science, the Pennsylvania University.

John, D. B. (1984). '*Standards and Specifications for Geodetic Control Networks'.* Federal Geodetic Control Committee; Rockville, Maryland

Joshua, S. Jennifer, M. S. and Raechel, A. B. (2012). '*Mapping of our changing World'*. Department of Geography, the Pennsylvania University.

Mikael, L., Rob. S. Volker, S. (2010). '*GNSS CORS - Reference Frames and Services*', Geodetic Research Division, Lantmäteriet,

Nwilo, P. C. (2021). '*Establishment of National GNSS Network in Nigeria'* ggim.un.org

Owodunni, O. A. (2015). '*Re-coordination of Survey Controls using Total Station and Digital level within the University of Lagos*'.

Ovstedal O. (2002). *'Absolute Positioning with Single-Frequency GPS Receivers'.* Department of Mapping Sciences, Agricultural University of Norway

Rietdorf, A. Daub, C. and Loef, P. (2006); *Precise Positioning in Real-Time using Navigation Satellite and Telecommunication*

Schofield W. and Breach M., (2007); '*Engineering Surveying, 6th edition'*: Elsevier Publishers Ltd, U.K.

Sickle J. V. John A. D. (2020). '*GPS and GNSS for Geospatial Professionals*'. e-education Institute, College of Earth and Natural Science, the Pennsylvania University. Wanninger and Lambert (2018). '*Introduction to Network RTK'.*

Intercontinental Geoinformation Days

igd.mersin.edu.tr

Establishment of a geodetic network for deformation monitoring of the third mainland bridge, Lagos Nigeria

Samuel O. Akintoye, Hamed O. Olanrewaju*, Hannah O. Abioye Chukwuma J. Okolie Samuel A. Akinnusi Usman O. Adegbite

University of Lagos, Faculty of Engineering, Department of Surveying and Geoinformatics, Lagos, Nigeria

Keywords
Third Mainland Bridge
GNSS Survey
Deformation Monitoring
Geodetic Network
Bridge Collapse

ABSTRACT

There have been several cases of bridge collapse all over the world leading to loss of lives and valuable infrastructure. Such incidents can be averted if bridges are properly monitored through deformation surveys. This study aims at establishing a geodetic network for deformation monitoring of the Third Mainland Bridge in Lagos State, Nigeria. High precision Global Navigation Satellite System (GNSS) surveys were deployed for the observation. Points in the network were established by simultaneous redundant observation from three existing first order controls (XST series) in static mode. The raw field data was subjected to least squares adjustment and the redundant observations were reduced to give the three-dimensional (3D) coordinates of the points that make up the network. With this network in place, the positional integrity of the bridge can be continuously monitored.

1. Introduction

The provision and maintenance of a secure and reliable highway network is a constant challenge for transportation authorities. Bridges are not only an essential component of the network, but they are also expensive investments. To protect this investment, transportation authorities must fully comprehend the condition and actions of bridge systems in order for the bridge to remain accessible to traffic, weather-resistant, and unperturbed by millions of loadings cycles each year – all while incurring minimal maintenance costs (Van Cranenbroeck, 2007). High cost of maintenance compounded with budget-driven policies often contributes to the postponement of routine bridge repairs. These lapses can lead to the occurrence of a bridge collapse, which is unacceptably dangerous.

The Third Mainland bridge has had haphazard repairs since its inception. The Nigerian Federal Government announced in August 2018 that the bridge will be temporarily closed for four days to allow for investigative maintenance testing. The government declared in July 2020 that the bridge will be closed for six months to begin repair works. Construction was to take place in two stages, with each carriageway taking three months to complete. As part of ongoing reconstruction work, the Federal Government declared in early January that the Lagos Island-bound traffic on the Third Mainland Bridge would be closed for two weeks beginning on Wednesday, January 13, 2021 (Construction Review Online, 2021).

There are several methods for monitoring the structural integrity of bridges to prevent or reduce hazards such as bridge deformation, bridge failures or collapses. For decades, Surveyors, Geodesists and Engineers have relied on the establishment of geodetic control networks for bridge monitoring. Having multiple control stations in the reference network is critical for improving the reliability of deformation surveys, and for investigating the stability of reference monuments over time (Alademomi et al., 2020).

Given the foregoing, this study aims to establish a geodetic control network for the deformation monitoring of the Third Mainland Bridge in Lagos State Nigeria. Following established procedures, the geodetic network was designed. The three-dimensional coordinates (3D) of the reference stations and monitoring stations were determined using differential Global Navigation Satellite System (GNSS) surveys.

The establishment of such a network is imperative in the setting up of a structural health monitoring (SHM) scheme for the bridge. The findings of this study can facilitate the attainment of sustainable development goal (SDGs) No. 9 (Industry, Innovation and Infrastructure) and No. 11 (Sustainable cities and communities) in Nigeria and Africa.

* **Corresponding Author**

*(hmddgreat@gmail.com) ORCID ID 0000-0002-4423-332X

Cite this study

Akintoye S O, Olanrewaju H O, Abioye H O, Okolie C J, Akinnusi S A, Adegbite U O (2021). Establishment of a geodetic network for the deformation monitoring of the third mainland bridge. 3rd Intercontinental Geoinformation Days (IGD), 66-69, Mersin, Turkey

2. Methods

2.1. Study area

The Third Mainland Bridge is the longest of three bridges connecting Lagos Island to the mainland; the others are the Carter Bridge and the Eko Bridge. The Third Mainland Bridge was the longest bridge in Africa until 1996 when the 6th October Bridge located in Cairo was completed. The former starts from Oworonshoki which is linked to the Apapa-Oshodi expressway and Lagos-Ibadan expressway, and ends at the Adeniji Adele Interchange on Lagos Island. The bridge was built by Julius Berger Nigeria PLC. The phase one of the project was commissioned by President Shehu Shagari in 1980 and completed by President Ibrahim Babangida in 1990; it measures about 11.8 km in length (Construction Review Online, 2020; The Guardian News, 2020).

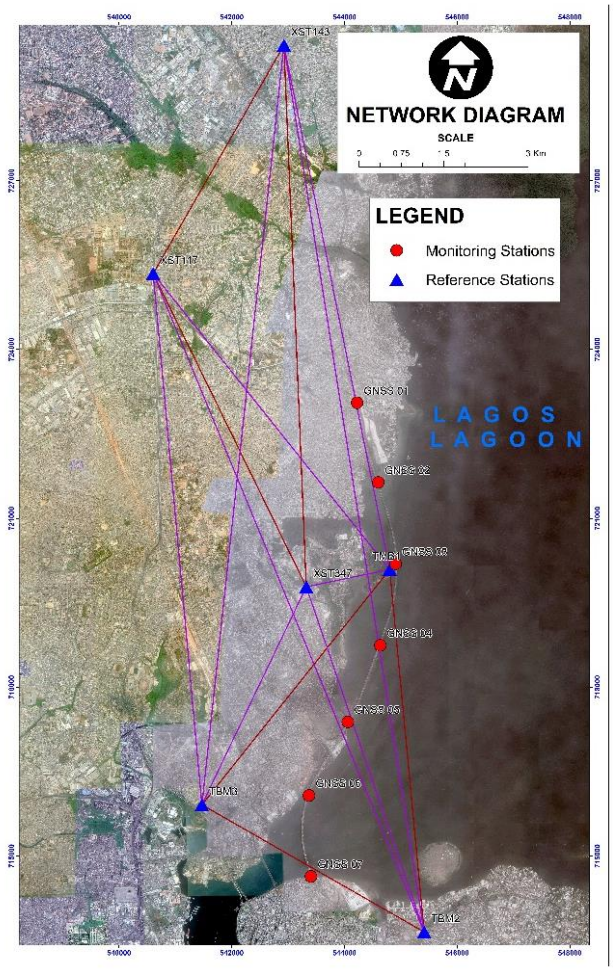

Figure 1. Network Diagram

2.2. Project planning and network design

A preliminary reconnaissance was done with the aid of Google Earth (GE) imagery and site visits. Analysis of the GE imagery enabled a holistic perspective of the survey area and provided insights such as: possible locations for establishment/monumentation of reference stations and monitoring stations, and approximate spacing between monitoring stations. Additional insights were gained during site visits such as: suitable times for field observations, stability of proposed monumentation locations, and likely human and vehicular interferences.

The network was designed with a good geometry, near-uniform spacing between monitoring stations (approx. 1.5km), well distributed reference stations and monitoring stations which span the entire length of the bridge.

2.3. GNSS observation

The 3D coordinates of the reference stations and monitoring stations were determined using 10 GPS dual frequency differential Global Positioning System (GPS) receivers and accessories. The observation was done using the following GPS equipment: UniStrong G970II Pro and Stonex S900A. The control points were referenced to Minna datum (UTM Zone 31N).

Three first order control points - XST347, XST143, and XST117 (Table 1) established by the Office of the Surveyor General, Lagos State were used as the starting points for coordination of the reference stations and monitoring stations. The UTM coordinates of the reference stations (TMB01, TMB02, and TMB03) were determined by taking simultaneous observations relative to the 1st order controls in static mode with an occupation time of 2 hours for each station. Subsequently, simultaneous observations were carried out on the monitoring stations. Three differential GPS were set on the reference stations and seven on the monitoring stations. Observations were taken for a period of one hour in static mode at each monitoring station to form the deformation monitoring baseline data.

Table 1. Coordinates of the Stations

Station	Eastıng (m)	Northing (m)	Height
XST 117	538760.513	725413.102	29.079
XST 143	542923.610	729471.575	13.072
XST 347	543241.676	719895.816	4.701

2.4 Data processing and network adjustment

The Trimble Business Centre software environment was used to post-process the GNSS data. The coordinate system of the post-processing operation was set to UTM 31N based on the WGS84 ellipsoid. For the baseline processing of the observation set, the existing coordinates of the base station were keyed in, and the post-processed coordinates were generated as the software was configured to repeatedly compute the baselines in the network.

After the adjustment, the results were subjected to statistical testing using the Trimble Business Centre. This was accomplished by comparing the observation's a priori standard deviation against its residual using a goodness-of-fit ($\chi 2$). Other tests include: blunder detection, variance of the unit weight, quality assurance test, repeated vector analysis test, tau test and observation residuals test. The goodness-of-fit test results for control network and monitoring points on the right and left of the bridge, respectively appear to follow the normal distribution and the sizes of their residuals indicated that the data appear to be consistent. The

blunder was used to detect problems associated with the adjustment. The tools assist in determining if blunders exist in any of the observations used in the adjustment, or if any problems exist in the network construction that would hamper the ability for an adjustment to be performed. The results in both the establishment of the control points and monitoring station on the bridge indicated that the observations were free of blunders.

For proper adjustment of an entire dataset of observations, the connectivity between all sections of the dataset was made and the results determined that there were no subsets of the data set that are not connected by observations. The Variance of Unit Weight and the Standard Error of Unit Weight monitored the relationship between the uncertainties assigned with the observations and the magnitude of the change required to each observation (residuals) in the adjustment. Changes to the observations were small and were significantly greater than the uncertainties associated with the observations. The Variance of Unit Weight and Standard Error of Unit Weight gauged the magnitude of the observation changes (residuals) compared to the observation uncertainties for the entire network. Analyzing the magnitude of the computed Variance of Unit Weight and Standard Error of Unit Weight revealed that the changes to the observations (residuals)were within expected levels.

In the least-squares adjustment, small corrections were applied to the observations to obtain the best fit of all observations producing one solution for all points. These results indicated that the results were free of blunders because in both cases the residuals were small and even negligible in some cases. In addition, the resulting differences between repeat observations were compared to the user-defined accuracy specification. The results for all campaigns portrayed that difference between the repeated observations of a vector were smaller than the allowable error computed from the accuracy specification. The achievable accuracy in GPS measurements for deformation monitoring is between 0.1 – 2 ppm (part per million).

3. Results

The results of the processed observations are shown in Table 1 and Table 2. Table 1 shows the 3D coordinates of the reference ponts. Table 2 shows the 3D coordinates of the monitoring stations.

Figure 1 shows the final network diagram obtained from Trimble Business Centre showing the connectivity from each of the reference stations to the monitoring stations.

Table 2. Coordinates of the reference stations

Station	Easting (mE)	Northing (mN)	Height (m)
TMB1	544802.127	720089.740	1.526
TMB2	545414.493	713648.646	2.399
TMB3	541469.552	715908.690	1.910

Table 3. Coordinates of monitoring stations

Station	Easting (mE)	Northing (mN)	Height (m)
GNSS1	544217.625	723064.482	4.372
GNSS2	544692.683	721336.426	7.019
GNSS3	544899.132	720194.732	6.417
GNSS4	544235.308	717681.752	1.012
GNSS5	544064.787	717413.401	1.879
GNSS6	543431.590	716241.792	3.285
GNSS7	543408.300	714638.715	2.421

4. Discussion

This monitoring baseline is such that the subsequent epochs observations will be compared with them to ascertain any displacement. Following the determination of the coordinates, the equation that can be adopted for calculating deformation is given by Handayani and Taufik (2015):

$$dp = r'p - rp = dp(Xp, Yp, Zp; t) \quad \ldots\ldots\ldots\ldots\ldots\ldots\ldots\ldots (1)$$

Where;
rp = position of particle p at time $t = 0$ (before deformation);
in this study expressed as the mean position,
r'p = position after deformation at $t > 0$

5. Conclusion

In this study, we established a geodetic network for deformation monitoring of the Third Mainland Bridge. The reference and monitoring stations can be used to assess the bridge's deformation for the first epoch which is expected to take place in 2021. An active monitoring scheme should be set up for the Third mainland bridge to ensure its structural integrity and serve as an early warning system so that catastrophic loss of life and infrastructure due to bridge collapse, which could have been avoided if a monitoring system was put in place would not occur.

Acknowledgements

The authors wish to acknowledge the contributions of Oduyebo Mumiyebo, Akinsullie Maryam, Jinadu Azeez, Tomisona Isijola and Oludolabo Oludemilade during the data acquisition phase of the study.

References

Van Cranenbroeck, J. (2007). Innovation and experience in GNSS bridge real time SD-monitoring system. *Bridge Design, Construction and Maintenance - Proceedings of the Two-Day International Conference Organised by the Institution of Civil Engineers, ICE*, 507–515. https://doi.org/10.1680/bdcam.35935.0055

Handayani, H. H., & Taufik, M. (2015). Preliminary study of bridge deformation monitoring using GPS and CRP (case study: Suramadu Bridge). Procedia Environmental Sciences, 24(2015), 266–276. https://doi.org/10.1016/j.proenv.2015.03.035

NO GOING BACK ON CLOSURE OF THIRD MAINLAND

BRIDGE a FG.. (2020) *>The Free Library.* (2014). Retrieved Nov 01 2021 from https://www.thefreelibrary.com/NO+GOING+BACK+ON+CLOSURE+OF+THIRD+MAINLAND+BRIDGE+a+FG.-a0628852564

THE THRID MAINLAND BRIDGE MAY COLLAPSE (2020). Sun News Online. Retrieved Nov 01 2021 from https://www.sunnewsonline.com/third-mainland-bridge-may-collapse-if/

"Nigeria: Phase 1 construction of Third Mainland Bridge on Schedule" (2020). Construction Review Online. Retrieved 28 December 2020.

"'Third Mainland Bridge structurally stable, maintenance to avert rigidity'"(2020). The Guardian Nigeria News - Nigeria and World News. Retrieved 28 December 2020.

Intercontinental Geoinformation Days

igd.mersin.edu.tr

Suitability analysis of solid waste dumpsites in Igabi LGA, Kaduna State

Atta Kaka Zenabu*[1], Stephen Dauda Yabo[1], Muhammed Nura [1]

[1]*Ahmadu Bello University, Environmental Design, Geomatics, Zaria Kaduna, Nigeria*

Keywords
Suitability Analysis
Environmental
Management
Dumpsite
Healthy living

ABSTRACT

Efficient management of solid waste is one problem that environmentalists, health workers, and city planners face in Nigeria. This problem caused by the generation of over 80 million kilograms of solid waste per day requires adequate and modern facilities to guarantee a healthy environment. So far, there is no efficient system to manage the existing refuse dump in Igabi LGA. Residents in the area are attacked by disease and unhealthy conditions. Large quantities of waste materials are being disposed of and burnt without collection thereby creating pollution and environmental uncertainties. That is why this study seeks to evaluate the suitability of the study location for the sitting of a landfill in the area. From the analysis carried out in this project, it shows that a total area of 95.3015km^2 is unsuitable, 39.4806km^2 is least suitable, 9.7741km^2 is moderately suitable and 1.6364km^2 is highly suitable. All the dumpsites identified within the study area fall under unsuitable areas. Therefore, it is recommended that they should be moved to highly suitable places.

1. Introduction

The rapid growth of population increases the non-renewable resources and disposal of effluent and toxic waste indiscriminately, are the major environmental issues posing threats to the existence of humans (Allen, 1997). The most common problems associated with improper management of solid waste include diseases transmission, fire hazards, odor nuisance, atmospheric and water pollution, aesthetic nuisance, and economic losses (Jilani, 2012).

There has been a significant increase in solid waste generation in Kaduna over the years from 100gm per person per day in small towns to 500grams per person per day in large towns. Presently most of the municipal solid waste in Kaduna is being disposed of unscientifically (KEPA, 2019).

Generally, municipal solid waste is collected and deposited in a sanitary landfill, such unscientific disposal attracts birds, rodents, and fleas to the waste dumping site and creates unhygienic conditions. The degradation of the solid waste results in the emission of carbon dioxide (CO2), methane (CH4), and other trace gases. The unscientific landfill may reduce the quality of the drinking water and causes disease like jaundice, nausea, asthma (Busu, 2010)

The present study intends to find out a suitable site for the disposal of solid waste generated from Igabi LGA municipality and surrounding areas with the help of GIS techniques.

2. Method

The methods used in this work are shown in Figure 1. Each of these criteria is generated as a layer in the GIS Environment (ArcGIS 10.4.1) using a number of data acquired from different sources. The information compiled from the literature (EPA, 2006) about the safe distance to a dump site was used to determine the buffer zones and varying degrees of suitability within each layer.

3. Results

3.1 Mapping of existing solid waste dumpsites

To achieve the first objective of this project, coordinates of the existing dumpsites were collected using hand-held Garmin GPS. The obtained coordinates were used to create a geodatabase for solid waste dumpsites in the study area. The Study area base map was digitized from the SAS planet satellite imagery. A total of 41 dumpsites were identified within the study area. The coordinates of the existing dumpsites obtained from fieldwork were keyed into the Microsoft excel 2013 software and imported into the ArcGIS software as an excel file then converted to shapefile to show the location of the dumpsites, and to present a Geo-database map for the dumpsites within the study area. Figure 2 below

* **Corresponding Author**

*(kakaattaz@gmail.com) ORCID ID 0000 – 0003 – 0672 – 4862
(stephenyabo@gmail.com) ORCID ID 0000 – 0003 – 0955 – 3608

Cite this study

Atta K Z, Nura M & Yabo S D (2021). Suitability analysis of solid waste dumpsites in Igabi lga, Kaduna State. 3rd Intercontinental Geoinformation Days (IGD), 70-73, Mersin, Turkey

shows the geo-database map of the existing dumpsites within the study area.

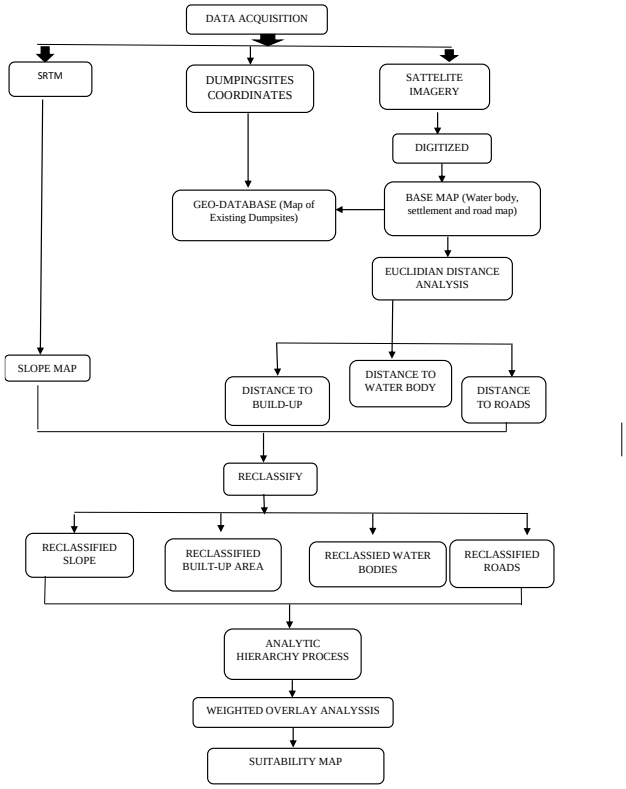

Figure 1: workflow diagram illustrating the steps adopted for the project**. Source: (**Author, 2019)

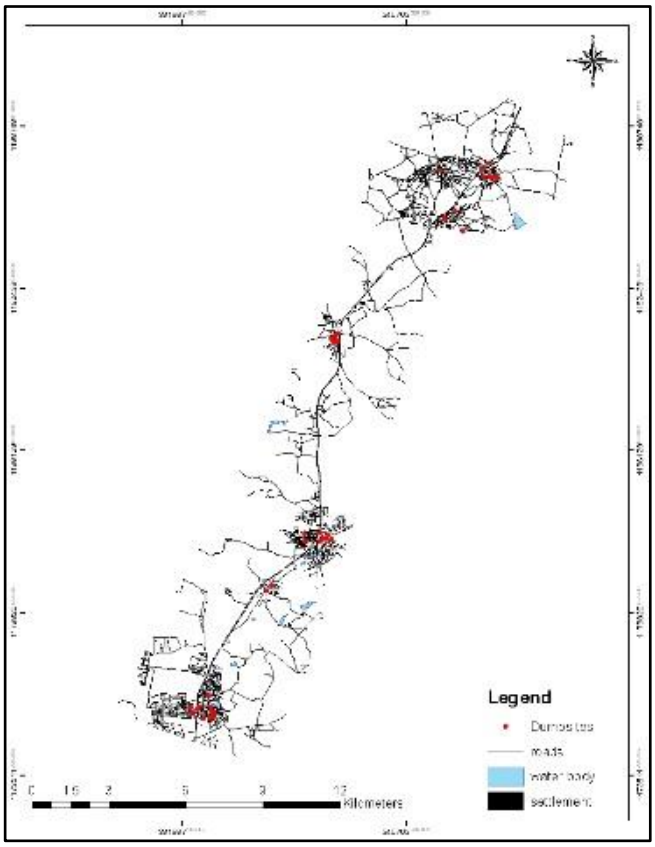

Figure 2. Showing the spatial location of the existing dumpsites

All the dumpsites identified within the study area, are located at unsuitable places. Table 1 & 2 below shows the minimum distance required for the dumping of solid waste according to the Environmental Protection Agency, 2006.

Table 1. Showing constraints criteria **Source:** (EPA, 2006)

S/N	Criteria	Unsuitable area
1	Distance to water body	Less than 160m
2	Slope	Area with slope greater than 15°
3	Distance to settlement	Less than 300m
4	Distance to roads	Less than 100m

Table 2. Showing factors criteria **Source**: (EPA Landfill manual 2006)

S/N	Criteria	Least suitable	Moderately suitable	Highly suitable
1	Distance to water body	160m – 480m	480m– 960m	>960m
2	Slope	10°- 15°	5°- 10°	0°- 5°
3	Distance to roads	100m-1000m	1000m–2000m	>2000m
4	Distance to settlement	300m – 500m	500m– 800m	>8000m
5	Soil	-	Alisols	Nitisols

3.1.1 Euclidean distance result

The Euclidean distance output raster contains the measured distance from every cell to the nearest source. The distances are measured as the crow flies (Euclidean distance) in the projection units of the raster, in meters and are computed from cell to cell. Below in figure 3. shows the results of the Euclidean distance result for the settlement, road network, and waterbody respectively with respect to the proposed dumpsite.

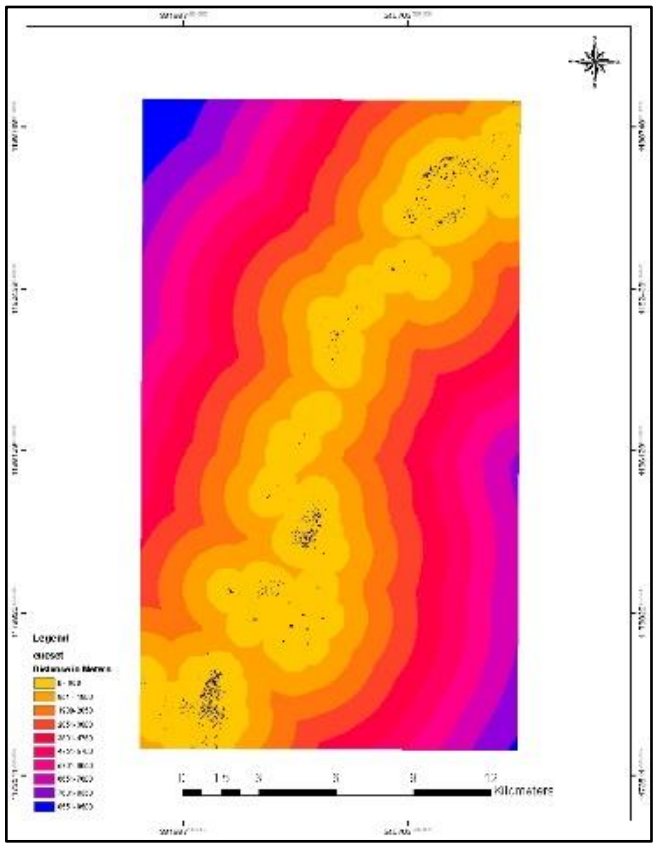

Figure 3. Euclidean distance analysis for settlement map

3.1.2 Reclassification of result

To create a single ranked map of potential areas to site solid waste dumpsite the value of classes between layers are compared by assigning numeric values to classes within each map layer. It is called reclassification. Having all measures on the same numeric scale gives them equal importance in determining the most suitable locations, hence all data map layers will be reclassified into new numeric values scoring as 10 to 1 (MC, 2011). The scores of 10 to 1 are used to identify the differences among areas of suitability. The slope dataset is reclassified at a score of 1 to 10 in order of priority (i.e. the lesser the slope the more suitable the area). Figures 4 and 5 show the reclassified datasets

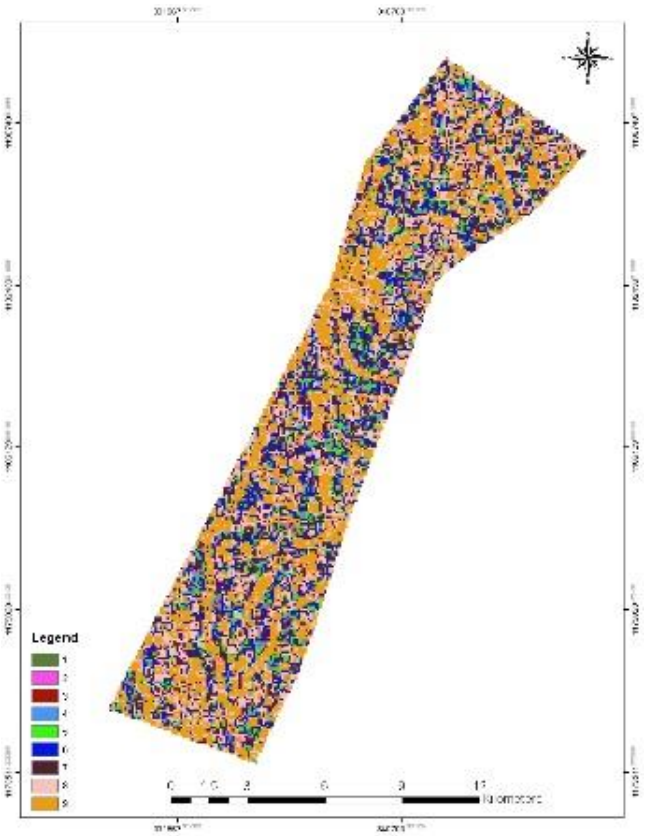

Figure 4. A map showing reclassified slope

3.1.3 Analytic Hierarchy Process (AHP)

The Analytic Hierarchy Process (AHP) is a structured technique for organizing and analyzing complex decisions, based on mathematics and psychology. It represents the most accurate approach for quantifying the weights of criteria (Saaty, 2000). The magnitude of each factor was estimated through pair-wise comparisons. After all pair-wise comparisons are formed, the vector weights are calculated based on Saaty's eigenvector method. Then, this eigenvector is normalized and then the weights and consistency ratio are computed.

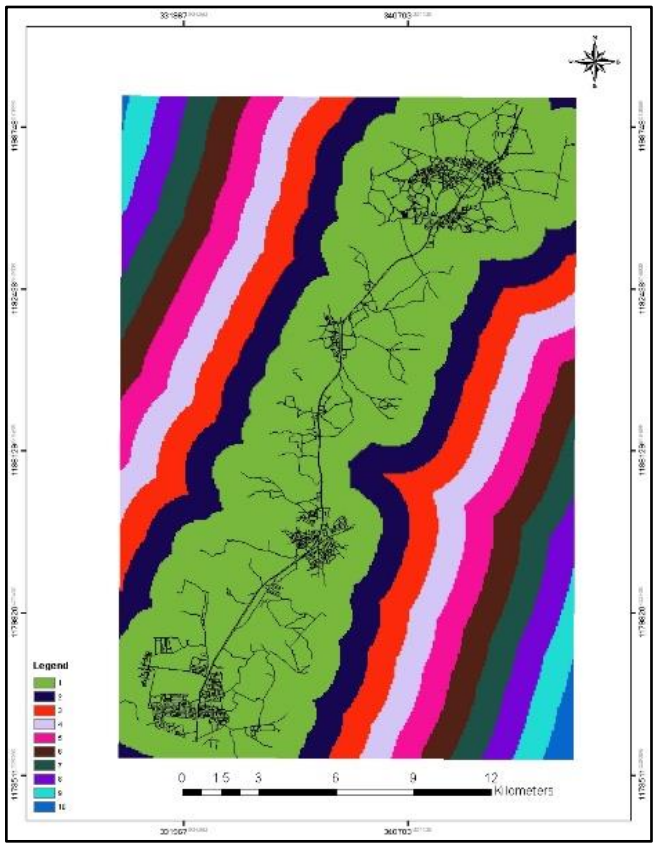

Figure 5. A map showing reclassified road networks

Table 3. pair-wise comparison of the criteria

S/N	Settlement	Water	Road	Slope
Settlement	1.00	2.00	6.00	9.00
Water	0.50	1.00	3.00	7.00
Road	0.17	0.33	1.00	3.00
Slope	0.11	0.14	0.33	1.00

Table 4. Shows the normalized matrix

S/N	Settlement	Water	Road	Slope	Eigenvector weights
Settlement	0.56	0.58	0.58	0.45	0.54
Water	0.28	0.29	0.29	0.35	0.30
Road	0.10	0.10	0.10	0.15	0.11
Slope	0.06	0.04	0.03	0.05	0.05
Total	1	1	1	1	1
Consistency ratio	1.6%				

3.1.4 Weighted overlay result

The final suitability map for locating solid waste is effected with the weighted overlay tool for each map layer using the weights computed from the AHP method. Then finally, all data map layer is ready to be overlaid by using the weighted overlay method to create a single rank map of suitability analyses, five rasters are ranked for developing suitability on a map of 1 to 10. And the weighted overlay results are further reclassified to a scale of 1 to 4 the result from figure 6 shows the area that is not suitable depicted as white, areas that are least suitable depicted as red, areas that are moderately suitable depicted as brown, and areas that are highly suitable depicted as green.

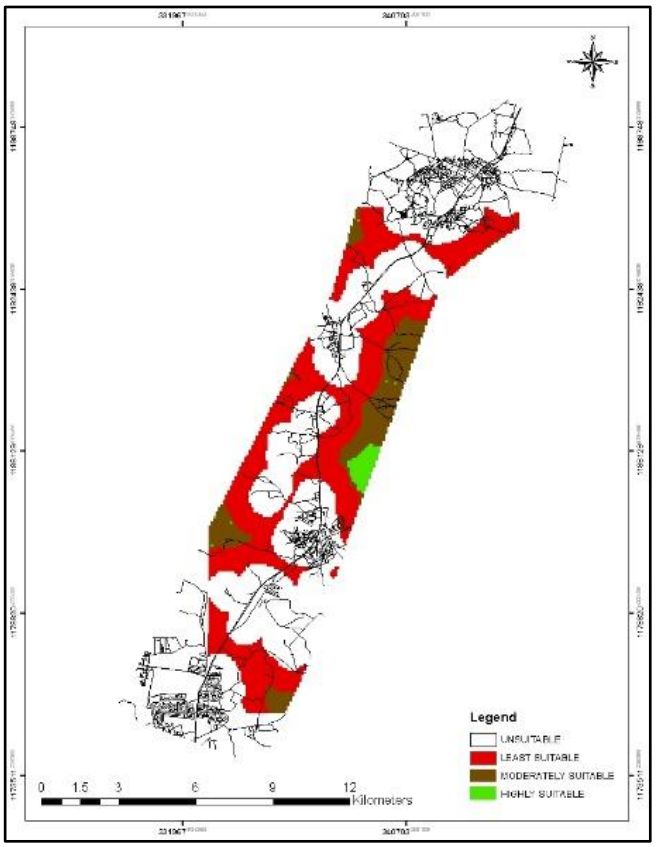

Figure 6. Suitability Map of Solid Waste Dumpsites

From the above analysis, it shows that an estimated total area of 95.3015km^2 is unsuitable, 39.4806km^2 is least suitable, 9.7741km^2 is moderately suitable and 1.6364km^2 is highly suitable.

4. Discussion

The project has shown the capability of GIS in capturing, storing, processing, and analyzing spatial data as well as creating a spatial database for solid waste dumpsites in Igabi LGA. Datasets for the work include road network, elevation, and Land use of study area, existing solid waste dumpsites, and water body within the study area. The coordinates of the existing dumpsites were captured with the handheld GPS and entered into an excel spreadsheet and exported to ArcGIS 10.4.1. Spatial analyses were carried out which include slope, Euclidean distance, reclassification, and weighted overlay analyses in other to actualize the aim and objectives of the study. The criteria as related to the siting of a solid waste dumpsite according to the environmental protection agency.

5. Conclusion

The aim and objectives of this project have been achieved through the acquisition of the necessary dataset and the implementation of spatial analysis. The strength of this work lies in its simplicity, flexibility, and user-friendliness. The increase in commercial, residential, and infrastructural development due to the rapid increase in population growth in Igabi LGA, is directly affecting the amount of waste generation in that area. This study will serve as a catalyst in that area for the proper management of dumpsites in that area.

Acknowledgement

Acknowledgments of support for the project/paper/author are welcome.

References

Allen AR, D. (1997). *Approach to Landfill Site Selection in Ireland. Engineering geology and environmental.*

Busu, A. (2010). Selection of Landfill Sites for Solid Waste Treatment in Damaturce Town using GIS Techniques.

Jilani, T. (2012). *State of Solid Waste Management in Khulna City.* Khulna University. Khulna: Unpublished Undergraduate Thesis.

KEPA. (2019). *Solid Waste Management*. Retrieved from: www.kepa.org.ng

Wikipedia. (2019). *What is GPS*. Retrieved from: www.wikipedia.com

Intercontinental Geoinformation Days

igd.mersin.edu.tr

Comparative analysis of pedestrian stride length estimation methods

Nimet Karagöz[*1], **Fatih Gülgen** [1]

[1]*Yildiz Technical University, Faculty of Civil Engineering, Department of Geomatics Engineering, Istanbul, Turkey*

Keywords
Pedestrian navigation
Stride length estimation
Microelectromechanical system
Inertial sensors

ABSTRACT

The stride length estimation is a crucial step used in indoor and outdoor pedestrian navigation. The accuracy of the navigation process depends on how accurately the average stride length is calculated. The stride length estimation methods use some parameters such as step frequency, acceleration, and pedestrian height. These parameters are applied to different datasets containing various movements of pedestrians, such as running and walking. However, the limited datasets used in academic studies preclude scientific comparability in the literature. This study compares ten stride length estimation methods using the open-source datasets created by Wang and analyzes their accuracy. The case results show that Weinberg's approach was quite successful for navigation dynamics.

1. Introduction

In recent years, pedestrian navigation has gained popularity with the increase in the population living in complex and big cities and constructing substantial complex structures with developing engineering technologies (Zhang et al. 2018; Walchko 2002). It is sufficient for the accuracies to be in the order of kilometers for widely used vehicle navigation; the accuracy decreases to the level of meters for pedestrian navigation (Karimi, 2015). The fact that the designed pedestrian navigation applications have accuracy at the meter level is crucial for the pedestrians who do not have high mapping skills to follow the direction (May, 2003). In terms of simplicity and ease of use, virtual reality and augmented reality technologies are used in pedestrian navigation applications so that pedestrians can find their way easier with the help of visual and auditory tools (Dias et al., 2015). Global Navigation Satellite Systems (GNSS) are sufficient today, outdoors, in open areas to ensure enough accuracy. GNSS alone is insufficient in indoor or outdoor areas but areas surrounded by trees or high-rise buildings. For example, inertial measurement unit (IMU) sensors working with GNSS affect the accuracy positively (Kim et al., 2004; Kang et al., 2018). In addition, algorithms such as Kalman filter, extended Kalman filter, artificial intelligence are used in indoor pedestrian navigation to increase accuracy (Ladetto et al., 2001).

Pedestrian stride length estimation (SLE) accuracy, which is one of the primary stages of pedestrian navigation, has critical importance not only in the field of navigation but also in many fields such as medicine, the military, the study of human behavior, and sports (Ladetto et al., 2002; Rampp et al., 2014; Rasouli et al., 2017; Díez et al., 2018; Zeng et al., 2018). Studies in each area need to meet different expectations. In this context, there are various studies in which step lengths are for pedestrians such as running, fastly, or slowly walking (Shin et al., 2007; Martinelli et al., 2017). They use many technologies such as cameras, GNSS, IMU, and microelectromechanical system (MEMS) sensors in smartphones for stride length (SL) calculation (Kang et al., 2018; Wang et al., 2019).

On the other hand, since the datasets used in the studies were not open source and were not produced to a certain standard in terms of pedestrian behavior, technologies, and accuracy, SL calculation methods could not be adequately compared and analyzed (Ho et al., 2016; Xing et al., 2017). Wang et al. (2019) used an open-source dataset containing different pedestrian behaviors (Wang et al., 2019). This study compared the results obtained using ten other SL calculation methods.

* **Corresponding Author**

*(nmtkrgz@gmail.com) ORCID ID 0000 – 0002 – 6563 – 8393
(fgulgen@yildiz.edu.tr) ORCID ID 0000 – 0002 – 8754 – 9017

Cite this study

Karagöz N & Gülgen F (2021). Comparative analysis of pedestrian stride length methods. 3rd Intercontinental Geoinformation Days (IGD), 74-77, Mersin, Turkey

2. Method

2.1. Dataset and data preprocessing

The data collected with the Huawei Mate 9 smartphone with an octa-core 2.4 GHz processor includes sensor data in a 3D accelerometer, gyroscope, and magnetometer. The data collection frequency of the sensors is 100 Hz. The data includes step number, step length, total distance traveled, and time. The pedestrians are a total of five people, two women and three men. Their weight is between 45-80 kg, their age is between 23-32, and their height is 152-196 cm. Pedestrians carried the smartphone in their right hand at chest level with the screen parallel to the ground. Office, shopping mall, metro station, underground parking lot, street and pedestrian path are used as spaces. Running, walking, jumping, and taking the elevator were selected as pedestrian behaviors. An average of 122 pieces of data was recorded at each step. Less than 200 data was recorded in 99% of the steps.

Before applying the SLE methods, necessary unit transformations in the datasets were made. The effect of gravitational acceleration on the acceleration data is eliminated with the help of the rotation matrix calculated by using the accelerometer and magnetometer data recorded during the stance phase. The first two steps were omitted from all datasets to avoid degradation of data quality. One of the 30 datasets in total was excluded from the scope of the study due to missing data. As one dataset was used as a reference, analyzes of ten methods were performed on the remaining 28 datasets.

2.2. Stride length estimation methods and experiment

Ten SLE methods were evaluated in this study (Table 1). Data such as vertical acceleration, average acceleration, constants, and step frequency were used as parameters in the methods. The methods were implemented using Matlab 2020b software, where matrix calculations such as transformation matrix can be written quickly.

In the software, the time values given in the epoch are expressed in seconds to be compatible with the acceleration data. One of the datasets was selected, and the first data, including the pedestrian stance phase, was accepted as a reference. The smartphone's rotation in the pedestrian's hand was calculated from the acceleration data with the reference. A transformation matrix was generated from the obtained rotation. Each dataset was evaluated using this transformation matrix. The unknown parameters in each method were calculated with the selected reference data. The unknowns were placed in the formula, and the step lengths were calculated for the remaining datasets.

The accuracy of the SL's was calculated by assuming the SL measured by the IMU in each dataset as actual values. Equation 1-3 represents the relative error rate of SL and total walking distance and Root Mean Square Error (RMSE) of SL, respectively.

$$Relative\ Error_{SLE} = \frac{1}{N} \times \sum_{i=1}^{N} \left(\frac{|SL_e^i - SL_t^i|}{SL_t^i} \times 100\right) \quad (1)$$

$$Relative\ Error_{WD} = \frac{|\sum_{i=1}^{N} SL_e^i - \sum_{i=1}^{N} SL_i^t|}{\sum_{i=1}^{N} SL_t^i} \times 100 \quad (2)$$

$$RMSE_{SLE} = \sqrt{\frac{\sum_{i=1}^{N}(SL_e^i - SL_t^i)^2}{N}} \quad (3)$$

To calculate the relative error of the i-th SL, the difference of the calculated stride length (SL_e^i) from the actual stride length (SL_t^i) is calculated, and it is divided by the actual SL, and it must be multiplied by 100, and the result must be divided by the total stride length (N) in the dataset. Similarly, the relative error of the total walking distance is obtained by subtracting the sum of the actual SL's from the sum of the calculated SL's, dividing the result by the total actual SL, and multiplying by 100. RMSE is obtained by dividing the difference of the calculated step lengths from the actual step lengths by the number of steps and taking the square root of the result.

3. Results

Estimated step lengths according to the selected ten different step length methods; (1) When compared with the median value of the actual SL, it was seen that the Weinberg (2002) method had the closest values to the actual value in 11 of 28 datasets. It was the most accurate and sensitive method with 0.001 m from the actual value in one of the datasets. Tian et al. (2015) and Bylemans et al. (2009) results have been followed by Weinberg (2002); the methods that most deviate from the actual median are Ladetto (2000), Zeng (2018), Mikov (2013), and Alvarez (2008).

(2) When the RMSE was analyzed, the standard deviations of Zeng and Ladetto were found to be the smallest, with 0.019 m. Guo, Weinberg, and Bylemans are the best methods after Zeng and Ladetto, respectively. Weinberg's standard deviation was found to be the best in 18 out of 28 data sets. On the other hand, in datasets with more steps, Kim and Ladetto have better standard deviations. (3) It was observed that the relative SL error was the least in Weinberg's method in 16 data sets. It has been determined that Weinberg's method has the best mean relative error among other methods and the slightest error scatter. When the data sets are examined one by one, and the total is analyzed, Mikov's method gave the most error. Considering the absolute and relative error for the total travel distance, it was determined that Mikov's scattering was high, but on the contrary, it had the slightest error in some datasets. The Weinberg method gave better results than the relatively new methods when the absolute and relative total traveled distance errors were examined. Zeng and Alvarez do not give the most successful results in any of the datasets. Successful results were obtained from Kim, Mikov, and Bylemans in datasets which are containing more steps.

Table 1. Information of selected SLE methods

Models Source	SLE Methods	Parameters
Weinberg, 2002	$K \times \sqrt[4]{a_{vmax} - a_{vmin}}$	tunable constant (K), maximum and minimum vertical acceleration (a_{vmax}, a_{vmin})
Ladetto, 2000	$\alpha \cdot f + \beta \cdot v + \gamma$	coefficients (α, β, γ), walking frequency (f), the variance of acceleration (v)
Kim et al., 2004	$K \times \sqrt[3]{\sum_{i=1}^{N} \frac{\lvert a_i \rvert}{N}}$	coefficient (K), mean acceleration (a_i), number of the sample (N)
Scarlett, 2007	$K \times \frac{\sum_{i=1}^{N} \frac{\lvert a_i \rvert}{N} - a_{min}}{a_{max} - a_{min}}$	coefficient (K), mean acceleration (a_i), maximum and minimum vertical acceleration (a_{max}, a_{min})
Alvarez et al., 2008	$K_1 \cdot F + K_2$	tunable constants (K_1, K_2), step frequency (F)
Bylemans et al., 2009	$0.1 \sqrt[2.7]{a_{avg,abs} \sqrt{K \sqrt{\frac{F}{a_v}}}}$	tunable constant (K), step frequency (F), average absolute vertical acceleration ($a_{avg,abs}$), difference between the maximum and minimum vertical acceleration (a_v)
Mikov et al., 2013	$\frac{K}{F} \sqrt[4]{a_v}$	tunable constant (K), step frequency (F), difference between the maximum and minimum vertical acceleration (a_v)
Guo et al., 2016	$K_1 \sqrt[3]{a_{avg}} + K_2$	tunable constants (K_1, K_2), average absolute acceleration (a_{avg})
Tian et al., 2015	$K \times h \times \sqrt{F}$	coefficient (K), step frequency (F), pedestrian height (h)
Zeng et al., 2018	$\frac{\sqrt{K_2^2 - 4 \times K_1 \times (K_3 - F)} - K_2}{2 \times K_1}$	coefficients (K_1, K_2, K_3), step frequency (F)

4. Discussion

In the study, 28 different databases consisting of MEMS sensor data, formed from five users moving in six different environments at different speeds and patterns, were considered whole, and results were obtained. A transformation matrix was generated by looking at the first magnetometer and accelerometer records of a dataset. Likewise, while calculating the parameters in the methods, data from a single dataset were used. Median, standard deviation, absolute, and relative error were calculated from the obtained step lengths. It was observed that eight methods gave approximately the same results. The SL was calculated with an average error of 13.06%. However, Weinberg's method was the best method with an error of 7.44% and 5.61% in SL and total walking distance, respectively, while Mikov's method was the worst method with 54.34% and 44.63%. It is thought that more accurate results can be obtained if the acceleration rotation is calculated according to the median of the records for each dataset, rather than the transformation matrix. However, for a real-time pedestrian navigation system, this calculation is trivial because not all steps can be obtained. However, it is thought that the results can be improved if a separate parameter estimation is made for each method in each dataset. If the data are grouped according to the number of steps they contain, users, or walking environments and the parameters are calculated according to these groups; it is predicted that more accurate results can be obtained. For example, since the user's height information is not available, in the Tian method, the height is considered a constant and calculated by optimization. Changing the optimization method or choosing a different starting value has affected the accuracy of this method. It was concluded that Weinberg's method should be the first choice for many navigation applications, considering its accuracy and sensitivity, in the absence of sufficient attribute information about the database.

5. Conclusion

One of the essential stages of pedestrian navigation is SLE. Ten selected SLE methods were studied. Methods were applied to the open-source datasets shared by Wang et al.

Future research will be essential to produce a variety of open-source datasets that record data from more users, include more diverse human behaviors, and contain fewer and more steps. By training these datasets, more efficient results can be obtained with artificial

intelligence. In this way, more vital information can be provided in online applications by correcting the previous steps. Designing the analyzes made in the study as a desktop application and enriching it with artificial intelligence, automatically calculating step lengths according to the inputs of the dataset, and performing accuracy analysis for more various SLE methods will be the subject of future research.

References

Alvarez, D., González, R. C., López, A., & Alvarez, J. C. (2008). Comparison of step length estimators from wearable accelerometer devices. In Encyclopedia of Healthcare Information Systems (pp. 244-250). IGI Global.

Bylemans, I., Weyn, M., & Klepal, M. (2009, October). Mobile phone-based displacement estimation for opportunistic localisation systems. In 2009 Third International Conference on Mobile Ubiquitous Computing, Systems, Services and Technologies (pp. 113-118). IEEE.

Dias, M. B., Teves, E. A., Zimmerman, G. J., Gedawy, H. K., Belousov, S. M., & Dias, M. B. (2015). Indoor navigation challenges for visually impaired people. Indoor Wayfinding and Navigation, 141-164.

Díez, L. E., Bahillo, A., Otegui, J., & Otim, T. (2018). Step length estimation methods based on inertial sensors: A review. IEEE Sensors Journal, 18(17), 6908-6926.

Guo, Y., Sun, Y., Luo, H., & Guizani, N. (2016). Accurate indoor localization based on crowd sensing. Wireless Communications and Mobile Computing, 16(17), 2852-2868.

Ho, N. H., Truong, P. H., & Jeong, G. M. (2016). Step-detection and adaptive step-length estimation for pedestrian dead-reckoning at various walking speeds using a smartphone. Sensors, 16(9), 1423.

Kang, J., Lee, J., & Eom, D. S. (2018). Smartphone-based traveled distance estimation using individual walking patterns for indoor localization. Sensors, 18(9), 3149.

Karimi, H. A. (Ed.). (2015). Indoor wayfinding and navigation. CRC Press.

Kim, J. W., Jang, H. J., Hwang, D. H., & Park, C. (2004). A step, stride and heading determination for the pedestrian navigation system. Journal of Global Positioning Systems, 3(1-2), 273-279.

Ladetto, Q. (2000, September). On foot navigation: continuous step calibration using both complementary recursive prediction and adaptive Kalman filtering. In Proceedings of the 13th International Technical Meeting of the Satellite Division of The Institute of Navigation (ION GPS 2000) (pp. 1735-1740).

Ladetto, Q., Gabaglio, V., & Merminod, B. (2001). Two Different Approaches for Augmented GPS Pedestrian Navigation.

Ladetto, Q., Van Seeters, J., Sokolowski, S., Sagan, Z., & Merminod, B. (2002). Digital magnetic compass and gyroscope for dismounted soldier position & navigation. In Military Capabilities enabled by Advances in Navigation Sensors, Sensors & Electronics Technology Panel, NATO-RTO meetings, Istanbul, Turkey (No. CONF).

Martinelli, A., Gao, H., Groves, P. D., & Morosi, S. (2017). Probabilistic context-aware step length estimation for pedestrian dead reckoning. IEEE Sensors Journal, 18(4), 1600-1611.

May, A. J., Ross, T., Bayer, S. H., & Tarkiainen, M. J. (2003). Pedestrian navigation aids: information requirements and design implications. Personal and Ubiquitous Computing, 7(6), 331-338.

Mikov, A., Moschevikin, A., Fedorov, A., & Sikora, A. (2013, October). A localization system using inertial measurement units from wireless commercial hand-held devices. In International Conference on Indoor Positioning and Indoor Navigation (pp. 1-7). IEEE.

Rampp, A., Barth, J., Schülein, S., Gaßmann, K. G., Klucken, J., & Eskofier, B. M. (2014). Inertial sensor-based stride parameter calculation from gait sequences in geriatric patients. IEEE transactions on biomedical engineering, 62(4), 1089-1097.

Rasouli, A., Kotseruba, I., & Tsotsos, J. K. (2017). Are they going to cross? A benchmark dataset and baseline for pedestrian crosswalk behavior. In Proceedings of the IEEE International Conference on Computer Vision Workshops (pp. 206-213).

Scarlett, J. (2007). Enhancing the performance of pedometers using a single accelerometer. Application Note, Analog Devices, (AN-900).

Shin, S. H., Park, C. G., Kim, J. W., Hong, H. S., & Lee, J. M. (2007, February). Adaptive step length estimation algorithm using low-cost MEMS inertial sensors. In 2007 IEEE sensors applications symposium (pp. 1-5). IEEE.

Tian, Q., Salcic, Z., Kevin, I., Wang, K., & Pan, Y. (2015). A multi-mode dead reckoning system for pedestrian tracking using smartphones. IEEE Sensors Journal, 16(7), 2079-2093.

Xing, H., Li, J., Hou, B., Zhang, Y., & Guo, M. (2017). Pedestrian stride length estimation from IMU measurements and ANN based algorithm. Journal of Sensors, 2017.

Walchko, K. J. (2002). Low cost inertial navigation: Learning to integrate noise and find your way (Doctoral dissertation, University of Florida).

Wang, Q., Ye, L., Luo, H., Men, A., Zhao, F., & Huang, Y. (2019). Pedestrian stride-length estimation based on LSTM and denoising autoencoders. Sensors, 19(4), 840.

Weinberg, H. (2002). Using the ADXL202 in pedometer and personal navigation applications. Analog Devices AN-602 application note, 2(2), 1-6.

Zeng, G., Cao, S., Liu, C., & Song, W. (2018). Experimental and modeling study on relation of pedestrian step length and frequency under different headways. Physica A: Statistical Mechanics and its Applications, 500, 237-248.

Zhang, M., Wen, Y., Chen, J., Yang, X., Gao, R., & Zhao, H. (2018). Pedestrian dead-reckoning indoor localization based on OS-ELM. IEEE Access, 6, 6116-6129.

Intercontinental Geoinformation Days

igd.mersin.edu.tr

Monitoring and prediction of land cover change in the Anambra River Basin using neural network classification and Ca-Markov model

Nwilo P.C.[1], Njar N.G.[1], Inyang U.B.[1] Okolie C.J.[1], Daramola O.E.[1] Orji M.J.[*1,2], Olanrewaju H.O.[1] Akinnusi S.A.[1], Egogo-Stanley A.O.[1]

[1]University of Lagos, Faculty of Engineering, Department of Surveying and Geoinformatics, Lagos, Nigeria
[2]University of Strathclyde, Faculty of Engineering, Department of Naval Architecture, Ocean and Marine Engineering, Glasgow, United Kingdom

Keywords
Land Cover Change
Land Cover Prediction
Neural Network
Cellular Automata
Markov Chain

ABSTRACT

This study investigates the spatio-temporal variations in land cover within the Anambra River Basin of south-eastern Nigeria at three epochs: 1987, 2000, and 2018. The land cover scenario for 2030 was also predicted. Land cover was extracted using neural network classification, while the prediction was implemented with the Cellular Automata (CA) Markov chain modeling tool in Idrisi TerrSet 18.31 software. Results show that between 1987 and 2018, there was a loss of 1431.73km^2 in the wetlands. In the same period, there was a gain of 214.59km^2, 1,176km^2, 34.72km^2 and 4.19km^2 in the areal extent of built-up areas, vegetation, bare lands, and water bodies respectively. This outcome could be attributed to the rise in the human population within the basin, increasing demand for agricultural land, infrastructural development, and housing. The land cover projection between 2018 and 2030 shows a loss of 0.79km^2, 12.62km^2, and 4.96km^2 in the water bodies, wetlands, and bare lands respectively. In comparison, there was a gain of 23.6km^2 in vegetation. It is recommended that sustainable conservation practices and good land cover management policies be established to safeguard the river basin.

1. Introduction

Land cover change detection is essential for a better understanding of landscape dynamics (Rawat and Kumar, 2015). The neural network classification technique is widely used in land cover change modelling. It uses standard backpropagation for supervised learning, has an easy adaptation to different types of data and input structures, and has good generalization capabilities over statistical and analytic approaches (Huang et al., 2002; Thakur, 2017; Nair, 2016; Boateng et al., 2020).

Simulation of land cover change can provide insights into the pattern and trajectory of future development. Land cover change simulation models can provide probabilistic prediction of where the change may occur (Halmy et al., 2015). The Cellular Automata and Markov Chain (CA-Markov) model is useful in land use policy design, and it may also be used as an early warning system (Parsa et al., 2016). Authors that have applied the CA-Markov model include Subedi et al. (2013), Rendana et al. (2015), Nguyen et al. (2017), Singh et al. (2017) and Koko et al. (2020).

The aim of this research is to monitor land cover changes in the Anambra River Basin between 1987 and 2018, and to predict the future scenario for 2030. The land cover was extracted using the neural network classifier, and the prediction for 2030 was done using the CA-Markov chain technique.

2. Methods

2.1. Study area

The Anambra River Basin is one of the energy-rich inland sedimentary basins in Nigeria and is situated west of the Benue Trough between longitudes 6° 47' 15.47" E to 6° 52' 43.95" E, and latitudes 6° 17' 30.49" N to 6° 21' 33.12" N. The basin covers a total area of approximately 11,179km^2. The basin has a maximum elevation of 600m and a minimum elevation of 3m. It is characterized by two seasons, the dry season (October/November – March) and the rainy season (April –

*Corresponding Author
*(orjimichael23@yahoo.com) ORCID ID 0000-0002-1971-4367

Cite this study
Nwilo P, Njar N, Inyang U, Okolie C, Daramola O, Orji M, Olanrewaju H,Akinnusi S, &Egogo-Stanley A (2021). Montoring and Prediction of Land Cover Change in Anambra River Basin Using Cellular Automata and Markov Chain Technique. 3rdIntercontinental Geoinformation Days (IGD), 78-81, Mersin, Turkey

September/October), which approximately corresponds to the dry and flood phases of the hydrological regimes of the region. The area has accumulative annual rainfall between 1900 - 2707mm. The study area map is shown in Figure 1.

2.2 Datasets

Landsat 4-5 Thematic Mapper (TM) and Landsat 8 Operational Land Imager (OLI) imageries covering the study area were downloaded from the United States Geological Survey (USGS) data archive.

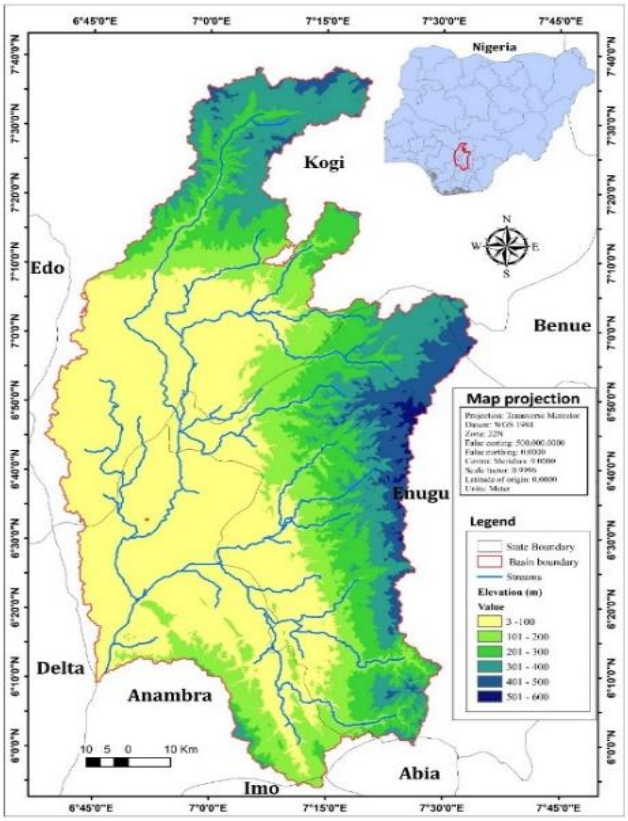

Figure 1. Map of Anambra River basin

2.3 Image Processing and Analysis

The neural network classifier in ENVI 5.3 was adopted for the land cover extraction. Post-classification refinement was performed within ArcGIS software. In the CA-Markov model, the prediction of future land cover changes can be calculated based on the conditional probability formula (Yousheng et al., 2011; Ma et al., 2012):

$$S(t+1) = P_{ij} \times S(t) \dots\dots\dots\dots\dots\dots (1)$$

$$P_{ij} = \begin{pmatrix} P_{11} & P_{12} & P_{1n} \\ P_{21} & P_{22} & P_{2n} \\ P_{n1} & P_{n2} & P_{nn} \end{pmatrix} \dots\dots\dots\dots\dots\dots (2)$$

$$\left(0 \le P_{ij} < and \sum_{j=1}^{N} P_{ij} = 1, (i, j = 1, 2, \dots\dots n) \right)$$

Where S(t) is the state of the system at time t, S (t +1) is the state of the system at time (t +1), and Pij is the matrix of transition probability in a state. To predict the land cover of 2030, we first predicted the land cover of 2018 so that the performance of the prediction could be compared with the actual data obtained from the image classification. A transition probability matrix for 1987–2000, suitability maps, and a 5 × 5 contiguity filter were used for this purpose. Using the kappa coefficient statistic, a comparison was carried out between the actual and simulated maps of 2018. Based on the successful simulation, the 2018 map was then set as a base map and the transition probability matrix for 2000–2018 was used to simulate land cover for 2030.

To perform the land cover change detection, a post-classification detection method was employed. The area was calculated using the "calculate geometry" function in ArcGIS to populate the field with area values. The statistics shows sum of the area obtained. The area values for all the classes were transferred to a Microsoft Excel worksheet for further analysis.

3. Results

The imageries of the study area obtained for each year were classified and the features were grouped into 5 categories (Waterbody - WB, Built-up area - BA, Wetland - WL, Vegetation – VG, and Bare land - BL) as shown in Figure 2. Table 1 shows that between 1987 and 2018, bare lands, vegetation, built-up areas and water bodies increased by 34.72km^2, 1,776km^2, 214.59km^2 and 4.19km^2 respectively. However, there was a 1431.73km^2 loss in wetlands.

Table 2 shows that between 1987 and 2018, vegetation had the highest probability of 92.37% to remain as vegetation in 2018. Whereas water bodies, built-up areas, wetlands, and bare lands had 73.01%, 50.98%, 42.83%, and 17.20% probabilities respectively to remain unchanged.

Table 1. Changes in land cover area (km^2) for 1987-2000, 2000-2018 and 1987-2018

	1987-2000	2000-2018	1987-2018
WB	4.88	-0.68	4.19
BA	33.14	181.45	214.59
WL	-1377.57	-54.16	-1431.73
VG	1270.49	-94.49	1176
BL	66.73	-32.01	34.72

Table 2. Transition probability matrix for land cover from 1987–2018

Changing from:	Probability of changing by 2018 to:				
1987	WB	BA	WL	VG	BL
WB	0.730	0.002	0.102	0.128	0.038
BA	0.000	0.510	0.000	0.468	0.022
WL	0.002	0.003	0.428	0.567	0.000
VG	0.009	0.025	0.037	0.924	0.014
BL	0.022	0.063	0.000	0.743	0.172

WB - Water body; BA- Built-up area; WL – wetland; VG – vegetation; BL – Bare land

To validate the land cover prediction given by the CA-Markov model, the simulated land cover was compared with the actual land cover (Table 3).

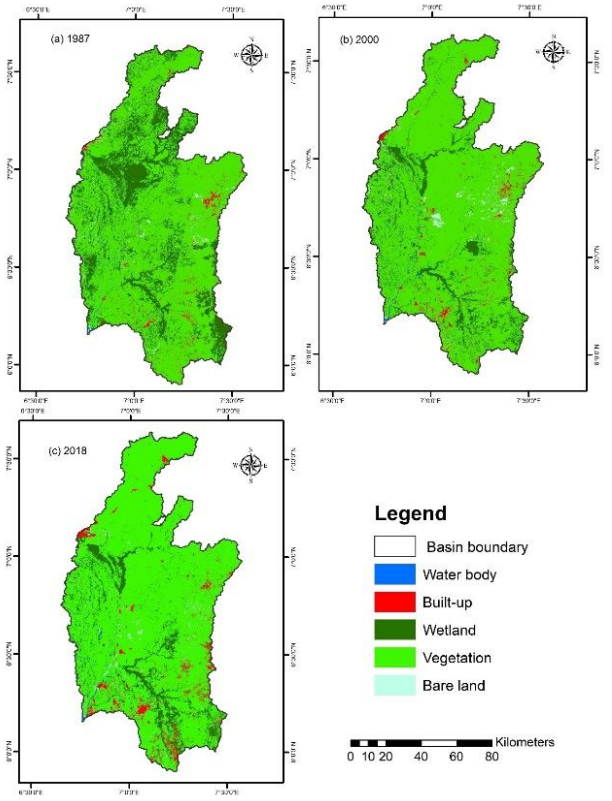

Figure 2. Land cover maps – (a) 1987 (b) 2000 (c) 2018

Table 2. Transition probability matrix for land cover from 1987–2018

Changing from:	Probability of changing by 2018 to:				
1987	WB	BA	WL	VG	BL
WB	0.730	0.002	0.102	0.128	0.038
BA	0.000	0.510	0.000	0.468	0.022
WL	0.002	0.003	0.428	0.567	0.000
VG	0.009	0.025	0.037	0.924	0.014
BL	0.022	0.063	0.000	0.743	0.172

WB - Water body; BA- Built-up area; WL – wetland; VG – vegetation; BL – Bare land

To validate the land cover prediction given by the CA-Markov model, the simulated land cover was compared with the actual land cover (Table 3).

Table 3. Comparison of actual and simulated land cover area (km^2) for 2018

Class	Actual 2018	Simulated 2018
WB	45.38	45.82
BA	382.87	199.98
WL	1047.99	1095.17
VG	9549.34	9655.30
BL	153.02	181.88
Total	11178.58	11178.14

WB - Water body; BA- Built-up area; WL – wetland; VG – vegetation; BL – Bare land

Table 3 indicates that water body, wetland vegetation and bare land have agreeable areas. There is a wide gap in built-up areas with 382.87km^2 actual and 199.98km^2 simulated area. A possible explanation for this is that the model was unable to capture random developing areas.

The results in Table 4 show that between 2018 and the projected 2030, there was a decrease in water body, wetland and bare land by 0.79km^2, 12.62km^2, 4.96km^2 respectively. Results also shows an increase in vegetation by 23.60km^2. The decrease in built up areas could be explained by other factors that drive land cover change which are not within the scope of this study.

Table 4. Comparison of 2018 and projected 2030 land cover area (km^2)

Class	2018	Projected 2030	2018 – 2030 change
WB	45.38	44.59	-0.79
BA	382.87	377.93	-4.94
WL	1047.99	1035.37	-12.62
VG	9549.34	9572.94	+23.60
BL	153.02	148.06	-4.96
Total	11178.58	11178.90	+0.32

4. Discussion

The natural environment such as wetland resources have been threatened due to the drastic reduction of 1431.73km^2. The increase in human population attracted infrastructural development and expansion of housing estates in the area, which consequently can have negative influences. The states within the Anambra River basin are known for their intensive agricultural practices such as fishing, field crop farming in small and large scale and animal pastorage etc. This is evident in the increase in vegetation as Government and private sectors are investing heavily in agriculture.

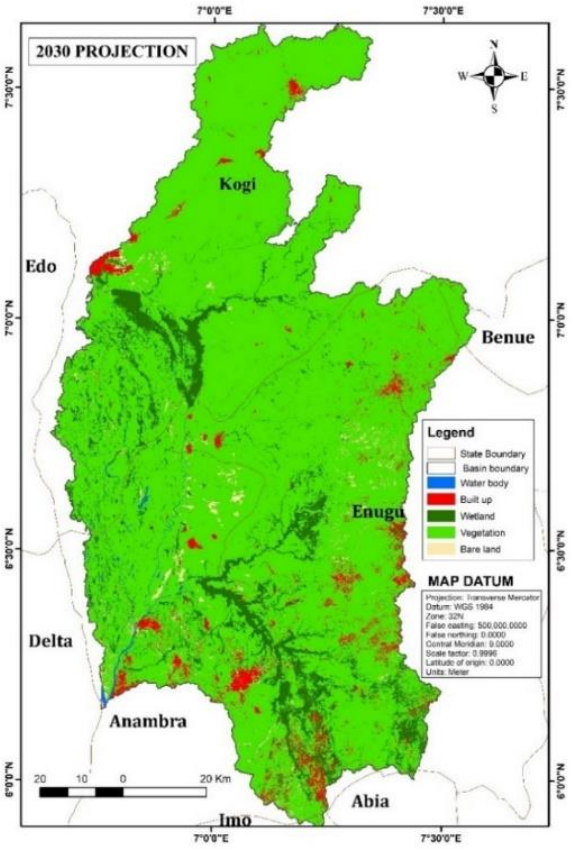

Figure 3. Map showing projected land cover for 2030

5. Conclusion

This research has established the usefulness of spatial and temporal analysis approach in monitoring and predicting land cover change. CA-Markov has proven to be useful in the prediction of land cover change. A further study could employ biophysical, socio-economic and policy-related factors in the prediction.

Acknowledgements

The Landsat images used in this investigation were provided at no cost by the United States Geological Survey.

References

Al-sharif, A. A., & Pradhan, B. (2014). Monitoring and predicting land use change in Tripoli Metropolitan City using an integrated Markov chain and cellular automata models in GIS. Arabian journal of geosciences, 7(10), 4291-4301.

Halmy, M. W. A., Gessler, P. E., Hicke, J. A., Salem, B. B. (2015): Land use/land cover change detection and prediction in the north-western coastal desert of Egypt using MarkovCA. – Applied Geography 63: 101-112.

Koko, A. F., Yue, W., Abubakar, G. A., Hamed, R., &Alabsi, A. A. N. (2020). Monitoring and Predicting Spatio-Temporal Land Use/Land Cover Changes in Zaria City, Nigeria, through an Integrated Cellular Automata and Markov Chain Model (CA-Markov). Sustainability, 12(24), 10452.

Ma C, Zhang GY, Zhang XC, Zhao YJ, Li HY. Application of Markov model in wetland change dynamics in Tianjin Coastal Area, China. Procedia Environ Sci. 2012; 13:252±62. https://doi.org/10.1016/j.proenv.2012.01.024.

Nguyen TA, Le PMT, Pham TM, Hoang HTT, Nguyen MQ, Ta HQ, et al. Toward a sustainable city of tomorrow: a hybrid Markov±Cellular Automata modeling for urban landscape evolution in the Hanoi city (Vietnam) during 1990±2030. Environment, Development and Sustainability. 2017. https://doi.org/10.1089/sus.2017.29092.aml

Parsa V A, Yavari A, Nejadi A (2016). Spatio-temporal analysis of land use/land cover pattern changes in Arasbaran Biosphere Reserve: Iran. Model. Earth Syst. Environ, 2, 1–13.

Rawat, J., & Kumar, M. (2015). Monitoring land use/cover change using remote sensing and GIS techniques: A case study of Hawalbagh block, district Almora, Uttarakhand, India. The Egyptian Journal of Remote Sensing and Space Science, 18(1), 77-84.

Rendana M, Rahim SA, Mohd RIW, Lihan T, Rahman ZA. CA-Markov for predicting land use changes in tropical catchment area: a case study in Cameron Highland, Malaysia. Journal of Applied Sciences. 2015; 15(4):689±95.

Singh SK, Laari PB, Mustak S, Srivastava PK, SzaboÂ S. Modelling of land use land cover change using earth observation data-sets of Tons River Basin, Madhya Pradesh, India. Geocarto Int. 2017:1±34.

Subedi P, Subedi K, Thapa B. Application of a Hybrid Cellular Automaton±Markov (CA-Markov) Model in Land-Use Change Prediction: A Case Study of Saddle Creek Drainage Basin, Florida. Science & Education. 2013; 1(6):126±32.

Yousheng W, Xinxiao Y, Kangning H, Qingyun L, Yousong Z, Siming S. Dynamic simulation of land use change in Jihe watershed based on CA-Markov model. Transactions of the Chinese Society of Agricultural Engineering. 2011; 2011(12). https://doi.org/10.3969/j.issn.1002-6819.2011.12.062

Intercontinental Geoinformation Days

igd.mersin.edu.tr

Geospatial intelligence (GeoINT) with geographic information systems (GIS)

Halil Ibrahim Onyıl[*1]

[1]*Geomatics Engineer, ONYIL Geomatics and Engineering Co., Ağrı, Turkey.*

Keywords
Intelligence
Geospatial Intelligence (GeoINT)
(GIS)
Forecasting with Risk Maps

ABSTRACT

Collecting, evaluating, analyzing and presenting location and spatial data, which is the field of study of the survey engineering profession, is at work in the military field as well as in many other fields. It is known that wars and operations cannot be considered independent of location. In this context, it is possible to carry the location and location data beyond just being a battlefield and to use it as a data that will guide the course of the war. One of the uses of spatial data is intelligence. This study focuses on the spatial dimension of intelligence and the human and war elements in the field of operation; it includes modeling and predicting risks in the field as an application of the mathematical theory of intelligence. Within the scope of the study, it is aimed to provide a future-oriented forecast against the risks and threats that may arise in the operation field. An exemplary model was established for this purpose in the study. In order to predict the operation style of the enemy element, the risks are revealed by producing risk maps in the GIS environment.

1. INTRODUCTION

Intelligence has been used effectively with different meanings by many civilizations from past to present. As an agent, in 5000 B.C. (BC), Egyptian King Tutmosis the 3rd determined his strategies in order to take the city of Jaffa; according to the intelligence reports of the agents he had previously sent to the country; he made his war plans. Thus, he captured the city of Jaffa with less cost (Acar, 2011; Odemis, 2014).

Today, fully institutionalized intelligence agencies have reached the national level institutional structure.

For domestic intelligence in the USA; Federal Bureau of Investigation (FBI), Central Intelligence Agency (CIA) for foreign intelligence, National Intelligence Organization (MIT) in our country, Federal Intelligence Service (BND) in Germany, Foreign Intelligence and Special Operations (MOSSAD) in Israel, Iran The Intelligence of the Islamic Republic of Iran (VAJA) is institutionalized with 7 different intelligence agencies in the British Kingdom (Wiki,2020).

The task of these intelligence agencies, which have been established in many countries and have survived to the present day, is to provide data flow to decision makers about current or potential risks, threats and opportunities. (Kucukbas, 2015).

The answer to the question of what is intelligence, in many languages; We see that it means different things. In English, 'intelligence', intelligence, mind, knowledge, 'reseignement' in French, (information), 'razvedka' in Russian, 'nachricten' in German, in Turkish intelligence is derived from the word news in Arabic (Ozkan, 2003; Oztoprak, 2011).

Intelligence, by definition, is a product information produced as a result of processing (extracting, interpreting) news (raw data). (Ilter, 2002, Oztoprak, 2011).

According to another definition, "all kinds of data, information and information obtained as a result of the use of all kinds of tools from all open, semi-open or confidential sources that can be accessed, according to their importance and accuracy after collecting them for the purpose of realizing national general or special policies and preventing damage to national policies. It is the information obtained as a result of the process of classification, comparison, analysis and evaluation" (Ozdag, 2009).

Although the types of intelligence gathering are expressed in different ways, they are classified according to its purpose, level and method (Oztoprak, 2011; Gundogar, 2007).

In spatial/spatial intelligence with the recently developing spatial technologies; took its place in technical intelligence. With this intelligence method, it is important that satellite images and data from the field can be evaluated together.

Spatial intelligence is called Geospatial Intelligence (GEOINT) in English.

*Corresponding Author

*(hibrahimonyil@gmail.com) ORCID ID 0000-0002-7916-8820

Cite this study

ONYIL H İ, (2021). Geospatial Intelligence (GeoINT) with Geographic Information Systems (GIS). 3rdIntercontinental Geoinformation Days (IGD), 82-85, Mersin, Turkey.

Geospatial intelligence is a discipline that contains three basic elements as shown in Figure 1. These are imagery, imagery intelligence and geospatial information.

The image includes any natural or man-made object; It is the recording of the existing range in the electromagnetic spectrum from satellite, aircraft or unmanned aerial platforms with remote sensing technologies.

Imagery intelligence is an auxiliary material that allows interpretations and analyzes of geographic area with the help of images.

Geospatial information, on the other hand, is information that describes the spatial information and characteristics of a natural geographical area. This information is remote sensing, geodetic data and mapping products (GEOINT Basic Doctirine, 2006).

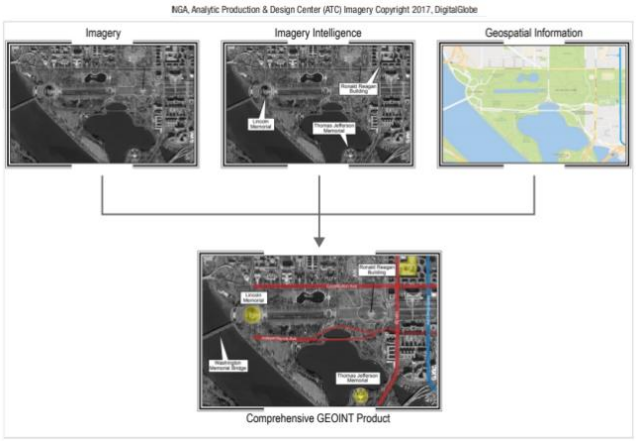

Figure 1. Geospatial Intelligence and the Three Elements (GEOINT, 2018)

When we look at the features of geospatial intelligence, geographic data set collection is performed using many different advanced sensors, shown in Figure 2.

It brings together map data from many different sources. By providing three-dimensional (3D) and 4-dimensional (4D) thinking ability, it provides an intelligence opportunity that is used to determine the time and course of action in a dynamic and interactive way. (GEOINT Basic Doctirine, 2006).

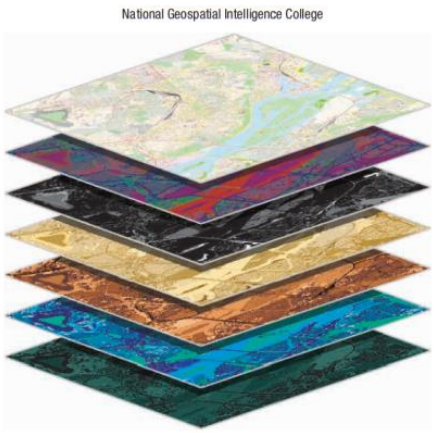

Figure 2. Geographic Datasets (GEOINT, 2018)

Geographical information systems (GIS) is one of the most effective tools that spatial intelligence uses in data analysis and interpretation, with its ability to combine many data sets, three-dimensional analysis and map production. GIS is an information system that provides results and outputs with the collection, storage, query and analysis possibilities of the data obtained through the observation of geographical information (Yomralioglu and Doner, 2000).

In the GIS environment, it is possible to bring together spatial data of different types and formats, to query and analyze separately or in an integrated way. With these capabilities, GIS acts as a decision-support system (Sarı and Turk, 2020). The spatial analysis opportunity of GIS provides the opportunity to come up with stronger and sustainable solutions to problems by analyzing spatial data under certain values and conditions (Onyil and Yilmaz, 2020).

Among the wide usage areas of GIS, there are many areas such as earthquake, urban planning, urban transformation, production of epidemiological maps. (Erdogan, 2010; Yalcin and Sabah, 2017; Ledoux et al. 2021; Biljecki et al. 2021). In this context, GIS has become a must for hazard and risk analysis studies with its strong analysis capabilities. And it has been used in many risks and hazard analysis studies. (Udono and Sah, 2002; Fell et al. 2008; Yalçın and Sabah, 2018; Hepdeniz and Soyaslan, 2018; Sarı and Turk, 2020).

There are many GIS-based hazard and risk analysis studies in the literature. In the study carried out by Karakaş et al. (2004), crime maps were produced with GIS. Within the scope of the study, it was stated that dangers and risks would be prevented by producing maps of time and places that pose risks, which were analyzed depending on different variables.

Yalçın and Sabah (2017)'s within the scope of the studies of industrial organizations in Edirne Province and its districts that analyze the earthquake risk, earthquake risk analysis was carried out with the Analytical Hierarchy Process (AHP) method in the open-source GIS software (QGIS) environment. As data sets; Active fault lines, geological formation status, earthquake epicenter points between 1908-2016 and locations of industrial establishments were used. As a result of the analysis, dangerous districts and industrial establishments were determined. Thematic maps were produced. As a result, it was stated that the earthquake hazard value of 59 industrial establishments in Enez and Keşan districts is high.

Aydar (2020)' s It is a study that includes the three-dimensional modeling of risky areas in hunting areas, in wildlife ecology, in a GIS environment. In the study, a survey was conducted by spatially correlating the wildlife data in Çanakkale Province, Kalkım Town pilot region. Obtained survey data were modeled via GIS with three-dimensional terrain model and satellite images; The maps were produced and the follow-up was given to the hunters and the personnel of the Provincial Directorate of National Parks to obtain information about the risky areas.

2. Method

In this study, within the scope of literature and developing technologies, against the risks and threats that may come in the operation area, for military base areas; It is aimed to provide a foresight for the future.

The study includes the operation area; Modeling in the GIS environment and predicting the risks that may come, so that; To contribute to the preparation of complex action plans and the development of measures against the risks that may exist. In this study, an exemplary model was established for this purpose.

The data of the established model were analyzed statistically. Afterwards, correlations between model data were revealed. In order to be able to predict the data, the mode of operation of the enemy element and the risks, risks were revealed by producing risk maps in the GIS environment. Thus, whether there is a significant relationship between the behaviors of people and war elements and risk black points were tested on the sample model.

At this stage, the model consists of the steps of establishing the military base area, analysis and correlation of the data of the model, and production of risk maps in the GIS environment. The flow diagram shown in Figure 3 has been designed for the process steps to be performed during the implementation phase.

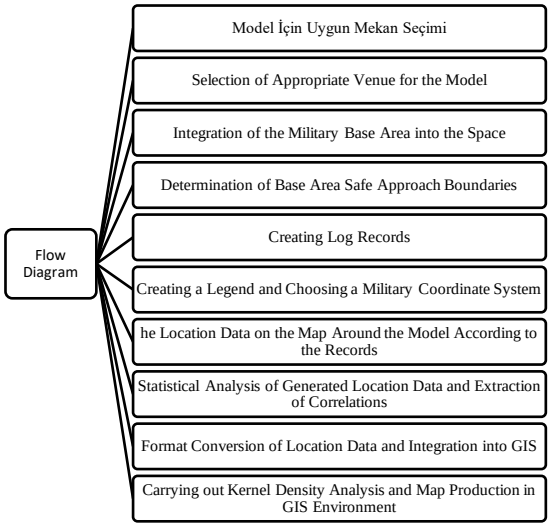

Figure 3. Flow Diagram

According to the flow chart, firstly, a suitable location was selected for the model military base area, then a 3D base area model was designed and the base area was placed in its position on the map for data generation, then; Ceride records of safe approach boundaries and daily living space mobility were produced by the author.

Then, a legend group was created according to the data records, and the data were processed around the model with the military coordinate system, according to the data records. At the last stage, the application phase of the study was completed with the statistical analysis of the data and finally the transfer of the data to the GIS environment and the production of risk maps as shown in Figure 4.

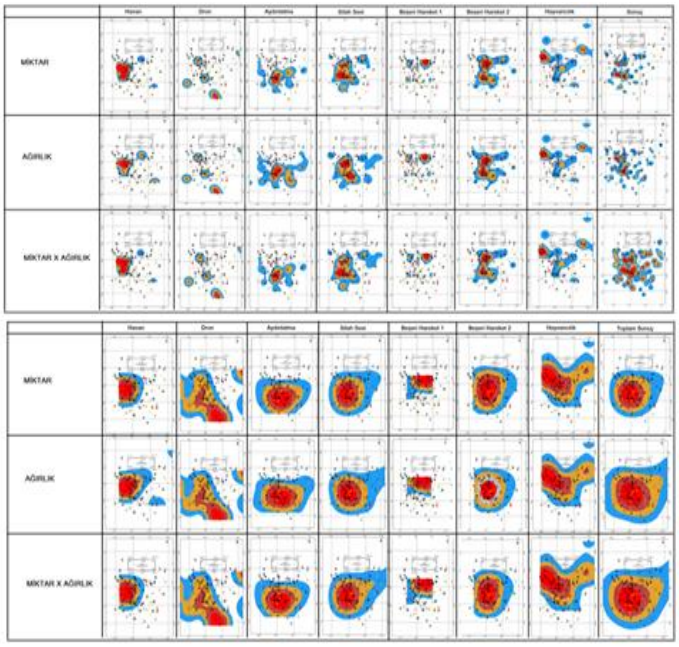

Figure 4. Risk Maps

3. Results

With the operation steps carried out within the scope of the study, a risk analysis was carried out with GIS in terms of spatial intelligence of the model military base region. The following findings were obtained with the process steps.

- It has been observed that the implementation phase, which starts with data acquisition, is practical in terms of modeling the reality.
- It has been found that the statistical analysis of the data is important for the analytical evaluation process of intelligence and will form the basis for the spatial analyzes to be carried out in the process.
- The predictive modeling capability of the GIS for the future has been shown to be at a good level by testing the model on the military base area.
- It has been seen that the production of visual models of data through maps by using GIS can be used as an effective intelligence report source and will provide decision support for complex operation plans.

4. Discussion

The success of this study is possible if the personnel in the military base area have been given intelligence and counter-intelligence (IKK) training, complete map information training, and speed, accuracy and analysis are carried out on time and delivered to the relevant units and institutions. In addition, a good temporal resolution can be gained with the 2.5 m resolution Gokturk-2 Satellite Images as a base satellite image for the studies.

In the coming years, time can be saved by transferring the data directly from the personnel in the position to the military operations center and from

there to the joint operations centers with encrypted and user-friendly, easy, useful mobile software applications.

Finally, the analysis of the data and the production of the maps can be accelerated by developing a desktop and mobile application that will query and analyze the incoming data with user interfaces.

5. Conclusion

Within the scope of the study, a model military base area was established, enemy element data was produced considering the operation area and statistical analyzes were carried out. Spatial data representation and estimation success of the operation area have been demonstrated.

Finally, a situation map was produced to show the current state of spatial data via GIS. Then, 72 different Kernel Density analyzes were carried out according to the 7 legend values of the data, the determined weight values, the recorded amount values and the multiplication of the amount and weight values.

Thus, the risky areas around the military base areas located in the dangerous area within the operation area were presented as a visual product with maps.

References

Acar, Ü. (2011). İstihbarat. Akçağ Yayınları. Ankara.

Aydar, U. (2020) Coğrafi Bilgi Sistmeleri Kullanılarak Yaban Hayatı Çeşitliliği ve Avlak Alanları Risk Haritaların Üretilmesi. Türkiye Coğrafi Bilgi Sistemleri Dergisi. Cilt: 2. Sayı: 2.ss. 44-56.

Biljecki, F., Stouff, R., Kalantari, M., (2021). Emeging topics in 3D GIS. Transactions in GIS. 25(1), 3-5.

Erdogan, S., (2010). Epidemiyolojide CBS Uygulamaları: Konumsal Kümeleme Yöntemlerinin Karşılaştırılması-Menejit Örneği. Harita Teknolojileri Dergisi. 2(2), 23-31.

Fell, R., Corominas, J., Bonnard, C.H., Cascini, C., Leroi, E., Z. Savage, W. (2008). Guidlines for landslide susceptibility hazard ve risk zoning for land use planinig. Engineering Geology. 102, 99-111.

Geoint (2020) https://en.wikipedia.org/wiki/Geospatial_intelligence adresinden 03.02.2021 tarihinde alındı.

Geoint Basic Doctirine. (2006). National Geospatial Intelligence Agency. USA.

Geoint Basic Doctirine. (2018). National Geospatial Intelligence Agency. USA.

Hepdeniz, K., ve Soyaslan, İ.İ., (2018). CBS ve Frekans Oranı Yöntemi Kullanılarak Isparta-Burdur Dağ Yolu Heyelan Duyarlılığının Değerlendirilmesi. Mehmet Akif Ersoy Üniversitesi Fen Bilimelri Enstitüsü Dergisi. 9(2, 179-186). Doi: 10.29048/makufebed.414392

Ilter, E. (2002). Mill İstihbarat Teşkilatı Tarihçesi.MİT Basımevi. Ankara. 20.11.2009 tarihinde Bilgi Portalı: http://www.mit.gov.tr/tarihce/index.html adresinden alındı.

Karakas, E., Karadogan. S., Arslan. H., (2004). Suç Haritaları ve Bilgisayar Teknolojisi. Pamukkale Üniversitesi Mühendislik Fakültesi Mühendislik Bilimleri Dergisi. Cilt:10. Sayı: Özel Sayı. ss: 37-42.

Kucukbas, H. (2015) Bilgi Yönetimi Yaklaşımlarındaki Değişimin İstihbarat Analizine Etkisi, Harp Akademileri Stratejik Araştırmalar Enstitüsü, Yüksek Lisans Tezi. İstanbul.

Ledoux, H., Biljecki, F., Dukai, B., Kumar, K., Peters, R., Stoter, J., & Commandeur, T. (2021). 3dfier: automatic reconstruction of 3D city models. Journal of Open-Source Software, 6(57), 2866.

Onyil, H.I., Yilmaz, M., (2020). Açık Kaynak Kodlu Yazılımlarla Web Tabanlı Mekansal Analizlerin Gerçekleştirilmesi. Türkiye Coğrafi Bilgi Sistemleri Dergisi. Cilt: 2. Sayı: 2. ss. 76-82.

Odemis, R.G. (2014) Terörle Mücadelede İnsan İstihbaratı ve Teknik İstihbarat İlişkisi, Harp Akademileri Stratejik Araştırmalar Enstitüsü Yüksek Lisans Tezi, İstanbul.

Ozkan, T. (2003). MİT'in Gizli Tarihi. (7.b.). Alfa Basım Yayın.İstanbul.

Oztoprak, M. (2011) Karar Destek Sistemlerinin İstihbarat Amaçlı Kullanımı ve 2005-2010 Arası Dönemde Türkiye ve İsrail'in Stratejik Karar Verme Modülü Yardımıyla İncelenmesi, Harp Akademileri Komutanlığı Stratejik Araştırmalar Enstitüsü. Yenilevent, İstanbul.

Ozdag, Ü. (2009). İstihbarat Teorisi. (3.b.). Kripto Yayınları.Ankara.

Gundogar, A.Ö. (2007). Küreselleşme Zemininde Modern İstihbarat. Harp Akademileri Komutanlığı. Stratejik Araştırmalar Enstitüsü. Uluslararası İlişkiler Ana Bilim Dalı. Yayınlanmış Yüksek Lisans Tezi. İstanbul.

Udono, T., ve Sah, A.K. (2002). Hazard mapping and vulnerability assesment, Regional Workshop on Total Disaster Risk Managment, 7-9 August 2002.

Sarı, S., Turk, T., (2020). Depremde Meydana Gelebilecek Bina Hasarlarının Coğrafi Bilgi Sistemleri İle İncelenmesi.Türkiye Coğrafi Bilgi Sistemleri Dergisi. 2 (1), 17-25.

Yalcin, C.,Sabah, L., (2017). Açık Kaynak Kodlu CBS ve Analitik Hiyerarşi Süreci (AHP) Yöntemi Kullanılarak Edirne Sanayi İşletmelerinin Deprem Tehlike Analizi. Düzce Üniversitesi Bilim ve Teknoloji Dergisi. 5(2017), 524-537.

Yalcin, C., Sabah, L., (2018). CBS Tabanlı Bulanık Mantık ve AHP Yöntemleri Kullanılarak Adıyaman İlçelerinin Deprem Tehlike Analizinin Oluşturulması. Adıyaman Üniversitesi Mühendislik Bilimleri Dergisi. 8(2018), 101-113.

Yomralioglu, T., Döner F., (2000). Gezici Coğrafi Bilgi Sistemleri ve Uygulamaları. HKMO Jeodezi, Jeoinformasyon ve Arazi Yönetimi Dergisi. Sayı 93.

Wiki (2020). https://tr.wikipedia.org/wiki/%C4%B0stihbarat_te%C5%9Fkilatlar%C4%B1_listesi

Intercontinental Geoinformation Days

http://igd.mersin.edu.tr/2020/

Age and Gender differences in perceptions and health impacts of noise in an academic environment

Alfred Alademomi[1,2,3], Johanson Onyegbula*[1], Rahmat Adepo[1], Chukwuma Okolie[1,2,3], Abiodun Alabi[1,2], Babatunde Ojegbile[1,2], Olagoke Daramola[1,2], Nehemiah Alozie[4], Samuel Akinnusi[1,2], Taiwo Adewale[2,5]

[1]*University of Lagos, Faculty of Engineering, Department of Surveying and Geoinformatics, Lagos, Nigeria*
[2]*Geospatial and Environmental Research Group, University of Lagos, Nigeria*
[3]*Centre for Multidisciplinary Research and Innovation (CEMRI), Abuja, Nigeria*
[4]*University of Lagos, Faculty of Engineering, Department of Mechanical Engineering, Lagos, Nigeria*
[5]*Moshood Abiola Polytechnic, Department of Surveying and Geoinformatics, Ogun State, Nigeria*

Keywords
Noise Exposure
Noise Pollution
Perception
Health and Wellbeing

ABSTRACT

This study assessed age and gender differences in the perceptions and health impacts of noise exposure within the University of Lagos main campus. An opinion pool of staff and students (male and female) was sampled with an online questionnaire survey that inquired about the likely contributory sources of noise, and health impacts. The findings revealed that the perceptions of the impact of noise exposure were generally similar irrespective of gender, but varied by age group. This study provides crucial insights to inform the knowledge-based formulation of policies and regulations for noise abatement and control.

1. Introduction

Noise pollution, which has significantly risen especially in urban environments, is a major source of concern in our environment today (Gholami et al., 2012). Various sources of noise pollution have been identified and their impacts studied in various contexts (Ruge et al., 2013; Zuo et al., 2014), and can pose major threats to the wellbeing of individuals living in such environments.

There are several contributory sources of noise pollution in our environment, including vehicles, audio systems from social events and religious houses, construction and other human activities (Bublić et al., 2010; Sotiropoulou et al., 2020). Sequel to this rise in noise levels, various national and global agencies have suggested regulatory limits for acceptable noise levels (WHO, 2018). However, not many seem aware of the extent of the often negative impact of these noise sources of pollution to their wellbeing (Munzel et al., 2018).

In a previous study, Alademomi et al. (2020) had mapped the noise level variations within the University of Lagos main campus, with the use of spatial and statistical analysis, and a conformity assessment based on internationally recognized noise limits. In the study, it was shown that the noise levels within the university campus exceeded the tolerable limits for academic, commercial, and residential areas set by World Health Organization (WHO) and the National Environmental Standards and Regulations Enforcement Agency (NESREA).

In this study, we go further to assess the knowledge and perceptions of noise levels based on a well-structured questionnaire survey with members of the university community. We also evaluate the impacts of the noise on the attitudes and health of the respondents, based on age and gender.

2. Methods

2.1. Study area

The University of Lagos is a higher institution of learning and a popular choice for tertiary education by many residents of Lagos and Nigeria. Its urban location makes it a beehive of activities beyond academia, including commercial and social activities, thereby exposing it to regular noise pollution. The map of the study area is as shown in Fig. 1.

*Corresponding Author
*(johansononyegbula20@gmail.com) ORCID ID 0000-0002-1150-5122

Cite this study
Alademomi A, Onyegbula J, Adepo R, Okolie C, Alabi A, Ojegbile B, Daramola O, Olozie N, Akinnusi S & Adewale T (2021). Age and gender differences in perceptions and health impacts of noise in an academic environment. 3rd Intercontinental Geoinformation Days (IGD), 86-89, Mersin, Turkey

Figure 1. Map of the study area

2.2. Questionnaire survey and analysis

A questionnaire was created using Google forms. Google forms allow for either usage and/or customization of existing templates or creation of a new form using the Graphical User Interface (GUI) drag and drop elements. The latter was the chosen option for the design of the questionnaire; divided into two pages to limit the volume of information displayed per page and give users a feel of progress as they quickly finish a page before moving to the next. Most of the questions required respondents to select a single option on a 5-level intensity scale. Other questions had predefined options for selection (especially the checkboxes) and a single yes/no question was included as well. The questions asked in the questionnaire are summarized in Table 1 below.

3. Results

There was a total of 324 respondents comprising of 209 males (65%) and 115 females (35%). The age distribution is as follows: Less than 20 years (66.4%), 20 – 25 years (66.4%), 26 – 30 years (16.4%), 31 – 40 years (8.6%), above 40 years (0.9%). The findings are shown in Tables 2- 4 and Fig. 2.

From Table 2, it can be seen that majority of the male (113) and female (63) respondents perceive average noise level on campus as normal. Both genders also agreed that the noise level is far from being very low as only 2 respondents each chose this option. A similar trend is observed in their responses based on age. From Table 3, majority of the respondents (175) agreed that the noise level on campus is normal. About 67% of this (174) is from responses of the age group 20 – 25. Table 4 shows that both males and females on campus believe that noise level sometimes influences their sleep pattern. Majority of the males agreed that they seldom feel dizzy due to noise levels, while most female respondents believe noise levels never make them dizzy. A similar response was seen in the responses to influence of noise on headache. In Table 5, majority of the male and female respondents agreed that noise levels on campus rarely cause ear aches and tinnitus.

Figure 2 shows the impact of these noise levels on their concentration levels, with most of the respondents still faring quite well even at noise levels deemed beyond moderate to them. From Figure 3, social activities are percieved by both the male and female gender to be the main noise source causing irritation followed by interaction with humans.

Table 1. Summary of questions provided for survey.

S/N	Questions
1	Age
2	Gender
3	What is your assessment of the average noise level within the campus?
4	Which of the following challenges/issues do you experience due to excessive noise?
5	How often do you experience earaches as a result of noise?
6	How often do you experience headaches from excessive noise exposure?
7	How often do you feel dizzy after excessive noise exposure?
8	How often do you experience ringing in the ears (tinnitus) due to excessive noise exposure?
9	How well do you concentrate beyond noise levels deemed moderate to you?
10	What noise sources generally irritate you the most?

Table 2. Perception of average noise levels based on gender

Average noise level	Male	Female
Very High	13	5
High	60	43
Normal	113	63
Low	21	2
Very Low	2	2
Total	209	115

Table 3. Perception of average noise levels based on age

Average noise level	Age				
	< 20	20 – 25	26 – 30	31 – 40	> 40
Very High	1	13	3	1	0
High	5	66	23	7	2
Normal	16	117	24	18	0
Low	2	16	3	2	1
Very Low	1	3	0	0	0
Total	25	215	53	28	3

Table 4. Gender differences in response to noise causing sleeping difficulties, dizziness and headaches

	Sleeping Difficulties		Dizziness		Headaches	
Frequency	M	F	M	F	M	F
Every time	18	13	5	3	20	10
Never	25	11	62	41	12	8
Oftentimes	35	19	18	9	49	30
Rarely	51	32	86	36	49	34
Sometimes	80	39	38	25	79	33
Total	209	115	209	115	209	115

**M- male, F - female*

Table 5. Gender differences in response to noise causing earaches and tinnitus

Frequency	Earaches		Tinnitus	
	M	F	M	F
Every time	2	0	3	5
Never	40	27	59	24
Oftentimes	17	12	10	5
Rarely	112	53	101	54
Sometimes	38	22	36	26
Total	209	115	209	115

**M- male, F - female*

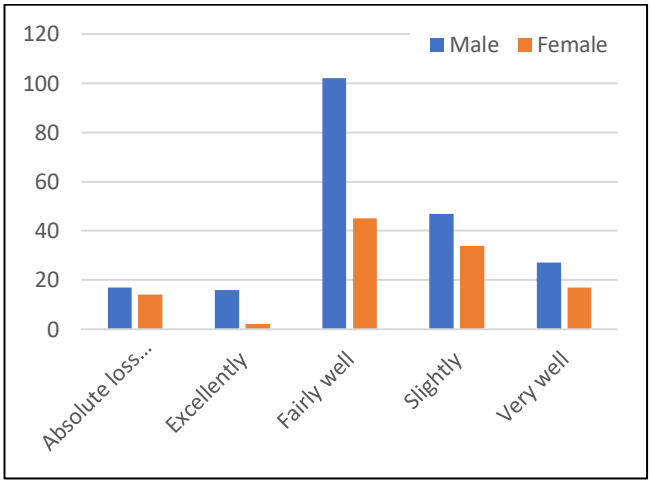

Figure 2. Gender differences in response to noise affecting concentration

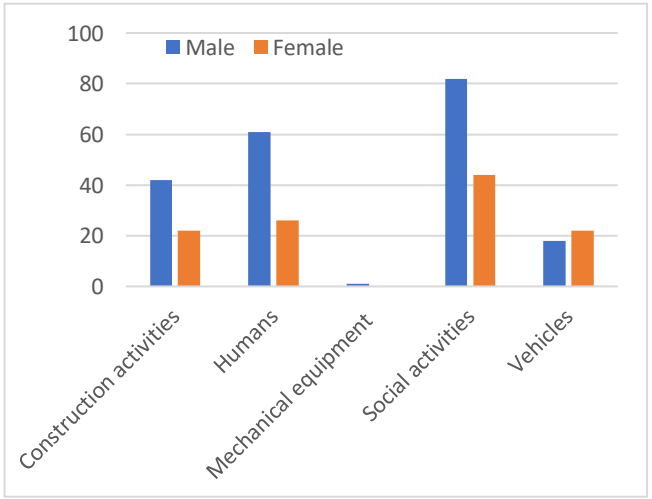

Figure 3. Gender differences in response to noise sources causing irritation

4. Discussion

A significant proportion of respondents below the age of 25 years, and between the ages of 31 – 40 perceive noise levels as being normal/moderate on the campus. With the exception of those between the ages of 31 – 40 years, the perception of moderate noise levels by the young population – under 25 years, relative to others is probably because of the high auditory preceptory levels which is generally expected in such a young population. It is possible that they might be major contributors to human sources of noise in the environment, hence the relative indifference/numbness to high noise levels. Between the ages of 26 – 30, most respondents are split between moderate and high noise level perceptions. While above 40 years of age, 2% think average noise levels are high, and the remaining perceive low noise levels. The perception that human and social activities are the major sources of noise on campus can be attributed to the constant social activities such as sports and student group interactions.

5. Conclusion

Prolonged exposure to noise levels can be detrimental to human well-being. Unfortunately, many are oblivious of the impact of noise pollution to their health and hence do not take adequate measures to mitigate this – since the impact can be due to other widely known sources. Severe noise can lead to mood swings, accumulated stress, loss of concentration among other ailments. And the impact of these noise-related effects varies across gender and age groups.

For a healthy learning environment, especially in an institution of higher learning, serenity is pertinent to ensure knowledge retention, focus and healthy living that ensures academic success. Hence, universities should introduce and implement regulations that would minimize exposure to unhealthy noise levels for the wellbeing of their students, staff and visitors.

Acknowledgements

Special thanks to everyone who contributed to the success of the work.

References

Alademomi, A., Okolie, C., Ojegbile, B., Daramola, O., Onyegbula, J., Adepo, R., & Ademeno, W. (2020). Spatial and Statistical Analysis of Environmental Noise Levels in the Main Campus of the University of Lagos. The Journal of Engineering Research [TJER], 17(2), 75-88.

Bublić I., Tudor I., Skelin D. (2010), Small scale noise mapping of industrial plants. 1st EAA-EuroRegio 2010. Congress on Sound and Vibration, 15-18 September 2010, Ljubljana, Slovenia.

Gholami, A., Nasiri, P., Monazzam, M., Gharagozlou, A., Monavvari, S. M., & Afrous, A. (2012). Evaluation of traffic noise pollution in a central area of Tehran through noise mapping in GIS. Advances in Environmental Biology, 6(8), 2365-2371.

Munzel T., Schmidt F., Sebastine S., Herzog J., Andrea D (2018), Environmental Noise and Cardiosvacular System. Journal of American College of Cardiology, 71: 688 – 697.

Ruge L., Altakrouri B., Schrader A. (2013), Sound of the city - continuous noise monitoring for a healthy city. In Proceedings of the 5th International Workshop on Smart Environments and Ambient Intelligen., 670–675. http://www.csee.usf.edu/~mlabrador/Share/workshops/papers/p670-ruge.pdf

Shield, B., & Dockrell, J. (2008). The Effects of classroom and environmental noise on children's academic performance. In 9th International Congress on Noise as a Public Health Problem (ICBEN), Foxwoods, CT.

Sotiropoulou, A., Karagiannis, I., Vougioukas, E., Ballis, A., & Bouki, A. (2020). Measurements and prediction of road traffic noise along high-rise building façades in Athens. *Noise Mapping*, *7*(1), 1-13.

World Health Organization. (2018). Environmental noise guidelines for the European region.

Zuo F., Li Y., Johnson S., Johnson J., Varughese S., Copes R., Liu F., Wu H. J., Hou R., Chen H. (2014), Temporal and spatial variability of traffic-related noise in the city of Toronto, Canada. Sci. Total. Environ., 15;472:1100-1107. https://www.ncbi.nlm.nih.gov/pubmed/24361745

Intercontinental Geoinformation Days

igd.mersin.edu.tr

FAHP and GIS based land use suitability analysis for agriculture in Aksaray City, Turkey

Süleyman Sefa Bilgilioğlu[*1]

[1]*Aksaray University, Faculty of Engineering, Department of Geomatics Engineering, Aksaray, Turkey*

Keywords
GIS
FAHP
Agriculture
Land use suitability

ABSTRACT

As a result of rapid population growth with the developing technology, resources are used unconsciously, and the need to use these resources effectively has emerged to transfer them to future generations. Land, which is a scarce resource, is among the most critical areas of use, agricultural lands. These areas meet the basic nutritional needs of living things, therefore, determining the suitability of the lands for agriculture, increasing productivity in agriculture, sustainability of resources, and contribution to the country's economy is of great importance. In the suitability analysis of agricultural areas, it is necessary to consider the land's specific use, the physical characteristics of the land, and the socio-economic and environmental characteristics in terms of land sustainability. Land use analysis is a complex process that includes multi-criteria decision-making analyses. This study aims to determine the areas suitable for agriculture in Aksaray city with Geographic Information System (GIS) and Fuzzy Analytical Hierarchy Process (FAHP). Nine parameters were used to determine the most suitable area. These parameters are; slope, aspect, elevation, proximity to water surfaces, drainage density, soil depth, land use capability, great soil group, land use capability sub-class. Expert opinions were taken in the weighting of the criteria and an agricultural suitability map was produced.

1. Introduction

For centuries, human beings have seen nature and resources as unlimited and used them unconsciously, causing severe damage to the environment and economy. As a solution to these problems, the concept of sustainable development, which is defined as ensuring the transfer of natural resources to future generations without being wholly consumed, has emerged. Sustainable development requires new land administration infrastructures and tools (Gazibey et al. 2014). Land management is one of these tools, and with the rapid population growth, the insufficient agricultural products obtained from the land and the development of industry, the land has been seen as a socially scarce resource and the need for effective management of this resource has arisen. As in Turkey, soil and natural resources are under threat due to the wrong planning of lands in many undeveloped and developing countries. As a result of unplanned land use, erosion and erosion in the soil occur as a result of flood-flood events. To benefit from natural resources with the highest efficiency, to ensure sustainable development in both rural and urban areas, in economic and social areas; that is, `Land Management' and `Land Management Systems' are used in order to produce the data needed in the preparation of policies for the efficient use of country resources (Inan 2021).

The agricultural sector has a significant role in Turkey's social, political and economic development. In the early stages of economic development, it is the dominant sector as in other societies. (Erdinç and Erdinç, 2000). Although the agricultural sector, which provides the most prominent primary food sources of human beings from the past to the present, is seen as a developed sector with mechanization today, its environmental damages are increasing. Therefore, sustainable agriculture has emerged to maintain productivity and benefit society in the long term. Sustainable agriculture includes the production of sufficient and quality foods at affordable costs, the economic vitality of agriculture, the protection of natural agricultural resources and the environment, and systems and practices that will improve the welfare of the world

* **Corresponding Author**

*(sbilgilioglu@aksaray.edu.tr) ORCID ID 0000-0002-0881-0396

Cite this study

Bilgilioğlu S S (2021). FAHP and GIS based land use suitability analysis for agriculture in Aksaray City, Turkey. 3rd Intercontinental Geoinformation Days (IGD), 90-93, Mersin, Turkey

population (NRC 2010). With the developing technology, the need for effective use of agricultural lands has arisen due to the increase in population day by day and the noticeable decrease in agricultural lands. For sustainable agriculture to thrive, it is essential to determine suitable areas for agriculture. Identifying suitable areas for agriculture is an essential issue in ensuring the protection of resources for future generations and ensuring economic development. Suitable site selection studies require the processing of large amounts of spatial data. Processing this data about site selection with traditional methods is a time-consuming and challenging task (Bilgilioglu et al. 2021). For these reasons, additional tools called Multi criteria decision making (MCDM) have been developed so that decision-makers can work more effectively and efficiently instead of land use planning, which is widely developed with traditional methods today. MCDM consist of multiple selection criteria and a management system that produces the most helpful solution in managing the criteria (Uyan and Yalpır 2016).

This study aims to determine land-use suitability analysis for agriculture in Aksaray City, Turkey. Another goal of this study is to create a model that can be transferred to the information system for farmers engaged in agriculture in Aksaray. In this context, it is aimed to increase productivity in agriculture, reduce environmental damage and revitalize the economy. Nine criteria were used to determine the most suitable area. These criteria are; slope, aspect, elevation, proximity to water surfaces, drainage density, soil depth, land use capability, great soil group, land use capability sub-class. As a result of the analysis made by using these factors, an agricultural suitability map was created for Aksaray city.

2. Method

In decision-making problems, MCDM models are the tools that allow the best decision to be taken as quickly and efficiently as possible by evaluating more than one criterion simultaneously. The primary purpose of this study is to determine the suitable areas for agriculture in Aksaray with an MCDM model. FAHP, an MCDM model, was used for this purpose.

Fuzzy set theory, first introduced by Zadeh (1965), allows the grading of membership functions. The primary purpose of the method is to formulate linguistic variables mathematically (Zadeh 1971). However, linguistic variables obtained from experts cannot be expressed numerically according to classical set theory and methods such as AHP based on this theory cannot reflect human thinking style. To solve these problems, FAHP has emerged by combining AHP and fuzzy logic theory.

There are many suggested BAHYs in the literature. In this study, the order analysis method, developed by Chang (1996) and frequently preferred in site selection studies, was used to solve MCDM problems.

Aksaray city was chosen as the study area. Agriculture is an essential source of livelihood in the study area. The region has a total area of 7626 km^2. The study area is shown in Figure 1.

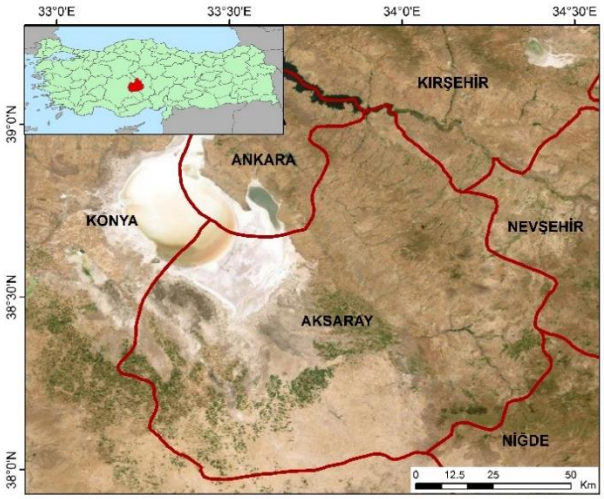

Figure 1. Study area

Different criteria have been determined as a result of the literature research to determine the agricultural land use suability (Akıncı et al. 2013; Pramanik 2016; Yalew et al. 2016; Memarbashi et al. 2017; Tashayo et al. 2020). These criteria are; slope, aspect, elevation, proximity to water surfaces, drainage density, soil depth, land use capability, great soil group, land use capability sub-class.

3. Results and discussion

The pairwise comparison matrix was created through interviews with experts and a literature study. In order to understand whether the pairwise comparisons created for the criteria are consistent or not, consistency analysis was performed and the results of the calculations; The consistency ratio (TO) = 0.0412 was calculated. It has been understood that the comparisons made are consistent since the obtained CTR value is less than 0.10. The criteria weights calculated with BAHP are shown in Table 1.

Table 1. Weights of criteria

Criteria	Weigths
Slope	0.084
Aspect	0.072
Elevation	0.025
Prox. To water surfaces	0.124
Drainage density	0.118
Soil depth	0.096
Land use capability	0.162
Great soil group	0.173
Land use capability sub-class	0.146

All data collected from different sources were converted to raster data with a pixel size of 20 m in the UTM (36-3) projection coordinate system. Criteria with different values are normalized in the range of "0-1" to be compared. A suitability index of "0" indicates that those regions are unsuitable, and "1" indicates that those regions are highly suitable. Maps of the criteria are shown in Figure 2.

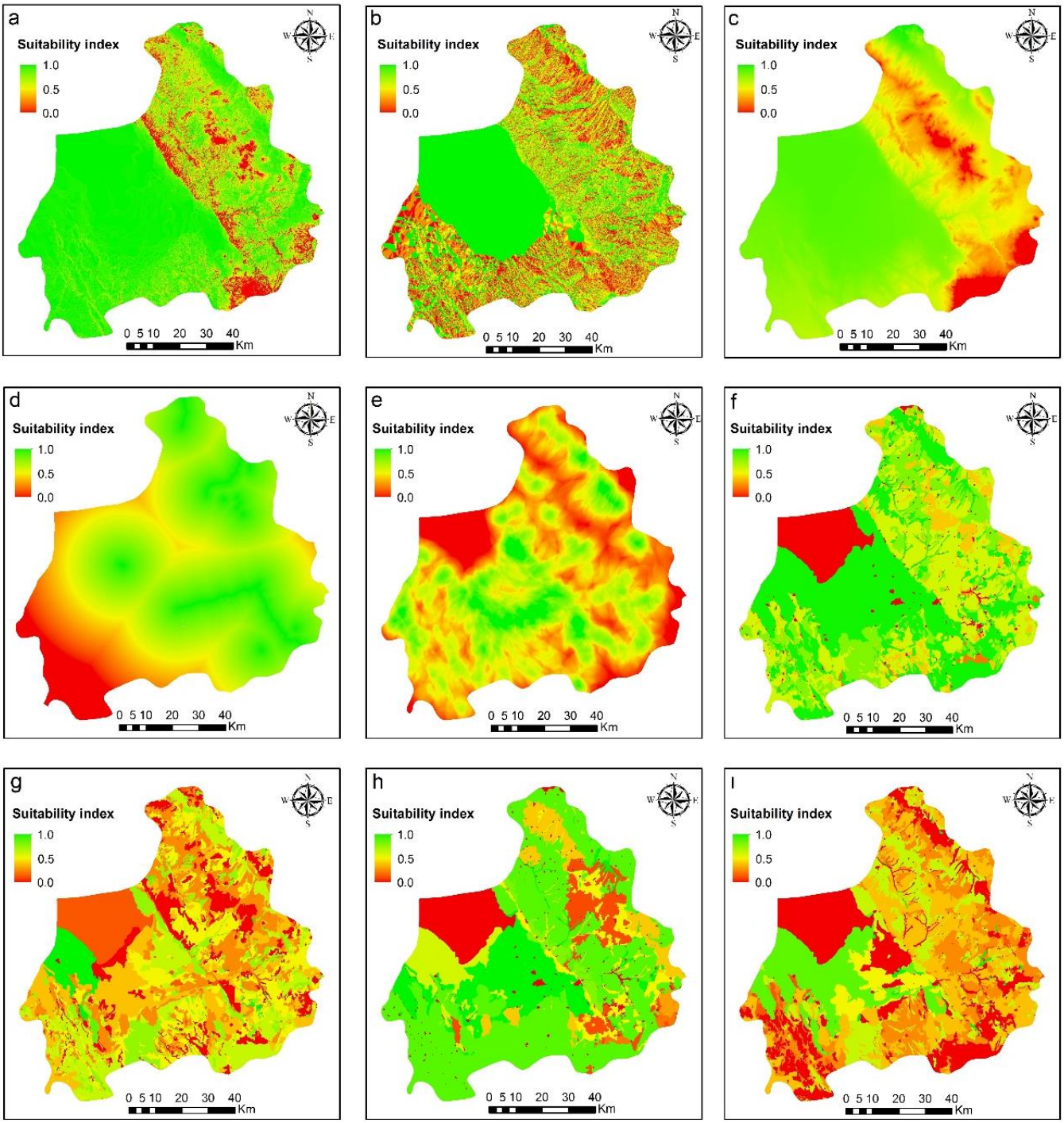

Figure 2. a: Slope b: aspect c: elevation d: proximity to water surfaces e: drainage density f: soil depth g: land use capability h: great soil group ı: land use capability sub-class

Nine criteria, which were normalized after being obtained, were combined using weighted linear combination overlay analysis in ArcGIS software, taking into account the weight values given in Table 1, and the suitability map shown in Figure 3 was produced.

The criterion weights show the relative importance of these criteria at the suitable site selection. In this context, it has been determined that land use capability, great soil group, land use capability sub-class are more effective in the agricultural land use suability analysis, while the elevation and aspect are less effective.

4. Conclusion

In this study, a model that can be evaluated effectively and quickly has been developed by integrating GIS and FAHP methods to determine the suitable areas for agriculture in Aksaray city. For this purpose, considering the characteristics of the study area, nine criteria were selected according to the expert opinions and the results of the literature study, their weights were calculated, and a suitability map was created with overlay analysis. It is thought that these results can be accepted as reasonable and applicable by managers and decision-makers, especially by farmers. Within the scope of sustainable agriculture, it is crucial

to determine the most suitable areas in terms of economy and productivity. For this reason, the criteria to be used must be determined very carefully and by experts. It is thought that the criteria used in this study will also be used in future studies in the Central Anatolian region.

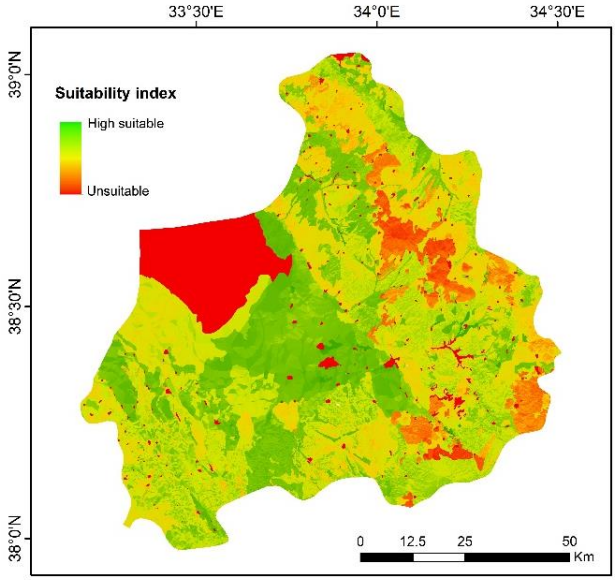

Figure 3. Agricultural land use suability map

Acknowledgement

This study has been supported by Research Fund of the Aksaray University. Project Number: 2020-018.

References

Akıncı H, Özalp A Y, & Turgut B (2013). Agricultural land use suitability analysis using GIS and AHP technique. Computers and electronics in agriculture, 97, 71-82.

Bilgilioglu S S, Gezgin C, Orhan O, & Karakus P (2021). A GIS-based multi-criteria decision-making method for the selection of potential municipal solid waste disposal sites in Mersin, Turkey. Environmental Science and Pollution Research, 1-17.

Chang, D Y (1996). Applications of the extent analysis method on fuzzy AHP. European Journal of Operational Research, 95(3), 649–655.

Erdinç Y & Erdinç M H (2001). "Türkiye'de Tarım Reformu". Eskişehir Osmangazi Üniversitesi Sosyal Bilimler Dergisi 2 (1)

Gazibey Y, Keser A, & Gökmen Y (2014). TÜRKİYE'DE İLLERİN SÜRDÜRÜLEBİLİRLİK BOYUTLARI AÇISINDAN DEĞERLENDİRİLMESİ. Ankara Üniversitesi SBF Dergisi, 69(3), 511-544.

Inan H I (2021). Spatial Data Model for Rural Planning and Land Management in Turkey. Journal of Agricultural Sciences, 27(3), 254-266.

Memarbashi E, Azadi H, Barati A A, Mohajeri F, Passel S V & Witlox F (2017). Land-use suitability in Northeast Iran: application of AHP-GIS hybrid model. ISPRS International Journal of Geo-Information, 6(12), 396.

National Research Council (2010). Toward sustainable agricultural systems in the 21st century. National Academies Press.

Pramanik M K (2016). Site suitability analysis for agricultural land use of Darjeeling district using AHP and GIS techniques. Modeling Earth Systems and Environment, 2(2), 56.

Tashayo B, Honarbakhsh A, Azma A, & Akbari M (2020). Combined fuzzy AHP–GIS for agricultural land suitability modeling for a watershed in southern Iran. Environmental Management, 66(3), 364-376.

Uyan M, Yalpır Ş, (2016) Site Selection for Medical Waste Sterilization Plants by Integration of Multi Criteria Decision Making Model with GIS. Afyon Kocatepe Üniversitesi Fen ve Mühendislik Bilimleri Dergisi, 16 (3), 642-654 https://doi.org/10.5578/fmbd.36294

Yalew S G, Van Griensven A, & van der Zaag P (2016). AgriSuit: A web-based GIS-MCDA framework for agricultural land suitability assessment. Computers and Electronics in Agriculture, 128, 1-8.

Zadeh L A (1965). Fuzzy sets. Information and Control, 8(3), 338–353.

Zadeh L A (1965). Quantitative fuzzy semantics. Information sciences, 3(2), 159-176.

Intercontinental Geoinformation Days

http://igd.mersin.edu.tr/2020/

SfM photogrammetry for monitoring urban developments

Chima Iheaturu[1], Chukwuma Okolie[2], Emmanuel Ayodele[2], Andy Egogo-Stanley*[2] Solomon Musa[3]

[1]*University of Bern, Institute of Geography, Switzerland*
[2]*University of Lagos, Faculty of Engineering, Department of Surveying and Geoinformatics, Lagos, Nigeria*
[3]*Federal Capital Development Authority, Department of Survey and Mapping, Abuja, Nigeria*

Keywords
UAV
SfM Photogrammetry
Google Earth
Historical Imagery
Urban Change Detection

ABSTRACT

Structure-from-Motion (SfM) Photogrammetry is a valid alternative to traditional photogrammetric methods. This study presents a simplified approach for mapping and monitoring of urban developments in a section of Kuje Area Council in Abuja, Nigeria, utilizing SfM Photogrammetry alongside Google Earth Historical Imagery. The capture of the UAV images in year 2020 was followed by the acquisition of the 2005 Google earth historical image, which was used in tracking and ascertaining the development over time. The two images (the 2020 and the 2005 images) were geometrically aligned to enhance comparison. Features identifiable in both images such as buildings and plots were vectorized. The analysis revealed that the Kuje Area Council has witnessed 120 building constructions in the past 15 years which on average implies 8 building constructions per year. The maps produced can facilitate well informed urban planning in the area.

1. Introduction

Structure-from-Motion (SfM) Photogrammetry is a valid alternative to traditional photogrammetric methods, Terrestrial Laser Scanning (TLS) and Airborne Laser Scanning (ALS) (Raoult et al., 2017). Its ability to extract high resolution and accurate spatial data using cheap consumer-grade digital cameras and smartphone cameras appears truly remarkable (Fonstad et al., 2013; Tarolli, 2014).

The deliverables of SfM include orthophotos, 3D point clouds and digital surface models (DSMs). With orthophotos, one can create maps and models of properties, construction projects, and earthworks. Orthophotos can also be used to extract features manually or semi-automatically for map creation or update (Koeva et al., 2018; Gbopa et al., 2021).

Orthophotos are extremely valuable for manual or semi-automatic feature extraction for map production or updating (Sarp et al., 2014), as well as for change detection (Gbopa et al., 2021; Koeva et al., 2018; Sarp et al., 2014). For city monitoring and disaster response, as well as updating maps and three-dimensional models, urban change detection is critical (Qin, 2014). When compared to satellite images, the use of unmanned aerial vehicle (UAV) images for change detection analysis offers obvious benefits in terms of spatiotemporal resolution and cloudlessness (Yao et al., 2019). Images with high spatial resolution are especially preferred for the accurate processing of variations in urban land cover. This requirement can be met by UAVs through the provision of precise data measurements (Jumaat et al., 2018; Franklin and Wulder, 2002).

This study presents a simplified approach for mapping and monitoring of urban developments in a section of Kuje Area Council in Abuja, Nigeria, utilizing SfM photogrammetry and Google Earth historical imagery.

2. Methods

2.1. Study area

The Kuje Area Council is one of the main sub-catchments of Abuja, the Federal Capital Territory (FCT) of Nigeria and is shown in Fig. 1 below. Kuje has an area of 1,644 km^2 and a population of 97,367 as of the 2006 census. Abuja is the capital city of Nigeria located in the center of the country within the Federal Capital Territory (FCT). Abuja's geography is defined by Aso Rock, a 400-meter (1,300 ft) monolith left by water erosion.

***Corresponding Author**

*(andyegogo@gmail.com) ORCID ID 0000-0002-2634-9046

Cite this study

Iheaturu C J, Okolie C J, Musa S, Ayodele E G & Egogo-Stanley A O (2021). SfM photogrammetry for land use change analysis in a sub-urban area of Nigeria. 3rdIntercontinental Geoinformation Days (IGD), 94-96, Mersin, Turkey

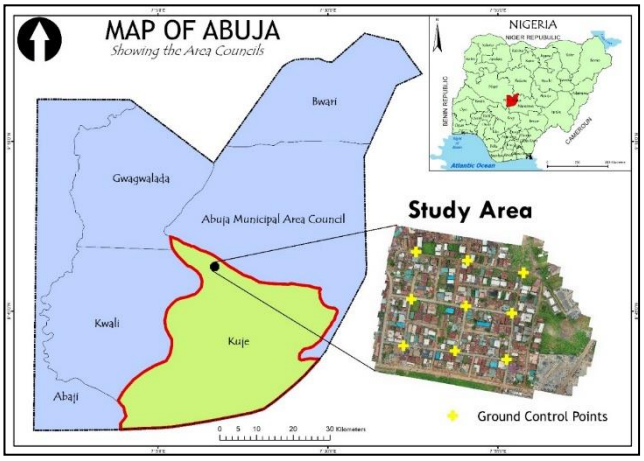

Figure 1. Map showing the location of the study area

2.2 Data acquisition and processing

The first step was to carry out a UAV flight of the study area and processing using the already established SfM method on the Pix4D Mapper software. The UAV flight was carried out in the year 2020. The flight path was predefined on the Dronedeploy software installed on the iPhone 7s device which was attached to the remote controller of the UAV. The degree of overlap maintained during the survey was 60% (forward) and 75% (side). A historical image for the year 2005 was also downloaded from Google Earth.

The two images (the 2020 and the 2005 images) were geometrically aligned to enhance comparison. The procedure was carried out using manually selected GCPs, where identifiable keypoints in both images were used to geometrically align the 2005 satellite image with the 2020 UAV image.

2.3 Image vectorization

The images were imported into ArcGIS software where the features in the area were converted into a series of points, lines and polygons by digitizing directly from the screen display on ArcMap. The main features vectorized in both images were the buildings (completed and uncompleted) and the plots (developed and undeveloped).

3. Results

The orthophoto generated from the Pix4Dmapper processing is shown in Fig. 2.

The orthophoto has a spatial resolution of 1.43 cm. A point-to-point validation done by the Pix4Dmapper software using 9 checkpoints showed an RMSE of 21.108mm, 25.347mm and 96.060mm in the x, y and z directions respectively. This shows that the orthophoto has high positional accuracy.

Digital maps were produced within the ArcMap environment, one for 2005 (see Fig. 3b) and the other for 2020 (see Fig. 3a).

The analysis of the changes in urban developments are shown in Table 1.

Figure 2. Orthophoto map of the study area – year 2020

Figure 3. (a) 2020 digitised map from the orthophoto (b) 2005 digitized map from the acquired Google Earth Historical Image

Table 1. Comparison between the maps

Class	Count - 2005	Count - 2020	Change
Completed buildings	185	313	128
Uncompleted buildings	15	7	-8
Total	200	320	120
Developed plots	182	234	+52
Undeveloped plots	68	16	-52
Total	250	250	-

4. Discussion

Several differences can easily be spotted in the distribution of features in both maps. The maps show the extent of undeveloped plots within the study area in green. At first glance, it can be observed that a lot of the undeveloped plots noticed in the 2005 map have now been developed.

In the year 2005, there were 200 buildings within the study area, 185 (92.5%) of which were already fully erected and 15 (7.5%) still under construction. The total number of buildings recorded in the year 2020 is 320, with 313 (97.81%) fully completed and 7 (2.19%) still under construction. As can be deduced from the table the period of study (2005 to 2020) has recorded an increase of 120 buildings. It is also observed from the map that all the buildings under construction in 2005 are now fully completed.

The study area was divided into 250 plots. In 2005, only 182 (72%) of the plots had been developed. The study period however witnessed the development of 52 more plots, bringing the total number of developed plots to 234 (93.60%).

5. Conclusion

This study conducted on a section of Kuje Area Council has shown that Unmanned Aerial Vehicles (UAVs) and SfM Photogrammetry can be effectively utilized for different purposes, such as urban change detection analysis and infrastructural planning and monitoring. The maps produced will facilitate a more informed decision-making process for various urban planning activities in the area.

Acknowledgements

Special thanks to everyone who contributed to the success of the work and to Pix4D for their free and accessible help files.

References

Fonstad, M.A., Dietrich, J.T., Courville, B.C., Jensen, J.L., & Carbonneau, P.E. (2013). Topographic structure from motion: a new development in photogrammetric measurement. Earth Surface Processes and Landforms, 38(4), 421-430.

Franklin, S. and M. Wulder (2002). "Remote sensing methods in medium spatial resolution satellite data land cover classification of large areas." Progress in Physical Geography 26(2): 173-205.

Gbopa, A. O., et al. (2021). "Unmanned Aerial Vehicles for Three-dimensional Mapping and Change Detection Analysis." Geomatics and Environmental Engineering 15(1).

Jumaat, N., et al. (2018). Land cover change mapping using high resolution satellites and unmanned aerial vehicle. IOP Conference Series: Earth and Environmental Science, IOP Publishing.

Koeva, M., et al. (2018). "Using UAVs for map creation and updating. A case study in Rwanda." Survey Review 50(361): 312-325.

Qin, R. (2014). "An object-based hierarchical method for change detection using unmanned aerial vehicle images." Remote Sensing 6(9): 7911-7932.

Raoult, V., Reid-Anderson, S., Ferri, A., & Williamson, J.E. (2017). How Reliable Is Structure from Motion (SfM) over Time and between Observers? A Case Study Using Coral Reef Bommies. Remote Sensing, 9(7), 740.

Sarp, G., et al. (2014). "An approach for detection of buildings and changes in buildings using orthophotos and point clouds: A case study of Van Erriş earthquake." European Journal of Remote Sensing 47(1): 627-642.

Tarolli, P. (2014). High-resolution topography for understanding Earth surface processes: Opportunities and challenges. Geomorphology, 216, 295-312.

Yao, H., et al. (2019). "Unmanned aerial vehicle for remote sensing applications—A review." Remote Sensing 11(12): 1443

Intercontinental Geoinformation Days

igd.mersin.edu.tr

Monitoring the change of coastline with remote sensing and GIS: a case study from Izmit and Gemlik Gulfs, Turkey

Tümay Arda*[1], Melis Uzar [1]

[1]*Yildiz Technical University, Faculty of Civil Engineering, Department of Geomatics Engineering, Istanbul, Turkey*

Keywords
Remote sensing
Change detection
Object-based classification
Satellite imagery

ABSTRACT

Humanity has preferred to settle down in coastal areas since its existence. This situation brings socioeconomic and cultural benefits, as well as a better quality of life for the development of civilizations. Although coastal areas are of great benefit to the population and economy, they can be affected by natural or artificial disasters such as erosion, tsunami, and flooding. Nowadays, it is necessary to monitor the change of the coastline to better manage coastal areas and take precautions against disasters. In recent years, instead of traditional measurement methods, changes in coastal areas can be more accurately determined by remote sensing methods and satellite imagery. In this study, an analyzes was conducted to detect the change in coast of Sea of Marmara, Gemlik and Izmit Gulf using Landsat-5 and Landsat-8 satellite imagery from 1985-2020. First, using the object-based classification method, rule sets were developed, and the coastal class was generated. During the segmentation and classification stages, parameter analyses were performed to create corresponding rules, and accuracy analyses were conducted. In the second stage of the study, the target classes were exported to the geographic information system environment and a coastal change detection analyzes was performed.

1. Introduction

It is vital to monitor the change of coastlines in in terms of sustainable development and environmental protection. In particular, global climate change, which is one of the most important environmental problems of our time caused as a result of human activities that directly or indirectly affect the composition of the atmosphere should be monitored over specific time periods and anticipating and modeling possible negative consequences of global climate change and taking precautions are among the priority issues at the national and international levels.

Coastal areas are one of the most vulnerable regions in the world affected by human impacts such as natural disasters and climate change. Erosion, flooding, rise of water level and unusual weather conditions are the most common natural disasters in these regions (Paravolidakis et al. 2018). However, a large part of the human population lives in coastal regions. On the coasts of the countries that belong to the European Union, this percentage reaches up to 20% of the total population (Koroglu et al. 2019). Because of coastal areas are so vulnerable to damage and are home to much of the human population, it is important to identify coastal areas and coastlines and monitor the changes of them. In addition, it is necessary to monitor the natural or artificial changes on the coast to create city models, prepare urban and regional plans, plan the use of natural resources in the region, thus protecting the environment.

When examining the studies conducted in recent years, it was found that the analyses of coastal changes are carried out using remote sensing methods. Sahin et al. 2021 used image processing techniques to determine the change in coastal settlements in the Izmit Gulf. Wang et al. 2017 observed coastal changes using Landsat imagery for the Ningbo coast. Hossain et al. 2021 derived the coastline of the southeast coast of Bangladesh and automatically detected the coastal change using NDWI. Abualtayef et al. 2021 used GIS and remote sensing techniques to determine the changes in the Gaza coast. Yan et al. 2021 observed coastal changes on the Yangcheng coast using the Digital Shoreline Analyzes System. In this study, within the framework of Gemlik and Izmit Gulfs of the Marmara region, coastal changes between 1985 and 2020 were monitored and the target classes are created using remote sensing methods and

* **Corresponding Author**

*(tumay.arda@gmail.com) ORCID ID 0000-0002-4526-8727
(auzar@yildiz.edu.tr) ORCID ID 0000-0003-0873-3797

Cite this study

Arda T & Uzar M, (2021). Monitoring the change of coastline with remote sensing: a case study from Izmit and Gemlik Gulfs, Turkey. 3rd Intercontinental Geoinformation Days (IGD), 97-100, Mersin, Turkey

coastal change analyses were performed by exporting them to the GIS environment.

2. Method

In this study, object-oriented rule-based classification method was used. In order to detect the coastal change, 4 different target classes have been created as land, water, island and lake. Digital image processing techniques and automated water extraction index were used in the development of rule set and classification. With the object-based classification method, the class assignment process is carried out by determining the appropriate parameter analyzes of the segmentation and classification stages. In addition, digital image processing techniques and appropriate indexes are used in the rule set created for automatic target classes extraction. In particular, the Automated water extraction index, which helps to distinguish between land and water classes, was used in the creation of the land class. This index, which is used for the separation of surface waters, was published by Feyisa et al, 2014. According to Feyisa et al, it consists of two equations. In this study, these two equations and difference of these equations is used.

$$AWEInsh = 4 * (Band2 - Band5) - 0.25 * Band4 + 2.75 * Band7 \quad (1)$$

$$AWEIsh = Band1 + 2.5 * Band2 - 1.5 * (Band4 + Band5) - 0.25 * Band7 \quad (2)$$

$$AWEIDiff = AWEInsh - AWEIsh \quad (3)$$

2.1. Study area and dataset

One of the most important factors in choosing the Izmit and Gemlik Bays as the study area is the rapid industrialization and urbanization in the coastal areas with the increase in human population density in this region in recent years. It is important for local and private administrations to determine the social, economic, and cultural effects of the coastal formations in this region.

Landsat Collection 2 Level 2 satellite images were used in the application. 2 Landsat-5 satellite images of 1985 and 2 Landsat-8 satellite images of 2020 were used. The features of the satellite images used are given in Table 1.

Table 1. Features of the satellites

	Landsat-5	Landsat-8
Spatial Resolution	30m	30m
Radiometric Resolution	16bit	16bit
Temporal Resolution	16 days	16 days
Year	1985	2020

In order to apply the same rule, set during classification in satellite images, bands with the same or close spectral range are used. The spectral ranges of the bands and the band aliases used during classification are shown in Table 2. In addition, the emissivity band in level-2 products is also used to increase the classification accuracy with EMIS alias.

Table 2. Bands and their respective spectral ranges.

Landsat-5 Bands	Spectral Range(μm)	Landsat-8 Bands	Spectral Range(μm)	Band Alias
SR_B1	0.45 – 0.52	SR_B2	0.452 – 0.512	BLUE
SR_B2	0.52 – 0.60	SR_B3	0.533 – 0.590	GREEN
SR_B3	0.63 – 0.69	SR_B4	0.636 – 0.673	RED
SR_B4	0.76 – 0.90	SR_B5	0.851 – 0.879	NIR
SR_B5	1.55 – 1.75	SR_B6	1.566 – 1.651	SWIR1
SR_B7	2.08 – 2.35	SR_B7	2.107 – 2.294	SWIR2

2.2. Process and analyzes

In this study, the workflow steps given in Fig. 1 were applied to perform shore extraction and change. In the proposed method, firstly, satellite images were normalized according to Landsat 4-7 Collection 2 Level 2 Science Product Guide and Landsat 8 Collection 2 Level 2 Science Product Guide. In the second step, the image is segmented with multiresolution segmentation. As a result of parameter analyzes for multiresolution segmentation, the most suitable parameters were found. The parameters used are given in Table 3.

Table 3. Multiresolution segmentation parameters.

Parameter		Value
Image Layer Weights		
	BLUE	0.25
	GREEN	0.25
	RED	0.25
	NIR	0.75
	SWIR1	0.50
	SWIR2	0.50
	EMIS	0.50
Scale		40
Shape/Color		0.3
Compactness		0.5

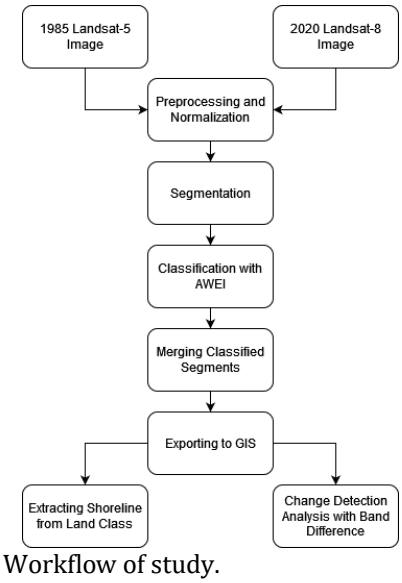

Figure 1. Workflow of study.

In the third step, the generated segments were classified using the Automated Water Extraction Index. The parameters used during this classification were calculated with the help of Equations 1 and 2. The land class was classified with the help of the difference (Equation 3) between the two obtained parameters. Pixels that do not have any value defined as out of classification are classified according to NIR < 0 value.

Land class assignments are made for values that meet the conditions of AWEIsh <-0.002 and AWEInsh – AWEIsh> 0.098. As a result of these two processes, unclassified pixels are assigned to the Sea class. Sea class clusters within the land class were assigned as lakes, and land class clusters within the sea class were assigned as islands. Results are given for 1985 in Fig.2, 2020 in Fig. 3.

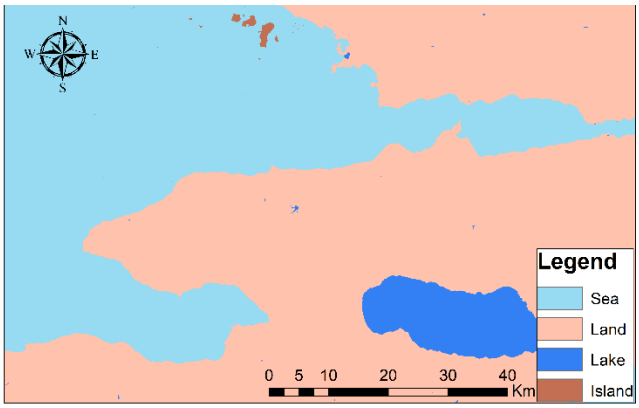

Figure 2. Classification results for 1985

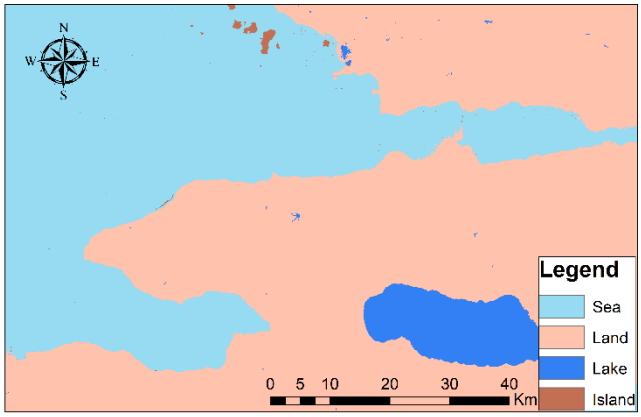

Figure 3. Classification results for 2020

In the fourth step, segments belonging to the same class were exported to the GIS environment as shapefiles using the merging algorithm. In the last step, the coastline was extracted using the vector data belonging to the Land class. Class files, which are vector data, were converted to raster data and the spatial variation in the coastal areas was determined by subtracting the two images from each other. The accuracy of the classification was calculated with error matrix based on TTA (train and test area) mask.

3. Results

In this study, 4 target classes, namely water, land, lake, and island, were created and the accuracy analyzes of these classes were carried out separately for every image used. Error matrices and overall accuracies is calculated with TTA Mask method. Accuracy analyzes result for 1985 images can be seen in Table 4. and Table 5., accuracy analyzes result for 2020 images can be seen in Table 6. and Table 7. Classification accuracies were 84% for Gulf of Izmit and 83% for Gulf of Gemlik in 1985, and 79% for Gulf of Izmit and 82% for Gulf of Gemlik in 2020. Kappa was calculated as 75% for Gulf of Izmit and 74% for Gulf of Gemlik in 1985, and 79% for Gulf of Izmit and 73% for Gulf of Gemlik in 2020.

Table 4. Error matrix based on TTA mask 1985-1

Class	Sea	Land	Lake	Island	Sum	User
Sea	386	46	23	10	465	0,830
Land	12	158	20	0	190	0,832
Lake	23	0	283	0	306	0,925
Island	33	3	0	32	68	0,471
Sum	454	207	326	42	1029	
Producer	0,850	0,763	0,868	0,762		
Overall Accuracy	0,835		Kappa	0.752		

Table 5. Error matrix based on TTA mask 1985-2

Class	Sea	Land	Lake	Island	Sum	User
Sea	286	33	13	12	344	0,831
Land	15	144	4	0	163	0,883
Lake	14	0	123	0	137	0,898
Island	22	12	0	44	78	0,564
Sum	337	189	140	56	722	
Producer	0,849	0,762	0,879	0,786		
Overall Accuracy	0,827		Kappa	0.743		

Table 6. Error matrix based on TTA mask 2020-1

Class	Sea	Land	Lake	Island	Sum	User
Sea	231	55	12	33	331	0,698
Land	12	273	20	0	305	0,895
Lake	9	1	91	0	101	0,901
Island	23	12	0	89	124	0,718
Sum	275	341	123	122	861	
Producer	0,840	0,801	0,740	0,730		
Overall Accuracy	0,794		Kappa	0.794		

Table 7. Error matrix based on TTA mask 2020-2

Class	Sea	Land	Lake	Island	Sum	User
Sea	309	55	21	9	394	0,784
Land	25	287	4	0	316	0,908
Lake	4	0	123	0	127	0,969
Island	40	14	0	55	109	0,505
Sum	378	356	148	64	946	
Producer.	0,817	0,806	0,831	0,859		
Overall Accuracy	0,818		Kappa	0.732		

After the classification process, the changes in the coastal areas were determined by the Band difference change analyzes. As a result of the analyzes, a total of 6.4 km^2 of landfill was detected in the coastal areas between 1985 and 2020.

4. Discussion

As a result of analyzes and evaluation, it was observed that majority of coastal change in the Gulf of Izmit was man made landfills. While it has been determined that there are landfill areas in the Gulf of Gemlik, it is seen that it does not cover as wide an area as the Gulf of Izmit. As seen in Fig. 5, new shipyards have been added to the existing shipyards. As a result of this addition, landfill of 1.72km^2 is made in Gulf of Izmit. Constructed ports on a landfill area of 1.3 km^2 can be seen in Fig.4 and Fig. 7. In Fig. 6, a filling of approximately 1 km^2 was made for the construction of the marina. When these changes in coastal region observed, it could be seen that these areas of landfill could become vulnerable to earthquakes, sea-level rise, and unusual weather effects. For this reason, coastal vulnerability of these regions for sea level rise

and natural hazards should be investigated. Data obtained from this study are important data source in terms of settlement and infrastructure planning in the region. By evaluating this data, it can be prevented that the changes made on the coast further deteriorate the integrity of the coast and increase its vulnerability.

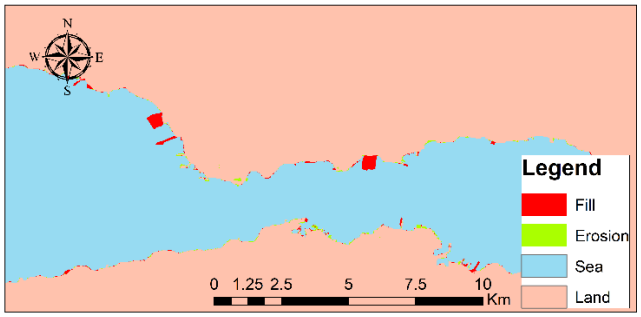

Figure 4. Change detection results for Gulf of Izmit.

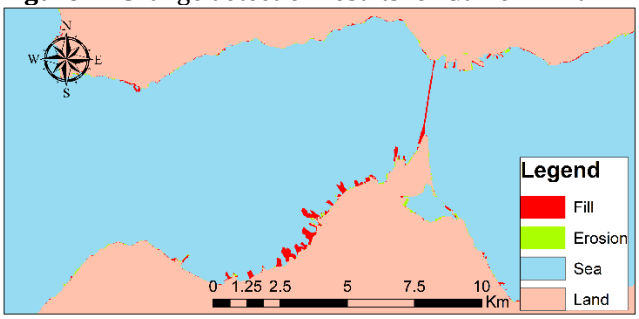

Figure 5. Change detection results for Gulf of Izmit.

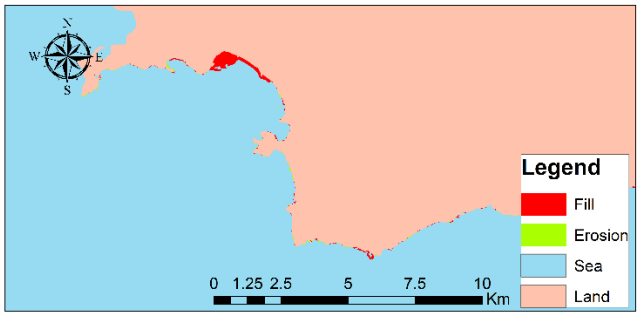

Figure 6. Change detection results for Gulf of Izmit.

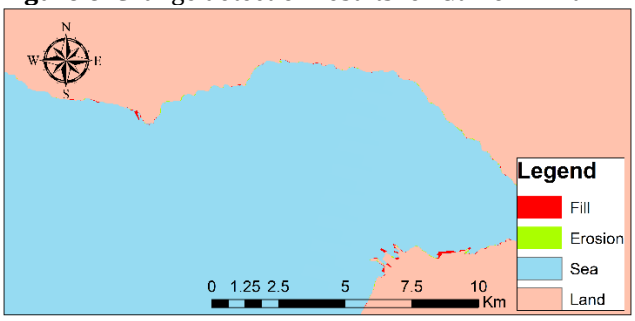

Figure 7. Change detection results for Gulf of Gemlik.

5. Conclusion

This paper presented an efficient workflow for monitoring the change of coastline with remote sensing and GIS. The proposed method in this study, based on object-based image analyzes, includes segmentation, analyzes and classification steps for the automatic shoreline extraction using Landsat data. The model parameters were determined with the analyses from the segmentation and classification steps to find the optimum strategy for extraction of shoreline and change detection analyzes. Accuracy analyzes was performed on the automatically extracted target classes of sea, land, lake, and island with kappa values 75% and 74% for 1985, and 79% and 73% for 2020. As a result of the change detection analyzes a total of 6.4 km^2 of landfill was detected in all study area between 1985 and 2020.

As a result of this study, it could be seen that identifying and monitoring the change of coastal areas and coastlines are important. In addition, it is necessary to monitor the natural or artificial changes on the coast to create city models, control of natural disasters, and crisis management, as well as for the tracking and prevention of unorganized urbanization and planning the use of natural resources in the region, thus protecting the environment. In future studies, rule set can be improved for better accuracy. With the usage of vulnerability indices, coastal vulnerability can be determined. In the next study, studies on coastal vulnerability will be conducted based on this study.

Acknowledgement

We would like to thank the Union of Marmara Municipalities for their scientific support to this study conducted within the scope of Yildiz Technical University master's thesis.

References

Abualtayef M, Rabou M A, Afifi S, Rabou A F, Seif A K & Masria A (2021). Change detection of Gaza coastal zone using GIS and remote sensing techniques. Journal of Coastal Conservation 25, 36. https://doi.org/10.1007/s11852-021-00825-4

Feyisa G L, Meilby H, Fensholt R, Proud S R (2014). Automated Water Extraction Index: A new technique for surface water mapping using Landsat imagery. Remote Sensing of Environment, 140, 23-35. https://doi.org/10.1016/j.rse.2013.08.029

Hossain S, Yasir M, Wang P, Ullah S, Jahan M, Hui S & Zhao Z (2021). Automatic shoreline extraction and change detection: A study on the southeast coast of Bangladesh. Marine Geology 441, 106628 https://doi.org/10.1016/j.margeo.2021.106628

Koroglu A, Ranasinghea R, Jimeneze J A & Dastgheiba A (2019). Comparison of Coastal Vulnerability Index applications for Barcelona Province. Ocean & Coastal Management, 178, 104799. https://doi.org/10.1016/j.ocecoaman.2019.05.001

Paravolidakis V, Ragia L, Moirogiorgou K & Zervakis M E (2018). Automatic Coastline Extraction Using Edge Detection and Optimization Procedures, Geosciences 8, 407. https://doi.org/10.3390/geosciences8110407

Sahin G, Cabuk S N & Cetin M (2021). The change detection in coastal settlements using image processing techniques: a case study of Korfez. Environmental Science and Pollution Research https://doi.org/10.1007/s11356-021-16660-x

Yan D, Yao X, Li J, Qi L & Luan Z (2021). Shoreline Change Detection and Forecast along the Yancheng Coast Using a Digital Shoreline Analysis System. Wetlands 41, 47. https://doi.org/10.1007/s13157-021-01444-3

Intercontinental Geoinformation Days

igd.mersin.edu.tr

Analysis of land-use/land-cover dynamics in Ibadan metropolis, Oyo State, Nigeria

Aliyu Zailani Abubakar[1], Swafiyudeen Bawa*[1], Yahaya Abbas Aliyu, Terwase Tosin Youngu, Usman Sani Ibrahim[1], Fatonyibo Ayo Olalekan[1]

[1]*Department of Geomatics, Faculty of Environmental Design, Ahmadu Bello University, Zara - Nigeria*

Keywords
Change Detection
Land use
Land cover
Landsat

ABSTRACT

One of the most important domains of human-induced environmental change has been identified as land transformation. Determining what feature of the land is changing to what, i.e., which land-use class is moving to the other, is a key part of change detection. With the availability of a broad spectrum of geospatial data and complex computing gadgets available to the geospatial world, land-use change detection for effective decision making is now simplified. Therefore, using Landsat TM, ETM+, and OLI, this work examined and tracked spatiotemporal variations in LULC patterns over the city of Ibadan, Nigeria, across three epochs (1999, 2009, and 2019). The build-up area seems to be the key driver for land usage, according to the findings of this research. The study suggests that the state government of the study region monitor urban sprawl and growth regularly, preferably using geospatial techniques to improve decision-making.

1. Introduction

The earth's surface is naturally covered with many land cover types, which are mostly distributed according to climatic patterns (Youneszadeh et al., 2015).

Land-use and land-cover (LULC) are two notions commonly used alternately when discussing LULC on the earth's crust (Hua, 2017; Mishra et al., 2020). Categorically, land-use affects Land cover and vice versa. The physical qualities of the earth's surface, such as plant, water, soil, and other physical features caused by human activities such as towns are referred to as Land Cover, while land-use refers to land exploited by humans for economic growth (Hua, 2017; Rawat & Kumar, 2015). LULC is a consequence of anthropogenic activities on the earth surface (Hao et al., 2021). In summary, the modification of the earth's lithosphere by the continuous activities of humans is referred to as LULC (Hassan et al., 2016).

LULC has certain implications that are not limited to increased land surface temperature, atmospheric pollution, etc. (Aliyu et al., 2020a). Therefore, for the long-term development and management of natural resources, accurate data on the rate of land-use pattern changes and urban expansion is critical (Das & Angadi, 2021). Based on this premise, the study analyses the variation in land-use-land cover dynamics in Ibadan Metropolis, Oyo state, Nigeria.

2. Study area

Ibadan City (Fig. 1) is located in the South-Western part of Nigeria. It lies between Latitudes 7º 20' 00'N and 7º 30' 00'N and Longitudes 3º 46' 00'E and 3º 60' 00'E. Ibadan metropolis covers an area of about 3080 km^2. By 2006 population census put the total population of Ibadan to 1,338,659 while the average population density was 435 persons per km^2 (Taiwo, 2021).

3. Method

3.1. Data acquisition

The study utilized Landsat satellite images. The Landsat satellite images were acquired for three epochs; 1999 (Landsat 5 TM), 2009 (Landsat 7 ETM+) and 2019 (Landsat 8 OLI) covering a period of 20 years. The images were checked to identify the scenes that had the minimum percentage of cloud cover before being acquired for the research. All the images were obtained

* **Corresponding Author**

(aliyuabubakarzailani@gmail.com) ORCID ID 0000-0002-8284-2601
* (bswafiyudeen@gmail.com) ORCID ID 0000-0002-2384-9432
(4yaaliyu@gmail.com) ORCID 0000-0001-8861-7109
(terwasey2000@gmail.com) ORCID ID 0000-0003-3707-5113
(saeeusmansai@gmail.com) ORCID ID 0000-0001-9810-9554
(fatalabaisboy@gmail.com) ORCID ID 0000-0003-3159-2013

Cite this study

Abubakar A Z, Bawa S, Aliyu Y A, Youngu T T, Ibrahim U S & Olalekan F A (2021) Analysis of land-use-land cover dynamics in Ibadan. Metropolis, Oyo state, Nigeria, 3rd Intercontinental Geoinformation Days (IGD), 101-104, Mersin, Turkey

from the United States Geological Survey (USGS) (glovis.usgs.gov).

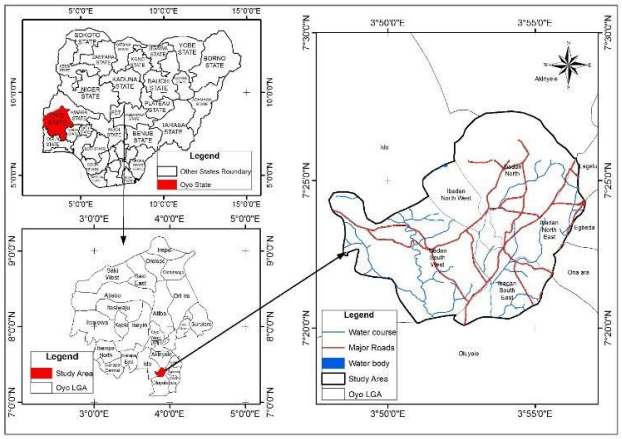

Figure 1. Study area showing the project location

3.2. Pre-processing and classification of images

Pre-processing of Landsat images before classification is very fundamental. Image pre-processing and classification. Since the data used were ortho-rectified, there was no need for geometric and radiometric correction. However, the datasets were registered to the geographic coordinate system (UTM Zone 31).

All bands of Landsat TM, ETM+ and OLI, excluding the thermal band, were considered for Layer stacking. The nature of these different bands had to be considered to decide which three-band combination would be most helpful for classification and visual interpretation. The false colour composite was employed in this project.

A supervised classification was performed on false colour composites (bands 4, 3 and 2 for Landsat 5 and 7 then bands 5, 4 and 3 for Landsat 8) into the following land-use and land-cover classes; Agricultural land, Built-up area, Forest cover, Grassland and Bare surfaces (see Table 1) (Anderson et al., 1976). Information collected during the field surveys was combined with the digital satellite image which was derived from SAS-planet software and used to assess the accuracy of the classification.

Table 1. Classification Scheme

S/N	Land-use/Land-cover	Description
1	Agricultural land	Lands used for farming (Plantation, cropland orchard)
2	Built-up land	Lands used for residential, industrial, commercial, etc.
3	Grassland/forest cover	Lands covered with natural vegetation
4	Bare surfaces	Lands devoid of vegetation, exposed soil
5	Water body	Areas with lakes, rivers, streams.

4. Results

4.1. Accuracy assessment of the classification

Accuracy analysis was undertaken using a confusion matrix otherwise referred to as the error matrix shown in Table 2. For each of the classes, statistical measures such as producer's accuracy and user's accuracy were used to calculate the overall accuracy and kappa index for the classification.

The overall accuracy of Landsat 5 TM (1999) was found to be 98% with a kappa index of 78%. Also, the overall accuracy of Landsat 7 ETM+ (2009) was found to be 98% with a kappa index of 79%. Finally, the overall accuracy of Landsat 8 OLI (2019) was found to be 99% with a kappa index of 79%.

Table 2. Classification accuracy assessment report

Land Cover Class	1999		2009		2019	
	Producer's Accuracy (%)	User's Accuracy (%)	Producer's Accuracy (%)	User's Accuracy (%)	Producer's Accuracy (%)	User's Accuracy (%)
Forest cover	100	100	100	100	100	100
Grass land	100	94	98	100	100	100
Built-up Area	94	98	100	94	100	94
Bare Land	100	100	94	94	100	100
Agricultural land	98	100	96	100	94	100
Overall Accuracy	**0.98**		**0.98**		**0.99**	
Kappa Statistic	**0.78**		**0.79**		**0.79**	

4.2. Changes in land cover between 1999 and 2019

Figs. 2, 3 and 4 show the LULC map of the study period for the area investigated for years 1999, 2009 and 2019 respectively. In 1999, built-up and agricultural land uses occupied about 45.71% and 31.65% of the total area, respectively. Additionally, Forest cover occupied only 8.24% of the total area. Bare land occupied 0.18%. Grassland occupied the third to the least class with 14.21% of the total area.

However, in 2009, the built-up area increased from 45.71% to 57.55% of the total area. This placed the built-up area as the class that witnessed the highest increase in 2009. The reason for the increase might be due to the influx of people in the area for businesses, industrial activities, academic purposes, to say the least. Thus, the built-up area witnessed a very high increase with a percentage annual rate of change of 11.83% between 1999 and 2009. Agricultural area reduced from 31.65% in 1999 to 27.22% in 2009. It was further observed that agricultural land decreased with a percentage annual rate of change of -4.44% of the total area. This decrease is due to an increase in the population of the area which led to increasing land-use for built-up areas. It was further observed that grassland decreased from 14.21% in 1999 to 11.56% of the total area in 2009. This may be attributed to the fact that the forest area was removed for built-up purposes. Further observation revealed that bare land decreased from 0.187% in 1999 to 0.12%. The negative change witnessed by bare land from 1999 to 2009 may be attributed to settlement and other activities. Finally, Forest cover also decreased from 8.24% in 1999 to 3.56% in 2009.

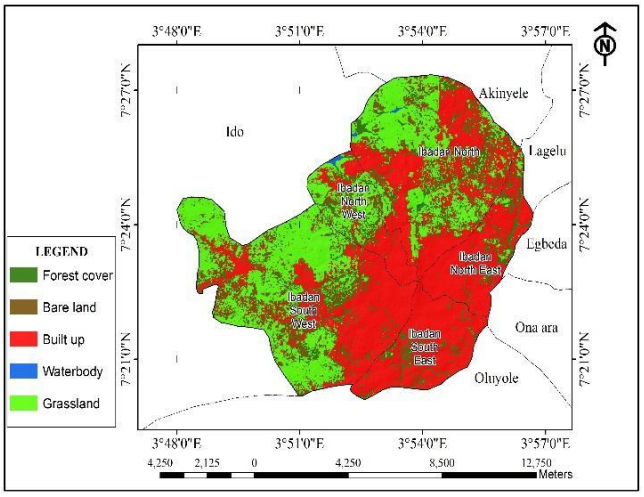

Figure 2. Land-use/land-cover Classification of Ibadan in 1999

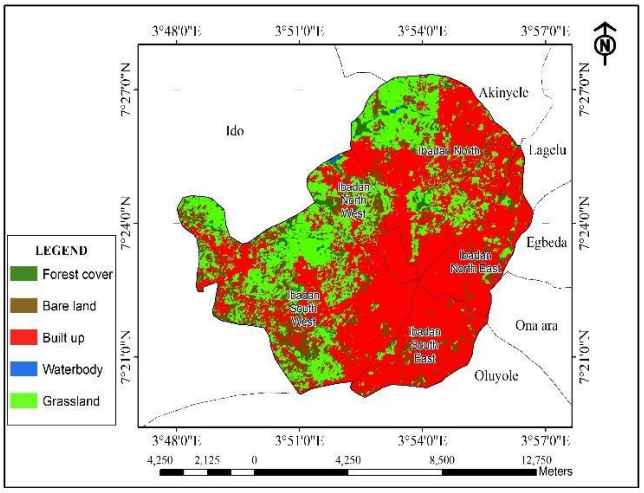

Figure 3. Land-use/land-cover Classification of Ibadan in 2009

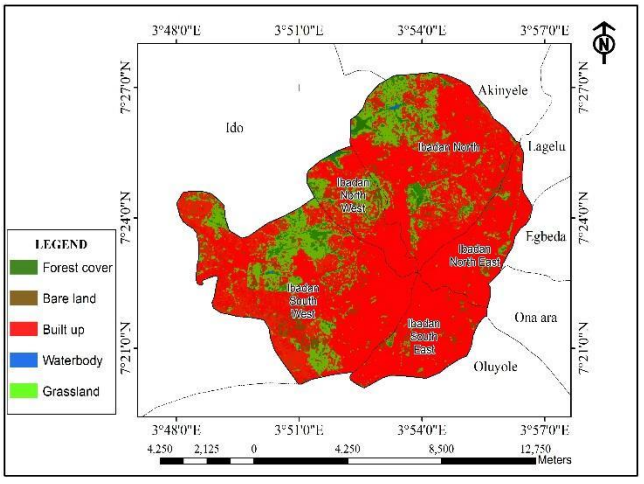

Figure 4. Land-use/land-cover Classification of Ibadan in 2019

In 2019, the built-up area increased from 57.55% to 76.39% with an annual rate of change of 18.85%. This annual increase is higher than all the other classes put together. The increase in the population of the area may be attributed to improvement in social and economic activities which has drawn people to the area for settlements. Meanwhile, agricultural land decreased from 27.22% to 16.09% with an annual rate of change of -11.13%. This decrease may not be unconnected with the increase in the population of the area which has transformed the Agricultural land to built-up and other human activities. It was also observed that Forest cover increased slightly from 3.56% to 3.81% with an annual rate of change of 0.26%. This may be attributed to the fact that natural forest was removed every year for farming activities and after harvesting, the farmlands were left fallow and eventually taken over by vegetation. As the population of the area increases, it is natural to expect a decrease in bare land in some areas. In this research, the bare land category decreased from 0.12% to 0.06% in 2019 with a rate of change of -0.12%. This increase may be attributed to the influx of people in the area who engage in other activities.

This analysis shows that there has been a steady increase in the built-up area between 1999 and 2019, which is of course as a result of expansion in residential areas coupled with more anthropogenic activities over the region resulting from dynamic population growth. The finding of this study also correlates with LULC studies conducted in other regions/states within Nigeria (Aliyu et al., 2020b).

5. Discussion

Fig. 5 shows the percentage summary of the LULC classification of Ibadan from 1999 to 2019. It further reveals that as human activities increased, the vegetation and other features began to decrease. This is because vegetation and bare lands were being replaced by built-up and other anthropogenic activities.

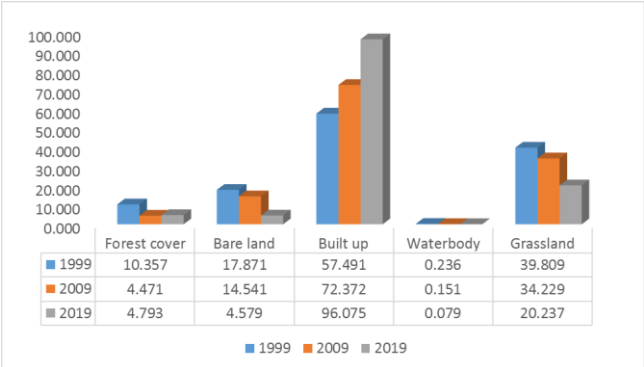

	Forest cover	Bare land	Built up	Waterbody	Grassland
1999	10.357	17.871	57.491	0.236	39.809
2009	4.471	14.541	72.372	0.151	34.229
2019	4.793	4.579	96.075	0.079	20.237

Figure 5. Land-use/land-cover Classification of Ibadan from 1999 to 2019

According to the classification of Landsat datasets of 1999, 2009 and 2019, the following classes; agricultural land, built-up, grassland, forest cover and bare land were mapped as land cover in the area. However, on visiting the site during ground-truthing, it was observed that areas that were classified as built-up consisted of the following; roads, residential areas, commercial areas, educational institutions, public offices and waste disposal sites, amongst others. The expansion in built-up areas, therefore, implies an expansion in settlements, roads, and offices, commercial and educational areas. Further observation revealed that some of the areas mapped as bare lands were originally vegetation and

areas affected by deforestation. These areas after being used for several years were left as fallow fields which appeared as bare land on the satellite images.

Based on these observations, it is evident that the main anthropogenic drivers in the study area are built-up areas. This is evident in Fig. 5. Within the built-up area, a series of anthropogenic activities were identified which includes roads, residential areas, commercial areas, educational institutions and public offices, amongst others.

6. Conclusion

This study assessed and monitored the spatiotemporal changes in LULC pattern across the metropolis of Ibadan, Nigeria at three epochs 1999, 2009 and 2019 using Landsat TM, ETM+ and OLI. The result of this study reveals that the major driver for land use is the build-up area.

The study recommends regular monitoring of urban sprawl and development by the state government of the study area especially with the aid of geospatial techniques for better decision making. This would go a long way in managing the excess and intrusion into

Acknowledgement

The authors wish to acknowledge USGS for making Landsat available.

References

Aliyu, Y. A., Youngu, T. T., Abubakar, A. Z., Bala, A., & Jesulowo, C. I. (2020a). Monitoring and forecasting spatio-temporal LULC for Akure rainforest habitat in Nigeria. *Reports on Geodesy and Geoinformatics*, *110*, 29–38. doi: 10.2478/rgg-2020-0009

Aliyu, Y. A., Azua, S., Youngu, T. T., Abubakar, A. Z., Bala, A., & Ngurnoma, N. Y. A multispectral assessment of sub-saharan cover change in Geidam Local Government Area (LGA), Yobe State, Nigeria. Journal of Geomatics and Environmental Research, 3(1), 15-33.

Anderson, J. R., Hardy, E. E., Roach, J. T., & Witmer, R. E. (1976). A land-use and land-cover classification system for use with remote sensor data. In *A land use and land cover classification system for use with remote sensor data* (USGS Numbered Series No. 964). doi: 10.3133/pp964

Das, S., & Angadi, D. P. (2021). Land-use-land-cover change detection and monitoring of urban growth using remote sensing and GIS techniques: A micro-level study. *GeoJournal*. doi: 10.1007/s10708-020-10359-1

Hao, S., Zhu, F., & Cui, Y. (2021). Land use and land cover change detection and spatial distribution on the Tibetan Plateau. *Scientific Reports*, *11*(1), 7531. doi: 10.1038/s41598-021-87215-w

Hassan, Z., Shabbir, R., Ahmad, S. S., Malik, A. H., Aziz, N., Butt, A., & Erum, S. (2016). Dynamics of land-use and land-cover change (LULCC) using geospatial techniques: A case study of Islamabad Pakistan. *SpringerPlus*, *5*(1), 812. doi: 10.1186/s40064-016-2414-z

Hua, A. K. (2017). Land-Use-Land-Cover Changes in Detection of Water Quality: A Study Based on Remote Sensing and Multivariate Statistics. *Journal of Environmental and Public Health*, *2017*, e7515130. doi: 10.1155/2017/7515130

Mishra, P. K., Rai, A., & Rai, S. C. (2020). Land use and land cover change detection using geospatial techniques in the Sikkim Himalaya, India. *The Egyptian Journal of Remote Sensing and Space Science*, *23*(2), 133–143. doi: 10.1016/j.ejrs.2019.02.001

Rawat, J. S., & Kumar, M. (2015). Monitoring land use/cover change using remote sensing and GIS techniques: A case study of Hawalbagh block, district Almora, Uttarakhand, India. *The Egyptian Journal of Remote Sensing and Space Science*, *18*(1), 77–84. doi: 10.1016/j.ejrs.2015.02.002

Taiwo, O. J. (2021). Modelling the spatiotemporal patterns of urban sprawl in Ibadan metropolis between 1984 and 2013 in Nigeria. *Modeling Earth Systems and Environment*, 1-20. doi: 10.1007/s40808-021-01095-7

Youneszadeh, S., Amiri, N., & Pilesjö, P. (2015). The effect of land-use change on land surface temperature in the Netherlands. *International Archives of the Photogrammetry, Remote Sensing and Spatial Information Sciences - ISPRS Archives*, *40*(1W5), 745–748. doi: 10.5194/isprsarchives-XL-1-W5-745-2015

Intercontinental Geoinformation Days

igd.mersin.edu.tr

Fully automated drought analysis from the products of the moderate resolution imaging spectroradiometer (MODIS)

Ali Levent Yagci[*1]

[1]*Gebze Technical University, Faculty of Engineering, Department of Geomatics Engineering, Kocaeli, Turkey*

Keywords
Remote sensing
Python
Agricultural Drought
MODIS

ABSTRACT

Remote sensing data have become one of the important data sources to monitor and analyze drought. However, how to access, retrieve, process, and analyze Earth observation data, and discover drought from them in an automated manner is a big challenge to researchers. In this study, one of the most common drought monitoring and analysis methods was implemented to streamline and automate the process of accessing to and downloading from the data server, pre-processing the data, calculating drought indices, and producing the drought maps following the well-known hierarchical concept: Data, Information, and Knowledge. All developed modules can act as independent components. They can also be seamlessly integrated into the process or reused by other researchers. Several open-source libraries in Python such as Geospatial Data Abstraction Library (GDAL) and Numerical Python (NumPy) were extensively exploited in the implementation. With the help of these libraries, one of the satellite data-derived vegetation indices named the Vegetation Health Index was calculated.

1. Introduction

In the recent two decades, monitoring drought using remote sensing data has gained too much attention because remote sensors onboard satellites acquire earth observation data continuously across the globe once a day, and they collect observations about all parts of the world in great spatial detail. These advantages in spatial and temporal resolution make satellite data become a common and popular source to monitor territorial vegetation conditions.

Drought monitoring methodology based on vegetation was first introduced by (Tucker and Choudhury 1987) that reduced photosynthetic activity can result from drought and such declines in photosynthetic capacity of terrestrial Earth surface can be detected by satellite remote sensing. The normalized difference vegetation index (NDVI) was found to be associated with green leaf area (Tucker 1979) and vegetation abundance (Price 1992). Therefore, It was proposed to quantify photosynthetically active biomass (Tucker 1979). Furthermore, the NDVI has been used extensively in global and regional drought monitoring applications (Kogan 1993; Yagci, Di, and Deng 2013; Deng et al. 2013; Yagci, Di, and Deng 2015).

Vegetation condition index (VCI) was calculated from NDVI which were obtained from NOAA's the Advanced Very High Resolution Radiometer (AVHRR) sensor in order to highlight weather impacts on vegetation (Kogan 1993). Later, two new indices were introduced by (Kogan 1995), Temperature Condition Index (TCI) and Vegetation Health Index (VHI). These indices have been very helpful and useful to detect important historical droughts, so they have been utilized for this purpose by many scientists (Quiring and Ganesh 2010; Singh, Roy, and Kogan 2003; Liu and Kogan 1996). NASA's Moderate Resolution Imaging Spectroradiometer (MODIS) sensors are currently available in space and have been acquiring Earth observation data since 2000. Originally, aforementioned indices were calculated from AVHRR data, in this study, datasets from the MODIS sensors will be used because of their better radiometric accuracy, and higher spatial and temporal resolution than the AVHRR data.

In brief, the drought methodology was built on the premise that vegetation health dynamics are good indicators of weather impacts on natural and cultivated vegetation such that unhealthy vegetation likely occur as a result of adverse weather.

* **Corresponding Author**

*(alyagci@gtu.edu.tr) ORCID ID 0000-0003-1094-9204

Cite this study

Yagci A L (2021). Fully automated drought analysis from the products of the moderate resolution imaging spectroradiometer (MODIS) 3rd Intercontinental Geoinformation Days (IGD), 105-108, Mersin, Turkey

2. Data & methods

2.1. Satellite data

Each MOD09Q1 file in Hierarchal Data Format (hdf) contains two tiled surface reflectance layers, Red-Visible (Red) band and Near Infrared Band (NIR), and one corresponding quality layer regarding the first two bands in 250m spatial resolution. Each product is collected by the MODIS sensor flown on NASA's Terra satellite. The first three letters of the product name indicate which satellite is MODIS instrument mounted and the last three letters after the dot denote the collection number. In this case, "MOD" means the MODIS instrument on Terra satellite, while "005" indicates 5th collection. Moreover, reflectance values in Red bands are collected at 620-670 nm channel, while surface reflectance values in NIR bands are acquired at 841-876 nm portion of the Electromagnetic spectrum. Each MOD09Q1 tile with the size of 4800 by 4800 is projected onto the sinusoidal projection. This product is essentially 8-day composite product, meaning that each pixel represents a period of 8-day. The best possible observation whose characteristic features are cloud/cloud shadow-free, aerosol-free and low view angle, from 8-day interval is assigned to the final composite product (Vermote, Kotchenova, and J. P. Ray 2011).

The MOD11A2 is a Land surface Temperature (LST) & Emissivity product derived from the MODIS sensor onboard NASA's Terra satellite. It is an 8-day composite product in 1km (1000m) spatial resolution. Each pixel is comprised of an average of clear sky observations in 8-day period unlike the MOD09Q1.005 products. Each tile with 1200 by 1200 dimension is projected onto the sinusoidal like the MOD09Q1.005 product. In total, each MOD11A2 hdf file contains 12 different layers. However, the daytime LST layer and its corresponding quality layer are needed for this application. All LST products have been validated with ground-truth (Wan 2007).

The MOD44W is a Land-water mask in 250m resolution derived from several sources such as the Shuttle Radar Topography Mission's (SRTM) Water Body Dataset (SWBD) and the MODIS dataset from NASA's terra satellite. There is only one version of this dataset projected onto sinusoidal projection in 250m spatial resolution for each MODIS tile. This product is an improved version of land-water mask products derived from spectral data alone because the RADAR offers cloud-penetrating capability unlike the MODIS to detect terrestrial water bodies (Carroll et al. 2009).

2.2. The vegetation indices

Several vegetation indices from NDVI and LST were utilized in our study. They are NDVI, VCI, TCI and VHI. The NDVI is reliable and accurate measure of vegetation vigor or greenness (Kogan 1993).

The VCI is used to extract the weather impacts on vegetation in the NDVI. Low VCI values indicate bad vegetation health due to adverse weather conditions, whereas high VCI values indicate healthy vegetation due to favorable weather conditions (Kogan 1993). It can be calculated by the following equation:

$$VCI_{ij} = \frac{(\mathrm{NDVI}_{ij} - \mathrm{NDVI}_{min})}{(\mathrm{NDVI}_{max} - \mathrm{NDVI}_{min})}\ x\ sf \qquad 1$$

where NDVI_{max} and NDVI_{min} are multi-year maximum and minimum NDVI values for a pixel, respectively. NDVI_{ij} is the NDVI value collected on the date of interest in yyyyddd (eg. 2011177 or 06/26/2011) format, year with trailing Julian day. For example, for the date of 2011177, the $\mathrm{NDVI}_{i=2011,j=177}$ value should be inserted into (2) and the VCI will take this form $\mathrm{VCI}_{i=2011,j=177}$. Finally, the sf, scale factor, can be any positive number. The suggested scale factor is 100, but 250 is used in this study to get more precision. Another index, TCI was designed to compensate the situation when both the NDVI and the VCI is depressed as a result of excessive soil wetness. In this case, small VCI value is interpreted as drought mistakenly. The TCI helps solve this shortcoming of VCI (Kogan 1995). The TCI can be computed by this formula to assess drought conditions;

$$TCI_{ij} = \frac{(\mathrm{LST}_{max} - \mathrm{LST}_{ij})}{(\mathrm{LST}_{max} - \mathrm{LST}_{min})}\ x\ sf \qquad 2$$

where LST_{max} and LST_{min} are multi-year maximum and minimum LSTs for a pixel, respectively. The date numbering of LST_{ij} and TCI_{ij} are exactly similar to the VCI's date numbering explained in the previous paragraph. The sf, scale factor, is exactly same with the scale factor utilized in the (1). It is important to note that high LST indicates low vegetation water content (Choudhury and Tucker 1987) as opposed to the premise that high NDVI signals healthy vegetation. In other words, negative relationship between NDVI and LST exists during warm months (Sun and Kafatos 2007). For this reason, this negative relationship is reflected in the TCI equation by subtracting the current value from maximum instead of subtracting minimum from the current value than so that both low values of TCI and VCI identify bad vegetation due to adverse weather. The VHI as a final index is designed to combine the reports from both VCI and TCI. It is an additive combination of the VCI and TCI as depicted by the following equation;

$$VHI_{ij} = a\ x\ VCI_{ij} + (1 - a)\ TCI_{ij} \qquad 3$$

where α is the empirical constant that defines contributions from two indices. The recommended constant for α in (3) is 0.5 (Bhuiyan, Singh, and Kogan 2006).

3. Implementation

In this section, implementations of the automated drought monitoring and analysis from MODIS data will be described. The open-source python modules and libraries are used in the development. Users who are familiar with the ESRI's ArcGIS can consider a Python module as a tool like tools in the ArcGIS toolbox.

3.1. Data download

The data download module is implemented, and users can use their functions to download the MODIS data of interest by calling the function named *dailyDownload*. This function needs three arguments

including the link of FTP server of MODIS data with the specified date, the full target path on the local machine, and the name of the MODIS tiles. The *dailyDownload* function will resolve the server's address, the folder on the server where the MODIS data are stored and the date of the MODIS data from the given ftp address. Then, the function will go into the folder and search the requested tiles. Finally, the requested tile for the specified date will be retrieved and saved into the given directory on user's local machine. To download multi-date MODIS data, a simple for loop is adequate by feeding the parameter of the ftp address with new dates.

3.2. The calculation of vegetation indices

Vegetation indices such as NDVI, VCI, TCI and VHI were implemented as separate generic functions or tools. The implemented python function can be regarded a tool that takes arguments from users and works with any type of data derived from different sensors. The NDVI tool takes RED and NIR band parameters along with land/water mask and output file parameters. In the end, water bodies are masked out and only land is preserved after the NDVI computation. Furthermore, the land/water mask parameter is designed to be an optional parameter. Like the NDVI function, the VCI tool takes a list of input files and their corresponding output files. Another implemented vegetation index function is the TCI function which takes a list of LST files and their corresponding output files that indicate where the TCI results will be saved into. The last function is the VHI. This function takes one VCI file and one TCI file. Obviously, both files must be acquired on the same date. These VI functions implemented based on the MODIS sensor data are generic functions so they will be able to work with Earth observation data from other Remote Sensing instrument (e.g., AVHRR).

3.3. Utility functions

The spatial resolutions of MOD11A2 and MOD09Q1 products are different. All bands such as Red band and NIR band in MOD11A2 product are in 250m resolution, whereas all bands in MOD09Q1 product are in 1000m (1km) spatial resolution. Therefore, each VCI result derived from MOD11A2 products has 4800*4800 pixels, while each TCI result derived from MOD09Q1 products has 1200*1200 pixels. Resampling function was implemented to resolve the dimension mismatch between VCI and TCI products prior. Moreover, another utility function, named *gdalMerge*, was developed from Geospatial Data Abstraction Library's (GDAL) gdal_merge.py program to mosaic tiled-based VHI results tiles into one. In addition, a utility function, named *extractbyshp*, was implemented to extract the VHI data for the specified administrative district from the large VHI files.

3.4. Drought classification

The threshold value to classify drought were recommended by (Kogan 2002). However, the threshold in the drought classification scheme were modified because the data range of the VHI-based drought maps is between 0 and 250 as opposed to recommended VHI's data range between 0 and 100 by (Kogan 2002). Moreover, the drought severity classes are adopted from the classification scheme of the US Drought Monitor (USDM).

4. Results

All implemented tools were imported and integrated into a "py" file, so that the whole process can run in an automated manner after the required parameters are fed. Here, the state of Texas, United States (US) was chosen to test the automated code for a specific Julian day, 177.

Firstly, the code begins to download satellite data from NASA's server and saved them into separate directories whose names are MOD09Q1, MOD11A2 and MOD44W.Next, all files with their full paths in the MOD09Q1 and MOD44W directories are written into different lists and then the NDVI function loops through the lists and calculates one NDVI image for each MOD09Q1 product and its corresponding water mask extracted from MOD44W products. For the TCI function, all LST files with the same pattern are noted in a list and fed to the TCI function, while all NDVI files with the same pattern are entered to the VCI function. After all VCI and TCI data are computed, all results in TCI and VCI directories with their full paths are written into separate lists. The VHI function loops through these two lists and calculates VHI results. After completion of VHI calculation, merge operation takes place by mosaicking five tiles in the study area. Later, extraction of Texas by state's administrative GIS shape file from mosaicked large VHI results one by one is completed. Consequently, drought classification scheme is applied to each VHI results. The flow of the drought model is well illustrated in Figure 1. One example VHI map is given in Figure 2.

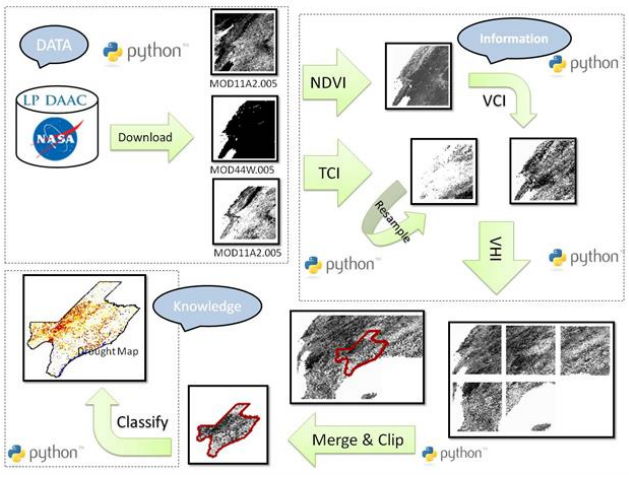

Figure 1. Flow chart of the study

5. Conclusion

In this study, satellite data-based drought indices calculation to detect droughts was successfully automated from data download through final drought products. The whole process is streamlined in the Python modules. An example of drought monitoring and analysis for the state of Texas is given to demonstrate this

method. The most prominent feature of the Python programming language is that programmer doesn't necessarily implement every function from scratch. Freely available packages implemented by other programmers in Python such as NumPy, SciPy (Scientific tools for Python) and GDAL can be downloaded from the internet. Later, users can integrate or reuse desired functions in these packages into their own programs. This integration is so intuitive and seamless that only a single line, importing user-desired function from the package, is adequate. Besides freely available open-source libraries, built-in methods in Python allow to list files in directories, search for a specific pattern in filenames and record filenames that match the pattern in lists very quickly and easily.

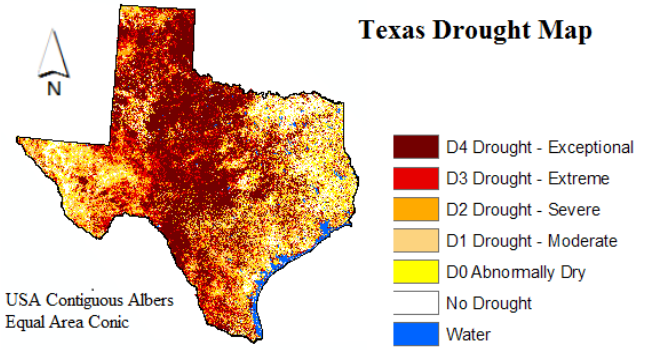

Figure 2. Resulting Drought Map

References

Bhuiyan, C, R Singh, and Felix N. Kogan. 2006. "Monitoring Drought Dynamics in the Aravalli Region (India) Using Different Indices Based on Ground and Remote Sensing Data." *International Journal of Applied Earth Observation and Geoinformation* 8 (4): 289–302. doi:10.1016/j.jag.2006.03.002.

Carroll, Mark, Charlene DiMiceli, John Townshend, Praveen Noojipady, and Robert Sohlberg. 2009. *UMD Global 250 Meter Land Water Mask User Guide*. College Park, Maryland.

Choudhury, B. J., and C.J. Tucker. 1987. "Monitoring Global Vegetation Using Nimbus-7 37 GHz Data Some Empirical Relations." *International Journal of Remote Sensing* 8 (7): 1085–1090. doi:10.1080/01431168708954754.

Deng, Meixia, Liping Di, Weiguo Han, Ali Levent Yagci, Chunming Peng, and Gil Heo. 2013. "Web-Service-Based Monitoring and Analysis of Global Agricultural Drought." *Photogrammetric Engineering & Remote Sensing* 79 (10): 929–943. doi:10.14358/PERS.79.10.929.

Kogan, F. 1993. "Development of Global Drought-Watch System Using NOAA/AVHRR Data." *Advances in Space Research* 13 (5). Elsevier: 219–222. doi:10.1016/0273-1177(93)90548-P.

Kogan, F. 1995. "Application of Vegetation Index and Brightness Temperature for Drought Detection." *Advances in Space Research* 15 (11). Elsevier: 91–100. doi:10.1016/0273-1177(95)00079-T.

Kogan, F. 2002. "World Droughts in the New Millennium from AVHRR-Based Vegetation Health Indices." *Eos, Transactions American Geophysical Union* 83 (48): 557. doi:10.1029/2002EO000382.

Liu, W. T., and F. N. Kogan. 1996. "Monitoring Regional Drought Using the Vegetation Condition Index." *International Journal of Remote Sensing* 17 (14). Taylor & Francis: 2761–2782. doi:10.1080/01431169608949106.

Price, John C. 1992. "Estimating Vegetation Amount from Visible and near Infrared Reflectances." *Remote Sensing of Environment* 41 (1): 29–34. doi:10.1016/0034-4257(92)90058-R.

Quiring, Steven M., and Srinivasan Ganesh. 2010. "Evaluating the Utility of the Vegetation Condition Index (VCI) for Monitoring Meteorological Drought in Texas." *Agricultural and Forest Meteorology* 150 (3): 330–339. doi:10.1016/j.agrformet.2009.11.015.

Singh, Ramesh P., Sudipa Roy, and F. Kogan. 2003. "Vegetation and Temperature Condition Indices from NOAA AVHRR Data for Drought Monitoring over India." *International Journal of Remote Sensing* 24 (22): 4393–4402. doi:10.1080/0143116031000084323.

Sun, Donglian, and Menas Kafatos. 2007. "Note on the NDVI-LST Relationship and the Use of Temperature-Related Drought Indices over North America." *Geophysical Research Letters* 34 (24): 1–4. doi:10.1029/2007GL031485.

Tucker, Compton J. 1979. "Red and Photographic Infrared Linear Combinations for Monitoring Vegetation." *Remote Sensing of Environment* 8 (2). Elsevier: 127–150. doi:10.1016/0034-4257(79)90013-0.

Tucker, Compton J., and Bhaskar J. Choudhury. 1987. "Satellite Remote Sensing of Drought Conditions." *Remote Sensing of Environment* 23 (2): 243–251. doi:10.1016/0034-4257(87)90040-X.

Vermote, E. F., S. Y. Kotchenova, and J. P. Ray. 2011. *MODIS Surface Reflectance User's Guide v1.3*.

Wan, Zhengming. 2007. *Collection-5 MODIS Land Surface Temperature Products Users' Guide*.

Yagci, Ali Levent, Liping Di, and Meixia Deng. 2013. "The Effect of Land-Cover Change on Vegetation Greenness-Based Satellite Agricultural Drought Indicators: A Case Study in the Southwest Climate Division of Indiana, USA." *International Journal of Remote Sensing* 34 (20): 6947–6968. doi:10.1080/01431161.2013.810824.

Yagci, Ali Levent, Liping Di, and Meixia Deng. 2015. "The Effect of Corn–Soybean Rotation on the NDVI-Based Drought Indicators: A Case Study in Iowa, USA, Using Vegetation Condition Index." *GIScience & Remote Sensing* 52 (3): 290–314. doi:10.1080/15481603.2015.1038427.

Intercontinental Geoinformation Days

igd.mersin.edu.tr

Development of a user-friendly program:" Real-Time image properties display"

Olaleye James Bola [1], Alabi Abiodun Olawale[1], Alademomi Alfred Sunday[1,2] Olatayo Damilola Emmanuel [*1] Salami Tosin Julius[1]

[1]*University of Lagos, Faculty of Engineering, Department of Surveying and Geoinformatics, Lagos, Nigeria.*
[2]*Center for Multidisciplinary Research and Innovation, Suite C59, New Bannex Plaza, Wuze 2, Abuja, Nigeria.*

Keywords
Photogrammetry
Image Processing
Computer Vision
Feature extraction
MATLAB

ABSTRACT

Image processing is a well-established field with researches involving its numerous applications and techniques constantly updated. However, there exists a gap in knowledge on the processing of images in real-time. Lately, real-time image processing has grown in applications. Applications which include face detection, traffic management, etc. However, processing of real-time images may require two or more of these toolboxes which may not be compiled either because of the complex coding involved or the low technical expertise of the user. Hence, the need for the design of a user-friendly program that can display the properties of digital images in real-time which this research aims to explore. The user-friendly program will require low technical expertise to operate. It will also collate together useful digital image processing toolboxes. To develop the above program, MATLAB software was used. The program was then compiled and tested with images acquired from various sources, the results of which successfully displayed various properties of images through operations like object detection and face detection in real-time.

1. Introduction

Digital image processing consists of the manipulation of digital images using digital computers (Silva & Mendonca, 2005). It typically involves filtering or enhancing an image using various types of functions in addition to other techniques to extract information from the images (Padmappriya & Sumalatha, 2018).

Some of the important applications of digital image processing include remote sensing, face detection, edge detection, feature extraction, computer vision, forecasting, optical character recognition (Padmappriya & Sumalatha, 2018). Even the multimedia system heavily relies on digital image processing. Despite growing applications of real-time image processing like face recognition, object detection. There exists a gap in knowledge on the processing of images in real-time. Also, processing of real-time images may require two or more of these toolboxes which may not be easily together easily accessed either because of the complex coding involved or the low technical expertise of the user. Hence, the need for the design of a user-friendly program that will display the properties of digital images in real-time which this project aims to explore. The user-friendly program will require low technical expertise to operate. It will also collate together useful digital image processing toolboxes.

During the time of the growth of image processing, programmers were working on designing a system that would process images mathematically (in form of vectors and matrices) in a simple, interactive way. Quite a few programming languages were developed for this purpose, but the MATLAB programming language gained global recognition, especially among teaching facilities for its ease of use and wide range of applications. Many libraries were then developed on MATLAB for image processing-related tasks; among them is the Image Processing Toolbox (Kalevo, 2019).

2. Method

The vital points considered when designing a software tool are that it functions. It can easily be read and understood, as these aid its systematic modifications when required. For a program to function properly, certain conditions and requirements associated with the

* **Corresponding Author**
*(olatayo80@gmail.com) ORCID ID 0000 – 0003 – 1499 – 1856

Cite this study
Olaleye J B, Alabi A O, Sunday A A, Olatayo D E, Julius S T (2021). Development of a User-Friendly Program: Real-Time Image Properties Display". 3rd Intercontinental Geoinformation Days (IGD), 109-112, Mersin, Turkey

problem or class of problems they are intended to solve must be satisfied. Likewise, the specifications which include a detailed description of the purpose, or function, inputs, method of processing, outputs, and any other special requirements) must be known to design an effective algorithm or computer program, which must work completely, correctly, and adequately well.

The steps taken in the design process are listed as follows:

Step 1 Problem analysis:

The research in context entails the development of a user-friendly program that will display the properties of an image in real-time.

Step 2 Problem statement

The research which aims to develop a user-friendly program that will display the properties of an image in real-time revolves around image processing and image analysis.

According to professionals like Stipanicev and Alasdair, digital image processing involves changing the nature of images either to improve their pictorial content for human interpretation or to make it more suitable for autonomous machine detection.

Digital image analysis is the extraction of meaningful information from digital images utilizing digital image processing techniques. Image analysis tasks range from the simple task of reading bar-coded tags to sophisticated ones such as face recognition from images.

Step 3 Processing Statement

The required input for the user-friendly program is a digital image (geospatial or non-geospatial). The outputs of the user-friendly program are information, geometric properties of the inputted digital image, and likewise a transformed and processed digital image.

Step 4 Flow chart

Fig. 1 shows the flowchart of the workflows of the processes adopted in the program design.

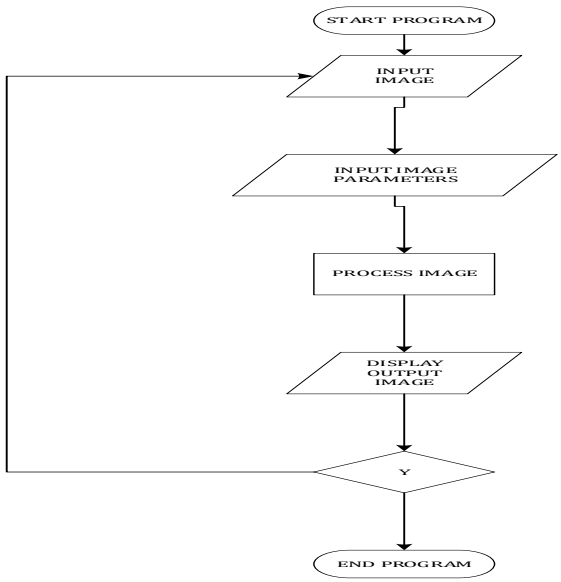

Figure 1. Flowchart of the workflows adopted in the program design

Step 5 Program algorithm

In designing a GUI, the proper visual composition is a must to give the user an aesthetically pleasing working environment. Colours, alignment, and simplicity of look should be chosen carefully. Every function, button, or any other object should have its meaning, simple and understandable by an average program user. Similar components should have conforming looks and usage. Functions ought to produce results quickly and with ease.

3. Results

3.1. Graphical user interface design implementation (GUI)

For the project, the GUI was designed using app designer. The components used are text boxes, push buttons, pop-up menu, static text, axes. Push buttons generate actions when clicked. For example, a clicked OK button might apply settings and close a dialog box. When you click a push button, it appears depressed; and raised when you release the mouse button.

The Graphical user interface was designed with a menu bar consisting of 7 menus with each of their respective submenus (see Fig. 2). The list of menus included in the menu bar was:

i. Menu – The menu tab was designed with a drop-down list of submenus – New, Open, Save, Save As, Resize, Compress, and Exit.

ii. Basıc Operatıons – The Properties, Pixel info, Thresholding, Image Negative, Bit Plane, Binary, Greyscale, Red Band, Green Band, Blue Band, and Brightness tab were included as submenus of the Basic Operations tab.

iii. Spatıal Operatıons – Laplacian, Sobel, Prewitt, Median filter, Averaging, and Weighted Averaging were included as submenus of the Spatial operations tab.

iv. Frequency Domaın – Gaussian Low pass, Gaussian High pass, Butterworth Lowpass, Butterworth High pass.

v. Hıstogram – Image Histogram, Histogram Equalizations

vi. Geometrıc Calculatıons – Coordinates, Distance, Area.

vii. Help – About, Instructions.

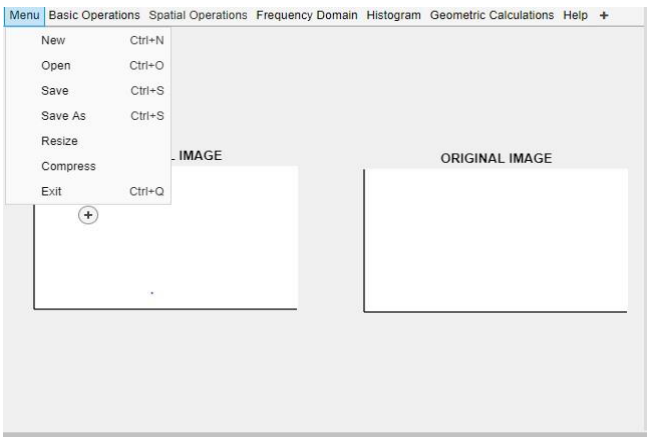

Figure 2. This is a screenshot of the interface of the user-friendly program designed with MATLAB

3.2 Program testing and debugging

Various operations were performed on test images using the user-friendly program. Results obtained are shown in Fig. 3 and 4. Properties of a test image derived by the program are shown in Fig. 4. Properties that can be extracted from the properties table are highlighted under the name column. For this particular image. The file format of the image is jpg i.e the image is a jpg file while the spatial resolution of the image is 144 by 144 and the image is a truecolour image.

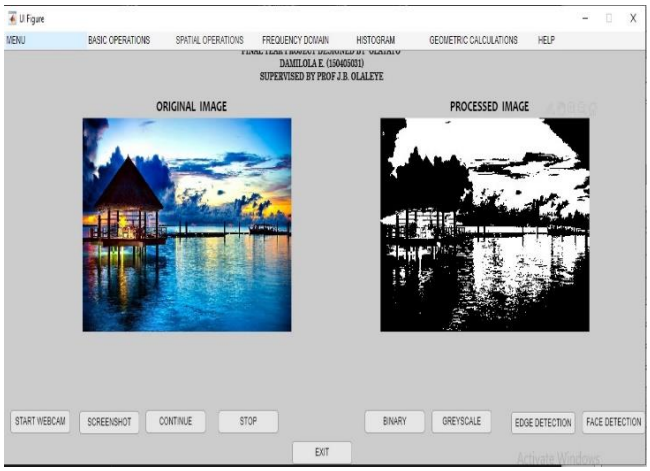

Figure 3. Image conversion to binary

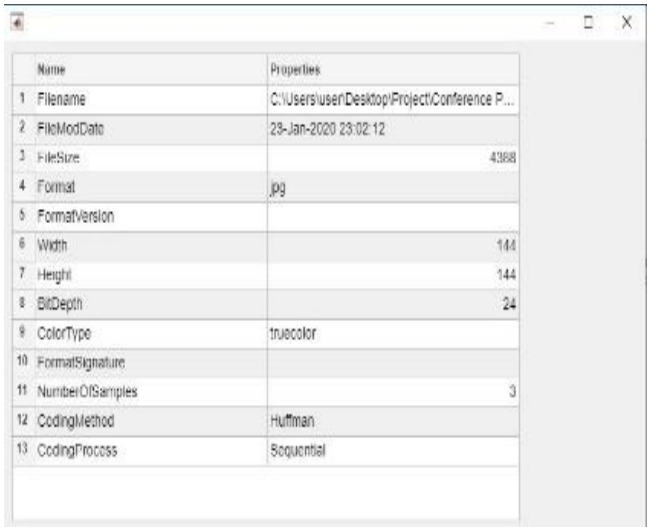

	Name	Properties
1	Filename	C:\Users\user\Desktop\Project\Conference P...
2	FileModDate	23-Jan-2020 23:02:12
3	FileSize	43888
4	Format	jpg
5	FormatVersion	
6	Width	144
7	Height	144
8	BitDepth	24
9	ColorType	truecolor
10	FormatSignature	
11	NumberOfSamples	3
12	CodingMethod	Huffman
13	CodingProcess	Sequential

Figure 4. Image properties generated with the user-friendly program

3.3. Real-Time image processing

The real-time images were gotten from a phone camera connected to the user-friendly program on the computer through the IP address of the phone. The videos are displayed on the interface of the program as a set of running frames with various operations like face detection (see figure 5) and edge detection performed on the frames of the videos with high accuracy

Figure 5. Screenshot of the face detected with the user-friendly program

4. Discussion

After conceptualization and design, the graphic user interfaces of each component program were the output/result of the program development. Each of these programs combined MATLAB app development components and data was passed efficiently through these development objects.

Real-time image processing operations like edge detection, face recognition were carried on real-time images gotten from cameras connected to the MATLAB GUI via IP address.

The final result of the development was a standalone application compiled through the MATLAB deploy tool, which can be used on any computer even if it does not have MATLAB installed on it.

5. Conclusion

This research paper outlines the use of MATLAB software to develop a program that displays image properties in real-time. It has been defined that the value and quality of information obtained through image processing is a function of the methods and software that are used, and is the fundamental benchmark of precision and accuracy on which any project is based on. Hence, an attempt was made to develop a program that can handle image processing in real-time.

This paper also includes the methodological adoption of the use of MATLAB program to design a graphical user interface, which is user-friendly and flexible.

Acknowledgement

The authors wish to thank Surv. Chukwuma J. Okolie for his review and guidance; and the Department of Surveying and Geoinformatics, the University of Lagos for their instructions and supervision.

References

Frédéric. (2003). An Introduction To Digital Image Processing.

Galitz. (2002). The Essential Guide to User Interface Design – An Introduction to GUI Design Principles and Techniques. United States of America. John Wiley & Sons.

Kalevo. (2019). Building a Graphical User Interface with MATLAB.

Padmappriya, & Sumalatha. (2018). Digital Image Processing Real Time Applications. International Journal of Engineering Science Invention (IJESI)(2319 – 6726), 46-51.

Pratt. (1991). Digital Image Processing (Second Edition). John Wiley and Sons.

Seyhan, A. B. (2018). Erzincan İlindeki Hayvansal Atıkların Biyogaz Potansiyelinin Araştırılması. Academic Platform.

Silva, & Mendonca. (2005). Digital Image Processing. Silva, & Mendonca içinde, Digital Image Processing (s. 891). Academic Press.

Tavares, & Manuel. (2010). Image Processing and Analysis: Applications and Trends. Porto, PORTUGAL: Institute of Mechanical Engineering and Industrial Management (INEGI), Porto, PORTUGAL.

Intercontinental Geoinformation Days

igd.mersin.edu.tr

Determination of Karina Lagoon surface area water temperature changes using remote sensing methods

Elif Akyel[*1], **Özşen Çorumluoğlu** [1]

[1]*Izmir Kâtip Çelebi University, Faculty of Engineering and Architecture, Department of Geomatics, İzmir, Turkey*

Keywords
Karina Lagoon
AWEI
Water Temperature
Thermal Band
Remote Sensing

ABSTRACT

Evaporation, inability to feed from land, and especially in areas where the lagoon joins the sea, deposits that form over time form embankments, such as lake level changes over time, causes a change in lake level. Remote sensing methods, which provide important advantages in the detection of this change, also provide information about the parameters affecting the lake ecosystem. One of the parameters affecting the lake ecosystem is the surface water temperature. In the study, the Karina Lagoon located in Aydın was examined. The aim of the study is to determine the temperature changes in the lake surface water between 1985 and 2020 using Landsat satellite images. Firstly, Automatic Water Extraction Index (AWEI) was applied to Landsat satellite images in order to determine the lake surface area. Firstly, the Automatic Water Extraction Index (AWEI) was applied to the Landsat satellite images to determine the lake surface area. Thus, the spatial change in the lagoon was determined as a decrease of 6.85%. The AWEI method worked with a minimum accuracy of 91%. Then, the lake surface temperatures were determined by using the thermal bands of the satellite images. Maximum measured water temperature of 30.42 ^{0}C, minimum measured 17.93 ^{0}C.

1. Introduction

One of the places that attract attention in terms of tourism and attract the most attention is the natural areas, especially national parks, which are under protection (Bekdemir et al., 2010). Dilek Peninsula Büyük Menderes Delta National Park is located at the last point where Dilek Mountain reaches the Aegean Sea within the borders of Aydın province and has an area of 27,675 hectares. 10,985 hectares of this area belong to Dilek Peninsula, which was declared a National Park on 19.05.1966, and 16,690 hectares to Büyük Menderes Delta, which was declared a National Park in 1994. Dilek Peninsula has a great importance in terms of containing elements of Mediterranean Flora Region and European Siberia Flora Region. Büyük Menderes Delta contained in Biological Diversity, endangered species, endemic species and the International Convention on wetlands (Ramsar), the European Convention for the protection of wildlife and habitats (Bern), the convention on Biological Diversity (Rio) and the convention on the protection of the Mediterranean Sea against pollution (Barcelona) is intended as within the scope of a protected zone. Büyük Menderes Delta, which is of international importance, has the feature of "Class A Wetland". Due to its diversity, Dilek Peninsula and Buyuk Menderes Delta National Park have been declared as a 'Flora Biogenetic Reserve Area' by the Council of Europe and have been protected.

As a result of the displacement of the river in the Büyük Menderes Delta and the separation of the alluvium it carries from the sea by blocking the way of the old bays and bays, many lagoons large and small have been formed in the delta. Karina Lagoon, one of the lagoons formed, is located within the borders of Dilek Peninsula Büyük Menderes National Park.

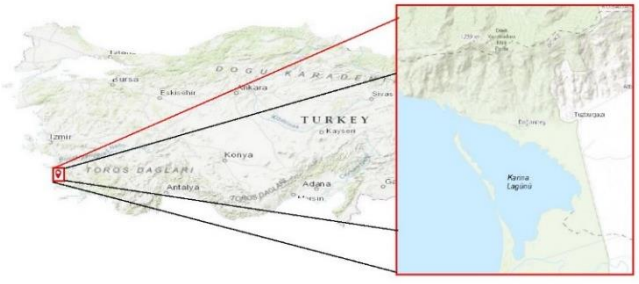

Figure 1. Study Area

* **Corresponding Author**

*(elif.akyel@ikc.edu.tr) ORCID ID 0000-0002-9355-7478
(ozsen.corumluoglu@ikcu.edu.tr) ORCID ID 0000-0002-7876-6589

Cite this study

Akyel E & Çorumluoğlu Ö (2021). Determination of Karina Lagoon surface water temperature change using remote sensing methods. 3rd Intercontinental Geoinformation Days (IGD), 113-116, Mersin, Turkey

Karina Lagoon, the location of which is shown on the map with Fig. 1, had an area of 2794.14 hectares in 1985, while it reached an area of 2602.71 hectares in 2020. However, the lagoon, which reached its widest limits in 2005 and reached its smallest limits in 2020, is an indication that there is no linear increase or decrease in the lake. In addition to this spatial change, when the changes in lake water temperatures are examined, it has been determined that the maximum temperature was 30.42^{0}C in 2000 and the minimum temperature was 17.93^{0}C in 2010.

2. Method

In the study, the Karina Lagoon water surface area change was examined using satellite images In this context, satellite images obtained from Landsat 5 TM and Landsat 8 OLI-TIRS sensors were used. Landsat satellite data has important advantages in monitoring and evaluating long-term land changes (Gülci et al.,2019).

Landsat 5 TM data from 1985-2011 and Landsat 8 OLI-TIRS data from 2013-2020 were used as image data in the study. Satellite images are available free of charge from the USGS (United States Geological Survey). While selecting satellite images, due to the fact that the weather conditions are approximately the same in the same season, it was paid attention to the images obtained in the same months while selecting images from different years. In order to minimize the effect of factors such as clouds and atmospheric humidity that directly affect the image quality, June was preferred when the cloudiness rate was low (Özcalik et al., 2020). The accuracy of the results obtained was tried to be improved by selecting images with 10% or less cloudiness.

2.1. Image preprocessing

Electromagnetic radiation detected by various sensors, gases moving towards the sensing sensor from the earth's surface, are exposed to atmospheric (scattering, absorption by aerosols, etc.) effects. Radiometric distortions occur due to the changes in the light falling on the images, the geometry of the view, atmospheric conditions and the response time of the sensor Atmospheric and radiometric corrections should be applied on satellite images in order to minimize the resulting system errors and to eliminate the distortions caused by atmospheric particles. (Bektaş et al.,2008 ; SONG et al., 2001; Liang, 2004). In order to achieve optimum accuracy in the analyzes in the studies on the detection of spatial changes that occur over time, preprocessing procedures should be applied to the images.

The formula given in Equation (1) and Equation (2) was applied to the obtained images. Then the classification process was carried out.

$$\rho\lambda = \pi * (((L_{MAX\lambda} - L_{MIN\lambda})/(Q_{CALMAX} - Q_{CALMIN})) * (Q_{CAL} - Q_{CALMIN}) + L_{MIN\lambda}) - (((L_{MAX\lambda} - L_{MIN\lambda})/(Q_{CALMAX} - Q_{CALMIN})) * (x - 1) + L_{MIN\lambda})) * d_2 / ESUN_\lambda * \cos\theta s \quad (1)$$

$$\rho\lambda = (((M_\rho * Q_{CAL}) + A_\rho) - ((M_\rho * x) + A_\rho)) / (\cos(35.20373 * \pi/180)) \quad (2)$$

2.2. Band ratio methods

A new image is obtained by applying arithmetic operations to bands representing different spectral ranges. It is possible to highlight the attribute of an object over the resulting image.

In this study, the characteristics of each target between different spectral bands were analyzed using the AWEI band ratio technique. Based on the analysis, the land is separated from the water surface by finding the differences between the water and other targets (Yu et al., 1998; Xu 2002).

2.2.1. AWEI

The AWEI band ratio index was developed to increase the contrast between water and other dark surfaces. The primary goal of the AWEI formulation is to maximize the separability of water and non-water pixels by applying band difference, splice and different coefficients. (Feyisa et al., 2014). The AWEI index can be calculated using the formula given in Equation (3).

$$AWEI = 4*(\rho green - \rho SWIR1) - ((0.25*\rho NIR) + (2.75x\rho SWIR2)) \quad (3)$$ (Feyisa et al.,2014;Şener,2016)

2.3. Determination of lake surface water temperatures using thermal band

In this study, surface water temperature values were determined using the thermal bands of Landsat 5 and Landsat 8 satellites. In order to determine the surface temperature values from the Landsat satellite image, the images were downloaded from the USGS web page with their metadata in GeoTIFF format. First, the digital number (DN) in the image was converted to spectral radiance values using formula (4) and formula (5).

Landsat 5 Digital number to radiance conversion:

$$L\lambda = (Lmax\lambda - Lmin\lambda)(Qcalmax - Qcalmin) * ((Qcal - Qcalmin) + (Lmin\lambda)) \quad (4)$$

Landsat 8 Digital Number to Radiance conversion:

$$L\lambda = ML*QCAL+AL \quad (5)$$

Where :
$L\lambda$: spectral radiance values (Watts/(m2*sr*µm),
$Lmin\lambda$: Spectral radiance values scaled to $Qcalmin$,
$Lmax\lambda$: Spectral radiance values scaled to $Qcalmax$,
$Qcal$: Calibrated pixel values
$Qcalmin$: Calibrated minimum pixel values
$Qcalmax$: Calibrated maximum pixel values

K1 and K2 Thermal Conversion Constants given by the USGS (2013) are used during the process (6) of converting radiance values obtained from Landsat satellite images to luminosity temperatures (Table 1).

$$T = K2/ln(K1/L\lambda + 1) \quad (6)$$

Where:

T : Temperature (oK)
$L\lambda$: spectral radiance values (Watts/(m2*sr*µm).
K1 : First thermal conversion constant of Landsat satellite
K2 : Second thermal conversion constant of Landsat satellite

Table 1. K1 and K2 thermal conversion constants of Landsat satellites (USGS, 2013)

Sensör		K1	K2
Landsat 5		607,76	1260,56
Landsat 8	Band 10	774,89	1321,08
	Band 11	480,89	1201,14

3. Results

Within the scope of the study, the water surface area in the satellite images was determined by firstly applying AWEI. Then, the spatial change that occurred between 1985 and 2020 was determined. The results of the AWEI technique applied to the satellite images are given in Fig 2. Looking at the results given in Table 2 and Fig 3, the spatial variation of the lagoon and the accuracy results of the method used can be reached. The resulting change is given in Table 3.

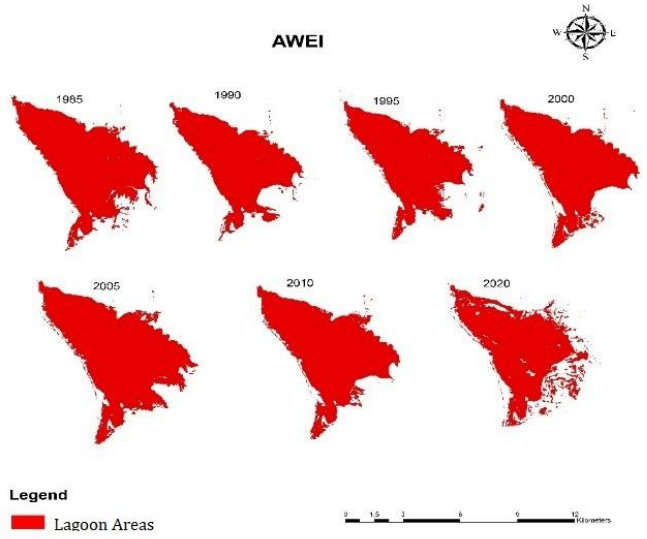

Figure 2. AWEI Index Results

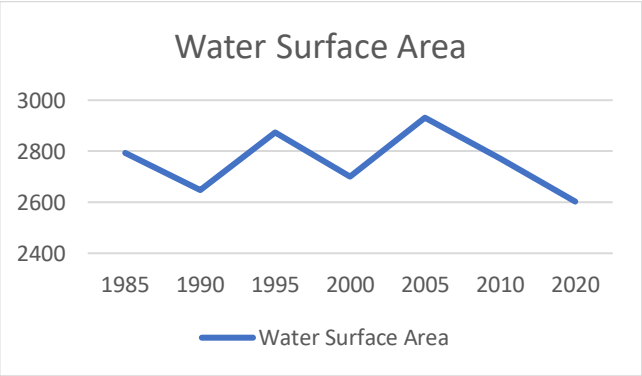

Figure 3. Water Surface Area (hectar)

Table 2. Areas and accuracy results calculated with AWEI index

Years	Water Surface Area (ha)	Overall Accuracy
1985	2794.14	99.00%
1990	2647.08	97.00%
1995	2873.34	94.00%
2000	2699.28	94.00%
2005	2931.39	91.00%
2010	2771.19	97.00%
2020	2602.71	97.00%

Table3. Area Changes

Years	Change (%)
1985-1990	-5.26%
1990-1995	+8.54%
1995-2000	-6.05%
2000-2005	+8.59%
2005-2010	-5.46%
2010-2020	-6.07%
1985-2020	-6.85%

Then, the temperatures of the Karina Lagoon water surface were determined by first converting the reflectance values of the thermal bands of Landsat 5 and Landsat 8 satellites to radiance and then converting the obtained radiance values to brightness temperature.

The change in the lagoon water temperature is given in Fig 4. and Table 4. The temperature changes are visualized on the graph given in Fig. 5.

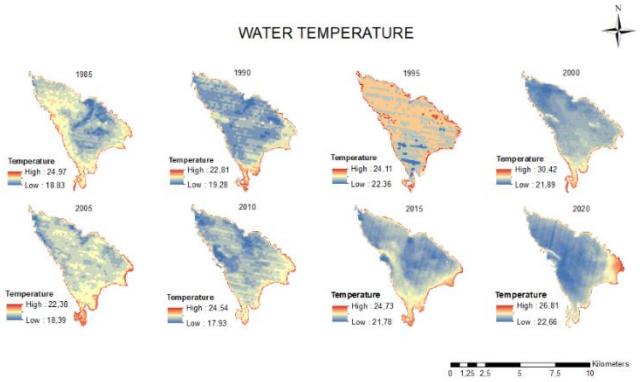

Figure 4. Water Temperature

Table 4. Water Surface Temperatures

	Water Temperature	
Years	Max (0C)	Min (0C)
1985	24.97	18.83
1990	22.81	19.28
1995	24.11	22.36
2000	30.42	21.89
2005	22.38	18.39
2010	24.54	17.93
2015	26.81	24.73
2020	22.66	21.78
Mean (0C)	24.84	20.65

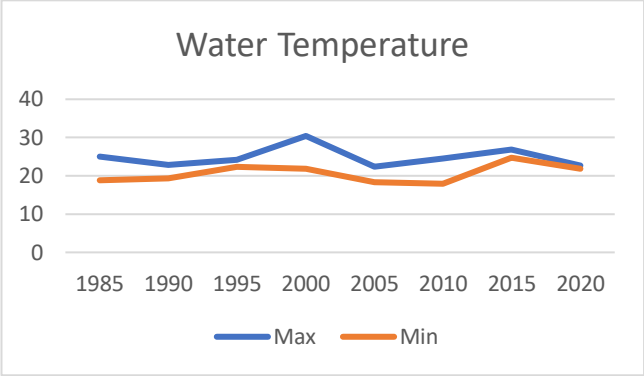

Figure 5. Water Surface Temperature (^{0}C)

4. Conclusion & Discussion

In this study, 6 Landsat 5 satellite images belonging to the years 1985-2011 and 2 Landsat 8 satellite images belonging to the years 2011-2020 were used. While selecting satellite images, summer months with less cloudiness were preferred and all images were obtained from June of the relevant year. After the images used were preprocessed, the surface area of the Karina Lagoon was determined by applying the AWEI technique. By comparing the determined water surface areas with each other, the amount and direction of the spatial change was determined. In this context, when the results of the AWEI index are examined, there is no linear increase or decrease. The lagoon area, which was 2794.14 hectares in 1985, was measured as 2602.71 hectares in 2020. The lagoon reached its widest area in 2005 with 2931.39 hectares. The lagoon area decreased by 6.85% in total from 1985 to 2020. As a result of the accuracy analysis, the AWEI technique, which works with a minimum of 91% accuracy, has been successful in extracting the water body.

In addition to the spatial change, the lagoon surface water temperatures and the change trend of the temperatures were examined and compared. Surface water temperatures were calculated using the thermal bands of the Landsat satellite. The surface water temperature, which reached the highest measured temperature at 30,42^{0}C in 2000, reached the lowest temperature at 17,93^{0}C in 2010. Surface water temperatures average 24,84^{0}C at the highest and 20,65^{0}C at the lowest. When the lagoon water surface temperature changes are examined on the dates evaluated within the scope of the study, the water temperature, which is relatively lower in the inner parts of the lagoon, was measured higher in the coastal areas. (Şener, 2016).

References

Balçık, F. B. & Göksel, Ç. (2010). SPOT 5 ve Farklı Görüntü Birleştirme Algoritmaları. Jeodezi ve Jeoinformasyon Dergisi, (101), 0-0. Retrieved from https://dergipark.org.tr/tr/pub/hkmojjd/issue/53143/704637

Bekdemir Ü,Elmacı S & Sezer İ (2010). Turizmin kıskacında bir doğa koruma alanı: Dilek Yarımadası-Büyük Menderes Deltası Milli Parkı

Feyisa G L, Meilby H, Fensholt R &Proud S R (2014). Automated Water Extraction Index: A new technique for surface water mapping using Landsat imagery. Remote Sensing of Environment. Pages 23-35. ISSN 0034-4257, https://doi.org/10.1016/j.rse.2013.08.029

Gülci S, Gülci N & Yüksel K (2019). Monitoring Water Surface Area and Land Cover Change by Using Landsat Imagery for Aslantaş Dam Lake and Its Vicinity." *Journal of the Institute of Science and Technology* 9 (1): 100–110. https://doi.org/10.21597/jist.419221.

Liang S, 2004: Quantitative Remote Sensing of Land Surfaces, John Wiley and Sons, New Jersey, USA

Özçalık H, Torun A T & Bilgilioğlu S S (2020). Landsat uydu görüntüleri kullanılarak Mogan Gölü'nün su yüzeyi ve arazi örtü değişiminin belirlenmesi. Türkiye Uzaktan Algılama Dergisi

Song C, Woodcock C E & Seto K C (2001). Classification and change detection using Landsat TM data: when and how to correct atmospheric effects? Remote Sensing of Environment 75:230–44

Şener E (2016). Burdur gölü yüzey suyu sıcaklığı mevsimsel dğişiminin Landsat 8 uydu görüntüleri kullanılarak belirlenmesi. Mühendislik Bilimleri ve Tasarımları Dergisi

USGS., 2013. Landsat 8 (L8) Data Users Handbook Version 1.0

Xu H (2002). Spatial expansion of urban/town in Fuqing of China and itsdriving force analysis. Remote Sensing Technology and Application.

Yu J, Huang Y & Feng X (2001). Study on water bodies extraction and classification from Spot image. Jornal of Remote Sensing.

Intercontinental Geoinformation Days

igd.mersin.edu.tr

Using remote sensing to monitor Aerosol Optical Thickness (AOT) and its relationship with land cover in Lagos Metropolis, Nigeria

Emmanuel Ayodele[1], Chukwuma Okolie[1,4], Samuel Akinnusi[*1], Erom Mbu-Ogar[1], Olagoke Daramola[1], Abdulwaheed Tella[2,4], Rose Alani[3,4], Alfred Alademomi[1]

[1]*University of Lagos, Faculty of Engineering, Department of Surveying and Geoinformatics, Lagos, Nigeria*
[2]*Universiti Teknologi PETRONAS (UTP), Department of Civil and Environmental Engineering, Geospatial Analysis and Modelling (GAM) Research Laboratory, Malaysia.*
[3]*University of Lagos, Faculty of Science, Department of Chemistry, Lagos, Nigeria*
[4]*University of Lagos, Air Quality Monitoring (AQM) Research Group, Lagos, Nigeria*

Keywords
Air quality
Aerosol optical thickness
Particulate matter
Lagos metropolis
Land cover

ABSTRACT

Aerosol Optical Thickness (AOT) is the most fundamental parameter for determining the optical properties of aerosols, which can be extracted from remotely sensed images using the atmospheric correction equation for atmospheric reflectance and radiative transfer model. This study used multi-temporal and multi-spectral Landsat imageries of Lagos Metropolis at two epochs (2002 and 2020) to evaluate the AOT levels in the metropolis. The 6S model was used to generate a Look-Up Table (LUT) using Py6S, a python based 6S module. This was used to simulate the AOT using land surface reflectance and top of atmosphere reflectance. A comparative assessment of the method against the ground-based measurements of particulate matter (PM) at three different locations shows a strong positive correlation between the imagery-derived AOT values and PM . Generally, the AOT values increased from 2002 to 2020 and this could be explained by the increased urban expansion in the metropolis. This alarming scenario requires urgent intervention and mitigation efforts. Remote sensing-based AOT monitoring is a possible solution.

1. Introduction

Air pollutants such as Ozone (O_3), Nitrogen dioxide (NO_2), Sulphur dioxide (SO_2), Carbon monoxide (CO), Particulate matter (PM, also known as aerosol) have negative impacts on human health and the environment (Nguyen et al., 2019; Althuwaynee et al., 2020). These pollutants have led to more deaths in Nigeria than in South Africa, Kenya, and Angola combined. Atmospheric aerosols from either natural or anthropogenic sources have significant impacts on air quality and climate. These aerosols consist of solid and liquid microscopic particles and gas carriers and are poly-disperse systems suspended in the atmosphere with particle sizes ranging between 10^{-3} µm and 10^{2} µm (Yang, 2017). According to Zhang et al. (2015), AOT is a typical atmospheric monitoring measure of aerosols. Ground-based sun photometers and satellite sensors are the two primary approaches for monitoring aerosols (Wei et al., 2020). The ground-based platforms can provide real-time data that can be used in calibrating satellite-borne AOT instruments to improve the accuracy of the AOT retrieval algorithm in the remote sensor. Also, satellite monitoring systems play vital roles in broad-level or macro-scale derivation of spatial data (Ranjan et al., 2020). Compared to the ground-based technique of aerosol monitoring, Remote Sensing (RS) and Geographic Information Systems (GIS) offer a cost-effective and timely approach to atmospheric aerosols monitoring. From a holistic perspective, this study assesses the spatio-temporal dynamics of aerosol concentration in the Lagos megacity, specifically within the 17 Local Government Areas (LGAs) of the metropolis using multi-spectral and multi-temporal Landsat imageries. The spatial variability of AOT was estimated based on the improved dark target method. The dense dark vegetation (DDV) technique was used to estimate the land surface reflectance. The DDV approach involves detecting dark pixels and estimating their reflectance and this mainly implements two visible bands (blue and red) and one SWIR band.

Furthermore, the retrieved AOT values were used to analyze the concentrations of fine particulate matter (PM), which is a major contributor to air pollution. Validation of the AOT results from the satellite imageries was done using ground-based PM measurements. Information concerning the concentration and variability

* **Corresponding Author**
*(akinnusisamuel1845@gmail.com) ORCID ID 0000-0002-6911-4490

Cite this study
Ayodele E, Okolie C, Akinnusi S, Mbu-Ogar E, Daramola O, Tella A, Alani R, Alademomi A S (2021). Using remote sensing to monitor Aerosol Optical Thickness (AOT) and its relationship with land cover in Lagos metropolis, Nigeria. 3rd Intercontinental Geoinformation Days (IGD), 117-120, Mersin, Turkey

could help decide where to set up air pollution monitoring stations in the state. With the view of making cities and human settlements inclusive, safe, resilient, and sustainable, this study contributes to the United Nations Sustainable Development Goal (SDG) Number 11. Specifically, goal 11.6 aims to reduce the adverse per capita environmental impact of cities, with special attention to municipal and other waste management by 2030. The rapid growth of the Lagos megacity and its projected increase justifies the need to study the dynamics and futuristic outlook of air quality in the state.

2. Methods

2.1. Study area

The study area (Lagos Metropolis, shown in Figure 1) lies between latitudes 6°20'00''N - 6°42'10''N and longitudes 3°02'30''E - 3°42'40''E. It comprises of 17 Local Government Areas (LGAs). Lagos Metropolis is known in Lagos State as one of the world's megacities experiencing rapid urbanization and urban sprawl (Obiefuna et al., 2018). The climate is controlled by two air masses: tropical continental and tropical maritime air masses. The latter is wet and originates from the Atlantic Ocean, while the former originates from the Sahara Desert and is warm, dry and dusty (Obiefuna et al., 2013). The region experiences typically two seasons: the rainy season (April-October) and the dry season (November-March). Lagos City is strongly affected by sea-based disturbances with an average wind speed of 4.3 km/h and monthly average temperatures ranging from 28.6 °C in July/August to 33.7 °C in February/March, whilst the air is very hot throughout the year (Ojeh et al., 2016).

Figure 1. Map of study area

2.2. Datasets

Landsat Imagery: Landsat 7 Enhanced Thematic Mapper (ETM) (2002-12-28) and Landsat 8 Operational Land Imager (OLI) (2020-01-20) satellite imageries were downloaded from the online archive of the United States Geological Survey (USGS) (https://earthexplorer.usgs.gov/).

Particulate Matter: Particulate matter ($PM_{1.0}$, $PM_{2.5}$, and PM_{10}) data were obtained with the ground-based air quality egg instrument. The device was used to acquire the PM data at the selected critical sites (Ojota, Iwaya, and Mushin). The data were measured on a weekly basis between 9:00 am and 5:00 pm from February 2019 – July 2019.

2.3. Land surface reflectance determination

The DDV technique was adopted in this study to estimate the land surface reflectance. This was done using the improved dark-pixel method developed by Levy et al. (2010), which is dependent on Normalized Difference Vegetation Index (NDVI) and scattering angle. The equations for determining the surface reflectance are given in Luo et al. (2015) and Ou et al. (2017).

2.4. Constructing the Look-up Table (LUT)

Radiative Transfer Models (RTMs) are commonly used in atmospheric science to simulate the passage of solar radiation through the atmosphere. They have a variety of applications, including atmospheric analysis and the design of solar energy systems, and are commonly used in remote sensing and earth observation, but with regard to the various parameters of input and outputs, they are also seen as challenging to use (Wilson, 2013). The 6S mode of radiation transfer is a model of atmospheric radiation transfer that has been used in the Earth-atmosphere system to simulate the transmission of solar radiation, and it is a commonly accepted and applied model (Vermote et al., 1997; Zhao et al., 2016). 6S is used operationally as part of the atmospheric correction procedure for Landsat Thematic Mapper (TM) and MODIS. In addition, 6S is often widely used by end-users for atmospheric correction of images from various sensors. Py6S is a Python interface to the 6S model. In this study, the 6S model was run on the Python interface to simulate the atmospheric properties of the Landsat 8 OLI and Landsat 7 ETM sensor for blue and red bands.

2.5. Image classification

Using the maximum likelihood classification algorithm, the satellite imageries were classified into five information classes – bare land, built-up area, vegetation, water body and wetland. This image processing operation was carried out with the ENVI Classic v 5.0.

2.6. Quantitative analysis and validation

The quantitative analysis enabled an understanding of the values associated with spatial and temporal changes. Descriptive statistics were used to summarize the data for interpretation. For validation, Pearson's correlation coefficient was used to infer the level of interdependence between imagery-based AOT for year 2020 and the ground-based PM data.

3. Results

This section presents the imagery-derived AOT maps and land cover maps for 2002 and 2020 and the spatial and temporal analysis, as well as the validation with

ground-based PM data. Figures 2 and 3 present the variation in aerosol optical thickness and the spatial variation in land cover respectively over Lagos Metropolis. Tables 1 and 2 present the AOT distribution per land cover class and the coefficients of correlation between PM and AOT.

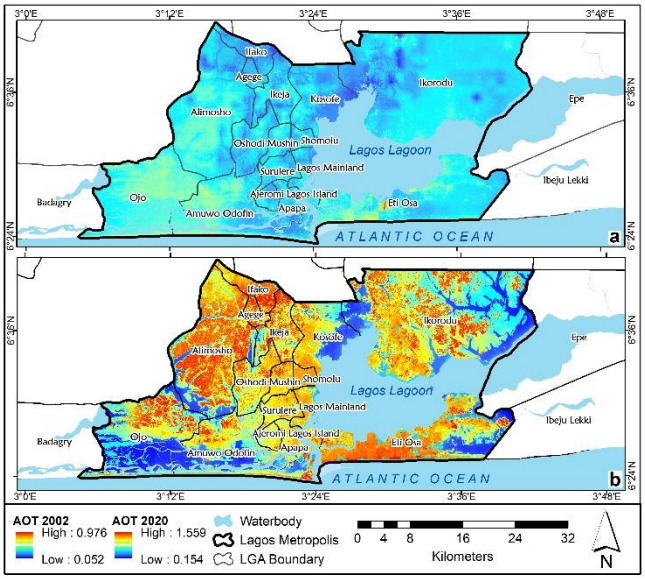

Figure 2. Variation in aerosol optical thickness over Lagos Metropolis – (a) 2002 (b) 2020

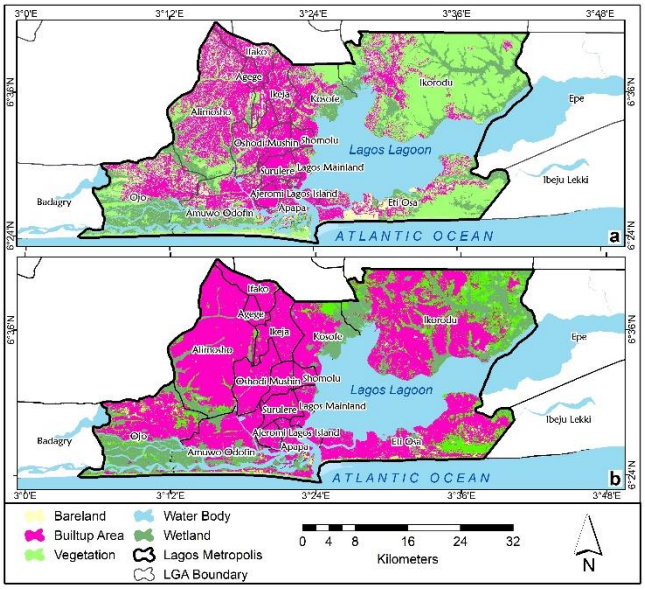

Figure 3. Spatial variation of land cover over Lagos Metropolis – (a) 2002 (b) 2020

Table 1. AOT distribution per land cover class

Class	Year	Count	Min	Max	Mean
Bare land	2002	131625	0.11	0.98	0.40
	2020	27294	0.37	1.70	1.25
Built-up area	2002	483444	0.05	0.60	0.35
	2020	896934	0.37	1.75	1.32
Vegetation	2002	554683	0.07	0.80	0.33
	2020	207787	0.37	1.68	1.03
Wetland	2002	231202	0.08	0.48	0.32
	2020	280720	0.36	1.66	0.73

4. Discussion

Generally, the AOT distribution over the Lagos metropolis is observed to have increased over the years. This could be due to the increasing urbanization as observed by Offor et al. (2016). It can be observed that the correlation between the imagery-derived AOT for year 2020 and the different sizes of PM in Ojota are negative, possibly, due to the time the data was acquired (evening) as opposed to the high positive correlation value in Okobaba, which was acquired during the daytime. The correlation values between AOT and PM in Iwaya are positive but less in magnitude in comparison to that of Okobaba.

Table 2. Correlation coefficients of the relationship between in-situ PM data and imagery derived AOT for year 2020

Location		PM_1	$PM_{2.5}$	PM_{10}	AOT
Ojota	PM_1	1.00	0.99	0.99	-0.62
	$PM_{2.5}$	0.99	1.00	0.99	-0.62
	PM_{10}	0.99	0.99	1.00	-0.67
	AOT	-0.62	-0.61	-0.67	1.00
Iwaya	PM_1	1.00	0.99	0.99	0.26
	$PM_{2.5}$	0.99	1.00	0.99	0.28
	PM_{10}	0.99	0.99	1.00	0.29
	AOT	0.26	0.28	0.29	1.00
Okobaba	PM_1	1.00	0.98	0.98	0.70
	$PM_{2.5}$	0.99	1.00	0.99	0.73
	PM_{10}	0.98	0.99	1.00	0.73
	AOT	0.70	0.72	0.73	1.00

The land cover classification results clearly showed that the study area had undergone tremendous spatial changes in its land cover. The observed changes in the land cover results are corroborated by the results of Obiefuna (2021), where an increase in the built-up area, decrease in bare land, and decrease in vegetation cover were observed between 2001 and 2019. In addition, a slight decrease in water bodies was also reported within the same period. Recently, Faisal et al (2021) reported a similar result in their study on the analysis of urban growth and land cover change scenario in Lagos.

The results of the relationship between AOT and Land cover reveal how AOT varied spatially with different land cover types. The high AOT observed in the built-up areas and bare lands agrees with the studies of Sun et al. (2016), and Liu et al. (2020). However, Liu et al. stated specifically that AOT values are highest in the spring season due to the presence of dust particles in the atmosphere. This corroborated the generally high AOT observed in this study. Although the AOT values over vegetation cover and wetland are relatively low compared to other land cover types, the values are still higher than usual. This could be due to some vegetation and wetlands being sandwiched in between the built-up areas and bare lands.

5. Conclusion

This paper has monitored and examined the AOT concentration in the Lagos Metropolis and its relationship with land cover at two epochs (2002 and 2020). This study only examined the air pollution distribution during the dry season (between December and January). Studies have shown that air pollution is higher in the dry season than in the wet season, during

which dust-laden north-easterly trade winds blow in from the Sahara Desert (Offor et al. 2016). Akinyoola et al. (2018) reported that the aerosol loading/concentration is of high increase in the south-south and southwestern (coastal) regions of Nigeria. This corroborates the generally high aerosol concentration observed in the study area in our findings.

The study showed how increased urbanization has increased the AOT concentration in the metropolis drastically over the years. The increased AOT observed in the area indicates the ever-present urbanization activities, including industrial and traffic activities. To curb the ever-increasing urban air pollution in the Lagos metropolis, more research should be carried out to examine the dynamics of AOT and Particulate matter concentration. This is because of the dynamic nature of air pollution in the coastal area has not been fully explored. Also, a full-scale monitoring of air pollution over the whole of Lagos State should be encouraged to inform the government and air quality control agencies of the present state of this perilous atmospheric phenomenon. Researchers should adopt satellite-based methods for air quality monitoring in Lagos State based on cost and timely benefits.

ACKNOWLEDGEMENTS

The authors would like to thank NASA/USGS for the free access to Landsat imageries, and the Air Quality Monitoring (AQM) Research Group, University of Lagos, for providing the ground-based PM data. The authors also commend Jorge Vicent Servera for their support in the use of the Py6S model.

References

Akinyoola, Julius Adekola, Emmanuel Olaoluwa, and Eresanya O. O. I. Orimoogunje. 2018. "Monitoring the Spatio-Temporal Aerosol Loading over Nigeria." Modeling Earth Systems and Environment 4(4):1365–75. doi: 10.1007/s40808-018-0485-2.

Faisal, Koko Auwalu, Wu Yue, Ghali Abdullahi Abubakar, Roknisadeh Hamed, and Akram Ahmed Noman Alabsi. 2021. "Analyzing Urban Growth and Land Cover Change Scenario in Lagos, Nigeria Using Multi-Temporal Remote Sensing Data and GIS to Mitigate Flooding." Geomatics, Natural Hazards and Risk 12(1):631–52. doi: 10.1080/19475705.2021.1887940.

Liu, Jie, Jianli Ding, Liang Li, Xiaohang Li, Zhe Zhang, Si Ran, Xiangyu Ge, Junyong Zhang, and Jingzhe Wang. 2020. "Characteristics of Aerosol Optical Depth over Land Types in Central Asia." Science of the Total Environment 727:138676. doi: 10.1016/j.scitotenv.2020.138676.

Luo, Nana, Man Sing, Wenji Zhao, Xing Yan, and Fei Xiao. 2015. "Improved Aerosol Retrieval Algorithm Using Landsat Images and Its Application for PM 10 Monitoring over Urban Areas." Atmospheric Research 153:264–75. doi: 10.1016/j.atmosres.2014.08.012.

Obiefuna, J. N., P. C. Nwilo, C. J. Okolie, E. I. Emmanuel, and O. Daramola. 2018. "Dynamics of Land Surface Temperature in Response to Land Cover Changes in Lagos Metropolis." Nigerian Journal of Environmental Sciences and Technology 2(2):148–59. doi: 10.36263/nijest.2018.02.0074.

Obiefuna, Jerry N., Peter C. Nwilo, Ajiri O. Atagbaza, and Chukwuma J. Okolie. 2013. "Land Cover Dynamics Associated with the Spatial Changes in the Wetlands of Lagos/Lekki Lagoon System of Lagos, Nigeria." Journal of Coastal Research 29(3):671–79. doi: 10.2112/JCOASTRES-D-12-00038.1.

Obiefuna, Jerry N., Chukwuma J. Okolie, Peter C. Nwilo, Olagoke E. Daramola, and Lawrence C. Isiofia. 2021. "Potential Influence of Urban Sprawl and Changing Land Surface Temperature on Outdoor Thermal Comfort in Lagos State, Nigeria." Quaestiones Geographicae 40(1):5–23. doi: 10.2478/quageo-2021-0001.

Offor, Ifeanyi F., Gilbert U. Adie, and Godson R. E. E. Ana. 2016. "Review of Particulate Matter and Elemental Composition of Aerosols at Selected Locations in Nigeria from 1985-2015." JH&P 6(10).

Ojeh, Vincent N., A. A. Balogun, and A. A. Okhimamhe. 2016. "Urban-Rural Temperature Differences in Lagos." Climate 4(2):1–18. doi: 10.3390/cli4020029.

Ou, Yang, Fantao Chen, Wenji Zhao, Xing Yan, and Qianzhong Zhang. 2017. "Landsat 8-Based Inversion Methods for Aerosol Optical Depths in the Beijing Area." Atmospheric Pollution Research 8(2):267–74. doi: 10.1016/j.apr.2016.09.004.

Ranjan, Avinash Kumar, Aditya Kumar Patra, and A. K. Gorai. 2020. "A Review on Estimation of Particulate Matter from Satellite-Based Aerosol Optical Depth: Data, Methods, and Challenges." Asia-Pacific Journal of Atmospheric Sciences. doi: 10.1007/s13143-020-00215-0.

Sun, L, J. Wei, D. H. Duan, Y. M. Guo, D. X. Yang, C. Jia, and X. T. Mi. 2016. "Impact of Land-Use and Land-Cover Change on Urban Air Quality in Representative Cities of China." Journal of Atmospheric and Solar-Terrestrial Physics 142:43–54. doi: 10.1016/j.jastp.2016.02.022.

Wei, Xiaoli, Ni Bin Chang, Kaixu Bai, and Wei Gao. 2020. "Satellite Remote Sensing of Aerosol Optical Depth: Advances, Challenges, and Perspectives." Critical Reviews in Environmental Science and Technology 50(16):1640–1725. doi: 10.1080/10643389.2019.1665944.

Wilson, R. T. 2013. "Py6S: A Python Interface to the 6S Radiative Transfer Model." Computers and Geosciences 51:166–71. doi: 10.1016/j.cageo.2012.08.002.

Yang, Haiou, Wenbo Chen, and Zhaofeng Liang. 2017. "Impact of Land Use on PM 2 . 5 Pollution in a Representative City of Middle China." doi: 10.3390/ijerph14050462.

Zhang, Lu, Runhe Shi, Chaoshun Liu, and Cong Zhou. 2015. "Retrieval of Aerosol Optical Depth over Beijing Using Landsat8 / OLI Data." Pp. 1–8 in Proceedings of SPIE. Vol. 9610.

Intercontinental Geoinformation Days

igd.mersin.edu.tr

Mapping of federal government dams in Nigeria

Sola Oluwayemi[*1], **Adedayo Olayiwola**[2]

[1]*University of Lagos, Faculty of Engineering, Surveying and Geoinformatics Department, Lagos state, Nigeria*
[2]*Federal School of Surveying, Surveying and Geoinformatics Department, Oyo, Nigeria*

Keywords
Dams
Nigeria
Geo-political zones

ABSTRACT

This paper focused on the various Federal Government dams in Nigeria, categories, location distribution and capacity. The study observed that the dams, though spread across many states that form the various geo-political zones in the country vary in number, structures, and are not evenly spread. The results obtained from this study showed that more quality dams are needed in the country.

1. Introduction

A dam is a structure built across a river or stream to hold back water. People have used different materials to build dams over the centuries. Ancient dam builders used natural materials such as rocks or clay. Modern-day dam builders often use concrete.

Nigeria is blessed with a vast expanse of inland freshwater and brackish ecosystems. Their full extent cannot be accurately stated as it varies with season and from year to year depending on rainfall. These water resources are spread all over the country from the coastal region to the arid zone of the Lake Chad Basin.

İn Nigeria like in many other parts of the world, dam projects are often seen as key to economic solution through hydroelectric power supply (Youdeowei, 2019). İt equally supports water supply and agricultural pursoses. (Oluwayemi, 2012) noted that some of the problems Geographic Information System (GIS) can tackle in a nation include making avaailable ready-made data for infrastructural and facilities distribution and enabling the nation to know her resources, their location and planning towards managing them.

Due to its relevance, some previous works had been done on dams e.g. (Ang et al. 2020) developed a framework of dam classification to organize the categories of the echohydrology relationship for implementing environmental flows while (Nasrat et al. 2020) worked on classification of dams by their potential hazards and how to prevent future failures.

2. Method

The methodology adopted was to collect data from the government ministry in charge (which in this case was the Federal Ministry of Water Resources).

A geodatabase was created with these data using ArcGIS software. Based on this, our analysis and results were generated.

2.1. The dams data

Data were not readily available so sourcing for it gave a little challenge. The data provided by the Federal Ministry of Water Resources (FMWR) was an excel file which classified the dam data and these classifications were used to carry out the analysis.

It displayed Dam name, Category (size), State, Coordinate, Dam type (Structure), Dam height/Capacity, Purpose, Completion year.

2.2. Database Creation

The Excel data were imported into the ArcGIS environment. Each dam location was plotted. With the attached attributes, querying became easier.

* **Corresponding Author**

*(oluwayesola@gmail.com) ORCID ID 0000-00002-4691-2879
(seundamola2000@gmail.com) ORCID ID 0000-00002-4866-4071

Cite this study

Oluwayemi S & Olayiwola A (2021). Mapping of Federal Government Dams in Nigeria. 3rd Intercontinental Geoinformation Days (IGD), 121-123, Mersin, Turkey

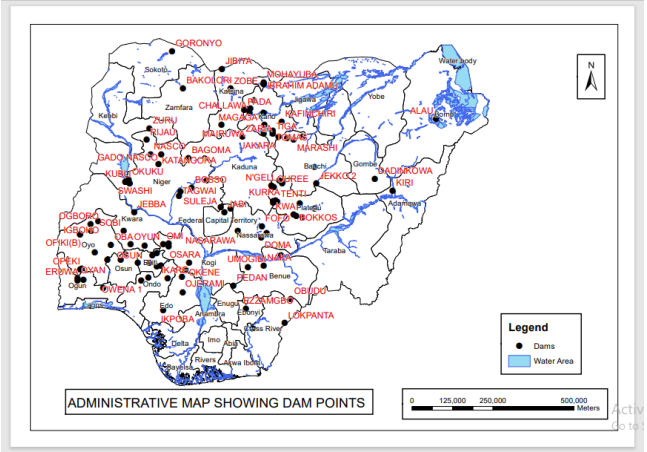

Figure 1. Map of Nigeria showing the dams spread

2.2.1. Geopolitical zoning

Nigeria currently consists of 36 states and the Federal Capital Territory. All, based on based on ethnic, cultural and historical ties, and for political reasons are further divided into six geopo[itical zones.

Below is a list of the zones in Nigeria.

NORTH CENTRAL- (6 States) Niger, Kogi, Benue, Plateau, Nassarawa, Kwara and FCT.

NORTH EAST- (6 States) Bauchi, Borno, Taraba, Adamawa, Gombe and Yobe.

NORTH WEST- (7 States) Zamfara, Sokoto, Kaduna, Kebbi, Katsina, Kano and Jigawa.

SOUTH EAST- (5 States) Enugu, Imo, Ebonyi, Abia and Anambra.

SOUTH SOUTH – (6 States) Bayelsa, Akwa Ibom, Edo, Rivers, Cross River and Delta.

SOUTH WEST- (6 States) Oyo, Ekiti, Osun, Ondo, Lagos and Ogun.

Figure 2. Map of Nigeria showing the six geopolitical zones

2.2.2. Dam category (Size)

Based on the available data, the dams were classified as small dams (with heights less than 8.5metres), medium dams (8.5 – 14.9metres), and large dams (15 metres and above).

2.2.2. Dam types (Structure)

The dams in Nigeria are classified into their various categories and types according to construction material.

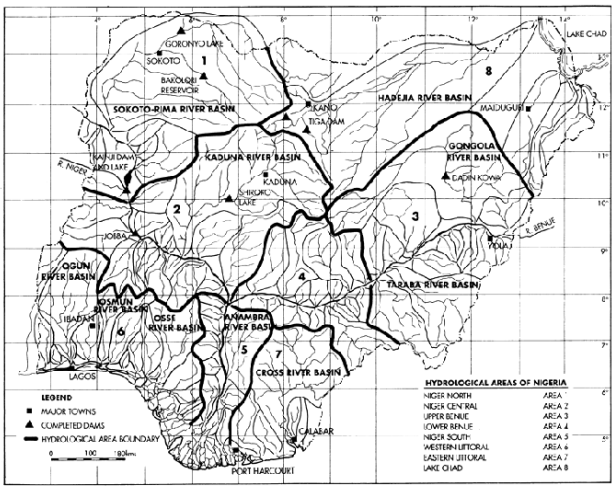

Figure 3. Nigeria hydrological zone

Classification based on construction material brings the Nigerian dam types into earthfill, rockfill, homogenous, zoned and concrete dams.

2.2.4. Location based on hydrological zone

Nigeria has about eight (8) different hydrological zones. The dams spread across all these zones.

3. Results

The results indicated that although the dams were spread across the different geopolitical zones, their numbers at each varied.

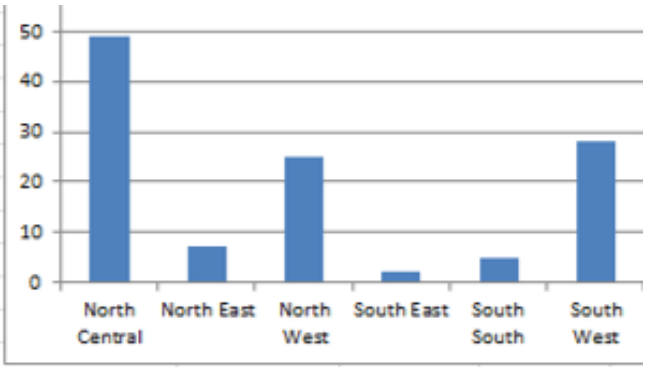

Figure 4. A bar-chart indicating number of dams per geopolitical zone.

The sizes of the dams varied. Using the specifications earlier stated, the dams' classification is indicated in the figure 5.

Majority of the dams in the country are earthfilled type of about 64%, concrete dams are 20%, homogeneous 13%, rockfill type – 4%, while the zoned are around 2% as shown in the following information.

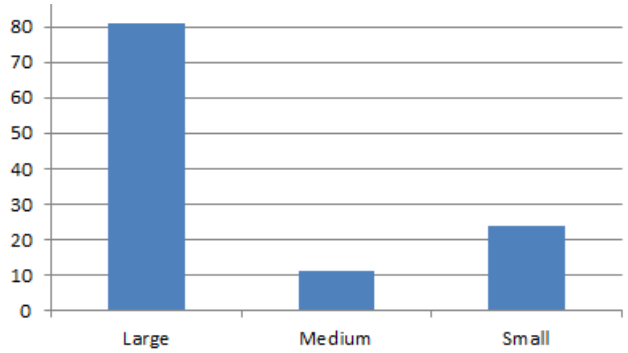

Figure 5. The dams category based on size

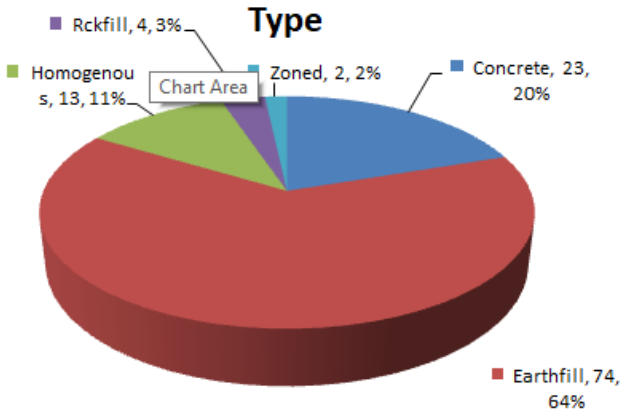

Figure 6. Proportions of the dam structures

The percentage of the dams in each hydrological zone differs and are indicated below.

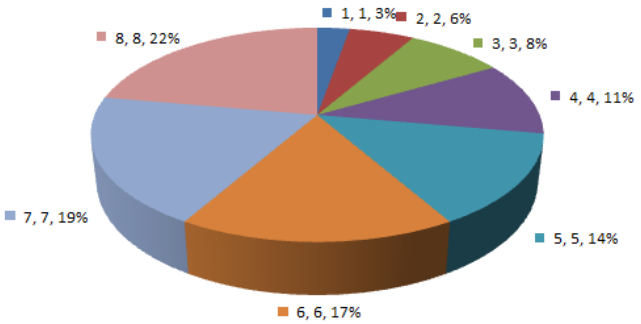

Figure 7. The dams on each hydrological zone

4. Discussion

Although this paper did not investigate the guiding factor(s) in siting the dams, it is however obvious that the federal government dams in the country spread through the parts of the country but did not cover all the states. Different geopolitical zones have varied numbers and the majority are earthfilled.

5. Conclusion

More dams are needed to cover the entire country and to meet the people's need. The government alone cannot continue to shoulder it and should embrace private participation in the people's interest.

References

Ang C, Miao W & Michael M (2020). Classifying dams for environmental flow implementation in China, Sustainability 2020, 12, 107. https://doi.org/10.3390/su12010107

Nasrat A, Nadhir A, Varoujan S & Jan L (2020). Dam safety and dam hazards. Journal of Earth Sciences and Geotechnical Engineering, Vol. 10, No. 6, 2020, 23-40

Oluwayemi S (2012). Mapping forest fire prone areas using Remote Sensing and Geographic Information System. MS Thesis, University of Lagos, Lagos (in Nigeria).

Youdeowei P O, Nwankwoala H O & Delsai D D (2019). Dam structures and types in Nigeria: Sustainability and effectiveness. Water conservation and management, 3(1): 20-26

Intercontinental Geoinformation Days

igd.mersin.edu.tr

Monitoring the spatial distribution of CO_2 within the University of Lagos Main Campus

Alademomi A. S.[1,2,3], Animashaun M. B.[*1,2], Abolaji O. E.[1,2], Okolie C. J.[1,2,3], Ojegbile B. M[1,2], Daramola O. E.[1,2] Alozie, N.S.I[4]

[1]*University of Lagos, Faculty of Engineering, Department of Surveying and Geoinformatics, Lagos, Nigeria*
[2]*Geospatial and Environmental Research Group, University of Lagos, Nigeria*
[3]*Centre for Multidisciplinary Research and Innovation (CEMRI), Abuja, Nigeria*
[4]*University of Lagos, Faculty of Engineering, Department of Mechanical Engineering, Lagos, Nigeria*

Keywords
Air Pollution
WHO
Air Pollutants
Environmental Policies

ABSTRACT

The University of Lagos environment chosen as a case study is a higher institution in Lagos Nigeria which is located within areas of residential, commercial and industrial activities. These activities put out emissions into the atmosphere through motor vehicles, use of electricity generating plants, firewood, coal, kerosine and refuse burning. Anthropogenetic substances such as carbon monoxide (CO), unburnt hydrocarbon (UC), oxides of nitrogen (NOx) and particulate matter (PM) are released into the atmosphere and pollute the air. Thus, effective pollution monitoring and control is required. To assess the University's air quality, the carbon dioxide (CO_2) concentration was mapped and evaluated. Although CO_2 is not an environmental pollutant in a strict sense, but its precursor, the CO is a dangerous one. CO_2 is a major indicator of carbon footprint, and a major issue in climate change studies. Data for the study was collected through direct field measurements using gas sensors. The USEPA Air Quality Index was used to rate the air quality. Also, a one-tailed ANOVA test was used to assess the land use influence on CO_2 variation. The results show that CO_2 emission is substantial around the University First Gate, Faculty of Education and New Hall. This suggests that the initial release of the pollutant CO, a precursor of CO_2 must have been high around these areas.

1. Introduction

Every living organism requires the atmospheric oxygen for survival and growth. Atmospheric air is naturally safe and clean for humans, animals and plants in the spectrum of our biodiversity. However, due to industrialization and other anthropogenic activities, the air gradually becomes polluted, making it unsafe for humans. Anyone living around heavily polluted environments will likely face the risk of respiratory diseases.

The World Health Organization (WHO) in a bid to effectively monitor the sustainable development goals (SDGs) of any global region has repeatedly reported that air pollution is highly responsible for many infectious and viral diseases such as tuberculosis, asthma, nearly all cancers, respiratory and skin diseases which has terminated more lives than AIDS (Mehta et al., 2013). In 2012, the report from WHO revealed an estimated global mortality of 10%, an equivalent of 7 million people resulted from air pollution in 2012 (WHO, 2014). The cause of high rate of mortality due to air pollution in low and middle-income countries can be connected with the remark from the work of Mohan et al. (2013) which revealed that toxicity of exhaust nanoparticles is rapidly growing due to increasing motor vehicle traffic and rapid industrialization which have contributed enormously to urban pollution.

In particular, the harmful impacts of air pollution on human health have been on the increase in the developing countries where electricity power supply is mainly through fossil fuel generating sets for both domestic and commercial purposes (WHO, 2014; Bernstein et al., 2004). Predominantly, the pollutants of global concern are CO, NOx (which comprises of nitrogen oxide – NO, and nitrogen dioxide - NO_2, PM, volatile organic compounds, hydrocarbon substances (HC), and sulphur oxides (SOx) (Bernstein et al., 2004).

* **Corresponding Author**

*(musaanimashaun@gmail.com) ORCID ID 0000-0002-2989-5771

Cite this study

Alademomi A S, Animashaun M B, Abolaji O E, Okolie C J, Ojegbile B M, Daramola O E, Alozie N S I (2021). Monitoring the spatial distribution of CO_2 within the University of Lagos Main Campus. 3rd Intercontinental Geoinformation Days (IGD), 124-127, Mersin, Turkey

This study is concerned with the mapping of the concentration of carbon dioxide. As stated, CO_2 is itself not a major pollutant but can indicate emission of CO, a very dangerous emission variable. Combustion studies have shown that in well-designed combustion systems, if there is complete combustion, the emissions variables are water (H_20) and CO_2. However, in most practical combustion systems or devices, combustion is never complete. This leads to emission of CO which upon further reaction with atmospheric oxygen yields CO_2. Therefore, increase in atmospheric CO_2 is indicative of increase in human activities involving the use of fossil fuels as a result of increase in population. One of the densely populated areas in Lagos State is the University of Lagos environment where the steady growth in social, commercial and industrial activities are ongoing. In recent times, these increases in human activities are in turn having significant effects in the air quality. Poor air quality in any environment has the potential to affect human health. The need to monitor and maintain good air quality as part of sustainable developmental goals is of interest to researchers in this study. In monitoring the air quality of any area of interest, the United States Environmental Protection Agency has designed a standardized air pollution level indicator for rating the air quality over an area. It is a rating scale for outdoor air called Air Quality Index (AQI). The lower the AQI value, the better the air quality. AQI rating A stands for Very Good (0 -15), B for Good (16 -31), C for Moderate (32 – 49), D for Poor (50 – 99) and E for Very poor (100 and over) (EPA, 2000). The air quality is determined with reference to the standard by the American Society of Heating, Refrigerating and Air Conditioning Engineers (ASHRAE). According to ASHRAE (2016), the standard for carbon dioxide is 1000ppm.

$$AQI_{POLLUTANT} = \frac{Data}{Standard} \times 100 \quad (1)$$

In this study, the geospatial mapping of the concentration of CO_2 has been considered as a first attempt because of the proven integrity of Geographic Information System (GIS) in air quality monitoring and management due to vehicular density within and around the University of Lagos environment.

1.1. Description of study area

The University of Lagos is a higher institution in Lagos State, Nigeria (Figure 1). It is located at approximately, latitudes 6°30'N to 6°31'N and longitudes 3°25'E to 3°27'E in the Lagos Mainland Local Government Area. The main campus which is largely surrounded by the scenic view of the Lagos lagoon and is located on 802 acres (3.25 km^2) of land in Akoka, northeastern part of Yaba, Lagos has been chosen as the study area. The focus on the main campus is justifiable based on the level of human activities as described and for the convenience of available geo-spatial data, as well as ease of environmental data collection.

2. Methods

2.1. Station selection

The siting of the monitoring stations has a profound effect on the resulting measurements and on achieving monitoring objectives. Thus, thirty-four (34) monitoring stations were established at strategic locations within the study area such as major road intersections (for vehicular emissions), dumpsites, commercial centers, academic areas, and residential sites as shown in Fig. 1.

2.2. Variables, equipment and measurement

The evaluated parameter was CO_2 gas which is a strong variable for assessing environmental air quality. To measure the concentration level of this gas, we adopted the use of a very simple device: calibrated hand-held solid-state gas sensor. Compu-Flow CO_2 Handheld meter, a gas monitor designed to provide continuous exposure monitoring of carbon dioxide was used to measure the CO_2 concentration levels in parts per million (ppm). Data was collected over six (6) observation windows within three days of observation. The average value for the pollution parameter readings were carefully recorded. All measurements were executed in 2-hour duplicates (i.e., repeated twice – morning peak period and afternoon off-peak period) over 3 days' observation period across all monitoring stations. The sampling was done in-situ and each sample station was geo-referenced using Garmin GPSMAP 78SC Marine handheld GPS. The duration for exposure was set at 5 minutes at a time per station. The average values for each of the locations were computed and recorded.

Figure 1. Study area extent and spatial distribution of measurement stations

2.3. Generation of CO_2 Distribution Map

The acquired data was transferred to a Microsoft Excel worksheet and imported into ArcGIS environment where it was represented by point shapefiles.

Kriging interpolation (an advanced geostatistical procedure that generates an estimated surface from a scattered set of points with values), was used to generate maps showing the spatial variation of CO_2.

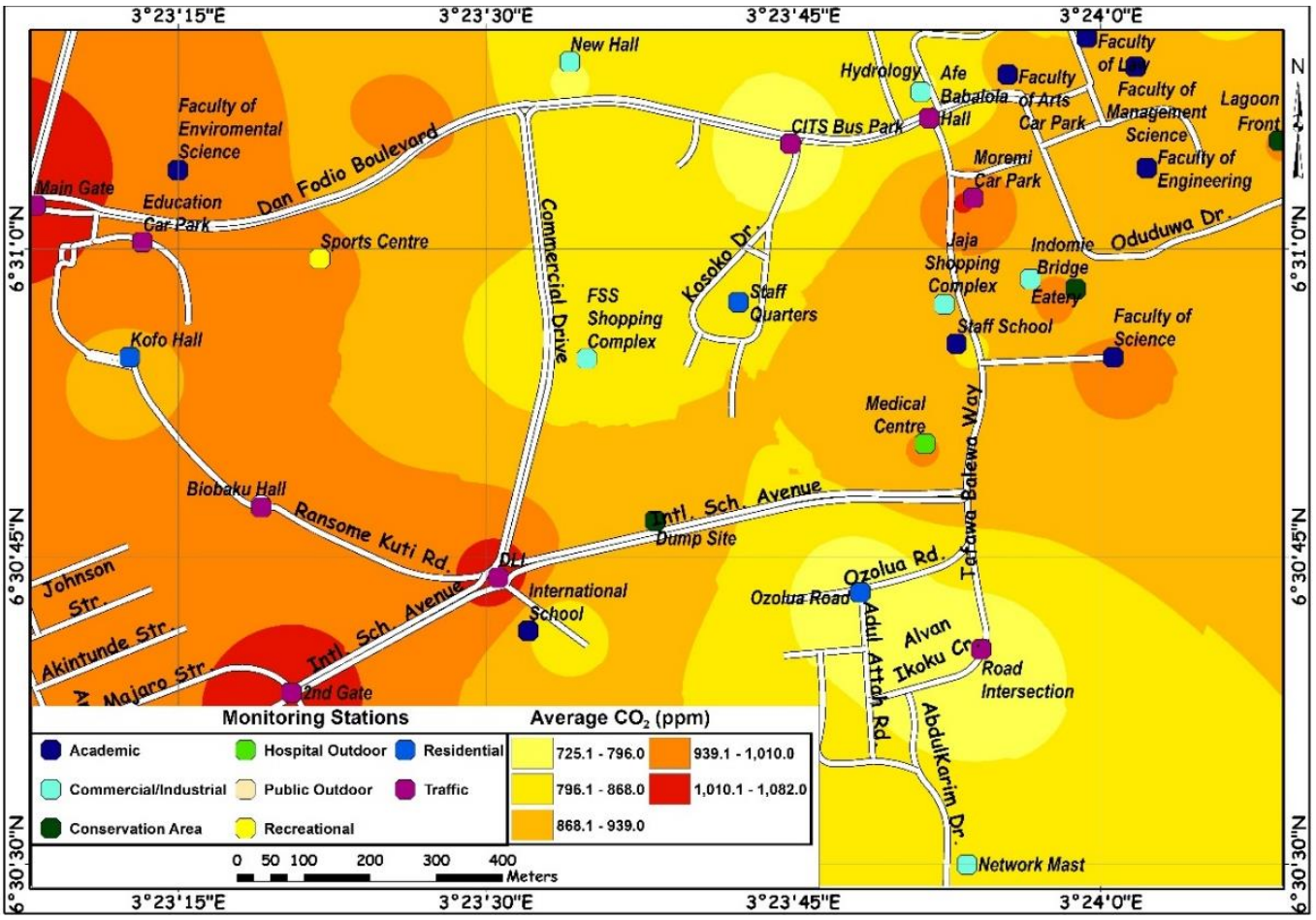

Figure 2. Spatial distribution of mean CO_2 for the entire duration of observation

Table 1. CO_2 statistics by land use type

Environment type	N	Mean	SD	SE	95% CI for Mean		Min	Max	AQI	Rating	Remark
					Lower Bound	Upper Bound					
Academic	10	861.3	52.1	16.5	824.04	898.64	788.2	982.6	86.13	D	Poor
Commercial/ Industrial/ Shopping	5	888.3	67.6	30.2	804.46	972.2	791.5	956.2	88.83	D	Poor
Conservation Area	4	889.8	48.3	24.2	812.92	966.75	825.8	942.6	88.98	D	Poor
Hospital Outdoor	1	945.7	.	.	.	.	945.7	945.7	94.57	D	Poor
Public Outdoors	1	894.3	.	.	.	.	894.3	894.3	89.43	D	Poor
Recreational	1	951.4	.	.	.	.	951.4	951.4	95.14	D	Poor
Religious	1	977.3	.	.	.	.	977.3	977.3	97.73	D	Poor
Residential	4	807.3	96.9	48.4	653.19	961.48	725.3	915.1	80.73	D	Poor
Traffic	7	985.6	122	46.1	872.87	1098.27	725.4	1082	98.56	D	Poor
Total	34	897.4	92	15.8	865.3	929.48	725.3	1082			

Table 2. Analysis of Variance (ANOVA) Test

		Sum of Squares	df	Mean Square	F	Sig.
AVG. CO_2	Between Groups	112156.2	8	14019.5	2.099	0.075
	Within Groups	166972.7	25	6678.91		
	Total	279128.9	33			

3. RESULTS

Table 1 shows the statistics of the data acquired with respect to environment types. As seen, the residential land use has the lowest mean concentration of 807.3ppm. CO_2 is mostly concentrated around the traffic corridors with mean 985.57ppm. The religious, recreational and

hospital outdoor maintained a close level of concentration averagely yielding 977.3ppm, 951.4ppm, and 945.7ppm respectively. The table also contains the calculated air quality index per land use and their corresponding rating values. In addition, Figure 2 represents the outcome of the kriging interpolation which is made into a map showing the spatial distribution of mean CO_2 for the entire duration of observation. Furthermore, Table 2 represents the outcome of the ANOVA test. When the relational impact of one land use is considered between it and the other land use types, the degree of freedom is 8 but when they are considered within the groups of the land use types, the degree of freedom is 25.

4. Discussion

The low concentration of CO_2 observed in the residential areas such as the Ozolua Junction and Staff Quarters in Figure 2 is as a result of minimal carbon-generating activities around there. On the other hand, the intense concentration noticed at the traffic cores (i.e., Main Gate, 2nd Gate, DLI Roundabout, and Moremi Car Park is linked to the massive vehicular movements around those places. Also, we can infer from Figure 2 that the western part of the school which is bounded by numerous road networks has higher CO_2 levels compared to the eastern end which is adjacent to the Lagoon. In addition, CO_2 level is generally high around the faculties and eateries and this is due to the presence of laboratories that utilize combustion engines and electricity generating plants as well as cooking. Also, the substantial concentration noticed around the dumpsite and Indomie Bridge (crossing a canal) is suspected to be as a result of CO_2 constituting 50% of the gas emitted due to decomposition of waste by microorganisms from landfills and canals. The AQI ratings in Table 1 further prove that the air quality with respect to CO_2 is generally poor in the campus.

5. Conclusion

In this study, atmospheric CO_2 was measured and analyzed at different environment types for variability over the duration of study using statistical and visualization approaches. The relationship between the gas and land uses was also analyzed. Also, the in-situ observed measurements have been compared with the ASHRAE standard for CO_2 (1000ppm). Furthermore, A one-tailed ANOVA test for content of the CO_2 was executed to ascertain the influence of the land use on the concentration. Overall, the study shows that CO_2 is majorly concentrated around traffic pivots, laboratories, eateries, and industrial areas, and is generally low in the residential areas of the university.

Acknowledgements

Our sincere gratitude goes to Prof. Alabi Soneye of the Department of Geography, University of Lagos for the provision of gas sensor which was used to acquire field data.

References

ASHRAE, A. (2016). ASHRAE Standard 62.1-2016, Ventilation for Acceptable Indoor Air Quality. American Society of Heating, Refrigerating, and Air-Conditioning Engineers, Inc.: Atlanta, GA.

Bernstein J, Alexis N, Barnes C, Bernstein IL, Bernstein JA, Nel A, Peden D, Diaz-Sanchez D, Tarlo SM, Williams PB. Health effects of air pollution. J Allergy Clin Immunol [Internet]. 2004 Nov [cited 2018 Jun 18];114(5):1116-23. Available from: https://www.jacionline.org/article/S0091-6749(04)02266-3/fulltext

EPA, US. (2000). National water quality inventory: 1998 Report to Congress. EPA-841-R-00-001. Office of Water Washington DC.

Mehta, S., Shin, H., Burnett, R., North, T., & Cohen, A. J. (2013). Ambient particulate air pollution and acute lower respiratory infections: a systematic review and implications for estimating the global burden of disease. Air Quality, Atmosphere & Health, 6(1), 69-83.

Mohan D, Thiyagarajan D, Murthy PB. Toxicity of exhaust nanoparticles. Afr J Pharm Pharmacol [Internet]. 2013 Feb 22 [cited 2018 Jun 18];7(7):318-31 Available from: http://www.academicjournals.org/article/article1380800058_Mohan%20et%20al.pdf

World Health Organisation. (2014). Ambient air pollution: A global assessment of exposure and burden of disease. Geneva, Switzerland: WHO

Intercontinental Geoinformation Days

http://igd.mersin.edu.tr/2020/

Spatial relationship between NDVI, EVI, SAVI and land cover change in the Lake Chad area from 1987 to 2017

Peter C. Nwilo, Chukwuma J. Okolie, Abdulkareem A. Umar, Samuel A. Akinnusi, Babatunde M. Ojegbile, Hamed O. Olanrewaju

University of Lagos, Faculty of Engineering, Department of Surveying and Geoinformatics, Lagos, Nigeria

Keywords
Land cover
NDVI
EVI
SAVI
Lake Chad

ABSTRACT

The interpretation and analysis of remotely sensed data for land cover change detection can be enhanced with the use of vegetation indices. This study used Landsat imageries to assess the relationship between the normalized difference vegetation index (NDVI), the enhanced vegetation index (EVI) the soil adjusted vegetation index (SAVI), and land cover changes in the Lake Chad area with a view to providing an informed perspective on changes within the lake's environment. The Landsat imageries were subjected to maximum likelihood classification to extract land cover and the VIs were calculated. The interim results show that between 1987 and 2017, built-up areas and bare lands increased by 174.69km^2 and 349.90km^2 respectively while vegetation increased by 2,290.10km^2. The water bodies reduced by 937.54km^2 during the period. The correlation coefficient between NDVI, EVI, and SAVI in 1987 and 2017 is strongly positive. These are interim results presented from an ongoing study. Further research can determine the pattern and trajectory of the observed changes in the Lake Chad area.

1. Introduction

The Sahelian region in Africa is experiencing unprecedented environmental changes in land cover and land quality (Lambin et al., 2001; Onyewotu et al., 2003). These changes over time are usually the accumulated impacts of both natural and anthropogenic interactions. The remote sensing technique of land cover analysis has proven to be one of the most sensitive tools for assessing the dynamics of these interactions, especially in an arid environment, where the ecosystems are considered fragile (Zhou et al., 2008; Humagain, 2012). The interpretation and analysis of remotely sensed data for land cover change detection can be enhanced with the use of Vegetation Indices (VIs).

The Normalized Difference Vegetation Index (NDVI) has found the widest applications because it is accurate, not computationally intensive, efficient and useful for agricultural land use mapping in tropical environments (Ali, 2009; Meera et al., 2015; Mushtaq and Asima, 2016; Marco, 2019; Alademomi et al., 2020). Similar to NDVI, the Enhanced Vegetation Index (EVI) can be used to quantify vegetation greenness. EVI corrects for some atmospheric conditions and canopy background noise and is more sensitive in areas with dense vegetation. In arid regions where vegetation cover is low, the Soil-Adjusted Vegetation Index (SAVI) is often used. SAVI minimizes soil brightness influences using a soil-brightness correction factor.

Several studies have been done on the monitoring of land cover changes in the Lake Chad region (e.g., Babamaaji and Lee, 2014; Ikusemoran et al., 2017; Hussaini et al., 2020; Nwilo et al., 2019; Nwilo et al., 2020). Generally, these previous studies and others have established several trends on the ongoing land cover changes in the Lake Chad area. However, there has been little focus on the link between land cover changes and vegetation indices in the Lake Chad area. This is required for a deeper understanding of the environmental and ecological changes occurring in the Lake Chad environment. In the present study, a comprehensive classification scheme is employed for mapping the land cover around the Lake. Also, the study assesses the relationship between the land cover changes and VIs.

2. Methods

The image processing workflow from the image preparation to the land cover classification was done with ENVI Classic 4.3 and Erdas Imagine 14 software.

* **Corresponding Author**

*(akinnusisamuel1845@gmail.com) ORCID ID 0000-0002-6911-4490

Cite this study

Nwilo P C, Okolie C J, Umar A A, Akinnusi S A, Ojegbile B M & Olanrewaju H O (2021). Spatial relationship between NDVI, EVI, SAVI and Land Cover changes in the Lake Chad area from 1987 to 2017. 3rd Intercontinental Geoinformation Days (IGD), 128-131, Mersin, Turkey

2.1. Study area

Lake Chad (shown in Figure 1) is a freshwater lake in the African Sahel (Isiorho et al., 1996). The lake is bordered by Cameroon, Niger, Nigeria and Chad. Its depth varies from 1.5 - 10.5m and it is about 215m above sea level, with apparently no outlet (FAO, 2009). A characteristic physiography of the lake, according to Babamaaji and Lee (2014), is a shallow ridge or 'great barrier', which extends between the northern and southern parts of the lake, approximately 40km wide. Within the lake area, numerous islands have developed trapping pockets of water in between. The area has continuous high temperature (except during the June to September wet season), strong solar radiation and low humidity that has contributed to the evaporation responsible for its shrinkage over the years (Odada et al., 2006; LCBC, 2015; Nagarajan et al., 2018). These continuous variations in climate among other factors affect the vegetation of the Lake Chad area which are majorly scrubs and grasses (Onamuti et al., 2017).

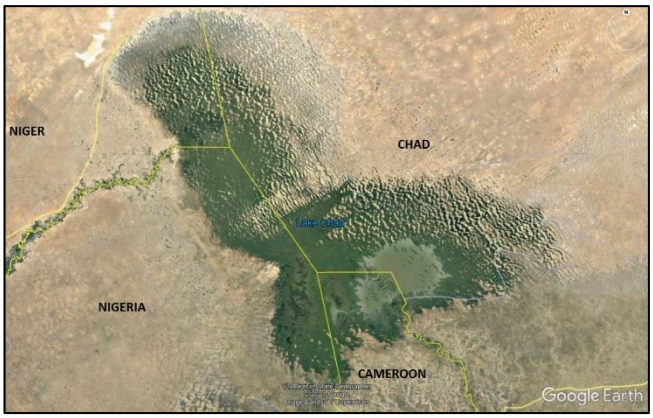

Figure 1. Imagery showing the location of Lake Chad (Source: Google Earth)

2.2. Datasets

Landsat satellite level 1 imageries covering the Lake Chad area at two epochs (1987 and 2017) were acquired to carry out image classification for this study. The level 2 NDVI, EVI, and SAVI image products for the same epochs were also downloaded for the study.

2.3. Data processing

To prepare the imageries for interpretation and classification, the imagery spectral bands were layer stacked and false color composites (FCCs) were created for each scene. The following band combinations were used to generate the FCCs: 1987 TM (4-3-2) and 2017 OLI (5-4-3). Afterwards, the scenes in each epoch were mosaicked together in Erdas Imagine. For the land cover classification, the mosaics were subsetted to the area covered. The maximum likelihood classification algorithm was used to classify the imagery into six classes: built-up area, bare land, sand dune, water body, vegetation, and soil.

The NDVI, SAVI, and EVI level 2 data were rescaled to actual index values by dividing the pixel values by 10000 to obtain index values between -1 and +1 for all the indices. The raster calculator on ArcMap Spatial Analyst tool was used for this operation.

3. Results

Figures 2 – 6 shows the results of the image classification and the processed vegetation indices. Table 1 shows the magnitde of areal changes between 1987 and 2017 while Table 2 shows the descriptive statistics of the VIs. Table 3 shows the correlation analysis between the VIs.

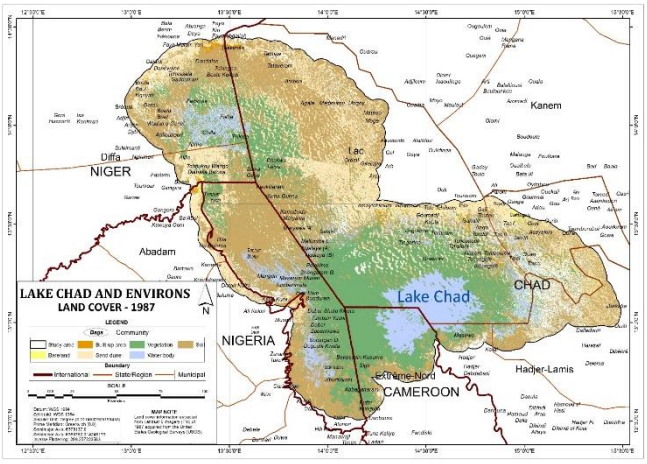

Figure 2. Land cover map of the Lake Chad area – 1987

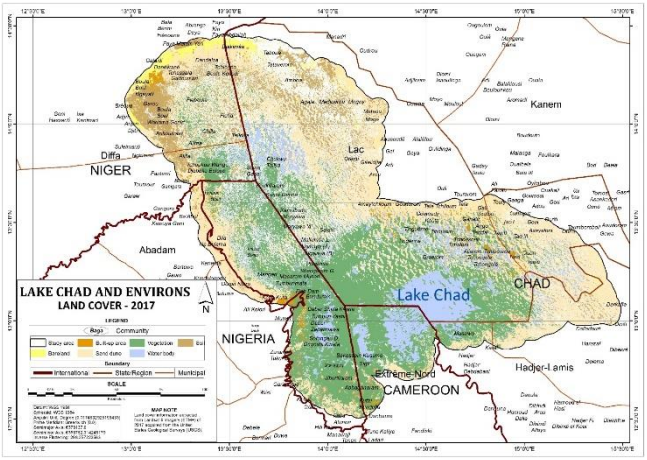

Figure 3. Land cover map of the Lake Chad area – 2017

Table 1. Magnitude of areal changes, 1987- 2017

Feature class	Magnitude of areal change (km²)
Built-up area	+174.69
Bare land	+349.90
Sand dune	+1069.92
Soil	+4868.49
Vegetation	+2290.10
Water body	-937.54

Table 2. Descriptive Statistics of the Vegetation Indices

Parameter	Year	Min	Max	Mean	Std. dev
NDVI	1987	-0.68	0.85	0.22	0.22
	2017	-0.72	0.89	0.26	0.27
EVI	1987	-0.02	0.65	0.16	0.13
	2017	-0.21	0.78	0.18	0.14
SAVI	1987	-0.31	0.8	0.15	0.12
	2017	-0.23	0.68	0.18	0.14

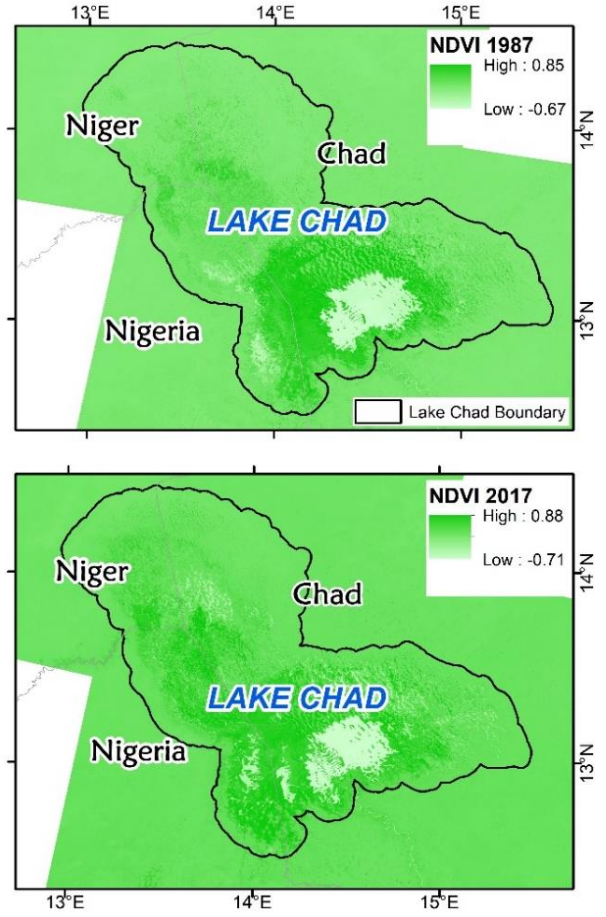

Figure 4. Normalised Difference Vegetation Index

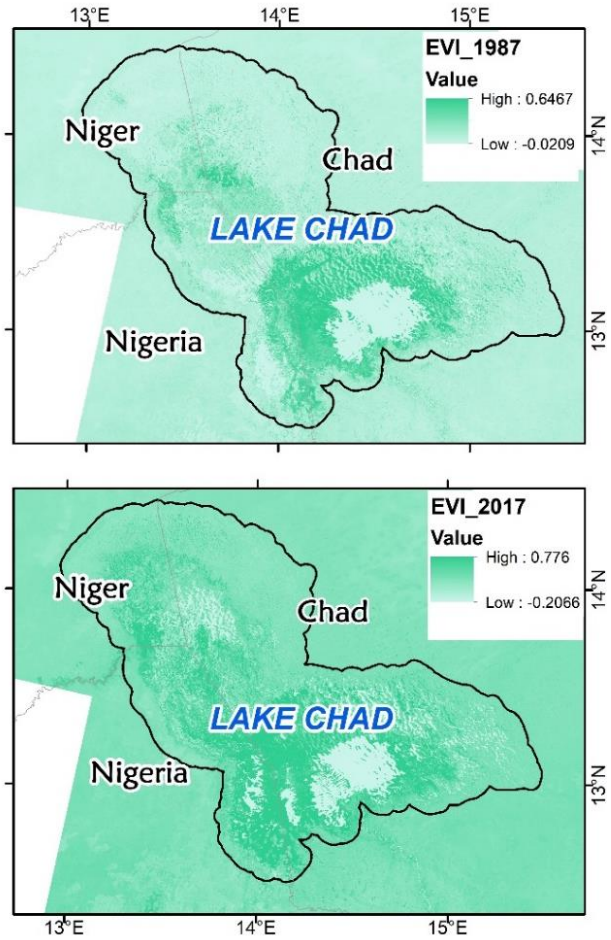

Figure 4. Enhanced Vegetation Index

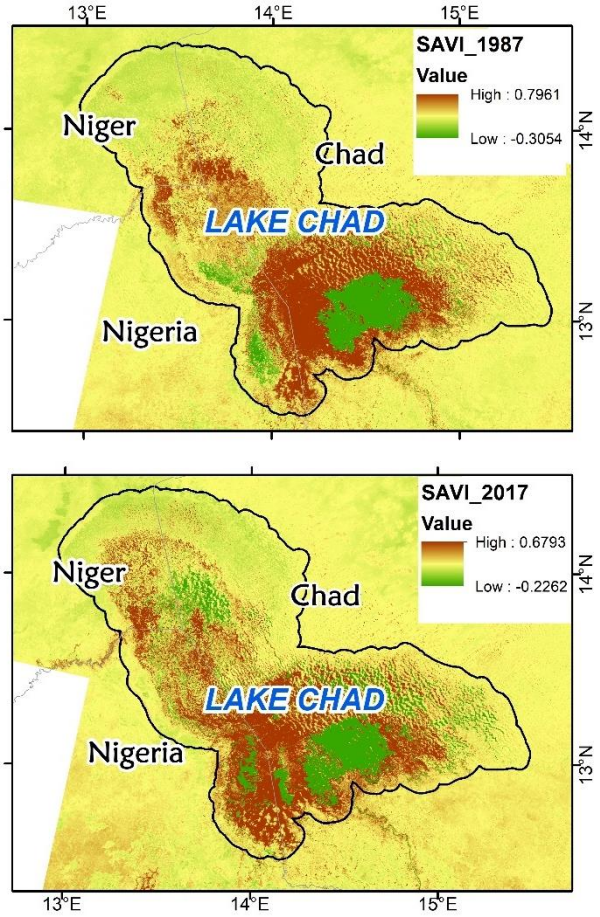

Figure 6. Soil Adjusted Vegetation Index

Table 3. Correlation coefficient (r) between the VIs

	NDVI 1987	NDVI 2017	EVI 1987	EVI 2017	SAVI 1987	SAVI 2017
NDVI 1987	1	0.57	0.95	0.51	0.97	0.52
NDVI 2017	0.57	1	0.45	0.95	0.48	0.96
EVI 1987	0.95	0.45	1	0.4	1	0.42
EVI 2017	0.51	0.95	0.4	1	0.43	1
SAVI 1987	0.97	0.48	1	0.43	1	0.44
SAVI 2017	0.52	0.96	0.42	1	0.44	1

4. DISCUSSION

Between 1987 and 2017, built-up areas and bare lands increased by 174.69km^2 and 349.90km^2 respectively while vegetation increased by 2290.10km^2. Also, there was a drastic reduction in surface water of about 937.54km^2. This alarming depletion translates to a staggering decrease in the surface area of the lake in a space of 30 years. The correlation coefficient between NDVI, EVI, and SAVI in 1987 and 2017 is positive. The highest is observed in SAVI-EVI for both years followed by NDVI-SAVI and NDVI-EVI respectively.

5. Conclusion

We have presented interim results from the ongoing study of the spatial relationship between NDVI, EVI, SAVI and land cover change in the Lake Chad area. In another paper, a comprehensive analysis and interpretation of the distribution of the VIs, and the interdependence between the VIs and land cover will be presented

Acknowledgements

The authors thank the editors and reviewers of this manuscript for their constructive criticisms which have contributed to the quality of the research output.

References

Alademomi, A. S., Okolie, C. J., Daramola, O. E., Agboola, R. O., and Salami, T. J. (2020). Assessing the relationship of LST, NDVI and EVI with Land Cover changes in the Lagos Lagoon environment. Quaestiones Geographicae. 39(3), 87-109. https://doi.org/10.2478/quageo-2020-0025

Babamaaji, R. A., & Lee, J. (2014). Land use / land cover classification of the vicinity of Lake Chad using NigeriaSat-1 and Landsat data. 4309–4317. https://doi.org/10.1007/s12665-013-2825-x

Babamaaji, R. A., & Lee, J. (2014). Land use / land cover classification of the vicinity of Lake Chad using NigeriaSat-1 and Landsat data. 4309–4317. https://doi.org/10.1007/s12665-013-2825-x

FAO (2009). Adaptive Water Management in the Lake Chad Basin. Addressing Current Challenges and Adapting to Future Needs. FAO Water Seminar Proceedings of the World Water Week, Stockholm. August 16-22. URL: http://www.fao.org/nr/ water/docs/ChadWWW09.pdf.

Humagain, K., 2012. Examining Land Use/Land Cover Change and Potential Causal Factors in the Context of Climate Change in Sagarmatha National Park, Nepal.

Hussaini, A., Mahmud, M. R., & Tang, K. K. W. (2020). Change Detection for the Past Three Decades Using Geospatial Approach in Lake Chad , Central Africa Change Detection for the Past Three Decades Using Geospatial Approach in Lake Chad , Central Africa. IOP Conference Series: Earth and Environmental Science PAPER. https://doi.org/10.1088/1755-1315/540/1/012001

Ikusemoran, M., Alhaji, M. Abdussalam, B. (2017). Geospatial Assessments of the Shrinking Lake Chad. Adamawa State University Journal of Scientific Research 6(1), 114 – 130.ISSN: 2251-0702.

Isiorho, S. A., Matisoff, G., Wehn, K.S., (1996). Seepage relationships between Lake Chad and the Chad aquifers. Ground Water. 34(5), 819-826.

Lambin, E.F., Turner, B.L., Geist, H.J., Agbola, S.B., Angelsen, A., Bruce, J.W., Coomes, O.T., Dirzo, R., Fischer, G., Folke, C., George, P.S., Homewood, K., Imbernon, J., Leemans, R., Li, X., Moran, E.F., Mortimore, M., Ramakrishnan, P. S., Richards, J. F., Skanes, H., Steffen, W., Stone, G. D., Svedin, U., Veldkamp, T. A., Vogel, C., Xu, J. (2001). The causes of land-use and land-cover change: moving beyond the myths. Global environmental change. 11(4), 261-269.

Marco, H. (2019). Spatiotemporal Contextual Uncertainties in Green Space Exposure Measures: Exploring a Time Series of the Normalized Difference Vegetation Indices. Int. J. Environ. Res. Public Health 2019. 16, 852; doi:10.3390/ijerph16050852 www.mdpi.com/journal/ijerph

Meera, G.G., Parthiban, S., Nagaraj, T., Christy. A., 2015. NDVI: Vegetation Change Detection using Remote Sensing and GIS – A Case Study of Vellore District. 3rd International Conference on Recent Trends in Computing 2015 (ICRTC-2015). Procedia Computer Science 57 (2015), 1199 – 1210. 1877-0509 © 2015 Published by Elsevier B.V. doi: 10.1016/j.procs.2015.07.415

Mushtaq, A.G., Asima, N. (2016). Determining the Vegetation Indices (NDVI) from Landsat 8 Satellite Data. Article DOI:10.21474/IJAR01/1348. International Journal of Advance Research (IJAR). 4(8), 1459-1463. http://dx.doi.org/10.21474/IJAR01/1348

Nwilo, P. C., Olayinka, D. N., Okolie, C. J., Emmanuel, E.I., Orji, M. J., and Daramola, O. E. (2020). Impacts of land cover changes on desertification in northern Nigeria and implications on the Lake Chad Basin. Journal of Arid Environments, Vol 181, 2020, 104190. https://doi.org/10.1016/j.jaridenv.2020.104190

Odada O.E., Oyebande E., Oguntola, J.A., 2006. Lake Chad: Experience and Lessons Learned Brief. http://erepository.uonbi.ac.ke/bitstream/handle/11295/36094/Full%20text.pdf?sequence=1&isAllowed=y

Onamuti, O. Y., Okogbue, E. C., & Orimoloye, I. R. (2017). Remote sensing appraisal of Lake Chad shrinkage connotes severe impacts on green economics and socio-economics of the catchment area. Royal Society Open Science, 4(11), 0–10. https://doi.org/10.1098/rsos.171

Onyewotu, L. O. Z., Stigter, C. J., Abdullahi, A. M., Ariyo, J. A., Oladipo, E. O., Owonubi, J. J. (2003). Reclamation of desertified farmlands and consequences for its farmers in semiarid northern Nigeria: a case study of Yambawa rehabilitation scheme. Arid Land Research and Management, 17(1), 85-101.

Zhou, Q., Li, B., Kurban, A., (2008). Trajectory analysis of land cover change in arid environment of China. International Journal of Remote Sensing. 29(4), 1093-1107.

Intercontinental Geoinformation Days

http://igd.mersin.edu.tr/2020/

Health impacts of noise exposure in an academic environment

Alfred Alademomi[1,2,3], Johanson Onyegbula[1], Rahmat Adepo[1], Chukwuma Okolie[1,2,3], Babatunde Ojegbile*[1,2], Abiodun Alabi[1,2], Olagoke Daramola[1,2], Nehemiah Alozie[4], Andy Egogo-Stanley[1,2], Inioluwa Ayantayo-Ojo[1,2]

[1]*University of Lagos, Faculty of Engineering, Department of Surveying and Geoinformatics, Lagos, Nigeria*
[2]*Geospatial and Environmental Research Group, University of Lagos, Nigeria*
[3]*Centre for Multidisciplinary Research and Innovation (CEMRI), Abuja, Nigeria*
[4]*University of Lagos, Faculty of Engineering, Department of Mechanical Engineering, Lagos, Nigeria*

Keywords
Noise Exposure
Noise Pollution
Noise Mapping
University of Lagos
GIS

ABSTRACT

In the face of increasing exposure to various environmental pollutants, the peculiarity of noise has made it to pervade even well-structured societies. This study assessed the health impacts of noise exposure within the University of Lagos main campus. An opinion pool of staff and students was taken with an online questionnaire survey that inquired about the likely health effects of noise. Common noise-related problems reported by the survey participants include increased distractions, loss of concentration, and issues of health and mental wellbeing. It is recommended that immediate measures be put in place to checkmate the negative impacts of prolonged noise exposures in university campuses nationwide.

1. Introduction

Noise as a pollution and nuisance, has dramatically increased in our environments, prompting many individuals to consider relocation to quieter areas (Obaidat, 2008). Urbanization and industrialization have compounded the problem of environmental noise all over the world (Gholami et al., 2012).

The difficulties faced by noise pollution cannot be overstated, as most people are unaware of not just the deleterious repercussions of long-term exposure to it, but also what it is (Luqman et al., 2013). In general, the public overlooks several factors that contribute to increasing sound levels in the surroundings (Obiefuna et al., 2013). Increased sound levels from sources considered acceptable could, however, be sources of noise pollution, as the long-term consequences are similar to those generated by repetitive exposure to those considered as unpleasant.

Noise comes from a variety of places in the environment, including the neighborhood (Laze, 2017), industrial operations (Bubli et al., 2010), and transportation (Sotiropoulou et al., 2020). Individuals are often unaware of these noise sources because they have been accustomed to it, in addition to passion for their investments of time and resources. Hence, their concentrations in everyday activities for personal goals. As a result, the negative consequences of failing to recognize rising noise pollution as a contributing factor to their poor health and reduced quality of life are amplified (Nwobi-Okoye et al., 2015).

Increased urbanization nowadays results in higher sound levels as a result of traffic congestion, industrialization, and other factors. Several studies have found a strong link between people's hearing loss, mental health issues, and annoyance and the noise levels exposures (Alimohammadi et al., 2019; Babisch, 2011).

High noise levels also have a negative impact on different learners' auditory, reading, and cognitive abilities in their learning contexts (Shield et al., 2003). These and other harmful consequences of noise have resulted in the development of laws and a variety of engineering solutions to manage and/or reduce its negative impact on human health (WHO, 2018).

In a previous study, we mapped noise level variations within the University of Lagos main campus, with the use of spatial and statistical analysis, and a conformity assessment based on internationally recognised noise standards (Alademomi et al., 2020). In the study, it was shown that the noise levels within the university campus exceeded the tolerable limits for

*Corresponding Author
*(babatundeojegbile@gmail.com) ORCID ID 0000-0003-2219-8970

Cite this study
Alademomi, A.S. et al. (2021). Health impacts of noise exposure in an academic environment. 3rd Intercontinental Geoinformation Days (IGD), 132-134, Mersin, Turkey

academic, commercial and residential areas set by World Health Organisation (WHO) and the National Environmental Standards and Regulations Enforcement Agency (NESREA). The present study goes further to assess the potential health impacts of noise exposure on members of the university community.

2. Methods

2.1. Study area

The University of Lagos is a higher institution of learning and a popular choice for tertiary education by many residents of Lagos and Nigeria generally. Its urban location makes it a beehive of activities beyond academia, including commercial and social activities, thereby exposing it to regular noise pollution. It is located in the low-lying Lagos metropolis between longitudes 3°23'00"E – 3°24'30"E and latitudes 6°30'00"N – 6°31'30"N. It is bounded eastwards by the Lagos lagoon and surrounded by dense residential and commercial buildings. The map of the study area is as shown in Fig. 1.

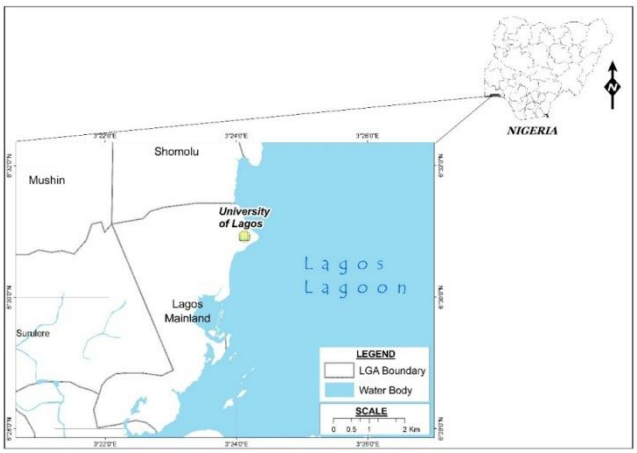

Figure 1. Geographic location of the study area, University of Lagos Main Campus, in Nigeria

2.2. Questionnaire survey and analysis

A questionnaire form was created with the Google forms tool. Most of the questions required respondents to select a single option on a 5-point scale. Whereas, others had predefined options for selection (especially the checkboxes) and a single yes/no question was included as well. The key questions asked in the questionnaire are summarized in Table 1. The link to the online questionnaire was distributed to members of the university community via Whatsapp messaging in the month of September, 2020.

The responses were transferred to a Microsoft Excel spreadsheet for statistical analysis and visualisation.

3. Results

There were a total of 324 responses. The health impacts of noise exposure were assessed and are presented in Fig. 2 and Tables 2- 3.

Table 1. Summary of questions provided for survey.

S/N	Questions
1	Which of the following challenges/issues do you experience due to excessive noise
2	How often do you experience earaches as a result of noise?
3	How often do you experience headaches from excessive noise exposure?
4	How often do you feel dizzy after excessive noise exposure?
5	How often do you experience ringing in the ears (tinnitus) due to excessive noise exposure?
6	Do you experience changes in your mood/attitude after prolonged exposure to the noise on campus?
7	How well do you concentrate beyond noise levels deemed moderate to you?

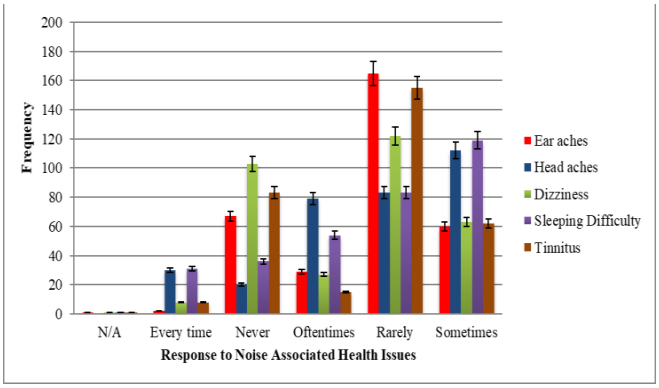

Figure 2. Frequency of health issues related to noise exposure

Table 2. Impacts of noise exposure on mood change

Mood changes	Frequency	Percent
N/A	7	2.2
No	94	29.0
Yes	223	68.8
Total	324	100.0

Table 3. Impacts of noise exposure on concentration

Ability to concentrate	Frequency	Percent
N/A	3	.9
Absolute loss of concentration	31	9.6
Excellently	18	5.6
Fairly well	147	45.4
Slightly	81	25.0
Very well	44	13.6
Total	324	100.0

4. Discussion

Fig. 2 above shows that 61 people experience difficulties with sleeping and headache every time. This number is above 9% of all the respondents. Other health issues reported include dizziness and tinnitus. Oftentimes and sometimes, respondents also experienced headache and sleep difficulties. Hence, the major illnesses associated with noise exposure at the

University of Lagos Campus are headaches and sleep difficulties.

Noise exposure also causes mood swings which can affect the healthy use of the brain in terms of memory retention and oftentimes leads to stress and outburst of anger (Yulia, 2014). From Table 2, 68.8% of the respondents in this study experience mood changes. These mood changes caused by noise exposure could affect the assimilation rate of the students and others which can lead to mental stress and discouragement.

5. Conclusion

Exposure to prolonged noise pollution has deleterious impacts on the health of any anyone who stays within the vicinity of such an environment. Some of the health issues that have been identified to be the result of noise exposure include tinnitus (itching/ringing ear), headaches, dizziness, loss of sleep, stress and poor concentration.

The effect of noise exposure on concentration levels could manifest in the absence of a good grasp of the knowledge being shared and the critical logical reasoning involved in research and learning process. This is a major cause of concern that shows the need for the University management to publish necessary regulations that can help to curb continuous noise levels.

The university management thus needs to administer necessary rules and give orientation to sensitize every member of the University of Lagos community about how to minimize noise level rise especially from social activities and other human activities.

Acknowledgements

Special thanks to everyone who contributed to the success of the work.

References

Alademomi, A., Okolie, C., Ojegbile, B., Daramola, O., Onyegbula, J., Adepo, R., & Ademeno, W. (2020). Spatial and Statistical Analysis of Environmental Noise Levels in the Main Campus of the University of Lagos. The Journal of Engineering Research [TJER], 17(2), 75-88.

Alimohammadi, I., Kanrash, F. A., Abolghasemi, J., Vosoughi, S., & Chalak, M. H. (2019). Relationship between noise annoyance and cognitive performance in automotive workers exposed to chronic noise. Journal of UOEH, 41(4), 375-385.

Babisch, W. (2011). Cardiovascular effects of noise. Noise and health, 13(52), 201.

Gholami, A., Nasiri, P., Monazzam, M., Gharagozlou, A., Monavvari, S. M., & Afrous, A. (2012). Evaluation of traffic noise pollution in a central area of Tehran through noise mapping in GIS. Advances in Environmental Biology, 6(8), 2365-2371.

Laze, K. (2017). Findings from measurements of noise levels in indoor and outdoor environments in an expanding urban area: a case of Tirana. Noise Mapping, 4(1), 45-56.

Luqman, Y. A., Rowland, A. G., Zhang, Y., & Umar, O. Z. (2013). Work environment noise levels and risk locations in two selected commercial areas in Ibadan, Nigeria. *Global J. Med. Res*, *13*(6).

Nwobi-Okoye, C. C., Uyaelumuo, A. E., Okoronkwo, G. O., & Duru, C. A. (2015). Analysis and Modelling of Road Traffic Noise in Onitsha Metropolis, Nigeria. International Journal of Advanced Multidisciplinary Research Reports, 1(1).

Obaidat, M. T. (2008). Spatial Mapping of Traffic Noise Levels in Urban Areas. In Journal of the Transportation Research Forum (Vol. 47, No. 1424-2016-117907, pp. 88-102).

Obiefuna, J. N., Bisong, F. E., & Ettah, E. B. (2013). A GIS analysis of noise islands in Calabar metropolis, Nigeria. *J. Environ. Sci*, *3*, 12.

Shield, B., & Dockrell, J. (2008). The Effects of classroom and environmental noise on children's academic performance. In 9th International Congress on Noise as a Public Health Problem (ICBEN), Foxwoods, CT.

Sotiropoulou, A., Karagiannis, I., Vougioukas, E., Ballis, A., & Bouki, A. (2020). Measurements and prediction of road traffic noise along high-rise building façades in Athens. *Noise Mapping*, *7*(1), 1-13.

World Health Organization. (2018). Environmental noise guidelines for the European region.

Yulia Gershfeld (2014). Mood Swings: An application to track, understand and share emotions for people who need to control mood swings. Master's Thesis, Department of Communication and Information Science, Tilburg University, Tilburg. June 20014.

Intercontinental Geoinformation Days

igd.mersin.edu.tr

Application of gis and analytical hierarchy process for flood vulnerability assessment in Adamawa Catchment, Nigeria

Ayila E. Adzandeh[1,2], Dupe N. Olayinka-Dosunmu[1,3], Isa A. Hamid-Mosaku[1], Chukwuma J. Okolie[1], Peter C. Nwilo[1], Caleb O. Ogbeta *[4]

[1]*University of Lagos, Faculty of Engineering, Department of Surveying and Geoinformatics, Lagos, Nigeria*
[2]*African Regional Institute for Geospatial Information Science and Technology (AFRIGST), Ile-Ife, Nigeria*
[3]*Federal School of Surveying, Oyo, Nigeria*
[4]*Bells University of Technology, Department of Surveying and Geoinformatics, Ogun State, Nigeria*

Keywords
Adamawa catchment
AHP
Assessment
GIS
Flood vulnerability

ABSTRACT

This study applies Geographic Information System (GIS) and Analytical Hierarchy Process (AHP) to assess flood vulnerability in the Adamawa Catchment of Nigeria. Seven criteria (drainage, rainfall distribution, geology, land cover, elevation, slope, and soil) were analysed, and a pairwise comparison matrix was constructed. The analysis resulted in a flood vulnerability map depicting different levels of vulnerability. The reliability of the approach and results were validated with a Consistency Ratio of 0.0944 and found to be within the acceptable value for reasonable consistency. The methodology used therefore disclosed the areas vulnerable to flooding in the Adamawa catchment. The analysis revealed the following levels of vulnerability - low vulnerability (19.9%), moderate vulnerability (31.4%), high vulnerability (31.8%), and very high vulnerability (16.9%) respectively. The main river and tributaries are pinpointed as areas highly vulnerable to floods and therefore, might be significant contributors to flooding events in the catchment.

1. Introduction

In recent years, the frequency and severity of large-scale flood catastrophes have grown internationally, resulting in deaths, property devastation, and massive economic losses. Similarly, hydrological and meteorological calamities such as floods, droughts, and weather storms have been prevalent across the planet. Despite the availability of sophisticated technological skills for coping with floods in industrialized countries, flood catastrophes are becoming increasingly common and devastating. The United Nations International Strategy for Disaster Reduction describes flooding as a threat to sustainable development and poverty-reduction initiatives (UN-ISDR, 2009).

Flooding claims more lives and causes damage to property and infrastructure than any other natural phenomena (Dilley et al., 2005; Nwilo et al. 2012; Olayinka et al. 2012). In a period of 6 years (1989–1994), 80% of declared Federal disasters in the United States (US) were related to flooding and averaged four billion dollars annually in property damage alone (Wadsworth, 1999).

Many scholars have given a variety of definitions for vulnerability in various contexts. According to the UK Department for International Development (DFID), vulnerability is defined as the interrelationship between a system's exposure, susceptibility, and coping capability (White et al., 2005; Roy and Blaschke, 2015). Likewise, several authors have assessed flood vulnerability using different methods. Nwilo et al. (2012) adopted Remote Sensing and Cellular Automaton Evolutionary Slope and River (CAESAR) model to determine inundation levels and assess vulnerability of settlements in Adamawa State. Roy and Blaschke (2015) used an Analytical Hierarchy Process (AHP) and Geographic Information System (GIS) weighted overlay to build a grid-based technique for assessing the vulnerability of floods in Bangladesh's coastal areas.

* **Corresponding Author**

*(ogbetac@gmail.com) ORCID ID 0000-0002-8719-4965

Cite this study

Adzandeh A, Olayinka-Dosunmu D, Hamid-Mosaku I, Okolie C, Nwilo P & Ogbeta C (2021). Application of GIS and Analytical Hierarchy Process for Flood Vulnerability Assessment in Adamawa Catchment, Nigeria. 3rd Intercontinental Geoinformation Days (IGD), 135-138, Mersin, Turkey

Several researchers or organizations employ the AHP or similar techniques in their investigations. For example, Feizizadeh and Blaschke (2011) employed AHP to create weights for a GIS weighted overlay landslide susceptibility mapping. In a comparison of AHP, weighted linear combination (WLC), and ordered weighted average (OWA), Feizizadeh and Blaschke (2013) discovered that AHP was an effective method for evaluating the consistency of the assessment measures and alternatives proposed by decision makers. They found that the AHP technique effectively reduced the judgment problem's complexity to a series of pairwise comparisons that could be synthesized in a ratio matrix.

Flood problems along the Benue River in Adamawa State of Nigeria have affected more communities in recent times. There is increasing vulnerability of populations and infrastructure to flooding and flood related hazards. Although studies have demonstrated the impacts of flooding in the region, little attention has been paid to the physical factors that contribute to vulnerability to flooding particularly in Adamawa catchment. The present paper therefore presents a set of criteria for estimating flood vulnerability. Based on these criteria, we then describe the preparation of thematic layers and construction of the final flood vulnerability map for Adamawa catchment using GIS techniques and AHP.

1.1. Study area

Adamawa catchment in Nigeria is located along River Benue in the Upper Benue drainage basin. The major river in the catchment area is River Benue. River Benue is an international river entering into Nigeria across the border with Cameroon, and runs for a distance of about 900 km from the border to the confluence with the Niger River at Lokoja. The Sub-catchment border is approximately defined by longitudes 11°46'E and 14°14'E, and latitudes 8° 37'N and 9°41'N as shown in Figure 1.

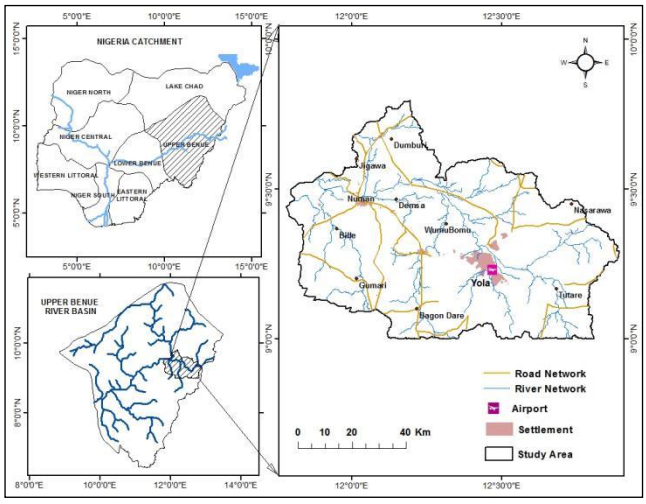

Figure 1. Study area location

2. Methods

Criteria such as drainage density, rainfall distribution, geology, land cover, elevation, slope and soil were reviewed and utilized to investigate flood vulnerability in this study. An empirical approach through the integration of multi-criteria AHP and GIS techniques was adopted for the analysis. AHP is a multi-criteria decision method that uses hierarchical structures to represent problems. Priorities for alternatives are then developed based on the judgment of the user. The following steps were taken based on the works of Saaty (1980) and Lee et al. (2008) to achieve the objectives of the study.

Step 1: Criteria selection
Step 2: Development of the pairwise comparison matrix
Step 3: Computation of the criterion weights
Step 4: Consistency check
Step 5: Generation of thematic layers

Each of the layers were reclassified into four classes and overlaid by computing their various weighted values from AHP techniques using Weighted Sum Analysis in ArcGIS environment to construct the final flood vulnerability map as provided in Eq. (1).

$$\text{Flood Vulnerability Zone Map (FVZM)} = \sum_{i=1}^{n} W_i X_j \quad (1)$$

where, W_i = % weight for each thematic map and X_i = reclassified map

The map produced was categorized into four levels of low, moderate, high and very high vulnerability.

3. Results

A pairwise comparison matrix was constructed as shown in Table 1. The fraction values were further reduced to decimal values and the sum of each column was calculated and then the matrix was normalized as depicted in Table 2. The weights were calculated by averaging the entire elements along the row and the percentage weight was computed. These calculated weights (Table 3) were used in GIS software for weighted sum analysis of the flood factors to produce a flood vulnerability map (Figure 2). Coherence values in Table 3 were obtained by multiplying the total values of pairwise comparison matrix (sum of each column) obtained by criteria weight which gives λmax = Eigen value (7.748). Since, n = total number of factors is 7, to validate the reliability of the approach and results, a Consistency Ratio of 0.0944 was determined from the judgment process. The Consistency Ratio 0.0944 < 0.10, shows that the pairwise matrix is reasonably consistent.

Table 1. The pairwise comparison matrix

Factors	LC	E	R	G	So	DD	Sl
LC	1	1/4	1/7	1/3	1/5	1/9	1/4
E	4	1	1/3	3	3	1/3	1/2
R	7	3	1	3	5	1/2	3
G	3	1/3	1/3	1	3	1/3	1/3
So	5	1/3	1/5	1/3	1	1/5	1/3
DD	9	3	2	3	5	1	5
Sl	4	2	1/3	3	3	1/5	1

LC – Land Cover, E – Elevation, R – Rainfall, G – Geology, So – Soil, DD – Drainage Density, Sl – Slope

Table 2. Normalized pairwise comparison matrix

Factors	LC	E	R	G	So	DD	Sl
LC	0.030	0.025	0.033	0.024	0.010	0.041	0.024
E	0.121	0.101	0.077	0.220	0.149	0.124	0.048
R	0.212	0.303	0.230	0.220	0.248	0.187	0.288
G	0.091	0.034	0.077	0.073	0.149	0.124	0.032
So	0.152	0.034	0.046	0.024	0.050	0.075	0.032
DD	0.273	0.303	0.461	0.220	0.248	0.373	0.480
Sl	0.121	0.202	0.077	0.220	0.149	0.075	0.096
Total	1	1	1	1	1	1	1

LC – Land Cover, E – Elevation, R – Rainfall, G – Geology, So – Soil, DD – Drainage Density, Sl - Slope

Table 3. Criteria weight and coherence

Factors	Weight	Weight (%)	Coherence
Land cover	0.027	2.688	0.891
Elevation	0.120	11.990	1.2
Rainfall	0.241	24.095	0.964
Geology	0.083	8.278	1.162
Soil	0.059	5.882	1.180
Drainage Density	0.337	33.661	1.011
Slope	0.134	13.405	1.34
TOTAL	**1**	**100**	**7.748**

4. Discussion

It was observed that River Benue and its tributaries are areas highly vulnerable to floods in the catchment and therefore, they might significantly contribute to flooding events. Results of the analysis reveal that the high vulnerability and very high vulnerability areas both account for about 50% of the total study area. Only about 19.9% of the area has low vulnerability to flooding. Table 4 provides detailed statistics of the flood vulnerability distribution.

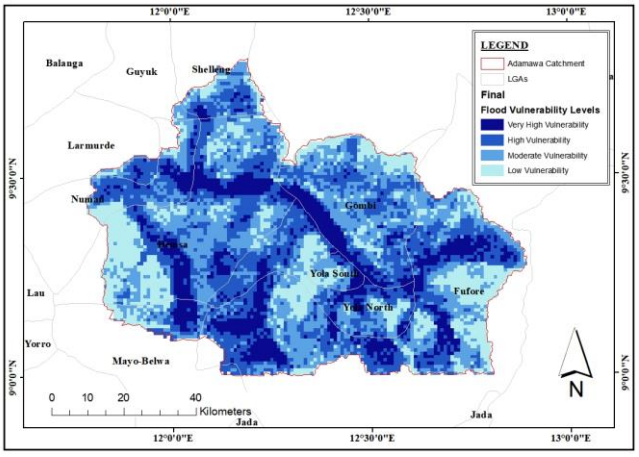

Figure 2. Final flood vulnerability map

Table 4. Distribution of vulnerability levels

Flood vulnerability classes	Area (km²)	Area (%)
Very High Vulnerability	1110	16.859
High Vulnerability	2094	31.804
Moderate Vulnerability	2070	31.440
Low Vulnerability	1310	19.897
Total	**6584**	**100**

For years, flooding has had a catastrophic impact on the local population, resulting in the loss of life and property, as well as a reduction in economic activity due to health concerns and mass migration to nearby towns and villages.

5. Conclusion

The goals of this present study were to examine the physical factors influencing flood vulnerability and to identify flood prone zones in Adamawa catchment. This is important to decision makers and for future research because it forms the baseline information for flood control and vulnerability management. Future studies should emphasize the linkages between economic processes and the inequities of uneven vulnerability. The analytical methodology applied in this study may be extended to evaluate a larger collection of case studies in African cities focused on urban susceptibility to flood risks and other factors that affect the uneven incidence of flood vulnerability. More research on the causes of urban settlements' susceptibility to flood risks is required to understand more about all the factors that contribute to socioeconomic disparities and unequal risk distribution.

References

Dilley, M., Chen, R S., Deichmann, U., Lerner-Lam, A.L. and Arnold, M. (2005). Natural Disaster Hotspots: A Global Risk Analysis. The World Bank, US, 150 pp.

Feizizadeh B., and Blaschke T. (2011). Landslide risk assessment based on GIS multi-criteria evaluation: a case study in Bostan-Abad County, Iran. J Earth Sci Eng. 1(1):66–71.

Feizizadeh B., & Blaschke T. (2013). GIS-Multicriteria decision analysis for landslide susceptibility mapping: comparing three methods for the Urmia Lake basin, Iran. Nat Hazards. 65(3):2105–2128.

Lee, A. H. L., Chen, W. C., and Chang, C. J. (2008). A fuzzy AHP and BSC approaches for evaluating performance of IT department in manufacturing industry in Taiwan. Expert Systems with Application. 34(1): 96 – 107.

Nwilo, P. C., Olayinka, D. N., and Adzandeh, E. A. (2012). Flood Modelling and Vulnerability Assessment of Settlements in the Adamawa State Floodplain using GIS and Cellular Framework Approach. Global Journal of Human Social Science. 12 (3): Version 1.0. 11-20.

Olayinka, D. N., Nwilo, C. P., Adzandeh, A. E. (2012). Predictive Modelling of Floods in Nigeria: Could They Have Been Prevented? Technical Proceedings for 47th Annual General Meeting (AGM) and conference of the Nigeria Institution of Surveyors on Surveying Disaster Management and Global Warming. 25-29th June, 2012 at Ilorin, Kware State, Nigeria.

Roy, D. C., & Blaschke, T. (2015). Spatial vulnerability assessment of floods in the coastal regions of Bangladesh. Geomatics, Natural Hazards and Risk, 6(1), 21-44. doi:10.1080/19475705.2013.816785

Saaty, T. L. (1980). The Analytical Hierarchy Process. McGraw Hill, New York.

UN-ISDR, (2009). Reducing Disaster Risks through Science: Issues and Actions. The Full Report of the

UN-International Strategy for Disaster Reduction (ISDR) Scientific and Technical Committee.

Wadsworth, G. (1999). Flood Damage Statistics. Public Works Department, Napa, CA.

White P., Pelling M., Sen K., Seddon D., Russell S., and Few R. (2005). Disaster risk reduction: a development concern. UK: DFID.

Intercontinental Geoinformation Days

igd.mersin.edu.tr

Locational analysis of infrastructural facilities in selected oil and non–oil producing areas of Akwa İbom State

Inyang Mbom. U*[1], Soneye A.S.O [1], Okolie C.J [2] Odunuga, S.S [1] Onyegbula, J.C [2] Akinnusi, S.A[2], Olanrewaju, H.O[2]

[1]*University of Lagos, Faculty of Social Sciences, Department of Geography, Lagos, Nigeria*
[2]*University of Lagos, Faculty of Engineering, Department of Surveying and Geoinformatics, Lagos, Nigeria*

Keywords
Coverage
Geospatial Analysis
Location-Allocation
Infrastructural Facilities
Optimal location zones

ABSTRACT

Location influences Infrastructural facilities' importance, efficiency, and performance. This study involves locational analysis of infrastructural facilities in twenty purposively selected oil and non-oil producing rural communities of Akwa-Ibom State. Coordinates of infrastructural facilities were acquired using a handheld Global Positioning System (GPS) device. Network analysis, infrastructure conformity assessment, and the minimize impedance analysis were carried out using ArcGIS. Results indicated that both oil and non-oil producing regions are within the service area of educational and water facilities, each having seven communities within the commercial infrastructure service area. Most oil-producing regions were within the service area of health facilities, while most non-oil producing areas were within the service area of small-scale industries. The infrastructure conformity assessment showed that 97% of infrastructures in the oil-producing regions were within the optimal location zones while 85% of infrastructure in non-oil producing areas were optimally located. Also, 21.3% and 17.6% of all infrastructures were closest to demand in the oil and non-oil producing regions, respectively. Ability to operationalize coverage issues and use location-allocation modeling optimally was demonstrated. The paper recommends enhanced infrastructure investment in areas outside infrastructure service areas and the use of location-allocation models in service provision to promote equity and spatial balance.

1. INTRODUCTION

In any nation, economic growth and development depends to a large extent on the adequate availability, spatial distribution/location of infrastructural facilities which provides the essential utilities and services necessary for a robust economy and improved standard of living (Udofia et al. 2013). The location of infrastructure has a lot to do with deciding to put an activity in one place rather than another, just to maximize value or to minimize expenses. However, by way of definition, location-allocation modelling is a simultaneous location of central facilities and the allocation of dispersed demand to them so as to optimize some objective function (Goodchild, 1984), where optimality is defined in terms of highest possible access within a given constraint (Kumar,2004).

The distribution and optimal location of Infratsructural facilities is the ease with which these facilities can be assessed and also shows effective planning of these facilities. It is envisaged that the sustainability of the environment and human life may not be successfully achieved until human settlement are economically, socially and environmentally vibrant through adequate provision and optimal location of infrastructures (Udofia et al. 2013).

In the light of Akwa Ibom State being the largest oil producing state in Nigeria and the continual receipt of far greater revenue from the federation accounts than any other states in the country. This study, therefore, integrates the location allocation modelling framework in analysing the existing infrastructures in the study area to ascertain its service area network, its conformity assessment to standard optimal location zones and the minimize impedance analyses of the infrastructures to various demands.

* **Corresponding Author**

*(mbomabasi@gmail.com) ORCID ID 0000-0002-4585-5745

Cite this study

Inyang M U, Soneye A S O, Okolie C J, Odunuga S S, Onyegbula J C, Akinnusi S A, Olanrewaju H O (2021). Locational Analysis of Infrastructural Facilities in Selected Oil and non-Oil Producing Areas of Akwa Ibom State, Nigeria. 3rd Intercontinental Geoinformation Days (IGD), 139-142, Mersin, Turkey

2. Method

The inventory of the identified socioeconomic infrastructures in the twenty communities of study was taken alongside their spatial location (x, y coordinates) with the help of a hand held GPS. Documented records of the existing infrastructures were collected from the Bureau of statistics of the Ministry of Economic Planning and Development, Akwa Ibom State.

2.1 Location allocation analysis

The network analyst toolset on the ArcMap software was used to perform the location allocation analysis. A three-step approach of service area network analysis, infrastructure conformity assessment (circular buffer analysis), and minimized impedance distance location/allocation technique (nearest facility to demand) were used for this analysis.

2.1.1 Service area network analysis

The service area network analysis was used to delineate service areas around each facility. It showed the demand points that fall within the areas serviced by each facility based on the standard distance of 1km for all water facilities as posited by UNICEF and WHO; 1.5km for all school facilities, commercial and small scale industry infrastructures (Menezes and Pizzalato.,2014 and Ayoade, 2014) and 1km for primary health centers and 3km for General/Cottage hospitals (Onokerhoraye, 1982)

2.1.2 Conformity assessment (Circular buffer analysis)

The circular buffer analysis was used to create buffers around each demand points based on a specified standard distance to show how the percentage of infrastructures that conform to the optimal zones. A buffer radius of 1km for all water facilities as posited by UNICEF and WHO,1.5km for all school facilities, commercial and small scale industry infrastructures (Menezes and Pizzalato.,2014; Ayoade, 2014), 1km for primary health centers and 3km for General/Cottage hospitals (Onokerhoraye, 1982) was created set around each of the demands. It showed the count or spatial distribution of the infrastructures that fell within or without the buffers. These buffers created are also considered as optimal zones for siting new infrastructures or reallocating the existing ones

2.1.3 Minimized impedance distance analysis (Nearest facility to demand)

The minimized impedance distance analysis was used to determine the closest infrastructures to each demand points based on a standard impedance distance cutoff of 1km for all water facilities as suggested by WHO and UNICEF (2014), 1.5km for all school facilities (Menezes and Pizzalato.,2014), 1k for primary health centers and 3km for General hospitals (Onokerhoraye, 1982). However, 1.5km was applied for rural markets, banks, and small-scale industries because it shows a regular accessibility distance as posited by Ayoade (2014). The minimize impedance problem technique, also known as the p-Median problem was applied in this study by using the existing infrastructures as candidates and the communities as demands. The aim of the model is to minimize the total distance travelled by residents from demands to access infrastructures.

3. Results

3.1 Education infrastructure

All communities in the oil and non-oil producing areas fall within 1.5km service areas of all educational infrastructures. In the oil-producing area, 100% of the infrastructures satisfied the infrastructure conformity assessment of being within 1.5km optimal location with 21% of it chosen by minimize impedance as closest to all the demand (communities) while in the non-oil producing area, 93% of the infrastructures satisfied the 1.5km optimal location conformity assessment with 25.9% of the facilities chosen as closest (below 1.5km) to eight demands exception of Ikot Essien and Odot 111 with distances of 2.72km and 1.59km respectively. The distances range of the closest facilities to demand is between 0.06km to 0.79km in the oil-producing area and 0.23km to 0.89km in the non-oil producing area, all below the ideal home school distance of 1.5km (Fig.1 and 2).

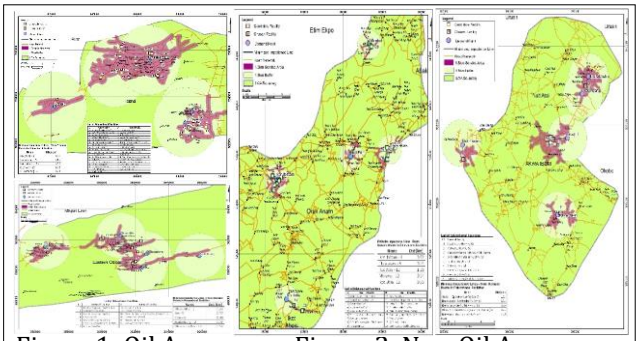

Figure 1: Oil Area Figure 2: Non-Oil Area

3.2 Health infrastructures

Only four communities comprising of Odot111, Okoro Nsit, Ikot Ibritam, and Ekparakwa out of ten in the non-oil-producing area are within 1km service areas of primary health centers with 60% of the existing health facilities satisfying the conformity assessment of being within 1km optimal location (Figure.3) and also chosen as the closest to three demands with primary health centers distances from demand above 1km being indicated for Ikot Adia 11.54km, Mbiakot 10.87km, Ikot Essien 6.68km, Ikot Akpabio 5.48km, Ikot Inyang 4.29km, Ikot Etim 4.85km and Odot 111 1.5km (Figure. 3). Conversely, the oil-producing area has nine (9) of it communities comprising of Mkpanak, Upenekang, Iwuoachang, Okoroutip, Iwuokpom, Okoroette, Iko, Okoromboho and Atabrikang within 1km service area of primary health center, exception of Elile and three communities comprising of Upenekang, Iwuoachang and Okoroette within 3km service areas of general/cottage

hospital with 83% of all the existing health infrastructural facilities satisfying both the 1km and 3km conformity assessment (optimal location) and 66.6% facilities closest to nine communities namely Mkpanak, Upenekang, Iwuoachang, Okoroutip, Iwuokpom, Okoroette, Iko, Okoromboho and Atabrikang with only Elile as an exception, having to access the existing general hospital with a distance of 3.12km above acceptable standard distance of 3km. (Figure 4).

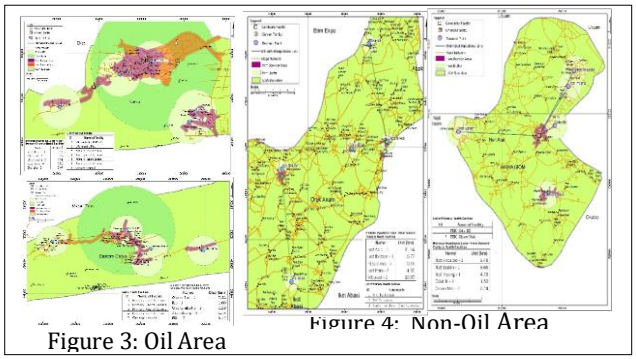

Figure 3: Oil Area

Figure 4: Non-Oil Area

3.3 Water Infrastructure

Both the oil and non-oil producing areas have all its communities within 1km service areas of all existing water infrastructures. Based on optimality of 1km walking distance to water facility, 97% of existing water facility in the oil-producing area satisfies the conformity assessment of being within 1km optimal location zones with 9.9% of it chosen as closest to all demands (communities) while the non-oil producing area has 77% infrastructure conformity assessment (optimality) with 11% of it chosen as closest to demand with distances all below 1km impedance cut-off. This makes the oil-producing area water infrastructure slightly optimally located than the non-oil area (Figure. 5 and 6).

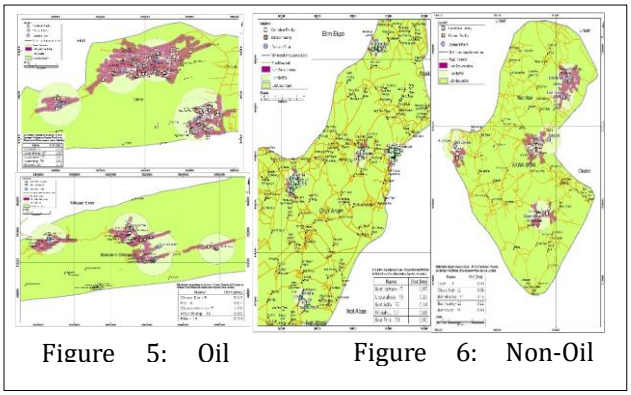

Figure 5: Oil

Figure 6: Non-Oil

3.4 Small Scale Industry Infrastructure

The oil-producing area has four of its communities namely Upenekang, Okoroette, Okoromboho and Iko within 1.5km service areas of small-scale industry infrastructures. All, the existing infrastructures satisfied the conformity assessment of being within 1.5km optimal location impedance cut-off and closest to four communities. The communities out of service area with distances to infrastructure above 1.5km are Iwuoachang 3.05km, Iwuokpom 3km, Mkpanak 2.61km, Okoroutip 6.19km, Elile 3.99km, and Atabrikang 3.82km. (Figure. 7). Conversely, the non-oil producing area has 8 out of 10 of its communities within 1.5km service area. They include Odot111, Ikot Essien, Okoro Nsit, Mbiakot, Ekparakwa, Ikot Ibritam, Ikot Etim and Ikot Adia. 95% of the infrastructures conform to 1.5km optimal location and 13% of it are closest to eight communities leaving out Ikot Akpabio and Ikot Inyang, with distances above 1.5km to the existing small-scale industry infrastructures (Figure. 8).

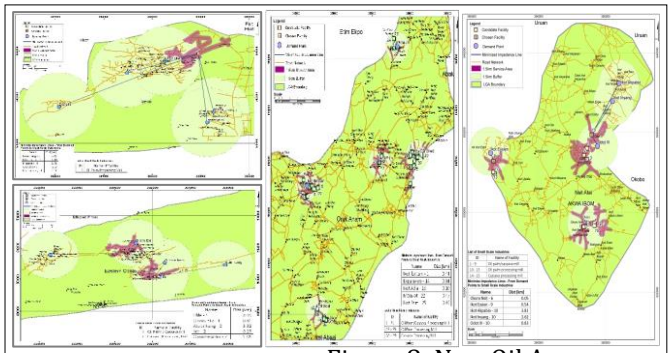

Figure 7: Oil Area

Figure 8: Non-Oil Area

3.5 Commercial infrastructure

Both the oil and non-oil producing areas have seven of its communities within 1.5km service area of existing commercial infrastructures. All the commercial infrastructures in the oil-producing area satisfies the conformity assessment of being within 1.5km optimal location zones and closest to seven demands (communities) namely Mkpanak, Upenekang, Iwuoachang, Iwuokpom, Okoroette, Okoromboho and Iko leaving out Elile, Atabrikang and Okoroutip with 4.73km, 3.90km and 3.92km distances to the infrastructures respectively which are above the standard 1.5km. Also, all infrastructures in the non-oil producing area satisfies the conformity assessment of being within the 1.5km optimal location zone and 77.8% of it were chosen as closest to seven demand (communities) including Ekparakwa, Ikot Ibritam, Mbiakot, Ikot Inyang, Ikot Akpabio, Ikot Essien and Odot111 with exception of Okoro Nsit, Ikot Adia and Ikot Etim which has 4.78km, 12.20km and 5.40km distances respectively above 1.5km (Figure. 9 and 10)

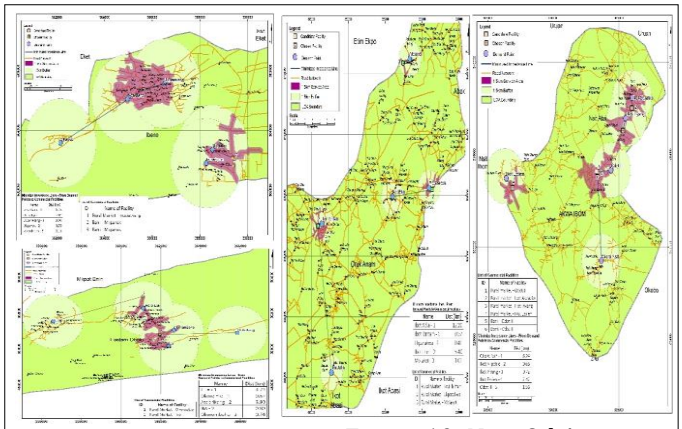

Figure 9: Oil Area

Figure 10: Non-Oil Area

4. Discussion

Provision and optimal location of infrastructural facilities is critical to national development especially when it is distributed in a way that equity and spatial balance are not compromised. Location allocation modelling provides the solution for spatial decision not only in finding the optimal locations for but also acts as tool to determine the coverage and solutions to distances between services and demand points. From the foregoing analysis, it is revealed that all communities in both areas of the study are within the education and water infrastructure service areas. Each of the oil and non-oil producing areas have seven communities within the service area of commercial infrastructure. Most of the communities in the oil-producing areas are within the service area of health infrastructure, while the non-oil producing areas have most of their communities within the service area of small-scale industry infrastructure. Aggregately, 97% of the existing infrastructures in the oil-producing areas are within the optimal location zones, while 85% of the infrastructure in non-oil producing areas is optimally located. Also, 21.3% and 17.6% of all infrastructures are chosen as the closest to demand in oil and non-oil producing areas, respectively.

Generally, although all communities in the oil and non-oil producing areas are within areas served by education and water infrastructures, the oil-producing areas have most of its communities served by health infrastructure. In contrast, the non-oil producing areas have most of its communities located within the small-scale industry infrastructure service area. According to the conformity to optimal location zones, the oil-producing areas are better conformed to an optimal location in the distribution of education, health, water, small-scale industry, and commercial infrastructure than the non-oil producing areas. However, though the percentage of the infrastructures closest to demand in both areas of the study is significantly small, the oil-producing areas have more demands being closed to education and health infrastructure, while the small-scale infrastructure is closest to more demands in the non-oil producing areas. Both areas of the study have an equal number of demands closest to water and commercial infrastructures.

5. Conclusion

It is a recommended practice in facility planning to regularly examine the existing infrastructure pattern and compare it to an optimal pattern. This will allow for a more efficient infrastructure location that could eliminate compromise in spatial balance. Applying the minimized distance option of the location-allocation model framework in this study generated the nearest facility to demand. It is assumed that users will always visit the nearest facility.

This study demonstrates the possibility of operationalizing the many problems of service delivery in development planning. The research findings imply that the continuous reliance on traditional paradigms by decision-makers for service location planning makes it impossible to effectively and accurately assess the degree to which service delivery patterns are consistent with stated goals. In this regard, decision-makers and planners have the opportunity to explore alternative location plans and evaluate their compatibility and consistency with pre-determined goals. These can prove invaluable in redefining the problem, generates new location options, and eventually decide on the best and acceptable plan to use'

References

Ayoade, M. A. (2014). Spatial accessibility to public maternal health care facilities in Ibadan, Nigeria. *The International Journal of Social Sciences*, *26*(1), 13 -28.

Goodchild, M. F. (1984). A location-allocation model for retail site selection. *Journal of Retailing*, *60* (1), 84 - 100.

Kumar, N. (2004). Changing geographical access to and locational efficiency of health services in two Indian districts between 1981 to 1996. *Social Science and Medicine*.*58* (10), 2045 – 2067.

Menezes, R. C., and Pizzalato, N. D. (2014). Locating public schools in fast expanding areas: Application of the capacitated p-Median and maximal coverage location models. *Pesquisa Operational*, *34*(2), 301-317.

Udofia, E. P., Atser, J., and Ikurekong, E. E. A. (2013). Linear discriminate analysis of multiple groups in rural settlement of Akwa Ibom State, Nigeria. *Journal of Rural Development, 32*(2), 121-138.

WHO and UNICEF. (2004*). Meeting the MDG drinking water and sanitation target: A mid- term assessment of progress*. Geneva, Switzerland.

Intercontinental Geoinformation Days

igd.mersin.edu.tr

Comparative analysis of forest change by type of natural park using CLEAR CUTS method

Eun Ha Park [1], Ji Young Kim [2], Jin Won Kim [2], Byeong-Hyeok Yu *[3]

[1]*National Institute of Ecology, Seocheon, Korea*
[2]*Korea National Park Research Institute, Korea National Park Service, Wonju, Korea*
[3]*Social Value & Innovation Office, Korea National Park Service, Wonju, Korea*

Keywords
Remote Sensing
NDVI
Protected Area
Buffer Zone
Zoning District

ABSTRACT

A natural park is a system in which protected areas are designated and managed for the conservation and sustainable use of natural ecosystems. In Korea, the management provisions for natural parks are equally applied to all four types (national parks, provincial parks, county parks, and geoparks), but the actual management is not applied equally, as the management authority differs depending on the type. Therefore, this study confirmed the effect of natural park types on forest changes in Korea by observing clear-cut land using satellite images and comparing it according to the type of natural park. The analysis showed that the proportion of severely damaged grade 3 clear-cut land was higher in provincial parks than in national parks. And marginal deforestation areas, which could not be seen inside the national park boundary, were found inside the provincial park boundary. To minimize forest changes in natural parks in the future, additional research is needed to derive the minimum buffer zone needed to perform its original function to supplement the provincial park management system and prevent the determination of development-friendly use districts.

1. Introduction

A natural park is a system in which protected areas are designated and managed for the conservation and sustainable use of natural ecosystems. Even after designation, protected areas are threatened by various influences (Cho & Lee 2010). Therefore, to properly conserve a protected area, it is necessary to manage it effectively after designation.

Protected areas of natural parks in Korea are managed by researching natural resources, establishing park plans, determining use districts, and designating prohibited acts for each use district. This applies equally to all four types of natural parks (national parks, provincial parks, county parks, and geoparks), but the management authority differs depending on the type of park. National parks are designated and managed by the central government, while provincial parks are designated and managed by local governments. Considering that forests often span multiple administrative districts, provincial parks that require consultation among various management entities have limitations in systematic management compared to national parks.

Therefore, this study confirmed the effect of natural park type on forest changes by observing clear-cut land using satellite images and comparing it according to the type of natural park.

2. Method

2.1. Site status

To compare forest changes according to the type of natural park, national and provincial parks with approximately the same distance from the city and city size were selected as target sites. In consideration of the size of the city, the analysis was conducted for a total of four natural parks, two each in metropolitan areas and non-metropolitan areas (Table 1).

* **Corresponding Author**

(paoseeh@gmail.com) ORCID ID 0000-0002-7797-0449
(kjy2050@knps.or.kr) ORCID ID 0000-0001-7460-6353
(whales9208@knps.or.kr) ORCID ID 0000-0002-9329-9608
*(bhyu@knps.or.kr) ORCID ID 0000-0001-5396-7969

Cite this study

Park E H, Kim J Y, Kim J W & Yu B-H (2021). Comparative analysis of forest change by type of natural park using CLEAR CUTS method. 3rd Intercontinental Geoinformation Days (IGD), 143-145, Mersin, Turkey

Table 1. Site status

	Site	Area (km²)
Metropolitan area	Bukhansan National Park	76.922
	Namhansanseong Provincial Park	36.400
Non-metropolitan area	Gyeryongsan National Park	65.335
	Daedunsan County Park	62.640

2.2. Clear-cuts

The clear-cuts detection method (Ose et al. 2016) was used to identify forest changes, and the details of the data used for the analysis are as follows.

Table 2. Data acquisition

Sort	Site	Data Acquisition
Metropolitan area	Bukhansan National Park, Namhansanseong Provincial Park	Landsat 8 (2014/5/30, 2018/5/9), Sub-divided Land Cover Map (2014)
Non-metropolitan area	Gyeryongsan National Park, Daedunsan Provincial Park	Landsat 8 (2015/5/26, 2018/5/21), Sub-divided Land Cover Map(2015)

Changes in the Normalized Difference Vegetation Index (NDVI) for each site five years after the production of the land cover map by the Ministry of Environment were examined, and the grade of clear-cut land was calculated based on the forest area classified at the time of the production of the land cover map (Table 3). For the satellite images used in the NDVI calculation, images with few clouds (<5%) were selected to minimize the analysis error. And among the clear-cut land classified into 3 grades, the objects presumed to be a cloud were manually deleted. To examine changes in the surrounding area outside the boundary of the protected area, the status of the occurrence of clear-cut land in the buffer section, which was 5 km from the boundary, was also analyzed.

Table 3. Grades of clear-cut land (Ose et al. 2016)

Grade	Description
0	Absence of clear-cuts
1	Clear-cuts with a low confidence degree
2	Clear-cuts with a medium confidence degree
3	Clear-cuts with a high confidence degree

3. Results

3.1. Comparison of the ratio of clear-cut land area

The ratio of clear-cut land area to total forest area did not show a significant difference according to the type of natural park (Table 4). Similar results were obtained inside and outside the boundaries of natural parks, and the difference according to the size of the city was not large.

However, within the boundary of natural parks, the ratio of grade 3 clear-cut land to the total area of clear-cut land was larger in provincial parks than in national parks (Table 5). The maximum value of grade 3 clear-cut land was also determined to be larger in provincial parks than in national parks both inside and outside the boundaries. This means that more heavily damaged clear-cut areas are appearing in provincial parks than in national parks and larger clear-cut areas are occurring in provincial parks.

Table 4. The ratio of the total area of clear-cut land to the total forest area (%)

	Sort	Grade of clear-cut land	Inside the boundary	Outside the boundary
Metro	Bukhansan	No clear-cuts	98.36	91.27
		Clear-cuts(1+2+3)	1.64	8.73
		Clear-cuts(3)	0.05	1.52
	Namhansanseong	No clear-cuts	97.46	93.39
		Clear-cuts(1+2+3)	2.54	6.61
		Clear-cuts(3)	0.44	2.62
Non-metro	Gyeryongsan	No clear-cuts	98.47	94.71
		Clear-cuts(1+2+3)	1.53	5.29
		Clear-cuts(3)	0.07	1.88
	Daedunsan	No clear-cuts	97.85	95.79
		Clear-cuts(1+2+3)	2.15	4.21
		Clear-cuts(3)	0.73	1.54

Table 5. Area ratio and maximum values of grade 3 clear-cut land compared to total clear-cut land

	Sort	Inside the boundary		Outside the boundary	
		Area ratio (%)	Maximum values (㎡)	Area ratio (%)	Maximum values (㎡)
Metro	Bukhansan	3.16	11,700	17.46	118,805
	Namhansanseong	17.32	42,458	39.58	1,161,163
Non-metro	Gyeryongsan	4.31	9,002	35.49	148,519
	Daedunsan	33.83	83,720	36.65	227,759

3.2. Clear-cut land type comparison

In the case of the clear-cut land type, there was a difference according to the type of natural park inside the boundary, whereas a difference according to the size of the city was found in the area around the boundary.

Within the boundary, various types of clear-cut land were analyzed for each target site in the use districts except for the park nature conservation district. In the case of Bukhansan National Park, changes in the area around temples and cultural heritage excavations were analyzed as grade 3 cleared areas, and changes around some highland bedrock areas were analyzed as grades 1 and 2 cleared areas. Gyeryongsan National Park showed changes in the area in which a landslide occurred in 2018 and around residential areas located in the Park Village District and Park Natural Environment District. In Namhansanseong Provincial Park, cleared land due to military facilities and deforested areas in the periphery was found, and in Daedunsan Provincial Park,

deforested areas in the periphery and bare areas around roads were analyzed.

In the case of natural parks located in metropolitan areas, development areas such as apartment complexes, artificial grasslands around roads, and deforested areas in the periphery were analyzed as grade 3 clearing areas. In the vicinity of natural parks located in non-metropolitan areas, a number of deforested areas in the periphery were analyzed. In addition, artificial grasslands and fields with arable land were designated as grade 3 cleared areas.

It was also observed that grade 3 clearing land appeared immediately outside of and adjacent to the boundary. In particular, in the case of a national park, even though there was a forest area that was connected without a break to the inside of the national park, it was not included in the boundary, so the open land where development such as apartment complexes was made was observed.

4. Discussion

Through analyzing the status of cleared land, it was found that the proportion of heavily damaged cleared land was higher in provincial parks than in national parks. In addition, it was determined that deforestation in the periphery, which was nonexistent inside national park boundaries, took up relatively large areas inside provincial park boundaries.

National parks and provincial parks are designated and managed under the same system, but their management bodies are different. Nevertheless, differences in forest change show the limitations of management systems in which the management entity is not unified.

In addition, it is judged that the fact that the park natural environment district does not function as a buffer zone among the use districts of natural parks also has an impact. Awareness of the conservation of provincial parks is relatively low compared to national parks, so a more development-friendly use district is inevitably determined.

5. Conclusion

Through the analysis of the status of cleared land, it was confirmed that the forest changes were different depending on the type of natural park. To minimize changes in forests in natural parks, it is necessary to supplement the management system so that provincial parks can be managed similarly to national parks. In addition, it is necessary to develop a plan to secure sufficient buffer zones when setting the boundaries of protected areas and determining the use districts.

To this end, it is necessary to identify landscape species and the minimum survival area for them to be maintained (Alexandre et al. 2010). And additionally, to derive the minimum buffer area that can perform its original function is needed. It is expected that the forest changes derived from this study can be superimposed for use in improving the boundaries of natural parks and use districts.

Acknowledgement

This research was supported by the Park Lab 2021 Research Program through the Korea National Park Service.

References

Alexandre B D, Crouzeilles R, & Grelle C E (2010). How can we estimate buffer zones of protected areas? A proposal using biological data. Natureza & Conservacao, 08, 165–170. https://doi.org/10.1016/j.sbspro.2016.05.227.

Cho Y H & Lee Y K (2010). A study on surveying and improving management of protected areas in Korea. Journal of Korean Institute of Landscape Architecture, 38(1) 64–73.

Ose K, Corpetti T & Demagistri L (2016). Multispectral satellite image processing. Optical Remote Sensing of Land Surface: Techniques and Methods, 57–124. https://doi.org/10.1016/B978-1-78548-102-4.50002-8

Intercontinental Geoinformation Days

igd.mersin.edu.tr

Shallow-water bathymetry using Landsat 8 imagery – example of Ibafon and Badagry Creeks, Lagos Nigeria

Chukwuma Okolie, Emmanuel Ayodele Oluwatobi Raji, Waliyah Adedokun, Olagoke Daramola, Samuel Akinnusi, Hamed Olanrewaju

University of Lagos, Faculty of Engineering, Department of Surveying and Geoinformatics, Lagos, Nigeria

Keywords
Remote sensing
Landsat 8
Stumpf's model
Shallow water bathymetry
Lagos

ABSTRACT

There is high demand for the seabed topography of water bodies. The shallow nature of some waterbodies makes it difficult to deploy the conventional bathymetry method, that is the use of echo-sounders on a vessel. Under these conditions, remote sensing methods thrive with significant advantages in terms of costs, coverage area and delivery time. In this study, Stumpf's algorithm was applied on Landsat imagery to derive bathymetric data in parts of Ibafon Creek and Badagry Creek in Lagos, Nigeria. In the findings, the depths were generally shallow with depth range between 0.7 m and 13.3 m and an average depth of 4.84 m. In several instances, the remote sensing method of bathymetry can serve as an alternative to the conventional methods in shallow waters, and can as well be used as a reconnaissance tool to obtain change in depth over several epochs.

1. Introduction

The majority of methods for estimating bathymetry are based on the concept of using time to infer distance (Dierssen et al., 2011). The fundamental physical principle underlying the retrieval of bathymetric information from optical remote sensing images is that when light passes through water it becomes attenuated by interaction with the water column (Raj et al., 2013). Deep areas appear dark on the image since the water absorbs much of the reflected light. Shallow areas appear lighter on the image since less light reflected from the seabed is absorbed in the passage through the water column. For survey of bathymetry at synoptic scale, the remote sensing method may be a viable alternative to the conventional bathymetric mapping using echo sounders.

Several techniques for estimating bathymetry from satellite imagery have been developed and applied at numerous sites in different parts of the world. This is evident in the high yearly turnover of scientific articles on satellite derived bathymetry (SDB) published in journals and conference proceedings. Despite this increased global awareness, there has been a very slow uptake of SDB by hydrographic researchers, professionals and agencies in Africa. The present study demonstrates the potential of SDB for estimating the bathymetry of shallow water bodies in Lagos, Nigeria.

Satellite derived bathymetric information, if well-utilized can support safety of navigation by providing up-to-date grids of the shallow water zone. This is paramount in areas with outdated charts in Nigeria. In addition to the bathymetric information, it can aid the identification of obstacles, which are hazardous to safe navigation. Therefore, this study applies the Stumpf's bathymetric algorithm to derive bathymetry in parts of Ibafon and Badagry Creeks of Lagos State Nigeria, and compares the depth values with the data obtained from the conventional means using an echo sounder.

Stumpf et al. (2003) model is robust and works well over variable bottom types. It also accounts for water turbidity. The algorithm requires only two tunable parameters which could be computed using the linear regression method between the ratio result and ground truth (Alsubaie, 2012).

$$Z = m_1 \frac{\ln(nR_w(\lambda_i))}{\ln(nR_w(\lambda_j))} - m_0 \qquad (1)$$

Where m_1 is a tunable constant to scale the ratio to depth, n is a fixed constant for all areas to assume that the algorithm is positive, and m_0 is the offset for a depth of 0m where (Z = 0). R_w is the reflectance of water, and $\lambda_{i,j}$ are two different bands.

* **Corresponding Author**

*(rajitobi27@gmail.com) ORCID ID 0000-0002-0812-4273

Cite this study

Okolie C.J, Ayodele E, Raji O, Adedokun W, Daramola O, Akinnusi S & Olanrewaju H (2021). Shallow-water bathymetry using Landsat 8 Imageries – Example of Ibafon Creek. 3rd Intercontinental Geoinformation Days (IGD), 146-148, Mersin, Turkey

This study aims to assess the overall adequacy of Landsat 8 satellite data for the derivation of shallow water bathymetry cost and timely benefits.

2. Methods

2.1. Study area

Ibafon creek is an inlet into the Badagry creek and opens into the Atlantic Ocean. It covers a length of 5.45 km from Ibafon to the Festac Lagoon and is bounded between 6°26'57.82" N and 3°19'01.31" E, and 6°26'57.82" N and 3°19'01.31" E. It also extends centrally towards Amuwo-Odofin and Okota. Badagry Creek is a creek that flows from Benin Republic into Commodore Channel in Lagos. These creeks can be described as very turbid; this is partly due to the human activities near the coastal area. The turbid nature of these water bodies presents a significant case study for investigation.

2.2. Datasets

The satellite image used is Landsat 8 imagery, which was downloaded from the United States Geological Survey (USGS) website. The in-situ bathymetry data used was collected from the Department of Surveying and Geoinformatics University of Lagos, Nigeria. The summary of the datasets collected are shown in Table 1.

Table 1. The summary of the datasets used

Data	Publisher/Source	Year	No. of Points
Bathymetric data	Field data acquired by the Department of Surveying and Geoinformatics.	2020	698
Landsat 8 Imagery	US Geological Survey (USGS)	2020	

2.3. Image processing

The downloaded Landsat 8 imagery was processed to generate the satellite-based bathymetry using ArcGIS software tools. The key processes carried out which were used to generate the bathymetry include: (i) water-land separation using threshold value (ii) spatial filtering (iii) generation of bathymetric raster using Stumpf's model. Further analyses were done to assess the relationship between the satellite-derived bathymetric values and field bathymetric values using statistical tools in Microsoft Excel software.

2.3.1. Land/water separation

The water body was separated from the land areas on the raster data using the threshold value of the point of transition between the water and land area. Profile graph and Pixel inspector tools in the ArcMap toolbox were used to determine the threshold value to separate the waterbody from the land areas.

2.3.2. Spatial filtering

A low-pass filter was used to enhance the imagery. Before performing spatial filtering, the float tool was used to convert the value of each pixel of the raster derived from the water-land separation into a floating-point representation. This was necessary to improve the precision of the pixel values.

2.3.3. Derivation of bathymetry

The final step to determine the satellite-based bathymetry involves the application of Stumpf's model. This model compares the bathymetry algorithm values and the in-situ bathymetric depth values to build a regression model to generate the satellite-derived bathymetric raster. Consequently, it is necessary to determine the bathymetry algorithm (bathyalg) model, which is the coefficient of m_1 in Stumpf's model. The bathyalg is the ratio of the filtered blue band (band 2) and green band (band 3). The sample in-situ depth points were plotted on ArcMap and the layer was used to extract bathyalg values for the same sample points with the "Extract Value to Point" tool in Arc Toolbox. The resulting attribute table was exported in txt format for further analysis on Microsoft Excel.

Equation 2 can be likened to a straight-line equation of $y = mx + c$. Hence, a regression-line graph of the bathymetric algorithm versus the true depth is plotted. The equation was inputted in the Raster Calculator tool on ArcMap to calculate the satellite-derived bathymetry.

$$Z = m_1(\text{Bathymetry algorithm}) - m_0 \dots\dots (2)$$

2.4. Quantitative analysis

A depth difference maps (ΔDepth) was calculated by subtracting the in-situ depth values from the imagery-derived depth values. This was also done to show the agreement of the SDB depth with the echo sounding data. The calculation was done in Microsoft Excel and exported with their respective coordinates into ArcGIS for plotting.

3. Results

Table 2 presents the summary statistics of the datasets, which showed consistent higher values in the field data than in the imagery-derived values. On the other hand, Figures 1 and 2 present the bathymetric charts from the two datasets and the difference in depths respectively. Further discussion of the results is presented in Section 4.

Table 2. Summary statistics of the depth comparison

	Landsat depth (m)	Echo sounding depth (m)	Difference (m)
Min	0.68	0.89	0.21
Max	9.84	12.16	2.32
Range	9.16	11.27	2.11
Mean	5.68	5.78	0.10
SD	2.51	2.97	0.46
Variance	6.28	8.82	2.54
SE	0.46		

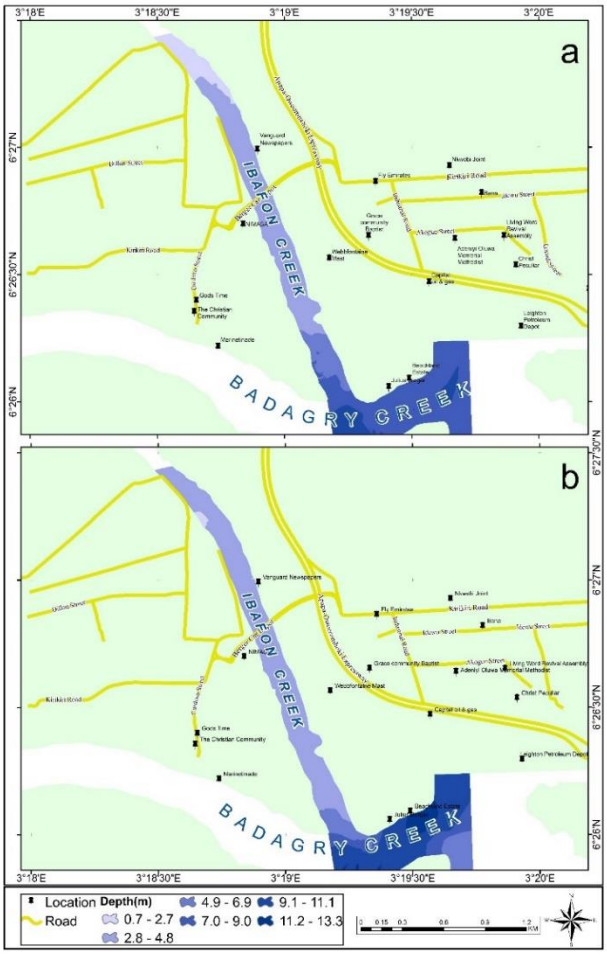

Figure 1. Bathymetric charts produced from (a) Landsat imagery (b) Echo sounding

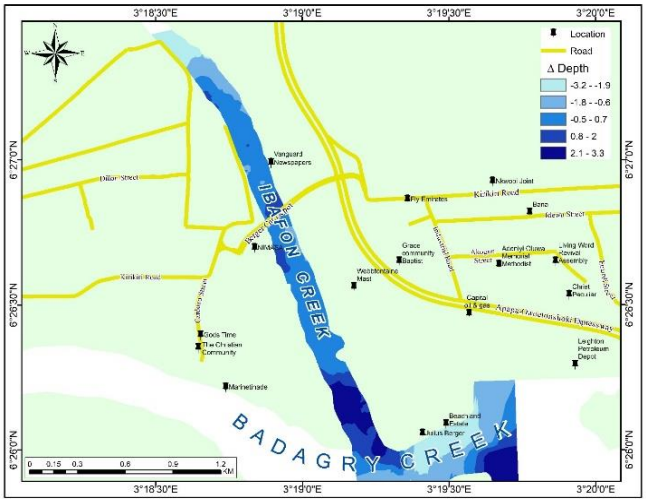

Figure 2. Map showing changes in depth

4. Discussion

The depths are generally shallow with depth range between 0.7 m and 13.3 m and an average depth of 4.84 m. Badagry Creek is the deepest part of the study area. Generally, the depth in Ibafon Creek is fairly uniform with most of the depth values between 2.7 m and 4.5 m compared to the Badagry Creek. In Figure 1b, the bathymetry of the narrow strip of the study area appears to be uniform. In Figure 2, the changes in depth ranged from -3.2m to 3.3m. The Landsat depths were very close to the in-situ depths along the narrow strip in Ibafon Creek. This confirms the claims that SDB is a promising technology for shallow water bodies.

5. Conclusion

This study has examined the application of satellite derived bathymetry (SDB) in a shallow water environment consisting of two creeks in Lagos Nigeria to understand applicability based on Stumpf model. The study found that the technology performed favorably well when compared with the echo-sounding approach. Accordingly, it can be deduced that the technology can be used to monitor beach erosion, sea level rise and general changes in coastline features. A set of time series maps can be generated to this effect. The data can also help scientists to study the habitats of bottom-dwelling aquatic organisms. Maps of coral habitats can also be generated to assist on conservation and monitoring. In a future study, the method of linear regression with statistical tests such as the coefficient of determination (R^2) will be used for validating the imagery-derived bathymetry. Also, a more detailed analysis on the correlation between the Landsat bathymetry and the echo-sounding data will be presented. Exploring the potential of this technology under a fit-for-purpose concept is a welcome idea.

Acknowledgements

The authors wish to acknowledge the Department of Surveying and Geoinformatics, University of Lagos and the USGS for providing them with echo sounding data and satellite images respectively. Special thanks to Abeeb Jimoh for his assistance in the acquisition of echo sounding data.

References

Alsubaie, N.M. (2012). The Potential of Using Worldview-2 Imagery for Shallow Water Depth Mapping. MSc Thesis. UCGE Reports Number 20368.

Dierssen, H.M., and Randolph, K. (2011). Encyclopedia of Sustainability Science and Technology (Springer).

Raj, A., and Sabu, P. (2013). Shallow water bathymetry using log-linear inversion technique: a case study at Vizhinjam. International Journal of Innovative Research in Science, Engineering and Technology. Proceedings of International Conference on Energy and Environment-2013 (ICEE 2013).

Stumpf, R.P., Holderied, K., and Sinclair, M. (2003). Determination of water depth with high-resolution satellite imagery over variable bottom types. Limnology and Oceanography, 48, 547-556.

Intercontinental Geoinformation Days

http://igd.mersin.edu.tr/2020/

Vegetation mapping from vegetation indices using a uav-based sensor

Emmanuel Ayodele[1], Chukwuma Okolie[1], Imole Okediji*[1], Olagoke Daramola[1], Kayode Omolaye[2]

[1]*University of Lagos, Faculty of Engineering, Department of Surveying and Geoinformatics, Lagos, Nigeria*
[2]*Geospatial Research Limited, Lagos State, Nigeria*

Keywords
Remote sensing
Unmanned Aerial Vehicle
Modified Green Red
Vegetation Index
Excessive Green Index
Red Green Blue
Vegetation Index

ABSTRACT

The current advances in technology in many fields have revolutionized conventional agricultural practices. However, the use of remotely sensed data for agricultural purposes has not been fully explored in Nigeria. This study explores this limitation to understand performance and usability. In this work, remotely sensed information in the form of UAV images were used to assess crop greenness and vegetation cover. A maize farmland of 6 hectares was captured in Ogun State using a DJI phantom 4 UAV (which operates in true colour, RGB);The 165 images acquired were mosaicked using Agisoft Metashape software. Vegetation cover and greenness were assessed through various RGB-based vegetation indices and the conclusion was that Red Green Blue Vegetation index (RGBVI) produced the best results in depicting both vegetation cover and greenness. Excessive Green Index (ExG) and Modified Green Red Vegetation Index (MGRVI) produced above-average results but were not as informative as RGBVI. From the maps of each vegetation index, information about crop greenness and vegetation cover was adequately derived. This study showed the adequacy of UAV-based sensors for vegetation mapping and is recommended.

1. Introduction

The use of Remote Sensing (RS) in the field of agriculture has been increasing in recent times. Typically, RS records the surface reflectance in the visible or near-infrared parts of the electromagnetic spectrum (Yao et al., 2011). Applying this to vegetation leads to extraction of various information ranging from greenness and external properties to the internal structure of plants. Reflectance of vegetation cover changes with biological aspects and the vegetation structure. Water content, age, stress, cover geometry, row spacing and orientation and leaf distribution in the cover alter vegetation reflectance (Bannari et al., 1995). Furthermore, reflectance is influenced by atmospheric composition, soil properties, soil brightness, and colour as well as solar illumination geometry and viewing conditions.

Vegetation indices (VIs) are developed to evaluate vegetation using spectral measurements in relation to agronomic parameters like biomass or PH (Bannari et al., 1995). They are commonly used for extracting information from RS data (Jackson and Huete, 1991). Numerous vegetation indices exist in Visible, Near Infrared and Shortwave Infrared spectral regions.

Research from the past 5 years has shown a move into the use of RGB-based vegetation indices rather than Multispectral indices. This is because RGB sensors are more affordable than Multispectral sensors (Neupane and Baysal-Gurel. 2021). This means using RGB-based indices is cheaper and more cost effective than using multispectral or hyperspectral indices. Although the near infra-red (NIR) and other multispectral bands give a better insight into biomass estimation, plant health information derivation, and other vegetation properties, RGB-based indices have also proven to be quite effective in the estimation of vegetation properties.

In this work, a maize farmland in Atan, Otta, Ogun State, Nigeria with an area of 6 hectares was captured using a DJI Phantom 4 unmanned aerial vehicle (UAV). The surface reflectance property of the crop was useful in the calculation of vegetation indices. The steps

*Corresponding Author
*(light99857@gmail.com) ORCID ID 0000-0001-6781-2669

Cite this study
Ayodele E, Okolie C, Okediji I, Daramola O & Omolaye K (2021). Vegetation Mapping from Vegetation Indices using a UAV-based sensor. 3rd Intercontinental Geoinformation Days (IGD), 149-152, Mersin, Turkey

followed by which vegetation maps were eventually formed are given in the sub-sections below. Specifically, the focus of this work was mapping vegetation cover and greenness of the maize farmland. This is yet another example of how Remote Sensing can be applied in Agriculture for effective output and increased crop yield.

2. Methods

This section describes the instrumentation, image acquisition and image processing. The UAV employed for image capture was a DJI Phantom 4 which was manufactured in 2018. The camera attached to its payload has a resolution of 20MP, flight time is approximately 30 minutes, and it has 2 obstacle avoidance sensors with vision sensors as well. Usually, the steps involved in UAV image capture can be broadly grouped into four (4) parts: mission, flight planning, the flight, and image processing. A mission can be defined as a process that consists of one or more flights within the mission area. The number of flights per mission is estimated by the software and depends on the size of the mission area. Flight planning is done in the field according to the aerial imaging technology employed.

2.1. Image acquisition

On the 15th of November, 2020, the mission was carried out at around 1pmto capture the greenness of the vegetation in Atan Farmland, with a total size of 6 hectares. The DJI Phantom 4 UAV was flown over the farmland at an altitude of 50m with 75% front and side overlap. A total of 165 images were captured, and Ground Sampling Distance (GSD) was derived to be 1.5cm/px. The UAV compass and Inertia Measurement Unit (IMU) was calibrated before deployment to keep the UAV straight and level in the air. The software employed was Drone Deploy and all necessary settings were performed. The images were captured with 4 flight lines as pre-planned. The single flight lasted about 14 minutes and all captured images were saved on the memory card of the UAV.

2.2. Image processing

After the acquisition of the images, Agisoft Metashape was used to create an orthomosaic from the set of overlapping images with the corresponding referencing information. This involved image corrections and mosaicking. To create orthomosaic, the images had to be aligned; first, by matching points between overlapping images, estimating camera position for each photo and building sparse point cloud model and mesh. The orthomosaic was stored in TIFF format and then exported into ArcGIS 10.4.1 for further processing.

After exporting the orthomosaic to ArcGIS, layers were created and vegetation indices applied. The three vegetation indices made use of were Red Green Blue Vegetation Index (RGBVI), Modified Green Red Vegetation Index (MGRVI) and Excessive Green Vegetation Index (ExG). Each one was applied with the aid of the Raster calculator in the Spatial Analyst toolbox. These three indices were used based on their reliability shown in the existing literature. These three indices effectively highlight vegetation and soil (Ashapure et al., 2019). Also, they have the potential for the study of agricultural production and for predicting crop biomass, and are good for observing mature canopy (Bendig et al., 2015).

2.3. Quantitative analysis

After applying the vegetation indices, the fishnet tool was used to do a point spread over the images, and the txt file was exported into Microsoft Excel. Statistical analysis was carried out and correlation coefficient table was derived.

3. Results

Figure 1 presents the orthomosaic of the study area. There is an inter-mingling of sparsely vegetated areas and averagely vegetated areas for the maize crop.

Figure 1. Orthomosaic of the study area

Summarily, the RGB orthomosaic gives a rough estimation of the extent of canopy cover, and helps to differentiate between sparse and dense vegetation. It also aids the identification and differentiation of various surface elements such as soil, water body, buildings, and vegetation.

The MGRVI map (Figure 2) ranges from -1 to 1. Densely vegetated areas were in the positive range of 0.51 to 1, sparsely vegetated areas fell in the range of 0.01 to 0.5, while the soil and bare grounds were in the negative range of -0.51 to 0.RGBVI (Figure 3) also ranges from -1 to 1, while ExG ranges from -1 to 2 as observed in Figure 4. A distinctive property of the indices was vegetation classification according to their respective ranges.

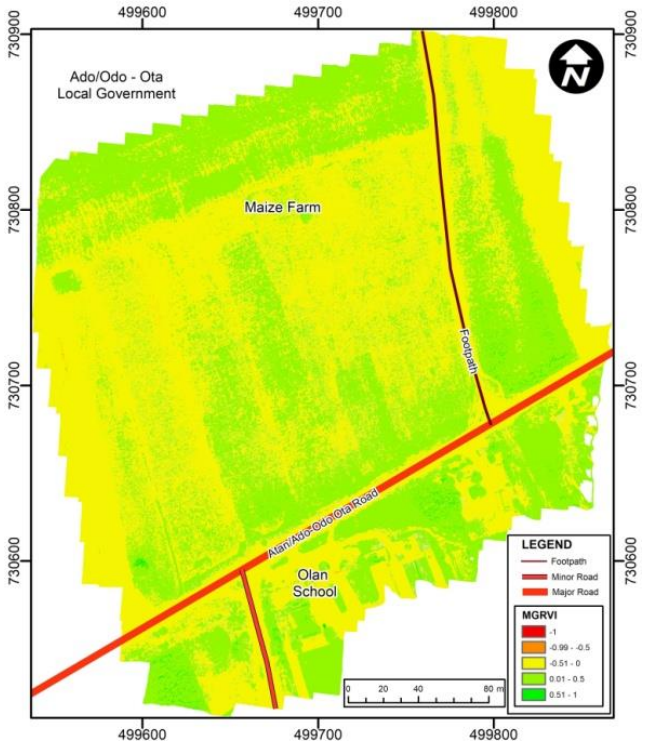

Figure 2. MGRVI map of the maize farmland

Figure 3. RGBVI map of the maize farmland

4. Discussion

From each map, the extent of vegetation cover and greenness was portrayed. However, the best approximation out of the vegetation index maps is the RGBVI map; it does not over or under-estimate the extent of vegetation cover, and the areas with sparse and dense vegetation are better delineated. This is in tandem with what has been recorded in literature and the RGBVI map can be relied upon by both farmers and mapping professionals as well. Also, there is a high correlation between the three indices but between RGBVI and ExG, the correlation is highest (0.97).

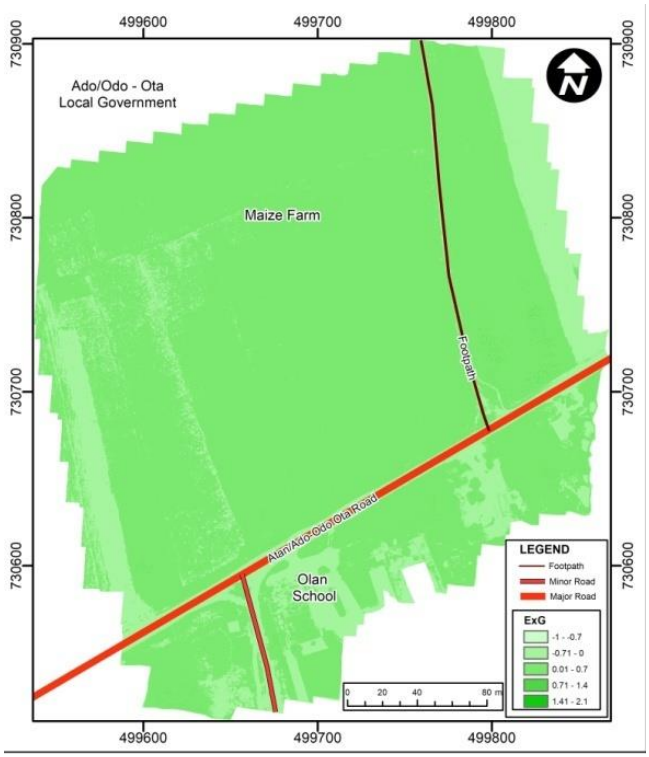

Figure 4. ExG map of the maize farmland

Table 1 shows the coefficients of correlation between the indices, which potrayed a strong positive correlation between all indices.

Table 1. Correlation coefficient of vegetation indices

	MGRVI	RGBVI	ExG
MGRVI	1		
RGBVI	0.705	1	
ExG	0.828	0.974	1

5. Conclusion

This study has examined the use of Unmanned Aerial Vehicle (UAV) sensor for vegetation mapping using vegetation indices. It can be concluded that RGB-based vegetation indices have the potential for estimating vegetation cover and greenness in a farmland. The use of RGB-based indices presents a cost-effective method for crop mapping. Accordingly, the outcome of this study justifies the need for further work and any future investments to improve agricultural production.

Acknowledgements

We appreciate the contributions of Olumide Awe, Shittu Ibrahim, Andy Egogo-Stanley, Hamed Olanrewaju and Samuel Akinnusi towards the success of this research.

References

Ashapure A, Jung J, Chang A, Oh S, Maeda M & Landivar J (2019). A Comparative Study of RGB and Multispectral Sensor-Based Cotton Canopy Cover Modelling Using Multi-Temporal UAS Data.

Bannari A, Morin D, Bonn F &Huete AR (1995).A review of vegetation indices. Remote Sensing Reviews, vol. 13, no. 1-2, pp. 95-120, 1995.

Bendig J, Yu K, Aasen H, Bolten A, Bennertz S, Broscheit J & Bareth G (2015). Combining UAV-based plant height from crop surface models, visible, and near infrared vegetation indices for biomass monitoring in barley. International Journal of Applied Earth Observation and Geoinformation 39, pp. 79–87

Jackson R D (1982) Canopy temperature and crop water stress. In Advances in Irrigation; Hillel, D., Ed.; Academic Press: New York, NY, USA, 1982; Volume 1, pp. 43–80

Jackson R D &Huete A R (1991). Interpreting Vegetation Indices. Preventive Veterinary Medicine, 11, 185-200. http://dx.doi.org/10.1016/S0167-5877(05)80004-2

Neupane K &Baysal-Gurel F (2021), Automatic Identification and Monitoring of Plant Diseases Using Unmanned Aerial Vehicles: A Review. RemoteSens. 2021, 13,3841.

Mutanga O & Skidmore A K (2004). Narrow band vegetation indices overcome the saturation problem in biomass estimation. International journal of remote sensing, vol. 25, no. 19, pp 3999-4014, 2004.

Hunt Jr E R, Doraiswamy P C, McMurtrey J E, Daughtry C S T, Perry E M & Akhmedov B (2013). A visible band index for remote sensing leaf chlorophyll content at the canopy scale. International journal of applied earth observation and Geoinformation, vol. 21, pp. 103-112.

Intercontinental Geoinformation Days

igd.mersin.edu.tr

Evaluation of Landsat and MODIS imagery fusion for high-resolution evapotranspiration mapping over large agricultural area

Ayoub Moradi

Tehran, Iran

Keywords
Evapotranspiration
Landsat
Modis
İmage fusion

ABSTRACT

Regarding to severe droughts and increasing shortages in water resources, in particular in the Middle East, evapotranspiration estimation is essential for irrigation management in agricultural lands. Evapotranspiration mapping is currently possible in a suitable spatial resolution from Landsat imagery; however, these data do not allow to obtain an optimal temporal resolution, required in agriculture management. In other hand, Modis imagery provide a dense temporal resolution, with however a deficiency in spatial resolution. In this study, we evaluated the fusion of 16-dayily Landsat and daily Modis imageries in order to obtain a sufficient spatio-temporal resolution for evapotranspiration mapping required in water management over agricultural areas. The image fusion is applied on the six-month Landsat and Modis images over large sugarcane farms in south-western Iran. The Spatial and Temporal Adaptive Reflectance Fusion Model (STARFM) are applied on the images. The evapotranspiration estimations are based on two algorithms: SEBAL and METRIC. The point extracted results are highly consistent with the evapotranspiration product from Modis in terms of temporal resolution. As well as, the Kappa index indicates on an acceptable accuracy in spatial resolution of estimations. Due to the smoothness of the region, no significant differences between SEBAL and METRIC estimations are resulted.

1. Introduction

Since the last half-century, remote sensing facilities have provided effective capabilities in evapotranspiration estimation and mapping over agricultural areas. The evapotranspiration estimations is required irrigation management particularly during the crop growing season. Different methods are developed to estimate reference and actual evapotranspiration, which are demonstrated in several research and applications.

Evapotranspiration is a principal contribution of energy and water balances. It is one of the most complex components of hydrological balance.

Field measuring of evapotranspiration is costly and time consuming., and thus, limited to local scales. However, satellite data has made possible estimating evapotranspiration in large-scale fields without requiring the calculation of complex hydrologic processes.

Although high temporal resolution instruments, such as Moderate Resolution Imaging Spectroradiometer (MODIS) and the Advanced Very High-Resolution Radiometer (AVHRR) sensors, provide temporally dense data, the coarse spatial resolution of these sensors make them inefficient to quantify evapotranspiration of vegetation covers at fine scales.

Over the past two decades, the most well-known algorithms that have been considered in this regard are Surface Energy Equilibrium Algorithms (SEBAL) and Mapping Evapotranspiration at high Resolution with Internalized Calibration (METRIC). These models are based on energy balance and spatial distribution of energy.

* **Corresponding Author**

*(ayoubmoradi@gmail.com) ORCID ID 0000 – 0001 – 6336 – 8847

Cite this study

Moradi A (2021). Evaluation of Landsat and MODIS imagery fusion for high-resolution evapotranspiration mapping over large agricultural area. 3rd Intercontinental Geoinformation Days (IGD), 153-155, Mersin, Turkey

2. Material

2.1. Study area

Iran, is a predominantly warm and dry country, where about 93 percent of renewable water is consumed by agricultural activities. This issue eventually led to the severe loss of underground water in most of plains in country, particularly in the south. Sugarcane farms in Khuzestan province (Figure 1) include large areas locateing around rivers of 'previously' large discharges. In the result of severe decrease in rivers discharges in recent years, irrigation of sugarcane farms become more and more challengus.

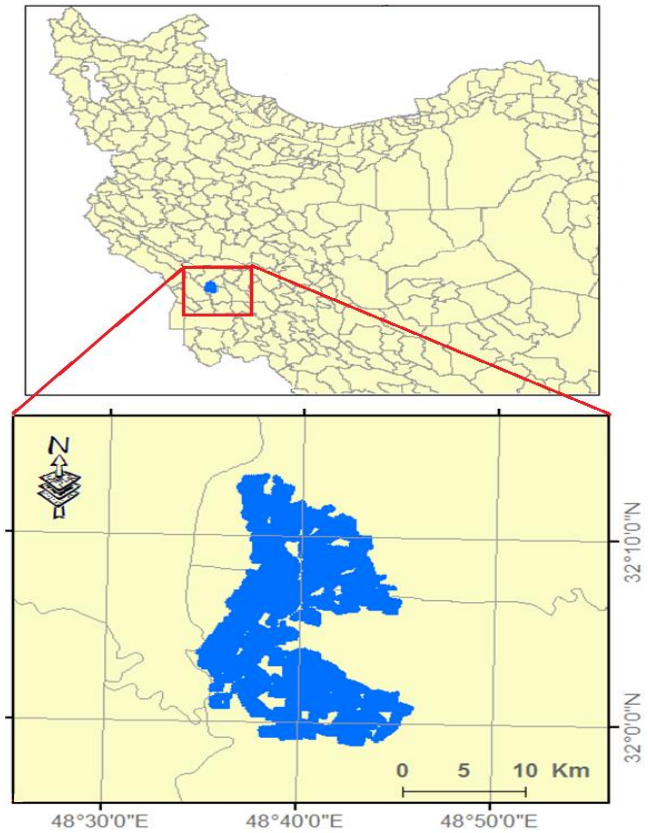

Figure 1. The study area

2.2. Data

The reflectance and thermal bands of MODIS/Terra at 500 meters resolution are obtained from lpdaac (USGS).

11 Landsat-8 images, dated from the late 2019 to the middle of 2020, are obtained from Alaska Satellite Facility (ASF) data center. A set of postprocessing are applied to mask cloud, cloud shadow, snow and outliers. Beside the imagery, subsidiary dare needed to calculate evapotranspiration include: digital elevation model and land cover map.

The MODIS/Terra Net Evapotranspiration 8-Day L4 Global 500 m SIN Grid (Mod16A2 v006), which is the global evapotranspiration product from Modis, is used as an evaluation source. The MOD16A2 Version 6 Evapotranspiration product include 8-day composites, at 500-meter resolution. This data is based on the Penman-Monteith method. The inputs include vegetation property dynamics, albedo, and land cover derived from Modis bands, along with daily meteorological reanalysis data.

3. Method

Two kinds of processing applied on the data: 1) time series of synthesis images are generated from the specified Modis and Landsat images; then, 2) evapotranspiration are estimated for the three set of images.

3.1. Image fusion

In this study we employed the Spatial and Temporal Adaptive Reflectance Fusion Model (STARFM) to fuse two image series ordered based on time intervals. This methos functions based on Euclidean distance of spectral and temporal similarities between the reference and target pixel.

After proposing in 2006 by Gao et al., the STARFM algorithm is latterly developed and optimized by researchers; The STAARCH (The Spatial Temporal Adaptive Algorithm for mapping Reflectance Change) algorithm, for example, is also based on the STARFM algorithm. STARFM generates synthetic Landsat-like images from a spatially weighted difference of one reference Landsat- MODIS pair, and one (or more) MODIS scene(s) to be downscaled. The outliers are minimized using a moving averaged window.

3.2. Evapotranspiration estimation

The three main components for calculating evapotranspiration include: 1- soil heat flux, 2 - tangible heat flux, and, 3 - net radiation reached to the surface. Estimating the three components, the latent heat flux is obtained. The latent heat is amount of energy that is spent in evapotranspiration. Therefore, evapotranspiration is the equivalent height of water associated to the latent heat.

By subtracting the tangible and soil heat flux from net radiation flux, the latent heat, and thus, actual evapotranspiration is estimated for each pixel of the image at the instant of the satellite passage. Hourly evapotranspiration values are converted to daily evapotranspiration by considering the average daily net radiation.

METRIC differs with SEBAL method in employing reference in-situ measurements. In METRIC algorithm based on the area to be studied at least one high quality climatological station is required to calculate the reference ET. Climatological data for the exact time of satellite image acquisitions are obtained from the Ahwaz synaptic station, locating at 40 km distant form the study area.

4. Results

The main characteristics of the estimated evapotranspiration from synthetic images include: 1- For the corresponding pixels, the amplitudes stand between the values of Landsat and Modis images, with an approximated distance of 60% and 40% relative to Modis and Landsat respectively. 2- The best results belong to

the inner areas of large parcels, far from the margins. A median filter would improve the accuracy of synthetic derived maps. And, 3- Generally, the similarity of estimations is higher in the areas of higher evapotranspiration than area of small evapotranspiration.

Generated evapotranspiration maps for three dates (12 January 2020; 29 January 2020 and 3 March 2020) are shown in Fig.1. Accordingly, the RMS between the synthetic derived estimations, and, both Landsat derived evapotranspirations and Modis evapotranspirations product (Mod16) are shown in Table 1. The RMSs with Mod16 are considerably lower than those with Landsat. It should be referred to the time smoothing of Mod16; which are composites over 8 days. Difference of results from SEBAL and METRIC algorithms are estimated between 4 and 6.2 percent. The small difference is because the area is flat, and is thus expected to be homogenous in terms of land surface temperatures. For the same reason the METRIC calculations are based on only one climatologic station.

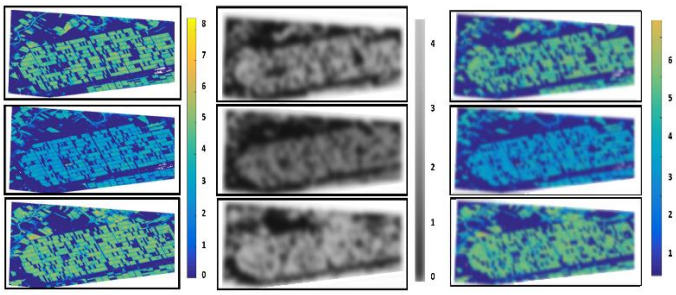

Figure 2. Estimated evapotranspiration from Landsat 8 (right column), from Modis (middle column), and from synthetic blended imaged (left column).

Table 1. The RMS between estimation from synthetic and Landsat images

Date	RMS (with Landsat)	RMS (with Mod16)	Difference % (Seb. & Met.)
Jan. 12	2.2	1.8	4
Jan. 29	2.7	2.2	6.2
Mar. 3	1.7	0.8	4.4

5. Conclusion

Fusion of high spatial resolution images such as Landsat with temporally dense images (as Modis) would allow to combine their strengths, and resolve their shortcomings. In the contest of increasing requirement to frequently and precisely estimating of evapotranspiration in arid and semiarid countries, such studies may play a vital role in water and agriculture managements in the national levels. Furthermore, the results are promising in order to assists developing precision agriculture. Evapotranspiration derived from blended images tend to be smoother than actual estimations; This should be due to averaging over large areas. Nevertheless, in vast homogenous vegetation cover such as large farms of single crops (e.g., sugarcane farms studied in the present study), the fusion method performs well enough. This method would also be effective in areas of frequent cloudy sky.

Acknowledgement

The author would like to acknowledge the Modis bands and Modis Evaporation product provided from LP-DAAC NASA.As well as, data obtained from the Landsat-8 image courtesy of the U.S. Geological Survey are acknowledged.

References

Niu, Zheng (2012). Use of MODIS and Landsat time series data to generate high-resolution temporal synthetic Landsat data using a spatial and temporal reflectance fusion model. Journal of Applied Remote Sensing, 6(1), 063507. doi:10.1117/1.JRS.6.063507.

Allen, R.G., Tasumi, M., Morse, A., Trezza, R., Wright, J.L., Bastiaanssen, W. (2007). Satellite-based Energy Balance for Mapping Evapotranspiration with Internalized Calibration (METRIC) Applications. Journal of Irrigation and Drainage Engineering, 133, 395-406.

Allen, R. G., M. Tasumi, R. Trezza, C. W. Robison, M. Garcia, D. Toll, K. Arsenault, J.M.H. Hendrickx, J. Kjaersgaard (2008); Comparison of Evapotranspiration Images Derived from MODIS and Landsat along the Middle Rio Grande. American Geophysical Union, Fall Meeting 2008, abstract id. H43G-1094.

Bashir, M., Hata, T., Abdelhadi, A., Tanakamaru, H., and Tada, A. (2006); Satellite-Based Evapotranspiration and Crop Coefficient for Irrigated Sorghum in the Gezira Scheme, Sudan. Hydrology and Earth System Sciences Discussions, 793-817.

Bastiaanssen, W.G.M., Menenti, M., Feddes, R.A. and Holtslag, A.A.M.A (1998); Remote Sensing Surface Energy Balance Algorithm for Land (SEBAL): 1. Formulation. Journal of Hydrology, 212-213, 198-212.

Bastiaanssen, W.G.M. (2000); SEBAL-based Sensible and Latent Heat Fluxes in the Irrigated Gediz Basin, Turkey. Journal of Hydrology, 229, 87-100.

F. Gao et al., (2018); On the blending of the Landsat and MODIS surface reflectance: predicting daily Landsat surface reflectance, IEEE Trans. Geosci. Remote Sens. 44(8), 2207, doi.org/10.1109/TGRS.2006.872081.

Ruhoff, A. L., Paz, A. R., Collischonn, W., Aragao, L. E., Rocha, H. R., and Malhi, Y. S. A (2012); MODIS-Based Energy Balance to Estimate Evapotranspiration for Clear-Sky Days in Brazilian Tropical Savannas. Remote Sensing, 4: 703-25.

Santos, C., Lorite, I.J., Allen, R.G., and Tasumi, M. (2012); Aerodynamic Parameterization of the Satellite-Based Energy Balance (METRIC) Model for ET Estimation in Rain fed Olive Orchards of Andalusia, Spain. Water Resources Management, 26, 3267-3283.

Tasumi, M., Trezza, R. and Allen, R.G (2006). METRIC Manual for MODIS Processing Version 1.0. University of Idaho R&E Center, Kimberly, Idaho. 67 p.

Walker J. J. et al. (2012), "Evaluation of Landsat and MODIS data fusion products for analysis ofdryland forest phenology," Rem. Sens. Environ. 117, 381–393, http://dx.doi.org/10.1016/j.rse.2011.10.014.

Intercontinental Geoinformation Days

igd.mersin.edu.tr

Accuracy assessment and conflation of DEMs over Kaduna State, Nigeria

Bawa Swafiyudeen*[1], Mefe Moses[1], Ebenezer Ayobami Akomolafe[1], Monye Joseph Chukwuweta[1], Lukman Abdulmumin[1], Abubakar Adamu Musa[1]

[1]*Ahmadu Bello University, Department of Geomatics Faculty, of Environmental Design, Nigeria*

Keywords
AW3D
ASTER
SRTM
GCP
DEMs
ALOS-PALSAR

ABSTRACT

Digital Elevation Models (DEMs) are a type of raster data layer in which each cell has a value corresponding to its elevation (z-values at regularly spaced intervals). This study assess the vertical accuracy of four freely available DEMs (AW3D, ASTER SRTM and ALOS-PALSAR) over two test sites (hilly and plain) with reference to ground controls available on the test sites. However, to obtain a much higher resolution DEMs, these DEMs were fussed using Multiple Linear Regression Model and the performance of the fused DEM was tested over the hilly and plain terrain. At the plain terrain, ASTER DEM is closer to those of the GCPs (ground survey) than those of the ALOS PALSAR, AW3D and SRTM. At the hilly terrain, AW3D is closer to those of the GCPs (ground survey) than those of the ALOS PALSAR, ASTER and SRTM. After conflation, the conflated DEM performed better than the whole DEMs put together in the hilly and plain terrain.

1. Introduction

Digital elevation models (DEMs) are evenly spaced grids which thus contain the elevations of a point on the earth surface corresponding with the position of the grid cell(Fuss, 2013). They are also known as DTMs (digital terrain models) or DSMs (digital surface models) (digital surface model)(Fuss, 2013; Poon, Fraser, Chunsun, Li, & Gruen, 2005). Traditional techniques such as ground-based surveying was used to acquire elevation data sets. Thanks to the advancements in remote sensing technology, elevation data for hard-to-reach survey locations are now available (d'Ozouville et al., 2008; Fuss, 2013; Gao, 2007).

Due to the growth and improvement of technology, there have recently been multiple creations of various types of DEMs that are extensively utilized across the world. Amongst these uses to mention a few are; terrain correction (Hirt et al., 2019), errioin risk assessment (Nitheshnirmal, Thilagaraj, Rahaman, & Jegankumar, 2019), flood susceptibility mapping (Ibrahim et al., 2021), geomorphology (Szypuła, 2017) etcetera. Among these DEMs are the Advanced Land Observing Satellite-Phased Array-Type L-Band Synthetic Aperture Radar (ALOS-PALSAR) Radiometrically Terrain Corrected (RTC) DEM, (SRTM) Shutter Radar Topographical Mapper and Advanced Space borne Thermal Emission and Reflection Radiometer (ASTER-GDEM) models, ALOS World 3D (AW3D) to name a few. These DEMs are notable for their good horizontal resolution and nearly worldwide coverage.

Studies such as (Elkhrachy, 2018; Forkuor & Maathuis, 2012; Suwandana, Kawamura, Sakuno, Kustiyanto, & Raharjo, 2012) have demonstrated that the accuracy of DEMs varies from region to region. The very recent release of these DEMs, particularly AW3D30 and SRTM-30, calls for opportunities to conduct localized assessments of the DEM's quality and accuracy to verify their suitability and improve on these DEMs using a fusion technique for a wide range of applications in hydrology, geomorphology, archaeology, and many others.

The process of integrating information from multiple data sources into a single one, thereby resolving differences is called conflation (Samsonov, 2020). It solves misalignment issues of DEMs by adjusting the spatial relationship or transferring attributes between them. Conflation can equally mean Fusion.

For example, there is currently no freely accessible topographic map that can easily offer topographic information for different scientific purposes in Kaduna State, and it is well-known that terrestrial collecting of

* **Corresponding Author**

*(bswafiyudeen@gmail.com) ORCID ID 0000-0002-2384-9432
(mefemoses@gmail.com) ORCID ID 0000-0003-4029-3736
(goldera2787@gmail.com) ORCID ID 0000-0001-6797-0114
(bawaswafiyudeen@gmail.com) ORCID ID 0000-0001-6797-0114
(labdulmumin54@gmail.com) ORCID ID 0000-0003-0750-3914
(abusumayya2018@gmail.com) ORCID ID 0000-0001-6797-0114

Cite this study

Bawa S., Moses, M., Akomolafe E. A., Chukwuweta, M. J., Abdulmumin L., & Abubakar A. M. (2021). Accuracy Assessment and Conflation of DEMs over Kaduna State, Nigeria. 3rd Intercontinental Geoinformation Days (IGD), 156-159, Mersin, Turkey

geospatial data is more tedious, time-consuming, and expensive than doing it remotely. Although several studies have been carried out on the accuracy assessment and conflation of DEMs in different parts of the world, yet there is no comprehensive study on the vertical accuracy and conflation of these freely available DEMs over Kaduna State. This Study hence addresses this problem.

2. Study area

The state of Kaduna, illustrated in Fig. 1, is located between Latitudes 9° 10'N and 11° 40'N and Longitudes 6° 02'E and 8° 50'E and spans an area of 44,408.3 square kilometers. The state is bordered to the south-west by Abuja – the Federal Capital Territory and Niger State, to the north-west by Katsina and Zamfara states, to the north-east by Kano and Bauchi states, as well as to the south-east by Plateau and Nasarawa states.

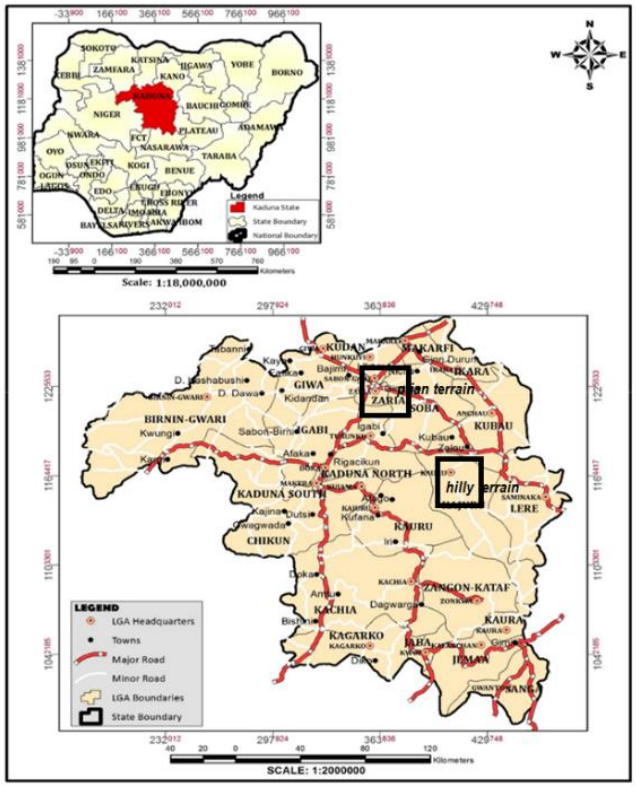

Figure 1. Inset map of the Study area.

3. METHOD

3.1. Datasets and source

Table 1 presents the data set and their sources adopted for the study. Ground control point height for two different terrain which is the plain terrain at Ahmadu Bello university campus, Zaria and hilly terrain at Kajuru local government all located at Kaduna state. 15 ground control points were established for plain terrain and 12 Ground control points were established for the hilly terrain. The corresponding ground control points (GCP) at the plain and hilly terrain were used for assessment.

Table 1. Dataset and source adopted for the study

S/N	Data	Resolution	Sources
1	SRTM	30m	*
2	ALOS PALSAR	12.5 m	**
3	AW3D	30m	*
4	ASTER	30m	*

* http://eaerthexplorer.usgs.gov/
**http://asf.alaska.edu.com

3.2. Data manipulation

Downloaded DEMs were mosaicked and clipped. Unlike the ALOS PALSAR 12.5m DEM having its projected coordinate system already in WGS 1984 ZONE 32N. The other DEMs like ASTER, SRTM and AW3D projection system were the GCS (Geographic Coordinate System) 1984. So, in other to avoid errors due to the varying projection systems, all the DEMs were re-projected to WGS 1984 zone 32N. Thereafter, corresponding spot height were extracted using the fish netting tool in ArcGIS 10.6.

3.3. Conflation of DEMs using multiple linear regression (MLR)

When it comes to merging different variables, regression analysis is crucial. By combining DEMs from many sources, the purpose of employing multiple regression models in elevation models is to achieve a reduced height error probability and improved dependability. The MLR model, as represented in Equation 1, is used.

$$Y=Ax1+Bx2+Cx3+Dx3+k \quad (1)$$

Where a, b, c, d are the respective coefficient and k is the constant and Y is the fussed DEM.

4. Results and discussions

4.1. Overall spot heights estimation performance

Corresponding heights for 15 points for plain terrain and 12 points for hilly terrain were obtained from the different DEMs spatial data generated from (SRTM 30, ALOS PALSAR, ASTER and AW3D.) and were compared with GCPs. Table 2 depicts the descriptive statistics for spot heights for plain terrain from which it is obvious that the calculated standard error, standard deviation and sample variance from the ASTER DEM is closer to those of the GCPs (ground survey) than those of the ALOS PALSAR, AW3D and SRTM. The descriptive statistics for the spot heights as presented in Table 2 clearly show the poor relationship of the ALOS PALSAR, AW3D and SRTM DEM data source when compared to the GCPs (ground survey) sources under investigation.

Fig. 2 presents the variations of spot height for plain terrain from the various sources of DEMs and it is clear that the ASTER and AW3D DEM tends to be closer to the reference source more than any other.

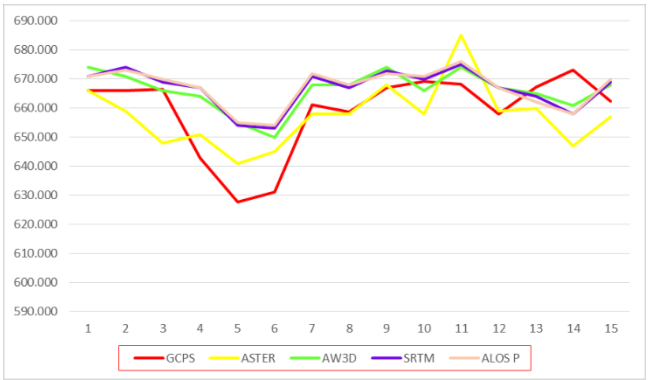

Figure 2. Scattered plot for spot height of the various DEMs for plain terrain

Table 3 depicts the descriptive statistics for spot heights for hilly terrain from which it is obvious that the calculated standard error, standard deviation and sample variance from the AW3D is closer to those of the GCPs (ground survey) than those of the ALOS PALSAR, ASTER and SRTM. This clearly shows the poor relationship of ALOS-PALSAR, ASTER and SRTM DEM data sources when compared to other data sources under investigation.

Table 2. Descriptive statistics of the various spot height for plain areas

S/N	Statistics	GCPS	ALOS-PALSAR	ASTER	AW3D	SRTM
1	M	659.07	667.09	657.33	666.07	666.80
2	SE	3.60	1.74	2.78	1.74	1.76
3	MD	666.15	670.02	658.00	667.00	669.00
4	SD	13.93	6.75	10.76	6.75	6.83
5	SV	194.11	45.58	115.81	45.50	46.60
6	KU	1.25	-0.20	2.13	1.27	0.21
7	SK	-1.52	-0.95	0.97	-1.07	-1.05
8	R	45.45	22.03	44.00	24.00	22.00
9	MI	627.68	653.99	641.00	650.00	653.00
10	MA	673.13	676.03	685.00	674.00	675.00
11	S	9886.06	10006.29	9860.00	9991.00	10002.00
12	C	15.00	15.00	15.00	15.00	15.00
13	CL	7.72	3.74	5.96	3.74	3.78

**Mean (M), Standard Error (SE), Median(MD), Standard Deviation (SD), Sample Variance (SV), Kurtosis (KU), Skewness (SK), Range (R) Minimum(MI), Maximum(MA), Sum(S), Count(C), Confidence Level(CL)((95.0%)

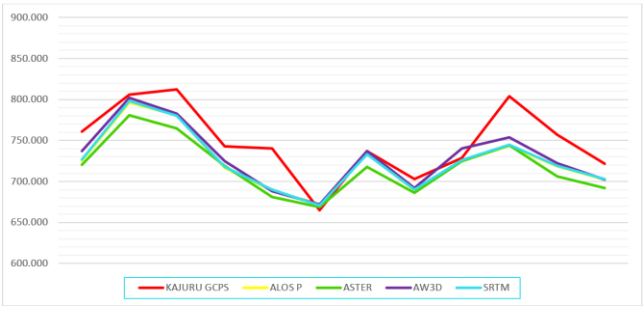

Figure 3. Scattered plot for spot heights for hilly terrain of the various

Table 3. Descriptive statistics of the various spot height for hilly areas

S/No	Statistics	GCPS	ALOS-PALSAR	ASTER	AW3D	SRTM
1	M	748.10	724.32	717.17	729.50	725.00
2	SE	12.64	10.56	9.74	11.08	10.57
3	MD	741.42	721.48	718.50	731.00	722.50
4	SD	43.78	36.59	33.73	38.39	36.63
5	SV	1917.12	1338.80	1137.61	1473.55	1341.64
6	KU	-0.15	0.25	-0.28	-0.21	0.30
7	SK	-0.09	0.69	0.52	0.42	0.69
8	R	147.30	125.97	112.00	130.00	127.00
9	MI	664.81	670.51	669.00	672.00	671.00
10	MA	812.11	796.48	781.00	802.00	798.00
11	S	8977.23	8691.89	8606.00	8754.00	8700.00
12	C	12.00	12.00	12.00	12.00	12.00
13	CL	27.82	23.25	21.43	24.39	23.27

**Mean (M), Standard Error (SE), Median(MD), Standard Deviation (SD), Sample Variance (SV), Kurtosis (KU), Skewness (SK), Range (R) Minimum(MI), Maximum(MA), Sum(S), Count(C), Confidence Level(CL)((95.0%)

Fig. 3 represents the variations of spot height for hilly terrain from the various sources of DEMs and it is clear that the AW3D and SRTM DEM tends to be closer to the reference source more than any other.

4.2. Overall spot heights estimation performance of the fussed DEM

The DEM for the study area were fussed and subsequently tested for the hilly and plain test sites, while considering ALOS-PALSAR as the reference DEM. To test the accuracy of the fused DEM, corresponding spot heights for the 15 points for plain terrain and 12 points for hilly terrain were extracted respectively. Table 4 depicts the descriptive statistics for spot heights for the fussed plain terrain from which it is obvious that the calculated standard error, standard deviation and sample variance from the FUSSED DEM is closer to those of the GCPs (ground survey) than those of the ALOS-PALSAR, ASTER, AW3D and SRTM.

Table 4. Descriptive statistics plain terrain

S/N	Statistics	ABU GCPS	ALOS-PALSAR	ASTER	AW3D	SRTM	FUSSED DEM
1	M	659.07	667.09	657.33	666.07	666.80	661.03
2	SE	3.60	1.74	2.78	1.74	1.76	2.75
3	SD	13.93	6.75	10.76	6.75	6.83	10.63
4	SV	194.11	45.58	115.81	45.50	46.60	113.04
5	MI	627.68	653.99	641.00	650.00	653.00	634.32
6	MA	673.13	676.03	685.00	674.00	675.00	675.04
7	CL	7.72	3.74	5.96	3.74	3.78	5.89

Table 5 depicts the descriptive statistics for spot heights for hilly terrain from which it is obvious that the calculated standard error, standard deviation and sample variance from the FUSSED DEM is closer to those of the GCPs (ground survey) than those of the ALOS PALSAR, ASTER, AW3D and SRTM.

Table 5. Descriptive statistics hilly terrain

S/No	Statistics	KAJURU GCPS	ALOS-PALSA	ASTER	AW3D	SRTM	FUSSED DEM
1	M	748.10	724.32	717.17	717.17	725.00	748.10
2	SE	12.64	10.56	9.74	9.74	10.57	11.36
3	SD	43.78	36.59	33.73	33.73	36.63	39.34
4	SV	1917.12	1338.80	1137.61	1137.61	1341.64	1547.87
5	MI	664.81	670.51	669.00	669.00	671.00	692.33
6	MA	812.11	796.48	781.00	781.00	798.00	832.56
7	CL	27.82	23.25	21.43	21.43	23.27	25.00

5. Conclusion

DEM are models used for the creation of relief maps, rendering of 3D visualizations, modelling of water flow for hydrology or mass movement, etcetera. In this study, we assessed the reliability and fusion of four freely available elevation data (ALOS-PALSAR, AW3D, ASTER AND SRTM) for public use. Using the multiple linear regression model technique, the four DEMs were fussed and tested over two different terrain (hilly and plain). The fussed DEM tend to have an improvement with respect to referenced GCP of the terrain. Finally, it is important to point out that accuracy of DEMs be properly understood before they are utilized in varying applications.

Acknowledgement

The authors thank USGS and JAXA for AW3D, ASTER SRTM and ALOS-PALSAR data.

References

d'Ozouville, N., Deffontaines, B., Benveniste, J., Wegmüller, U., Violette, S., & Marsily, G. (2008). *DEM generation using ASAR (ENVISAT) for addressing the lack of freshwater ecosystems management, Santa Cruz Island, Galapagos*. doi: 10.1016/J.RSE.2008.02.017

Elkhrachy, I. (2018). Vertical accuracy assessment for SRTM and ASTER Digital Elevation Models: A case study of Najran city, Saudi Arabia. *Ain Shams Engineering Journal*, *9*(4), 1807–1817. doi: 10.1016/j.asej.2017.01.007

Forkuor, G., & Maathuis, B. (2012). Comparison of SRTM and ASTER Derived Digital Elevation Models over Two Regions in Ghana—Implications for Hydrological and Environmental Modeling. In *Studies on Environmental and Applied Geomorphology* (pp. 219–240). Rijeka, Croatia. Retrieved from https://www.academia.edu/25703899/Comparison_of_SRTM_and_ASTER_Derived_Digital_Elevation_Models_over_Two_Regions_in_Ghana_-_Implications_for_Hydrological_and_Environment

Fuss, C. E. (2013). *Digital Elevation Model Generation and Fusion* (Masters Thesis). University of Guelph.

Gao, J. (2007). Towards accurate determination of surface height using modern geoinformatic methods: Possibilities and limitations. *Progress in Physical Geography: Earth and Environment*, *31*(6), 591–605. doi: 10.1177/0309133307087084

Hirt, C., Yang, M., Kuhn, M., Bucha, B., Kurzmann, A., & Pail, R. (2019). SRTM2gravity: An Ultrahigh Resolution Global Model of Gravimetric Terrain Corrections. *Geophysical Research Letters*, *46*(9), 4618–4627. doi: 10.1029/2019GL082521

Ibrahim, U. S., Youngu, T. T., Swafiyudeen, B., Abubakar, A. Z., Zainabu, A. K., Usman, I. A., … Abubakar, A. M. (2021). (13) (PDF) Flood Susceptibility Mapping of Makera District and Environs in Kaduna South Local Government Area of Kaduna State-Nigeria. *Nigerian Journal of Environmental Sciences and Technology, 5*(2). doi: 10.36263/nijest.2021.02.0287

Nitheshnirmal, S., Thilagaraj, P., Rahaman, S. A., & Jegankumar, R. (2019). Erosion risk assessment through morphometric indices for prioritisation of Arjuna watershed using ALOS-PALSAR DEM. *Modeling Earth Systems and Environment*, *5*(3), 907–924. doi: 10.1007/s40808-019-00578-y

Poon, J., Fraser, C. S., Chunsun, Z., Li, Z., & Gruen, A. (2005). Quality Assessment Of Digital Surface Models Generated From IKONOS Imagery. *The Photogrammetric Record*, *20*(110), 162–171. doi: 10.1111/j.1477-9730.2005.00312.x

Samsonov, T. E. (2020). Automated Conflation of Digital Elevation Model with Reference Hydrographic Lines. *ISPRS International Journal of Geo-Information*, *9*(5), 334. doi: 10.3390/ijgi9050334

Suwandana, E., Kawamura, K., Sakuno, Y., Kustiyanto, E., & Raharjo, B. (2012). Evaluation of ASTER GDEM2 in Comparison with GDEM1, SRTM DEM and Topographic-Map-Derived DEM Using Inundation Area Analysis and RTK-dGPS Data. *Remote Sensing*, *4*(8), 2419–2431. doi: 10.3390/rs4082419

Szypuła, B. (2017). Digital Elevation Models in Geomorphology. In *Hydro-Geomorphology—Models and Trends*. IntechOpen. doi: 10.5772/intechopen.68447

Intercontinental Geoinformation Days

igd.mersin.edu.tr

Applications of Remote Sensing in Solving Myriads of Geological Problems: A Review

Ogbonna Okpuru Aguta*[1], Maruf Orewole Oladotun [1], Sunday Olotu Jephthah [1]

[1]*National Centre for Technology Management (NACETEM), Obafemi Awolowo University, Ile-Ife, Nigeria*

Keywords
Remote sensing
Geological terrains
Electromagnetic spectrum
Geological mapping
Ground-truthing

ABSTRACT

Numerous geological problems can be conveniently solved through the application of remote sensing techniques. This work seeks to review the available literature on remote sensing utilization in geological and geotechnical sciences. It however observed that remote sensing makes possible the collection of data from dangerous or inaccessible geological terrains and is applicable in geological mapping, landform studies/characterization, mineral/rock identification, soil properties (such as soil texture, moisture content of the soil, soil organic carbon, and soil salinity), geodetic survey, geomorphological studies, and detection of geologic hazards. Other uses of remote sensing include oil spill detection and monitoring and by integrating with Geographical Information System (GIS), it is a perfect match for hydrological studies, landslide, and urban planning. Though remote sensing in geology has limitations such as limited capabilities, data volume for transmission and inconsistency in data acquisition and interpretation, ground-truthing surveys and repeated reconnaissance remain the irreplaceable solutions to these limitations.

1. Introduction

Remote sensing is used in the geological sciences as a data acquisition method complementary to field observation because it allows the mapping of geological terrains without physical contact with the areas being explored (Rees, 2013). About one-fourth of the earth's total surface area is exposed land where information can be extracted through observation of the earth via remote sensing (Kuehn et al., 2000).

Remote sensing is made possible by the detection of electromagnetic radiation by sensors. The radiation can be naturally sourced as applicable to passive remote sensing or produced by machines as applicable to active remote sensing and reflected off the earth's surface (Rees, 2013). The information carrier being electromagnetic radiation has two main variables: intensities of reflectance and travel-time of radiation.

The detection of intensities of reflectance at different wavelengths is plotted on a spectral reflectance curve. This spectral characteristic is aided by the physio-chemical properties of the surface of the target object and therefore are very vital in mineral identification and geological mapping, for example, hyper-spectral imaging (Rees, 2013). Additionally, the two-way travel time of radiation from and back to the sensor can be used to calculate the distance in active remote sensing systems, for example, interferometric synthetic-aperture radar. This is employed in geomorphological studies of ground motion and has the ability of illuminating deformations connected with earthquakes, landslides, volcanism, etc. (Gupta, 1991).

Geological studies with the aid of remote sensing commonly employ a multitude of tools classified according to short to long wavelengths of the electromagnetic radiation which various instruments are sensitive to. Shorter wavelengths are generally useful for site characterization up to mineralogical scale, while longer wavelengths reveal larger-scale surface information, such as regional thermal anomalies, surface roughness, etc (Gupta, 1991). Such techniques are particularly beneficial for the exploration of inaccessible areas, and planets other than Earth.

Remote sensing data can also help in the studies involving mapping of geological hazards and economic geology, that is, exploration for minerals, petroleum, etc. Soils and vegetation that preferentially grow above different types of rocks can be used to deduce the underlying geological patterns through remote sensing in geology.

* **Corresponding Author**

*(palogb316@gmail.com) ORCID ID 0000 – 0001 – 5075 – 3543
(morewole@gmail.com) ORCID ID 0000 – 0001 – 9983 – 5435
(jephotto@gmail.com) ORCID ID 0000 – 0002 – 5420 – 4135

Cite this study

Aguta O O, Oladotun M O & Jephthah S O (2021). Applications of Remote Sensing in Solving Myriads of Geological Problems: A Review. 3rd Intercontinental Geoinformation Days (IGD), 160-163, Mersin, Turkey

Remote sensing data is often visualized using Geographical Information System (GIS) tools (Gupta, 1991; Ray and Lazzari, 2020).

2. Techniques of remote sensing

Remote sensing techniques consist of a sensor which could be spaceborne (carried by satellite), airborne (carried by aircraft, or most recently, Unmanned Aerial Vehicle (UAV)) or ground-based (sometimes called proximal sensing) (Colomina and Molina, 2014) and is carried by a platform and which operates on the environment to produce data.

The data acquired from higher elevation capture a larger spatial coverage, but the resolutions are often low (Bürgmann and Thatcher, 2013) and are then transformed into information by several operations collectively called reduction and analysis. Such information gathered from the data will eventually be applied for different purposes (geology, mineral exploration, soils, forestry, military, disaster control, etc.) depending on the user's requirements.ed.

2.1. Sensors

The sensors used in remote sensing are varied in type and classification. For instance, sensors can be either active or passive. Active sensors produce their own energy in order to be able to gather data such as film photography, infrared, charge-coupled devices, and radiometers, while passive sensors depend on and utilize energy from external sources. Examples of passive sensors are Radio Detection and Ranging (RADAR) and Light Detection and Ranging (LIDAR).

Another classification is either imaging or non-imaging. Imaging sensors reproduce data in image format (like aerial photographic cameras, multi-spectral scanners, and side-looking radar (SLR)) whereas non-imaging sensors produce data which cannot be transformed into images (e.g. s194, an L-band radiometer system used in Skylab/EREP experiments). Sensor classification could also be according to the spectral region/bands within which they operate. Examples include visible light, infrared and microwave. All the mentioned classes of sensors are useful in geologic applications (Wikipedia.org).

2.2. Platforms

The platforms employed in carrying sensors for remote sensing are of different types. The most commonly used are aircraft, spacecraft, and Unmanned Aerial vehicles (UAV).

2.3. Environment

In natural resource surveys, the environment is usually part of the earth's surface. For geological purposes, however, this will naturally be restricted to the land-covered areas of the earth. Other examples of environment include extra-terrestrial bodies such as the moon, Mars, Jupiter, and other celestial bodies which in recent years have also been objects of remote sensing activities (Wikipedia.org).

2.4. Data

The data produced by the sensors can either be of the photographic type such as in the case with camera systems or of the digital type which is originally stored in magnetic tape, such as multi-spectral scanning systems (MSS) (FAO, 2020).

2.5. Information

We seek to derive information from data produced by the sensor. Afterward, operations called "data reduction and analysis" are carried out. This can be done purely visually as is done in conventional photo-interpretation or partly with the aid of machines/computers. Visual analysis is referred to as image orientation while digital (computer) analysis is called numerical orientation. Geologists seek to derive geological information usually stored on a format (such as thematic map) and may be accompanied by graphs, tabulations, and a report. The goal of these information depends on the users' interest. The trend of improvement of remote sensing emanates from panchromatic, multi-spectral, hyper-spectral to ultra-spectral which has greatly affected the quality of the information because of the rise in spectral resolution (Roy and Vandana, 2009).

2.6. Application

The final step in remote sensing is the application of the data. Applications depend on the users' interests. For instance, if a geological map is the final product of the analysis, the information contained in the map may find different applications in hydrogeology, engineering geology, mineral exploration, geological survey, or it may serve as a scientific document (Hakim et al., 2018 and Wikipedia. org).

3. Electromagnetic spectrum: the working principle of remote sensing

In remote sensing, two main variables are measured in a typical remote sensing system: the radiance (or intensity) and time of arrival for active systems (Rees, 2013). As a point to note, the data collected is a blend of both reflections of solar radiation and emission (according to Planck's law) from the object of visible and near-infrared (VNIR) region (Vincent, 1997). The thermal infrared (TIR) region measures mainly emission while the microwave region records the backscattering portion of reflection. The radiance is determined by radiation-matter interactions, which are governed by the physio-chemical properties of the target object (Vincent, 1997).

However, since the sensors are looking through the atmosphere to reach the target, there is atmospheric absorption and three main atmospheric windows, which allow penetration of radiation are involved and are therefore, the most useful range of the spectrum. They are 0.4–3 micro-meters (Visible and near-infrared (VNIR)), 3–14 micro-meters (Thermal Infrared TIR), and few millimeters to meters (microwave) (Rees, 2013; Vincent, 1997).

4. Applications of remote sensing in geology

Remote sensing finds various applications in geological sciences. They include:

4.1. Geological mapping

Remote sensing aids surficial geological mapping and landform characterization. Rock-bearing minerals are identified via aerial photographs using a logical method, which indicates those things the rocks contain that enable them to be seen in an aerial photograph. These logical methods are texture, colour, and tone of the photograph, drainage pattern, vegetation cover, and cultivation. Apart from mineral/rock identification, soil properties (such as soil texture, moisture content of the soil, soil organic carbon, and soil salinity), geodetic survey, geomorphological features, geologic hazards (such as tsunami, earthquakes, and volcanism), and mapping of inaccessible areas are made possible by remote sensing. The end product of remote sensing application in geological mapping is thematic map (Robert, 2007).

4.2. Petroleum exploration

The short wavelength region of visible and near-infrared (VNIR) can be used to estimate the petroleum reservoir because it provides both accurate distance measurements by LiDAR and spectral data from spectral scanning (Hodgetts, 2013). The study by Lord in 2017 at Pennsylvania, USA indicates that remote sensing application provided insights into seepage emanating from leaking abandoned wells in addition to the naturally occurring seepage.

4.3. Groundwater investigations

Remote sensed data can infer possible confined/ unconfined aquifers (Jha et al., 2007). For instance, in radar data (ground penetrating radar), which can penetrate deep meters into the ground, will indicate some diffuse reflection for a rough surface in relation to the wavelength used. The change in lithology may suggest soft rock and unconsolidated sediments with high porosity indicates groundwater accumulation (Wikipedia.org).

4.4. Planetary observation

Planetary explorations are made simpler without sending an astronaut into space by remote sensing. For most planetary explorations, due to the thick atmosphere, radar is suitable instrumentation to investigate planetary surfaces as it can penetrate the atmosphere and detect surface roughness. Also, from the mapping of Venus, it is seen that topographic maps could be obtained from radar altimetry and InSAR methods (Wikipedia.org).

4.5 Image processing

Image processing is crucial to converting raw data into useful information. For imaging remote sensing, where spectral data are collected and recorded in pixels of an image, a two-dimensional representation. After removal of noise and calibration, images are then geo-referenced to relate pixel to real-life geography. The first-hand data are then corrected to remove noise such as atmospheric disturbance, structural effects, and distortion. The image interpretation could be achieved by an interpreter or computation (Gupta, 1991).

5. Integration of remote sensing with geographical information system (GIS)

The techniques of remote sensing are closely connected to advance data interpretation and visualization, which is among the capabilities in Geographical Information System (GIS) (Jensen, 2007; Rees, 2013; Kuehn et al., 2000)). The GIS also allows the input of other information such as socioeconomic conditions and biophysical conditions in terms of layers (Jha et al., 2007). Further, analyses in the same spatial extent are carried out and thematic maps are then generated for presentation (Jensen, 2007; Rees, 2013).

6. The limitations of remote sensing application in geology

There is no ideal sensor capable or optimized to study everything in geology. Therefore, it is of geologist's preference and skill to choose which dataset and excerpt information therein (Gupta, 1991). For instance, in cloud-free areas, aerial photography is more sensible, but radar performs better for overcast weather. Resolution (spatial and spectral) and lack of stereoscopy in many geological investigations are also limiting factors of remote sensing application in geology (Bhan and Krishnanunni, 1983). There is a trade-off between spatial resolution and spectral resolution (Vincent, 1997).

Stratigraphic and lithologic discrimination which make rock types to appear with little or no spectral differences is also a limiting factor in geological mapping from space (Bhan and Krishnanunni, 1983).

Another limitation is the inconsistent data acquisition method, and their interpretation patterns/processes (Mulder *et al*., 2011).

6.1. The solutions to the limitations

Many authors like Bhan and Krishnanunni in 1983, Gupta in 1991, Colomina and Molina in 2014 and Mulder et al in 2011 considers the following as solutions to the above inherent challenges of applying remote sensing in geology.

6.1.1. Ground-truthing

Even with the present state of the art in remote sensing, it cannot totally replace conventional methods of field mapping because such ground-truthing makes remote-sensing data meaningful. Otherwise, roads will be interpreted as ore-bearing fractures while rounded building roofs will be interpreted as salt domes. Thus, remote sensing data are usually validated by ground-truthing surveys, which serves as training data in image

classification to ensure quality (Gupta, 1991, Mulder *et al*., 2011).

6.1.2. Repeated reconnaissance

Repeated reconnaissance is recommended for studying a specific geologic terrain (Colomina and Molina, 2014). Field observation and reconnaissance remain irreplaceable and shall never be taken over completely by remote sensing because field data greatly support remote sensing data interpretation. Remote sensing should be viewed as complementary to field survey aimed at providing instantaneous views of different scales, perspectives or spectral vision (Gupta, 1991).

6.1.3. Advances in sensor development

Bhan and Krishnanunni in 1983 opines that invention of sensors with finer spatial resolution and more spectral bands particularly in the region of middle and thermal infra-red with sharper spectral separation, and also, improvement in geometric fidelity and greater radiometric accuracy along with stereoscopy are the solutions to the remote sensing limitation on resolution and stereoscopy. More so, digital enhancement of MSS data using computer techniques made stratigraphic and lithologic discrimination possible (Bhan and Krishnanunni, 1983).

7. Conclusion

Remote sensing is an emerging technology with usefulness in solving many geological problems that cannot be exhaustive as it has the ability to explore and collect data from dangerous and inaccessible geological terrains with a limited view of the human eye. It also reduces the burden of fieldwork required for mapping of areas through synoptic studies. Hence, remote sensing helps in landform or geomorphological studies, groundwater and petroleum exploration, rock and mineral identification, geodetic survey, and detection of geologic hazards. In this paper, the remote sensing techniques, working principles, various application in geological sciences, its limitations and possible solutions were discussed, which could be a basic reference for future studies on the application of remote sensing in geological sciences.

References

Bhan S K and Krishnanunni K (1983). Application of Remote Sensing techniques to geology. Proc.Indian Acad. Sci (engineering and sciences), Vol. 6 Pt 4 Pp 297-311

Bürgmann R and Thatcher W (2013). Space geodesy: A revolution in crustal deformation measurements of tectonic processes. Geological Society of America Special Paper 500. 397–430.

Colomina I and Molina P (2014). Unmanned aerial systems for photogrammetry and remote sensing: A review. ISPRS Journal of Photogrammetry and Remote Sensing 92 (2014) 79–97

FAO (2020). Remote Sensing as a Data Source Chapter 4 available at https://www.fao.org/3/t0446e/t0446e04.htm. Accessed on 27th October 2020.

Gupta R P (1991). Remote Sensing Geology. Springer-Verlag.

Hakim S, Mohand B, Mohamed B. M, Nureddin M. S, Khalid M. S. A. B, and Robert W. A. (2018): Applications of Remote Sensing in Geoscience. Doi 10.5772/intechopen.75995

Hodgetts D (2013). Laser scanning and digital outcrop geology in the petroleum industry: a Review. Marine and Petroleum Geology, 46, 335–354.

Jensen J R (2007). Remote Sensing of the Environment an Earth Resource Perspective. Pearson.

Jha M K, Chowdhury A, Chowdary V M, & Peiffer S (2007). Groundwater management and development by integrated remote sensing and geographic information systems: prospects and constraints. Water Resources Management, 21(2), 427–467.

Kuehn F, King T V V, Hoerig B, Peters D C, Newcomb C, Toms H (2000). Remote Sensing for Site Characterization. Springer.

Lord B (2017). Remote Sensing Techniques for Onshore Oil and Gas Exploration. The Leading Edge Journal Volume: 36 DOI:10.1190/Tle36010024.1

Mulder V L, de Bruin S, Schaepman M E, Mayr T R (2011). The use of remote sensing in soil and terrain mapping — A review. Geoderma, 162, 1–19.

Ray R and Lazzari M (2020), Landslides: Investigation and Monitoring, 10.5772 IntechOpen 78130

Rees W G (2013). Physical Principles of Remote Sensing. 3rd Edition. Cambridge University Press. Remote sensing (geology). Available at https://en.wikipedia.org/wiki/Remote_Sensing_(geology). Assessed on 8th October 2021.

Robert A S (2007). Remote Sensing (Third Edition) CHAPTER 9 - Thematic Classification, Academic Press, (https://www.sciencedirect.com/science/article/pii/B9780123694072500127)

Roy P S and Vandana A (2009). Technology trends in Remote Sensing and data analysis. Available at https://www.geospatialworld.net/article/technology-trends-in-remote-sensing-and-data-analysis/

Vincent R K (1997). Fundamentals of Geological and Environmental Remote Sensing. Prentice Hall.

Intercontinental Geoinformation Days

igd.mersin.edu.tr

3D modeling of underwater objects using photogrammetric techniques and software comparison

Seda Nur Gamze Hamal[*1], **Ali Ulvi** [1]

[1]*Mersin University, Institute of Science, Remote Sensing and Geographical Information Systems, Mersin, Turkey*

Keywords
Underwater
Software
Photogrammetry
SfM

ABSTRACT

Most of the earth is covered with water. Most of these waters are oceans. Despite the fact that so many areas are covered with water, research on underwater photogrammetry is not as numerous as above ground research. However, in recent years, with the integration of cameras underwater, researchers have turned to underwater photogrammetry studies. In this study, it presents research on whether the selection of SfM-based software is suitable for the underwater environment. In the research, data collection was carried out by placing an object in a 1.5-meter-deep pool. In the data processing part, Agisoft Photoscan, Context Capture and Reality Capture software were used and 3D point cloud data were obtained and evaluated from each software.

1. Introduction

About 70% of the world is covered by water. While people are doing their research very comfortably on earth in the world they live in, the situation is not the same under water. The discovery of underwater life, archaeological remains, biological resources have remained secret for many years. However, in recent years, researchers have turned to underwater research, thanks to the ability to integrate cameras underwater and additionally technological innovations such as underwater drones. Thus, subjects such as the documentation of archaeological remains, the increase and decrease in biological diversity began to be studied. The most adopted method in these studies was underwater photogrammetry (Block et al., 2017; Polat et al., 2020).

Underwater photogrammetry is based on various systems and methodologies. The optical properties of water and lighting conditions seriously affect underwater images. Because light absorption mostly affects red wavelengths, colors are absorbed at different rates as depth increases, resulting in a green-blue image. Water also absorbs light energy and scatters optical rays, creating blurry images. These conditions hindered underwater photogrammetric studies. However, thanks to the SFM-based software developed in recent years, it affects these situations relatively less (Raoult et al., 2016; Casella et al., 2017; Vlachos et al., 2018; Yakar et al., 2015).

The rise of photogrammetric software packages has aided underwater photogrammetric studies that were nearly impossible before commercial software using SfM algorithms. As the commercial software market has expanded in recent years, many software packages using the sfm algorithm have emerged. In this case, it has been a matter of debate which of the several photogrammetric software packages available on point clouds of the underwater environment can provide better results (Drap et al., 2015; Çelik et al., 2020; Sefercik et al., 2020; Ulvi et al., 2020; Yiğit et al. Uivi, 2020).

Mangeruga et al. (2018) collected data from various underwater areas with different depth, turbidity and lighting conditions in their research. These data sets were compared by generating point clouds in different software. In their study, Burns and Delparte (2017)

* **Corresponding Author**

*(sedanurgamzehamal@gmail.com) ORCID ID 0000 – 0002 – 1050 – 3088
(aliulvi@mersin.edu.tr) ORCID ID 0000 – 0003 – 3005 – 8011

Cite this study

Hamal S N G & Ulvi A (2021). 3D Modeling of Underwater Objects Using Photogrammetric Techniques and Software Comparison. 3rd Intercontinental Geoinformation Days (IGD), 164-167, Mersin, Turkey

obtained the 3d point cloud in Agisoft and Pix4D software by collecting data on underwater coral reefs at different camera angles and at different heights. Then, they compared the errors of these two software and compared the obtained point clouds by performing Welch t-test statistical analysis. In their research, Vlachos et al (2019), after collecting data from an archaeological site, processed it in Agisoft Photoscan, VisualSFM, SURE, 3D Zephyr and Reality Capture software. Then, they made a comparison between the software by making cloud to cloud and surface density analyzes. In this direction, data were collected by placing an object in a pool 1.5 meters deep. It was processed using Agisoft Photoscan, Context Capture and Reality Capture software to process the collected data. Agisoft Photoscan is the most used software to obtain 3d point clouds in the literature. For this reason, the point cloud data obtained from this software was accepted as a reference and analyzes were made in CloudCompare software.

2. Method

2.1. Data collection

In the study, 80 overlay photographs were taken underwater.

For this purpose, Go Pro Black Hero 9 camera was used to collect the data of the underwater object. The technical information of the camera used in the study is shown in Table 1.

Table 1. Technical properties of Go Pro Hero Black 9 camera

Technical properties	Value
Sensor	1-Chip CMOS
Sensor Resolution	23,6 MP
Media Recording	1 x microSD / HC / XC (256 GB Maximum)
Still Image Support	JPEG - 20 MP
Shutter Speed	1/25 - 1/2000 Second (Photo)
Ptoho ISO Range	100 - 6400
Video ISO Range	100 - 6400
Image Stabilization	Digital
White Balance Modes	Auto

2.2. Data process

Agisoft Photoscan, Context Capture and Reality Capture software were used for photogrammetric evaluation. In all software used, it was paid attention to be in the same reference system while generating the point cloud.

The point cloud generated in Agisoft Photoscan software was accepted as a reference. This is because underwater photogrammetry is the most widely used software (Demesticha et al, 2014).

The following statistical results were obtained in the Cloud Compare software, which is the open-source software of the 3D point clouds produced.

In this software, analyzes were made based on surface density and roughness values.

Surface Density is estimated by counting the number of N neighbors for each point (within a sphere of radius R). The surface density used for this evaluation is defined by dividing the number of neighborhoods by the neighborhood surface. The software estimates the surface density for all points of the point cloud and then proportionally calculates the average value for an area of 1 m^2. Surface density is considered a positive metric because it describes the number of points on a potentially generated surface, excluding noise that is present as points outside that surface. This is why the surface density metric is used instead of the volume density metric.

Roughness The “roughness” value for each point is equal to the distance between that point and the optimal plane calculated at its nearest neighbors, which are points in a point-centered sphere. Roughness is considered a negative metric as it is an indicator of noise on the point cloud, assuming a generally smooth surface.

To facilitate an overall comparison of the tested software in terms of 3D reconstruction performance and to evaluate numerous outcomes, the surface density D and roughness R metrics have been normalized. Purposely, the metrics and results obtained are presented from a critical perspective, highlighting the pros and cons of each software for the dataset used. Following this, a general conclusion is reached as to which of the three software packages mentioned above performs best in this particular environment and for this particular dataset.

3. Results

First of all, the data obtained during the photogrammetric processing process was created as 3d point cloud data in Agisoft Photoscan, Context Capture and Reality Capture software, respectively. While the total process time was 98 minutes in Agisoft Photoscan software, it took 85 minutes in Context Capture software and 105 minutes in Reality Capture software.

In order to compare the obtained point clouds, Roughness analysis was first performed in Cloud Compare software. (Figure 1). The roughness calculation is called the shortest distance between the optimal plane calculated on the nearest neighbors of each point in the point cloud (Cloud Compare, 2021). Purpose of analysis, the lower the value in the legend part, the less jagged the point cloud is.

Roughness analysis was performed separately on the point clouds obtained as a result of all software. As a result of the analysis, the values found in the legend were normalized with the help of the equation given in equation 1. This is because it makes values visible and easy.

$$Z = \left(\frac{X - \min(x)}{\max(x) - \min(x)}\right) \quad 1$$

By normalizing the values in the roughness analysis of all point clouds, the values of 9 mm in Agisoft Photoscan software, 8 mm in Reality Capture software and 3 mm in ContextCapture software were found.

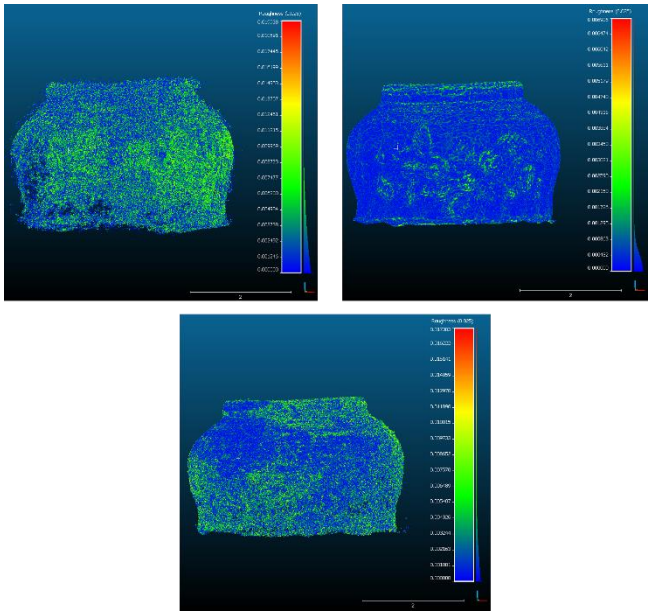

Figure 1. Roughness analysis in point clouds

Surface density analysis was performed in CloudCompare software to find the surface density of the model. The same calculations as in the roughness analysis were also used for the surface density analysis (Figure 2).

In the tested point clouds, it was noticed that the overall visual representation of the dense point cloud was better at medium quality as it appeared denser and less noisy.

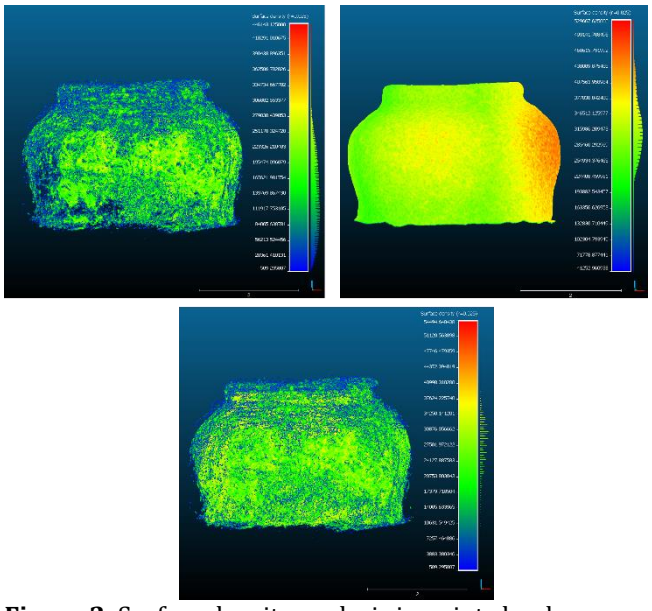

Figure 2. Surface density analysis in point clouds

As shown in Table 2, the number of points produced per point cloud varies considerably. Context Capture produced a much larger amount of points. On the other hand, Reality Capture and Photoscan appear to produce less point clouds. This potentially shows that the parameters used in sfm algorithms Reality Capture and Photoscan are very similar to each other.

Table 2. Number of point clouds produced by 3 different software, average surface density and average roughness

Software	number of point clouds	D	R
Agisoft Photoscan	1369087	282573.2692	0.009968706
ContextCapture	13196754	36678.44271	0.003452824
Reality Capture	1358769	260648.5283	0.008651706

4. Conclusion

Based on the evaluated metrics, it can be concluded where each software has grown and fallen. All software appears to produce complete point clouds.

However, it was noted that it was completed at different times during the process. Although there is not much difference in the process time of a small object, it is predicted that this time will be much different in the process of larger areas. For this reason, it is thought that the software should be selected according to the characteristics of the area to be studied.

While the number of point clouds was almost the same in Agisoft and Reality Capture software, ContextCapture software almost doubled the number of point clouds compared to the other two software. Having a large number of point clouds helps to see the details of the object better, but it can cause problems in terms of data storage. For this reason, software selection should be made according to the purpose of the study.

From the metrics evaluated during this particular study. Additionally, seeing results regarding roughness, it is notable that reality capture outperforms other software. Unfortunately, no clear conclusions can be drawn regarding surface density metrics as the number of neighboring points is proportional to the total number of points the point cloud has. Considering everything about point cloud integrity, number of points, point distribution and all the metrics evaluated, it can be said that the software used may be the best options for the generation of 3D dense point clouds underwater. Although some photogrammetric softwares seem to be more advantageous than others from these comparisons, the results of the dataset obtained with a single measurement may not be reliable. For this reason, it was concluded that more than one measurement should be evaluated in different underwater conditions, where the depths are variable and even the season and measurement times are different. Therefore, in the future, further evaluation with different datasets under different conditions may yield tangible results as to which photogrammetric package produces the best overall 3D point clouds in an underwater environment.

Acknowledgement

This research was supported by Mersin University Scientific Research Project (BAP), Project No: 2021-TP2-4295.

References

Block, M., Dworsky, C., Löw, C., da Fonseca, H. S., Gehmlich, B., Wittchen, D., ... & Ducke, B. (2017). Underwater Videogrammetry with Adaptive Feature Detection at" See am Mondsee", Austria. Studies in Digital Heritage, 1(2), 547-565.

Burns, J. H. R., & Delparte, D. (2017). Comparison of commercial structure-from-motion photogrammety software used for underwater three-dimensional modeling of coral reef environments. The International Archives of Photogrammetry, Remote Sensing and Spatial Information Sciences, 42, 127.

Casella, E., Collin, A., Harris, D., Ferse, S., Bejarano, S., Parravicini, V., ... & Rovere, A. (2017). Mapping coral reefs using consumer-grade drones and structure from motion photogrammetry techniques. Coral Reefs, 36(1), 269-275.

CloudCompare (Version 2.10 alpha) [GPL Software]. 2021. Available online: http://www.cloudcompare.org/

Çelik, M. Ö., Yakar, İ., Hamal, S. N. G., Oğuz, G. M., & KANUN, E. (2020). Sfm Tekniği ile Oluşturulan 3B Modellerin Kültürel Mirasın Belgelenmesi Çalışmalarında Kullanılması: Gözne Kalesi Örneği. Türkiye İnsansız Hava Araçları Dergisi, 2(1), 22-27.

Demesticha, S., Skarlatos, D., Neophytou, A., 2014. The 4th-Century B.C. shipwreck at Mazotos, Cyprus: New techniques and Methodologies in the 3D Mapping of Shipwreck Excavations. Journal of Field Archaeology, 39, 134–150. https://doi.org/10.1179/0093469014Z.00000000077

Drap, P., Merad, D., Hijazi, B., Gaoua, L., Nawaf, M. M., Saccone, M., ... & Castro, F. (2015). Underwater photogrammetry and object modeling: a case study of Xlendi Wreck in Malta. Sensors, 15(12), 30351-30384.

Mangeruga, M., Bruno, F., Cozza, M., Agrafiotis, P., & Skarlatos, D., 2018. Guidelines for Underwater Image Enhancement Based on Benchmarking of Different Methods. Remote Sensing, 10(10), 1652.

Polat, N., Mehmet, Ö. N. A. L., Ernst, F. B., Şenol, H. İ., Memduhoglu, A., Mutlu, S., ... & Hüseyin, K. A. R. A. (2020). Harran Ören Yeri Arkeolojik Kazı Alanınındın Çıkarılan Bazı Küçük Arkeolojik Buluntuların Fotogrametrik Olarak 3B Modellenmesi. Türkiye Fotogrametri Dergisi, 2(2), 55-59.

Raoult, V., David, P. A., Dupont, S. F., Mathewson, C. P., O'Neill, S. J., Powell, N. N., & Williamson, J. E. (2016). GoPros™ as an underwater photogrammetry tool for citizen science. PeerJ, 4, e1960.

Sanz-Ablanedo, E., Chandler, J. H., Rodríguez-Pérez, J. R., & Ordóñez, C. (2018). Accuracy of unmanned aerial vehicle (UAV) and SfM photogrammetry survey as a function of the number and location of ground control points used. Remote Sensing, 10(10), 1606.

Sefercik, U. G., Tanrıkulu, F. & Atalay, C. (2020). SFM Tabanlı Yeni Nesil Görüntü Eşleştirme Yazılımlarının Fotogrametrik 3B Modelleme Potansiyellerinin Karşılaştırması. Türkiye Fotogrametri Dergisi, 2 (2) , 39-45. Retrieved from https://dergipark.org.tr/en/pub/tufod/issue/58541/722293

Ulvi, A., Yakar, M., Yiğit, A. Y., & Kaya, Y. (2020). İHA ve yersel fotogrametrik teknikler kullanarak Aksaray Kızıl Kilise'nin 3 Boyutlu nokta bulutu ve modelinin üretilmesi. Geomatik Dergisi, 5(1), 22-30.

Vlachos, M., Berger, L., Mathelier, R., Agrafiotis, P., & Skarlatos, D. (2019). Software comparison for underwater archaeological photogrammetric applications. International Archives of the Photogrammetry, Remote Sensing and Spatial Information Sciences-ISPRS Archives.

Yakar, M., Orhan, O., Ulvi, A., Yiğit, A. Y., & Yüzer, M. M. (2015). Sahip Ata Külliyesi Rölöve Örneği. TMMOB Harita ve Kadastro Mühendisleri Odası, 10.

Yiğit, A. Y., & Ulvi, A. (2020). İHA Fotogrametrisi Tekniği Kullanarak 3B Model Oluşturma: Yakutiye Medresesi Örneği. Türkiye Fotogrametri Dergisi, 2(2), 46-54.

Intercontinental Geoinformation Days

igd.mersin.edu.tr

Documentation of cultural heritage by photogrammetric methods: a case study of Aba's Monumental Tomb

Engin Kanun*[1], Aydın Alptekin [2], Murat Yakar [3]

[1]*Mersin University, Faculty of Engineering, Department of Mechanical Engineering, Mersin, Turkey*
[2]*Mersin University, Faculty of Engineering, Department of Geological Engineering, Mersin, Turkey*
[3]*Mersin University, Faculty of Engineering, Department of Geomatics Engineering, Mersin, Turkey*

Keywords
Cultural heritage
UAV
Photogrammetry
3D model
Monumental tomb

ABSTRACT

Because of its geographical location, Turkey has hosted various civilizations. As a result, our country has a diverse cultural heritage inventory derived from the civilizations it hosts and the civilizations that it interacts. In terms of cultural heritage protection, preserving these assets and transmitting them to the future generations is critical. Ground and weather conditions, material degradation, natural disasters, fire, war, and misuse can all cause significant damage to these objects over time. It is vital to document the artifacts in such circumstances in order to conserve them and transfer them to the future generations. In order to transfer the cultural heritage to future generations, technological instruments and procedures are utilized to document existing artifacts and structures. Within the scope of this study, the UAV photogrammetry method was used to create the 3D point data and solid model of the Monumental Tomb of Aba built in the 2nd century AD, located in the Kanlıdivane region of Mersin province in Turkey. Images were taken with Parrot Anafi HDR unmanned aerial vehicle and a 3D model was produced. Combination errors of the photographs were also calculated and it was shown in the results that they were at an acceptable level.

1. Introduction

Aba's Monumental Tomb, which is an ancient artifact, built in the 2nd century AD and located in the Kanlıdivane region of the Mersin province of Turkey, has coordinates 36° 31' 38.5" north, 34° 10' 37.4" east. The location of the tomb is shown in Fig. 1.

Figure 1. Location of the Aba's Monumental Tomb

It is the most magnificent mausoleum of Kanytella. According to the inscription on the door of this monumental tomb, which was built in the type of Roman temples. It was built by a woman named Aba for herself and her husband Arios. The tomb monument was built on a low podium. There is a vaulted entrance on the front facade. There are Corinthian plaster caps on the four corners of the tomb. The tomb is dated to the 2nd century AD based on the inscription on it and other tombs (Turkey Culture Portal 2021).

The Monumental Tomb of Aba can be found north of the geological pit in the region. It is one of Kanlıdivane's most well-known landmarks. The building's principal construction method is cut stone masonry, with mortar as the binding material. The roof of the superstructure is shaped like a gable and is coated in stone. It's supported by a cut-stone barrel vault, which is subsequently filled

* **Corresponding Author**

*(ekanun@mersin.edu.tr) ORCID ID 0000 – 0002 – 2369 – 5322
(aydinalptekin@mersin.edu.tr) ORCID ID 0000 – 0002 – 5605 – 0758
(myakar@mersin.edu.tr) ORCID ID 0000 – 0002 – 2664 – 6251

Cite this study

Kanun E, Alptekin A & Yakar M (2021). Documentation of cultural heritage by photogrammetric methods: a case study of Aba's Monumental Tomb. 3rd Intercontinental Geoinformation Days (IGD), 168-171, Mersin, Turkey

with rubble stone to create a flat roof surface. The vault marks the main chamber's entrance on the south facade, which is topped by a pediment at roof level (Naycı 2020).

The last row of cut-stones in masonry walls was built in architrave style, with Corinth capital styling on the corner stones. Although the architectural integrity of the building has been retained, there are serious issues with the scale of the structure. The west and north walls, in particular, have material deterioration and structural deformations. On the north wall, there are serious fissures that have split the stone components in half. This graphic depicts the likelihood of a high impulse being triggered by lateral pressures or settlement issues. The structural degradation danger has been confirmed by external forces because the monument is placed extremely close to one of the site's geological discontinuity lines. The monument should be included in an architectural conservation program as soon as possible, before it loses its structural integrity, as it is one of the few examples of architectural and structural unity that still exists (Naycı 2020).

UAV photogrammetry is one of the methods widely used within the scope of documentation of cultural heritage. Generating a three-dimensional model of Gözne Castle, a medieval castle (Çelik et al. 2020), obtaining a 3D photogrammetric model of a historical inn (Yakar and Yılmaz 2008) are some of the examples of documenting cultural heritage with photogrammetric methods.

In a study, Roman tombs were examined in detail and the features of the mausoleum of Aba at Kanytellis were comprehensively presented (Mörel 2019).

2. METHOD

This study consists of two phases, namely field and office work. The steps of controlling the study area, preparing it for photographing and taking images of the monumental tomb with an unmanned aerial vehicle constitute the field study phase. In the office work phase, the steps of transferring the data received from the unmanned aerial vehicle to the computer environment and interpreting and processing were carried out.

2.1. Field Work Phase

At this stage of the study, first of all, necessary permissions were obtained to fly in the Kanlıdivane region, which is the study area. Then, the flight altitudes at which images will be taken around the tomb were determined. Images were taken with a Parrot Anafi HDR drone by manually.

UAV based modelling technique has been widely used since last decade such as landslide site modelling (Kusak et al. 2021), rockfall site modelling (Alptekin et al. 2019), shoreline detection (Unel et al. 2020), soil erosion mapping (Yılmaz et al. 2012) and pond volume measurement (Alptekin and Yakar 2020).

Figure 2. Parrot Anafi HDR UAV

The technical specifications of the unmanned aerial vehicle used are shown in Table 1:

Table 1. Technical specifications of the UAV (Parrot 2021)

Feature	Value
Drone	
Size folded	244x67x65 mm
Size unfolded	175x240x65 mm
Weight	320 g
Max transmission range	4km with controller
Max flight time	25 min
Max horizontal speed	15 m/s
Max vertical speed	4 m/s
Max wind resistance	50 km/h
Service ceiling	4500m above sea level
Operating temperature	-10°C to 40°C
Lens	
Sensor	1/2.4'' CMOS
Aperture	f/2.4
Focal length (35 mm eq.)	23-69 mm (photo)
Depth of field	1.5 m - ∞
ISO range	100-3200
Digital zoom	up to 3x (4K Cinema, 4K UHD, FHD)
Photo resolution	21MP (5344x4016) / 4:3 / 84° HFOV

The circumference of the mausoleum, which is approximately 50 km away from Mersin, is roughly 31.5 meters, and its sitting area is around 61 square meters. Every detail of the structure was tried to be captured by flying first at low altitude and then at high altitude. A total of 101 images were taken. Some of the images of the monumental tomb taken are shown in Fig. 3.

Figure 3. Images of Aba's Monumental Tomb

Camera calibration was done beforehand in photo shoots and no changes were made to the parameters. A smartphone was used together with the remote control during photo acquisitions. FreeFlight 6 and Pix4dcapture applications have been installed in order for the smartphone and the remote to work integrated.

2.2. Camera calibration

The camera used must be calibrated beforehand so that the merging and overlay operations of the images can be of high accuracy. It was mentioned in the previous section that there is a 5.92 mm sensor in the unmanned aerial vehicle used in this study. Images have a size of 4608x3456 pixels. Camera calibration was done in ContextCapture software. "Fig. 4" shows the distortion parameters obtained as a result of camera calibration:

	Focal Length [mm]	Focal Length Equivalent 35 mm [mm]	Principal Point X [pixels]	Principal Point Y [pixels]	K1	K2	K3	P1	P2
Previous Values	4.00	24.32							
Optimized Values	3.83	23.30	2323.59	1729.81	-0.0019	0.0078	-0.0069	0.0034	0.0003
Difference Previous / Optimized	-0.17	-1.02							

Figure 4. Camera calibration parameters

2.3. Office work phase

After the completion of the image acquisition within the scope of the field work, the office work phase was started. First of all, the data obtained from the field were transferred to the computer environment. The image file obtained after the flight took up 457 MB in total. Data processing was done in Bentley's ContextCapture software. The office work, which was started after half a day of field work, was completed in one day. The positions of the images taken relative to the mausoleum are shown in Fig. 5.

All the photos taken were used in the processes. Generic block type was chosen for the aerotriangulation process of the images based on experience from previous studies. No control point was used in this study. Positioning metadata of the images were utilized for rigid registration. High key points density option was selected. This step took only 5 minutes and 17 seconds. In the aerotriangulation process, 45125 tie points were formed. 31719 keypoints per image were detected by the software. Overlay error values of the photos are presented in the results section.

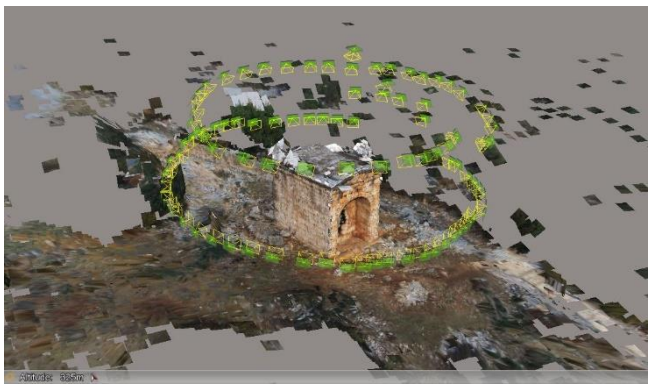

Figure 5. The positions of the images taken

After aerotriangulation step, reconstruction process was initiated by generic selection of matching pairs. Extra geometric precision (tolerance of 0.5 pixel in input photos) option was applied. In order not to deviate from the original geometry of the tomb, small hole-filling option was implemented. Finally, in this step, the spatial frame is reduced, avoiding the modeling of unnecessary regions and the use of excessive computer power. After the aerotriangulation process, it took 37 minutes and 31 seconds to obtain the 3D solid model. Computer used in processes has Intel(R) Core(TM) i7-7700HQ CPU @2.81GHz processor, 16 GB of RAM capacity and GeForce Nvidia 1050 Ti 4 GB graphics card.

3. Results and discussion

After the camera calibration, field studies and office work phases were completed, a 3D solid model of the Aba's Monumental Tomb was obtained. The surface texture was created by using photographs to add visuality to the obtained 3D solid model. Texture compression quality was selected as 100% quality and texture sharpening option was enabled. The three-dimensional model of Aba's Monumental Tomb is presented in Fig. 6.

The resulting 3D model is in one-to-one scale with the real work. While length measurements can be taken on the model, area and volume calculations can be made at the same time.

As a continuation of this study, it is planned to compare photogrammetric data with terrestrial laser scanner data. As a result of the comparison, which method is more suitable for such works will be evaluated in terms of cost, time, efficiency and applicability.

4. Conclusion

In this study, Aba's Monumental Tomb, which is an ancient artifact built in the 2nd century AD and located in the Kanlıdivane region of the Mersin province of Turkey was modeled in 3D using UAV photogrammetry. As a result of obtaining a real-scale model of this artifact, which is of great importance in terms of cultural heritage, the documentation process has been carried out. The

data obtained in this study can be used in possible studies by anthropologists, archaeologists and historians. The real-scale 3D model obtained can be utilized in the restoration and repair studies. The 3D model obtained within the scope of this study will also allow the promotion of the work within the scope of tourism activities.

Figure 6. 3D solid model of Aba's Monumental Tomb

Acknowledgement

The authors would like to thank the members of Mersin University Department of Geomatics Engineering for their contribution to this study.

References

Alptekin, A. & Yakar, M. (2020). Determination of pond volume with using an unmanned aerial vehicle. Mersin Photogrammetry Journal, 2 (2), 59-63.

Alptekin, A., Çelik, M. Ö., Doğan, Y. & Yakar, M. (2019). MAPPING OF A ROCKFALL SITE WITH AN UNMANNED AERIAL VEHICLE. Mersin Photogrammetry Journal, 1 (1), 12-16.

Bünyan Ünel, F., Kuşak, L., Çelik, M., Alptekin, A. & Yakar, M. (2020). Kıyı Çizgisinin Belirlenerek Mülkiyet Durumunun İncelenmesi. Türkiye Arazi Yönetimi Dergisi, 2 (1), 33-40.

Çelik M Ö, Yakar İ, Hamal S N G, Oğuz G M & Kanun E (2020). Sfm tekniği ile oluşturulan 3B modellerin kültürel mirasın belgelenmesi çalışmalarında kullanılması: Gözne Kalesi örneği. Türkiye İnsansız Hava Araçları Dergisi, 2(1), 22-27.

Kusak, L., Unel, F. B., Alptekin, A., Celik, M. O., & Yakar, M. (2021). Apriori association rule and K-means clustering algorithms for interpretation of pre-event landslide areas and landslide inventory mapping. *Open Geosciences*, *13*(1), 1226-1244.

Mörel A (2019). Kümbetbeleni Komenin (Doğu Dağlık Kilikia Bölgesi) Roma Dönemi Mezarları. Colloquium Anatolicum 2019/18, 93-121.

Naycı N (2020). Architectural inventory and building condition assessment research on masonry structures of Kanlıdivane archaeological site, Mersin. Cultural Heritage and Science, 1(1), 32-38.

Parrot (2021). Anafi white paper v1.4. Retrieved from: https://www.parrot.com/assets/s3fs-public/2021-02/anafi-product-sheet-white-paper-en.pdf

Turkey Culture Portal (2021). Kanlidivane Ruins – Mersin. Retrieved from: https://www.kulturportali.gov.tr/turkiye/mersin/gezilecekyer/kanlidivane

Yakar M & Yılmaz H M (2008). Kültürel miraslardan tarihi Horozluhan'in fotogrametrik rölöve çalişmasi ve 3 boyutlu modellenmesi. Selçuk Üniversitesi Mühendislik, Bilim Ve Teknoloji Dergisi, 23 (2), 25-33.

Yilmaz, H. M., Yakar, M., Mutluoglu, O., Kavurmaci, M. M., & Yurt, K. (2012). Monitoring of soil erosion in Cappadocia region (Selime-Aksaray-Turkey). *Environmental Earth Sciences*, *66*(1), 75-81.

MERSİN UNIVERSITY

IGD
Intercontinental Geoinformation Days

ISBN: 978 - 625 - 44303 - 7 - 4

http://igd.mersin.edu.tr/